Dam-break Induced Scour and Pore Water Pressure Variations around a Vertical Structure

Marieh Rajaie

Thesis submitted to the University of Ottawa in partial fulfillment of the requirements for the

Doctorate in Philosophy Civil Engineering

Academic advisors:

Dr. Ioan Nistor, Dr. Colin D. Rennie, Dr. Amir A. Azimi

Department of Civil Engineering
Faculty of Engineering
University of Ottawa

Abstract

Coastal areas in many parts of the world are vulnerable to tsunami waves. Large tsunamis are strong enough to bring about a substantial amount of sediment mobilization. Several post-tsunami field investigations performed in recent years have documented destruction induced by scouring process. For example, the 1993 Nicaraguan earthquake centred 100km off the Nicaraguan coast caused devastating tsunami-induced scour around structures and bridges (Satake et al., 1993). Differences in the scour depths were related to soil properties, shapes of structures, and tsunami hydrodynamics (Jayaratne et al., 2016). Furthermore, depending on the soil permeability, the flow and pressure propagate at different speeds within the soil, which affects water table fluctuations and the soil strength (e.g., Tonkin et al., 2003; Yeh and Li 2008).

The primary objective of this research was to study the effect of different inland-propagating dam-break bore heights on pore pressure variations and scour evolution in saturated beds with two different bed slopes (i.e., zero and +5% slope) by performing comprehensive laboratory studies at a 1:40 scale. To achieve the objective, tsunami-like dam-break bores generated by rapidly opening a swing gate and propagated towards and over a sediment section and hit a structure centred within a sediment bed. The secondary objective of this experimental investigation was finding a relation between scour depths and pore pressure values as a function of still-to-impoundment water depth ratio.

The results of this experimental investigation showed that effective pore pressures were consistently greater in the front face of a model than in the side face. Besides that, the highest effective pore pressures took place near the saturated bed surface. Such that, due to the propagation of supercritical bores the maximum effective pore pressure in the bottom of the front corner was 50% larger than the exact same location in the side face. While, this difference decreased to 10% in the case of subcritical bores. For the same hydrodynamic bore conditions, the maximum difference between effective pore pressure in the two faces of the model reduced by 70% in the inclined bed test than the horizontal bed tests and this difference was only 15%. However, the peak effective pore pressure around the model doubled in the inclined bed tests compared to the horizontal ones. The 5% upsloping decreased the maximum scour depths by two times as a result of the same hydrodynamic loading conditions.

Keywords: Dam-break bores, pore pressure variations, scour depths, inclined bed

Acknowledgement

I would first and foremost like to express my greatest gratitude to my uOttawa supervisors Professor Ioan Nistor and Professor Colin Rennie for all they have done. They provided me with unconditional guidance, opportunities, and support throughout my PhD studies. Moreover, I would like to acknowledge and thank also Dr. Azimi for joining this study; his supervision, valuable advice, and comments are much appreciated. Collectively, they sparked my interest, helped me grow as a researcher, and made my PhD study an enjoyable journey. Without their meaningful contributions and endless encouragement, nothing would be accomplished.

I would like to thank the large group of people that, in some capacity, assisted me during my PhD. uOttawa's lab technicians, Mr. Mark Lapointe, Mr. Leo Denner, and Mr. Jean Claude Célestin who were of great help and support for conducting the experiments in the Hydraulic and Geotechnical labs. I would also like to thank all the graduate students from Germany and France, who helped me to varying degrees with this project.

It's hard to put into words the appreciation I feel for my parents. They have offered encouragement and support my entire life, especially during my PhD despite being so far away from each other. Every single word of this thesis is dedicated to them and I attribute my future success to my parents for their endless support and love. Thanks to my beloved and caring sister, whom I am very grateful for having close by during these years, for her encouragement made seemingly insurmountable prospects feel possible. Thanks to my fiancé for always being by my side, celebrating my successes, and lending me strength for challenging periods. I consider myself honored and blessed, and love everyone who has been there for me all the more for it.

Lastly, I would like to acknowledge the University of Ottawa PhD International Scholarship and the NSERC Discovery grants of Prof. Nistor and Prof. Rennie for their financial support throughout my PhD in various capacities.

Table of Contents

List of Figures

List of Tables

List of Acronyms

ADV Acoustic Doppler Velocimeter

CFD Computational fluid dynamic

FEM Finite element method

FVM Finite volume method

GN Green-Naghdi equations

KFVS kinetic flux vector splitting

PTV Particle tracking velocimetry

SNR signal-to-noise ratio

SWE Shallow water equations

US Ultrasonic wave sensor

VIS Virtual instrument subroutines

VOF Volume of fluid

WG Wave gauge

3D Three-dimensional

List of symbols

B= Flume width (m)

B′ = Skempton's coefficient (-)

b = Width of the obstacle (structure) (m)

C_o= Initial velocity upon removing a vertical gate (m.s^{-1})

C_s = Compressibility of the soil grains

c_1 = Model parameter (-)

c_2 = Model parameter (-)

c_3 = Model parameter (-)

c_f = Friction coefficient

c_v = Terzaghi's coefficient of consolidation (m^2.s^{-1})

c' = Cohesion intercept (-)

D = Diameter of structure (m)

d= Diameter of sediment (mm)

d_{50}= Median diameter (mm)

d_b= Center to center spacing between the piers (m)

d_{sb} = Discharge per unit width (m^2.s^{-1})

d_o = Impoundment depth (m)

d = Diameter of sediment (mm)

e= Void ratio (-)

Fr = Froude number (-)

Frc = Critical Froude number (-)

f = Darcy friction factor (-)

f_N = Nyquist frequency of signals (–)

g = Gravitational acceleration (m.s^{-2})

H_o= Wave height (m)

h = Flow depth (m)

h_o= Still water depth (m)

h_M = Maximum flow depth (m)

h_{max}= Maximum bore depth (m)

hs = Soil depth (m)

h_1 , h_2 = Water depths at a normal and a contracted place (m)

Δh= Total head between to points (m)

I= Specific impulse (N.s)

I_p = Plasticity index (-)

Gs= Specific gravity of soil particles (kg/m^3)

K= Constant (-)

K_a= Correction factor for flow approach angle (-)

K_s = Bulk modulus of the soil bed (kg.m^3)

K_g= Bulk modulus of the soil grains (kg.m^3)

K_ω= Water bulk modulus (kg.m^3)

k = Von Karman's constant (-)

k'= Permeability (m/s)

k_f = Fitting parameter (-)

k'_x,= Soil permeability coefficient in x, y, and z direction (m/s)

k'_y = Soil permeability coefficient in x, y, and z direction (m/s)

k'_z = Soil permeability coefficient in x, y, and z direction (m/s)

L= Waterway length (m)

ΔL= Vertical distance between to points (m)

M= Specific momentum flux per unit width (m^3·s^{-2})

N = Element shape parameter (-)

n = Soil porosity (-)

P = Pore pressure (kPa)

P_{atm} = Atmospheric pressure (kPa)

P_o = Absolute pressure (kPa)

P_a = Air pressure (kPa)

P_e = Excess pore water pressure (kPa)

P_m = Maximum pore pressure (kPa)

P_s = Static pore pressure (kPa)

P_t = Total pore pressure (kPa)

P_h = Pressure variation due to water depth above the soil (kPa)

PWP= Pore water pressure (kPa)

ΔP= Pore pressure variation (kPa)

Q = Flow discharge ($m^3.s^{-1}$)

q_{st} = Volumetric sediment transport rate per unit movable width of scour hole at time t ($L^2.T^{-1}$)

q_{vt} = Volume of scour hole (m^3)

R_o= Rouse number (-)

R= Waterway ratio (-)

Re^* = Particle Reynolds number (-)

S= Equilibrium scour depth (m)

S_{max}= Maximum scour (m)

S_r = Degree of saturation (-)

S_{sf}^{max}= Non-dimensional final scour (-)

S_o = Bed slope (-)

s = Proportion of sediment grain density to water density (-)

T_o = Non-dimensional gate opening time (–)

ΔT= Time duration (s)

Δt = Time increment (s)

t = Time corresponding to the wave location (s)

t_m = Time to reach to maximum pore pressure (s)

t_o= Manually-achieved gate opening time (s)

t_M = Time to peak maximum flood (s)

t_n = The upper limit of the non-dimensional time integration (s)

t_o = Gate opening time (s)

t_R= Reference time (s)

t_{end} = Hydrograph duration (s)

U = Bore front velocity ($m.s^{-1}$)

U = Maximum of the flow velocity ($m.s^{-1}$)

U_c = Critical velocity ($m.s^{-1}$)

U_R = Reference velocity ($m.s^{-1}$)

u = Flow velocity ($m.s^{-1}$)

u^* = Shear velocity ($m.s^{-1}$)

u_{ave}= Average velocity ($m.s^{-1}$)

u_c= Critical depth-averaged velocity able to transport sediment ($m.s^{-1}$)

$u_c(z)$ = Flow velocity at a vertical distance of z above the bed surface ($m.s^{-1}$)

u_z = Flow velocity near the bed surface(m.s^{-1})

V_O= Initial wave velocity (m.s^{-1})

V_M = Parameter size (m)

ν_u = Undrained Poisson's ratio (-)

ν_p= Poisson's ratio (-)

W= Waterway width (m)

W*= Dimensionless effective flow work (-)

W_1 , W_2 = Normal and contracted width of waterway (m)

w_s= Sediment settling velocity (m.s^{-1})

X = Longitudinal coordinate (m)

Y = Lateral coordinate (m)

Y_{max}= Difference between depth of water at a normal location and contracted place upstream (m)

Z = Vertically upward coordinate (m)

z=Initial soil level (m)

z_o = Bed surface roughness height (m)

z_{scour}= Scour depth (m)

θ= Shields parameter (-)

θ_c= Critical Shields parameter (-)

τ = Bed shear stress (N.m^{-2})

σ = Total normal stress (N.m^{-2})

σ_{vo} = Normal stress due to soil depth (N.m^{-2})

σ' = Effective normal stress (N.m^{-2})

σ_* = Sediment nor-uniformity parameter (N.m^{-2})

σ_f' = Effective normal stress in a failure situation (N.m^{-2})

σ_x = Effective normal stress (N.m^{-2})

σ_z = Dimensionless normal stress (-)

$\Delta\sigma_{xx}$ = Variations of normal stress in x direction (N.m^{-2})

$\Delta\sigma_{yy}$ = Variations of normal stress in y direction (N.m^{-2})

$\Delta\sigma_{zz}$ = Variations of normal stress in z direction (N.m^{-2})

ε = Tensiometer distance from the soil surface (m)

ρ_w = Water density (kg.m^{-3})

ρ_s = Sediment density (kg.m^{-3})

ρ_{sat} = Saturated soil bulk density (kg.m^{-3})

φ = Angle of repose (°)

dp = Pressure variation along with the flow and induced by the structure-soil interaction (N.m^{-2})

μ = Flow dynamic viscosity (kg.m^{-1}.s^{-1})

ψ = Friction coefficient (-)

φ' = Angle of shearing resistance (°)

α= Bed slope (°)

β= Ratio diffusion to momentum diffusion (-)

β'= Water compressibility (Pa^{-1}),

β_c = Water storage capacity (Pa^{-1})

ν = Kinematic viscosity (m^2.s^{-1})

γ_b = Buoyant specific weight of the saturated soil (N.m^{-3})

γ_{sat} = Specific weight of saturated soil (kN.m^{-3})

γ_w = Unit weight of water (N.m^{-3})

Λ = Scour enhancement (-)

Chapter 1. Introduction

1.1 Background

A tsunami is a series of waves generated by underwater sources like earthquakes, volcanic eruptions, and landslides. The most recent tsunami events have occurred due to subduction zone earthquakes, resulting in huge water columns rapidly being displaced vertically (Al-Faesly, 2016). In deep water, when a tsunami wave is generated, it has a gentle slope which sometimes makes it unnoticeable, but as it approaches a coastline, the height increases and the velocity changes. Upon reaching the coast, the wave can have a tremendous force and create massive damage as it penetrates the sediment.

The United States' Federal Emergency Management Agency (FEMA) P-646 design guideline (2012) sorts tsunami waves based on the location of their trigger point, as near-source-generated, and far-source-generated. In near-source-generated events, the source is close and can reach the site in 30 minutes. In the case of a far-source-generated tsunami, it usually takes 2 hours or more for the wave to reach shores. Tsunami waves are characterized and distinguishable based on their shapes, and depending on how far away they originate, they may have foaming, steep, or violently turbulent fronts. The 2004 Indian Ocean Tsunami caused a wide range of structural devastation due to scour development under building foundations (Figure 1-1) (FEMA, 2019).

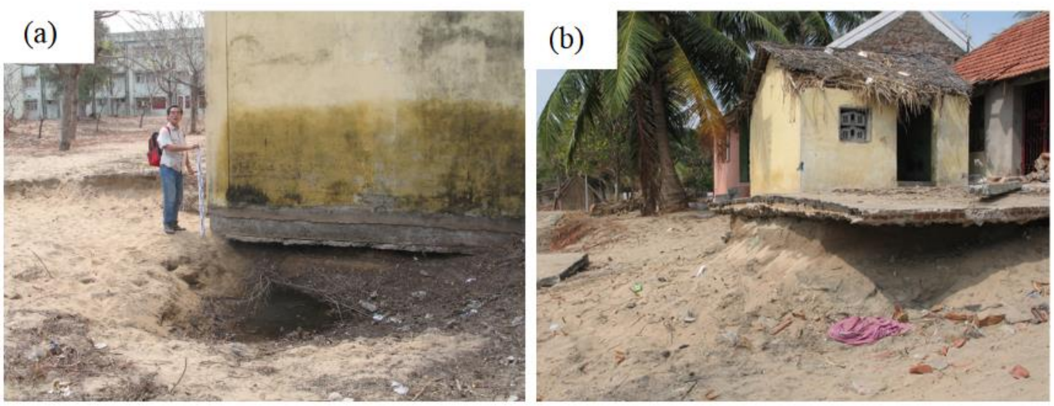

Figure 1-1. Scour holes around foundations of residential structures after the 2004 Indian Tsunami: a) around 1.5 m depth; and b) 1.4 m depth (Yeh and Li, 2008)

Generally, scouring results from the motion of sediment subjected to a shear force generate by flow velocity, and as this velocity increases, a deeper scour hole is expected. The degree of scour can be affected by factors such as: 1) a gradual increase of pore pressure in the soil (called residual liquefaction); 2) a sudden decrease in total normal stress; and 3) drainage of water to a region which leads to pore pressure variations within the soil that cause upward seepage (Yeh and Li, 2008). Pore pressure variations can appear during tsunami loading within soil with low permeability, and then high pore pressure remains for a longer time (Yeh and Li, 2008). Two stages of scouring happen during a tsunami incident. The first occurs when the wave first propagates up a sediment bed; during this stage high bed shear stress leads to a moderate degree of scouring. It is noteworthy to point out that the maximum depth of scour may be seen during the drawdown stage (Yeh and Li, 2008). This is because residual high pore pressures from the passage of the first wave can lead to liquefaction and upward seepage in the soil as the flow depth over the soil recedes during drawdown. Excess pore pressure can be equal to or greater than the submerged weight of the soil, which means that resultant effective normal stress equals zero (Zen and Yamazaki, 1991), leading to liquefaction conditions. Pore pressure magnitude increases under a wave crest and conversely decreases under a trough (Wang et al., 2020).

Tsunami incidents often result in considerable damage to coastal infrastructure. For example, the Tohoku Tsunami in 2011 generated devastating waves that scoured and deposited a huge volume of sediment along the shoreline, and tsunami-induced currents even reached harbors in California, USA. Post-tsunami field surveys in affected areas showed the direct influence of deep man-made channels along the coastlines on decreasing potential scour depth (Wilson et al., 2012). An in-depth field survey performed by Richmond and colleagues in May 2011 near Sendai in Japan mainly focused on erosion and sediment deposition mapping, and also tsunami wave features. These detailed reports showed inundation depths of 11 m above mean sea level within 500 m of the shoreline, which gradually decreased to 3 m at a distance of 2 km from the coast. As a result of flow acceleration due to hitting obstructions, sediment erosion around structures with an average depth of 0.5 m was one of the most frequently observed phenomena (Richmond et al., 2012).

Similarly, after the Indian Ocean Tsunami in 2004, comprehensive investigations were conducted in the affected regions (e.g., Rossetto et al., 2007). With a magnitude of 9, the triggering earthquake was considered to be the second-biggest earthquake ever recorded, after the Chile earthquake in 1960, and was felt in nine countries around the Indian Ocean. Different inundation depths were observed during the field survey. Along the southwestern coast of Sri Lanka, the average inundation depth was 4.5 m above sea level, and the maximum depth was 10 m in Kahawa. The highest runup was recorded in Thailand, at about 6 m, with a peak of 11 m in Khao Lak. The maximum velocity in the tsunami-induced runups as recorded by cameras was 6-8 m/s in Khao

Lak, Thailand. The severity of the damage differed depending upon structural vulnerability, differences in water-induced forces, vegetation in the coastal areas, and bathymetry. Documented observations revealed scour as one of the main causes of the damage (Figure 1-2) (Rossetto et al., 2007).

Figure 1-2. Collapsed bridge due to scour and erosion around its abutment (Rossetto et al., 2007)

The recent tsunami in Palu City, Indonesia, in September 2018, with a magnitude of 7.5 was investigated by many experts in this field. Tsunami inundation in Besusu Barat, east of the Palu River, reached up to 250 m inland, while the runup 550 m east of Patung Kuda reached 180m inland. Many structural failures were reported to have occurred due to scour and liquefaction around foundations (Paulik et al., 2019).

1.2 Thesis objectives

The main objective of this study was to attempt to find a relation between pore pressure variation and scour development under unsteady tsunami-like bores, while considering the effects of various tsunami-like bore heights and bed slopes in a saturated bed condition. This study also attempted to contribute to the provisions of the ASCE7 Chapter 6 by combining a part of the obtained results with a series of scaled experimental previously conducted with the goal of plotting the normalized scour depth versus the Fr number (ASCE7-16, 2016). The goal of these recommendations is to provide guidance for the design of nearshore infrastructures against the destructive effects of tsunami inundation (see Appendix A). Thereby, the overall objectives of this research are as follows:

1- Developing and conducting a comprehensive experimental program on scour around a structure due to the propagation of tsunami-like hydraulic bores.
2- Conducting measurements of the time history of the flow velocity propagating over a sand bed section as a function of various still-to-impoundment depth ratios and two different slopes in a saturated bed condition in order to study the effects of these variables on the flow velocity.
3- Conducting measurements of the time history of water surface elevation at various locations of interest along the flume and the time history of runup to study the effects of various still-to-impoundment depth ratios, two different bed slopes, and that of a saturated bed condition.
4- Conducting measurements of the time history of pore pressure variations around the structural model installed at the center of the sand bed section in order to investigate the effects of different impoundment and still water depths, bed slopes, and a saturated bed condition on the pore pressure spatio-temporal variation.
5- Conducting measurements of the spatio-temporal scour evolution around the structural model as a function of different impoundment and still water depths, bed slopes, in a saturated bed condition.
6- Calculating the variations of effective normal stress as a function of pore pressure values and scour depths influenced by different impoundment and still water depths, bed slopes, and a saturated bed condition.

1.3 Novelty

Results of forensic engineering tsunami field investigations demonstrated that 50% of observed structural failures occurred because of sediment scouring around structure foundations (Kato et al., 2012). This study aimed to investigate the local scouring process and pore pressure variations around a square model affected by various parameters (flow hydrodynamic conditions, bed slope in a saturated bed) to better understanding of these phenomena and improve the current design guidelines. More importantly, the tsunami waves in previously conducted studies using solitary waves which resemble wind waves after scaling up (Larsen et al., 2018; Madsen et al., 2008). Thereby, the difficulties in simulating tsunami waves at a small scale brought about the lack of realistic investigations, especially when it comes to the presence of a sufficiently long sustained inundation flow. Examination of induced scour and pore pressure changes in soil due to tsunami-like bores propagation has so far been studied by Tonkin el al. (2003), Qi et al. (2012), Nakamura et al. (2008a), and McGovern et al. (2019); however, in all these studies a piston was used to generated solitary and regular waves.

Thereby, the novelty of this study can be synthesized as follows: For the first time, the applicant investigated scour evolution and pore pressure spatio-temporal variation around a squared-shape model due to hydraulic bores generated by varying impoundment depths, different bed slopes, in saturated bed condition. Furthermore, this study focused on coupling interactions of scour depth and pore pressure variations with considering the effective normal stress and soil liquefaction around the model. The dam-break tsunami-like bore generating method was used to represent tsunami inundation. This method was demonstrated to provide hydraulic bores consistent with scaled-down tsunami waves in terms of their hydraulic characteristics (Chanson, 2006).

1.4 Scope of the thesis

The objective of this study was to provide a comprehensive experimental investigation on the relation between pore pressure propagation and scour development due to inland-propagating unsteady tsunami-like bores with different depths over a saturated bed with having two different bed slopes. Due to the time and physical constraints of the laboratory environment, this study possesses some inherent limitations:

- Due to limitations in the laboratory facilities, prototype scale tests could not be conducted. The experimental studies were performed at a geometric scale of 1:40.
- The experimental investigation did not include different structural sizes and/or shapes.
- The different sediment sizes or the layered ones were not studied in this physical modeling investigation and an idealized topography was executed.
- Due to the lack of field data of scour measurements during the tsunami incidents, the results of this experimental study could not be compared with field data; however, the candidate used a few available field data together with the results of this physical modeling which were included in the recommendation proposed for in ASCE7 Chapter 6 (ASCE7-16, 2016).
- Though significantly longer than the bores generated by solitary waves employed by previous researchers, the duration of the sustained flow used in this study was less than the scaled-down prototype. This is due to limitations related to the volume and size of the reservoir.

- In this study, the reverse (drawdown) flow was not considered due to the limitations of the flume. The candidate recognizes the importance of the drawdown flow in the scour process and recommends that this be investigated in future studies.

1.5 Contribution

1.5.1 ASCE7-16 change proposal

The current experimental results were included in the new revised proposal for section 6.12.2.4.1 Sustained Flow Scour of the ASCE 7 guideline, Chapter 6 on Tsunami Loads and Effect (Thesis: Appendix A). The proposal was balloted and accepted successively by all levels of approval of the ASCE standard committee.

1.5.2 Journal publications

Marieh Rajaie, Amir H. Azimi, Ioan Nistor, Colin D. Rennie. 2019. "Experimental investigations on hydrodynamic characteristics of tsunami-like hydraulic bores impacting a square structure ." submitted to Journal of Hydraulic Engineering, in review (Thesis: Chapter 3).

Marieh Rajaie, Amir H. Azimi, Ioan Nistor, Colin D. Rennie. 2021. " Experimental investigations on the impact of tsunami-like hydraulic bores on a square-shaped structure (Part 1): pore pressure variations." submitted to Journal of Waterway, Port, Coastal Engineering, ASCE, in review (Thesis: Chapter 4).

Marieh Rajaie, Amir H. Azimi, Ioan Nistor, Colin D. Rennie. 2021. " Experimental investigations of tsunami-like bores impacting on a vertical structure, Part II: local scour." submitted to Journal of Waterway, Port, Coastal Engineering, ASCE, in review (Thesis: Chapter 5).

Marieh Rajaie, Amir H. Azimi, Ioan Nistor, Colin D. Rennie. 2021. " Experimental investigations on the relation among dam-break bores induced excess pore pressure, liquefaction, effective normal stress, and scour evolution around a rigid structure ." (Thesis: Chapter 6).

1.5.3 Conference publications

Marieh Rajaie, Amir H. Azimi, Ioan Nistor, Colin D. Rennie. 2020. " Experimental Investigation of Tsunami-like Hydraulic Bore Front Velocity and Total Head on Two Different Bed Slopes (Abstract acceptance)." Coastlab2020 conference, Online.

Marieh Rajaie, Amir H. Azimi, Ioan Nistor, Colin D. Rennie. 2020. " Turbulent Bores–Induced Scour and Pore Pressure Variation Around a Vertical Structure." Online presentation, ICCE.

1.6 Outline of the thesis

The thesis comprises the following sections:

- **Chapter 1** outlines the current study's objectives, scope, novelty, contributions, and publications developed from this study.
- **Chapter 2** provides a comprehensive literature review on experimental and numerical investigations to study scour development and the variations of pore pressure values induced by tsunami-like bores. Moreover, this chapter consists of definitions of erosion, different types of scour, equations to estimate final scour depths. At the end of this chapter, is the research needs stemming from this review are discussed.
- **Chapter 3** provides a detailed analysis of hydrodynamic aspects of inland-propagating tsunami-like bores carrying out experimental work. The journal publication is now under its final revision in the Journal of Hydraulic Engineering (ASCE7-16, 2016), and is titled "Experimental investigations on hydrodynamic characteristics of tsunami-like hydraulic bores impacting a square structure". Different characteristics of a generated bore depths, bore velocity, specific momentum flux and the specific impulse of bores are assessed.
- **Chapter 4** describes the effects of various still-to-impoundment depth ratios and bed slopes on the spatio-temporal pore pressure variation around the model. Furthermore, it examines the effects of these variables on the occurrence of maximum pore pressure and its corresponding time. Finally, the contour plots of pore pressure variations around the structural models affected by different hydrodynamic bores are presented. This paper is in its first review in the Journal of Waterway, Port, Ocean, and Coastal Engineering (ASCE7-16, 2016), and is titled "Experimental investigations on the impact of tsunami-like hydraulic bores on a square-shaped structure (Part 1): pore pressure variations".
- **Chapter 5** aims to investigate scour evolution over time around the structural model impacted by various still-to-impoundment depth ratios and bed slopes. In addition, normalized maximum scour depths and normalized equilibrium scour depths observed around the model are studied as a function of various still-to-impoundment water ratios and bed slopes. This paper is in the first review in the Journal of Waterway, Port, Ocean, and Coastal Engineering (ASCE7-16, 2016), and is titled "Experimental investigations of tsunami-like bores impacting on a vertical structure, Part II: local scour".

- **Chapter 6** examines the relation between the dam-break bores induced excess pore pressure, liquefaction, effective normal stress, and scour evolution around the structural model as a function of different still-to-impoundment depth ratios ranging from 0.075 to 0.28, two bed slopes, and two flow regimes. The article is in revision state and is titled "Experimental investigations on the relation between the dam-break bores induced excess pore pressure, liquefaction, effective normal stress, and scour evolution around a rigid structure".
- **The Appendices** consist of the contribution in ASCE 7 Chapter 6 - Tsunami Loads and Effect (Appendix A) and the scaling effect (Appendix B).

Chapter 2. Literature Review

2.1 Scour generation mechanism

The Shields parameter is a fundamental criterion used to determine the incipient motion of sediment. This number is the proportion of shear stress to buoyant sediment weight and is depicted as follows:

$$\theta = \frac{\tau}{\rho_w g d(s-1)} = \frac{f u^2}{8 g d(s-1)} \quad (2\text{-}1)$$

where τ is the bed shear stress, g is gravitational acceleration, ρ_w is water density, d is the diameter of sediment (d_{50}, a median diameter is often used), s is the proportion of sediment grain density to water density $(\frac{\rho_s}{\rho_w})$, u is flow velocity, and f is the Darcy friction factor. A critical Shields parameter is considered as a threshold for sediment movement that is roughly a constant number ($\theta_c = 0.04\sim 0.06$). Close scrutiny of the Shields diagram and the critical Shields parameter was done by Cao and colleagues in 2006 in order to explore the effect of the particle Reynolds number ($Re^* = u^* d_{50} / \nu$) on the critical Shields parameter. Note that u^* is shear velocity and ν is kinematic viscosity. Initially, they provided a logarithmic diagram for critical Shields variations versus particle Reynolds number (Figure 2-1), but it was realized that for $Re^* \leq 6.61$, as the particle Reynolds number increases, the critical Shields parameter decreases, whereas for $Re^* \geq 282.84$, the critical Shields number could be assumed as a constant value (Cao et al., 2006).

$$\theta_c = 0.1414\, Re^{*-0.2306} \quad , Re^* \leq 6.61 \quad (2\text{-}2)$$

$$\theta_c = 0.045 \quad , Re^* \geq 282.84 \quad (2\text{-}3)$$

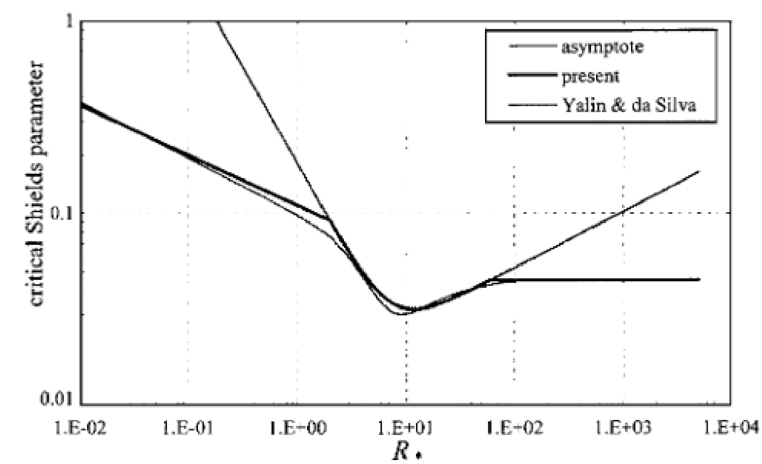

Figure 2-1. Relationship between particle Reynolds number and critical shear stress (Cao et al., 2006)

Scour is the process by which, as a result of sediment erosion, soil and materials covering a foundation move with the flow patterns downstream. Subsequently, the foundation becomes exposed to the water and the structure resistance decays, which could be considered as the main threat (Khan et al., 2016). About 60% of bridge structural failures occur because of scour (Lagasse et al., 1997). Scour formation can be divided into three main groups depending upon the main cause, as 1) local scour, 2) contraction scour, and 3) general channel degradation. If an obstacle is present in a waterway, the flow pattern changes into three dimensions and creates eddies around the obstruction. This type of scour is called “local scour”. The second type happens because of the existence of an obstacle and a waterway contraction, which contributes to flow velocity increase and flow turbulence formation (Khan et al., 2016). The last classification is general scour, which takes place regardless of an obstacle’s existence as either short-term or long-term scour. Short-term scour occurs during a short time due to the shape of the channel or river, like scour at bends or braids within a channel, while long-term scour is normally seen over a longer timescale, e.g., several years. Degradation is an example of long-term scour in which a riverbed is lowered over a long period; furthermore, bank erosion incidents like meander migration and riverbed-widening are also examples of long-term scour (Coleman and Melville, 2001).

Scour formation is classified into two categories: 1) clear water and 2) live bed. In clear water scour formation, sediment upstream does not move, and the shear stress imposed on the bed due to the flowing water is less than the critical shear stress. In this case, the scour depth around a structure will reach its equilibrium condition when the flow is no longer able to drag particles out of the scour hole. In the case of live-bed scour, the particles transported by the flow and the scour reach the equilibrium condition when the amount of the removed sediments from the scour hole equals the amount of supplied material. Figure 2-2a describes the behaviour of sediment transport in the cases of clear-water and live-bed scour. As can be seen, the scour in the clear-water condition increases with time until reaching the equilibrium condition, while for live-bed scour, the sediment transport reaches its maximum depth faster than the clear-water condition; however, in the equilibrium condition, the depth of the scour hole in the clear-water condition is deeper than the live-bed condition (Figure 2-2b). The peak in live-bed scour decreases with time until reaching a stable condition (Raudkivi and Ettema, 1983).

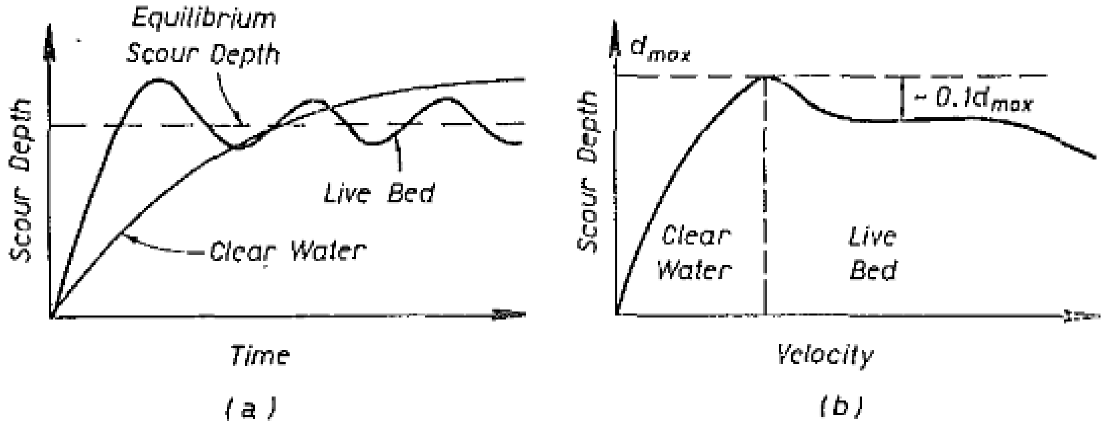

Figure 2-2. Scour hole development versus a) time and b) flow velocity (Raudkivi and Ettema, 1983)

The vortices formed around obstacles such as bridge piers are the main causes of scour hole development. The shape and strength of the vortex differ considerably with the shape of the obstruction and the vertical component of the flow velocity. As water flows downstream and hits a pier, the flow pattern and velocity changes lead to a variation in the flow distribution across the height of the pier and the generation of a horseshoe vortex at the bottom. In the case of a pier with a sharp nose, the flow separation occurs smoothly and the generated vortex will be more gentle. In contrast, in the case of piers with broad noses, destructive vortices are expected to evolve and extend further downstream (Breusers et al., 1977). In 1975, Melville conducted comprehensive physical modeling on flow patterns and scour hole evolution around a cylindrical pier, and it was found that the scour hole enlarged vertically as downward flows formed ahead of the pier. Also, the horseshoe vortices became more dominant in terms of size and circulation, even though their velocity diminished (Figure 2-3). At the back of the pier, downstream, rolling eddies called wake vortices are generated due to the flow separation and velocity changes within the wake region. These vortices are also influenced by the shape of the pier, and usually, wide-width piers have a stronger wake vortex (Melville, 1975).

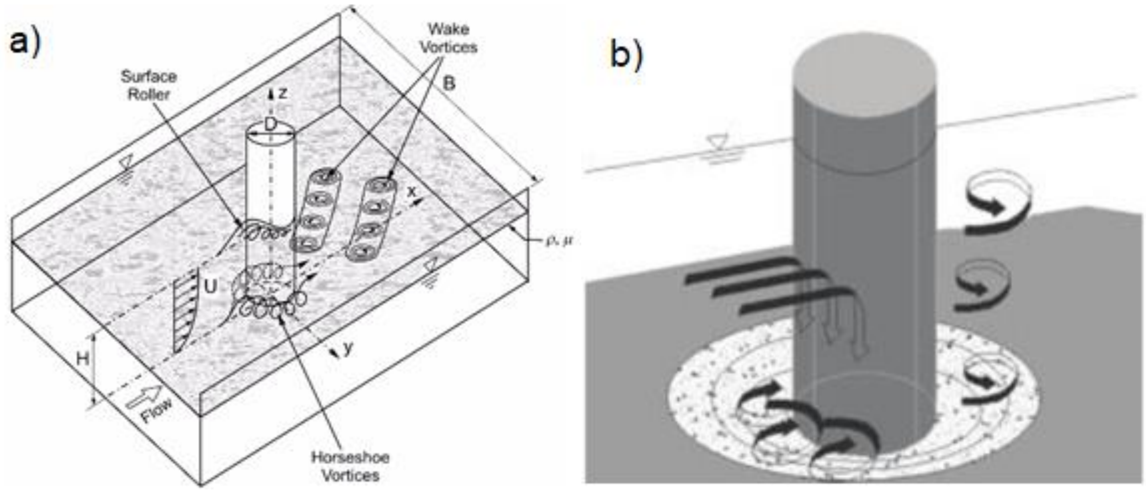

Figure 2-3. Main vortex formation around a pier: a) (Kirkil et al., 2005); b) (Khan et al., 2016)

Besides the shape of the obstacle, several other factors can affect the size and shape of the scour hole; e.g., contraction can impact the velocity by narrowing the waterway (Khan et al., 2016). It is also drastically affected by the bed materials. Scour holes are shaped quite differently in beds covered with cohesive materials compared to non-cohesive ones. While For cohesive materials, electromechanical bonding among particles governs the scour rate and depth (Ansari et al., 2003),

In ASCE chapter 6, there are comprehensive explanations on the effect of soil specification and water surface elevations on pore pressure generation and scour depth. Water surface variations and soil characteristics are two crucial parameters in designing the foundations of structures in coastal areas. As well, flow pattern changes around coastal structures and associated scour and sediment erosion should be taken into account in order to implement countermeasures such as barriers, ground improvement designs, and foundation protection. The design of deep foundations, like those built with pilings, is highly dependent on pore pressure variations and scour depth when the structure is subjected to tsunami inundation and loading. The maximum possible scour depths have been documented through research and observations conducted post-tsunami; moreover, advanced numerical analysis has helped to determine reasonable tsunami loadings. In terms of tsunami loadings and successive cycles such as runup and drawdown flows, it needs to be considered that areas around structures will remain flooded for some time and hydrodynamic pressures as it is exposed to the tsunami, and structural failure is likely to occur (ASCE7-16, 2016).

2.2 Estimation of future scour

Finding a formula to anticipate local scour depth under steady flow has been investigated extensively in the past, and the results of some of these studies are presented as follows:

$$Y_{max} = 0.32\,K.b^{0.62}.h^{0.47}.Fr^{0.22}.d_{50}^{-0.09} \quad \text{(2-4), (Froehlich, 1988)}$$

$$Y_{max} = 2.5\,h_1.(\frac{D}{h})^{0.6}.Fr^{2/3} \quad \text{(2-5), (Shen et al., 1966)}$$

$$Y_{max} = 1.5\,D.(\frac{h}{D})^{0.3} \quad \text{(2-6), (Neill, 1964)}$$

$$Y_{max} = 1.86\,D.\left(\frac{h}{D}\right)^{0.5}(Fr - Frc)^{0.25} \quad \text{(2-7), (Jain and Fischer, 1980)}$$

where K is a constant, b is the width of an obstacle, h is the flow depth upstream, Fr is the Froude number calculated based on this formula $(u)/(g*h)^{\wedge 0.5}$, Frc is the critical Froude number, and D is the diameter of a structure.

The Coastal Construction Manual 2000 edition provides a formula to calculate the scour depth around a rectangular-shaped obstacle:

$$S_{max} = 2.2\,h.\left(\frac{b}{2}\right)^{0.65} Fr^{0.43}.K_a \quad \text{(2-8)}$$

where K_a is a correction factor for the approaching angle of flow (FEMA, 2000; Chock et al., 2011).

In recent years, in-depth investigations have been done regarding the effects of different parameters on the depth of scour holes, and finding a function that includes all the influential factors. For example, Tavouktsoglou and colleagues (2017) carried out a series of physical modeling tests under a steady-state condition to predict the equilibrium scour depth around cylindrical structures with uniform and non-uniform geometries and diameters of 0.15 to 0.9 m. Their wide range of experimental results was combined with those of previous studies, followed by numerical simulations. Tavouktsoglou et al. (2017) examined flow-soil-structure interactions using non-dimensionalized parameters:

$$\frac{S}{D} = f\left(\frac{\frac{dp}{d\varphi}}{u^2\rho}, \frac{u}{\sqrt{gh}}, \frac{u}{u_c}, \frac{uD\rho}{\mu}, \frac{h}{D}\right) \quad \text{(2-9)}$$

in which φ is the angle of repose, dp is the pressure in the streamwise direction induced by the structure, u_c is critical depth-averaged velocity capable of transporting sediments, and μ is the dynamic flow viscosity. Different shapes of structures in terms of geometry were examined in Tavouktsoglou et al.'s study (Figure 2-4), and structures with a monopile base showed a greater contribution to the amplification of shear stress than conical-base structures (Tavouktsoglou et al., 2017).

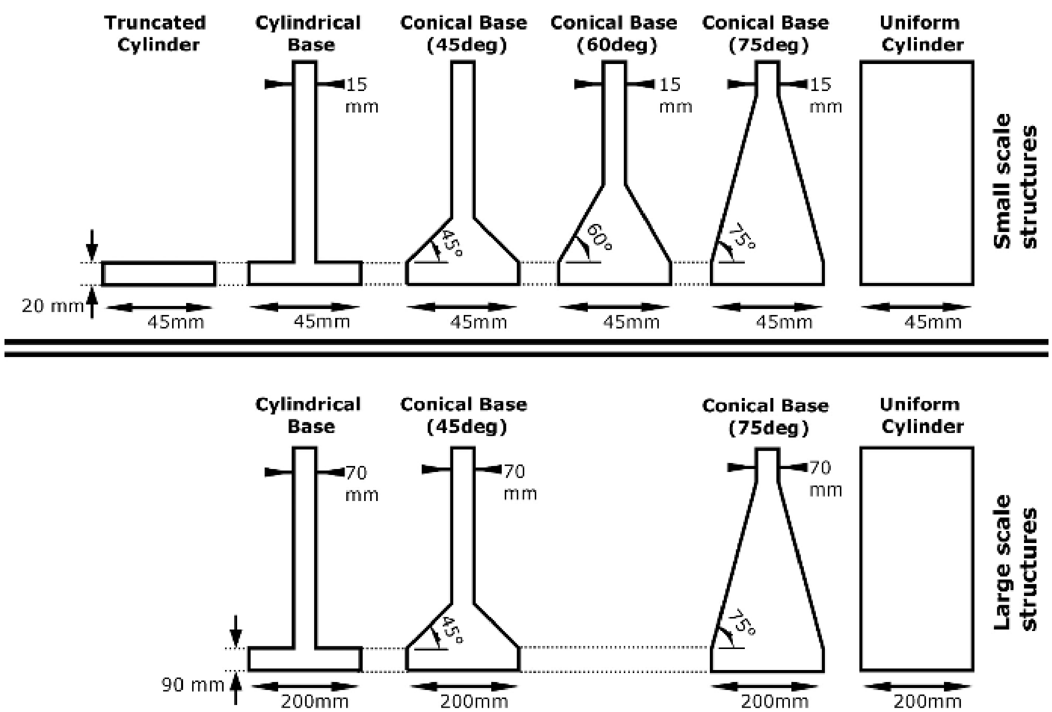

Figure 2-4. Different geometries used in Tavouktsoglou et al.'s study (Tavouktsoglou et al., 2017)

The combination of this study with the previous investigations led to a best-fit equation which illustrates the influence of the Reynolds number ((Re = u^*h/ν). The analysis of the experimental works revealed an inverse correlation between equilibrium scour depth and the Reynolds number, which is shown in the following formula (Tavouktsoglou et al., 2017):

$$S = 0.00022\, Re^{0.619} \tag{2-10}$$

In 2017, Mazumder proposed a different formula to calculate scour depths which depends upon the type of scour. For general scour, it was indicated that the formula suggested by Lacey in 1930 can be used to predict the maximum scour due to flowing water (Lacey, 1930):

$$S_{max} = KR \tag{2-11}$$

where K= 2 for piers and spill in abutments, K=1.27 for abutments with protected sloping riverside face, and K varies between 1.50 to 2.75 for bends depending on the location of scour.

When the waterway length is greater than its width (L > W):

$$R = 0.473(\frac{Q}{k_{sf}})^{\frac{1}{3}} \tag{2-12}$$

And R is defined for the restriction of (L < W):

$$R = 1.34(\frac{d_{sb}^2}{k_{sf}})^{\frac{1}{3}} \tag{2-13}$$

L is the sufficient clear waterway length in (m), and W is Lacey's width calculated by the following formula:

$$W = 4.8\, Q^{0.5} \tag{2-14}$$

$$k_{sf}=1.76(d_{50})^{0.5} \tag{2-15}$$

where Q is the flow discharge and d_{sb} is discharge per unit width (*Q/L*).

In the case of scour due to contraction, when clear-water or live-bed scour occur separately, previous researchers provided various equations to calculate the corresponding scour depths:

a) Clear-water

$$S_{max} = 1.48\, \frac{Q_2}{(d_m^{\frac{1}{3}}.W_2)^{\frac{6}{7}}}\ , \tag{2-16}$$

where,

$$d_m = 1.25\, d_{50} \tag{2-17}$$

b) Live bed

$$Y_{max} = (h_2 - h_1), \tag{2-18}$$

$$\frac{h_2}{h_1} = (\frac{Q_2}{Q_{1m}})^{\frac{6}{7}}(\frac{W_1}{W_2})^{K_1} \tag{2-19}$$

where W_1 and W_2 are the normal and contracted widths of a waterway and h_1 and h_2 are the water depths at a normal location and a contracted place upstream. K_1 varies between 0.59 to 0.69 for mostly transported bed loads and suspended ones, respectively (Mazumder, 2017).

Although most of the investigations in the past attempted to study the maximum scour depth in steady-state condition, in most cases in the natural incidence the scour forms due to propagation of unsteady flows. When unsteady flows take place the maximum discharge stays for a short time duration, so using scour-depth estimation equations in steady case for the same purpose in unsteady flows can cause overestimation for this depth.

The results of Kothyari et al. (1992) showed that the equilibrium scour depth is unsteady flows can be formulated as follows:

$$\frac{S}{d} = 0.99 * \left(\frac{h}{d}\right)^{0.67} \left(\frac{h}{d}\right)^{0.4} \alpha^{-0.3} \tag{2-20}$$

$$\alpha = \left(\frac{h-b}{b}\right) \tag{2-21}$$

in which, S is the equilibrium scour depth and d_b is the center to center spacing between the piers (Kothyari et al., 1992).

In 2011, Lu et al. suggested a developed equation through empirical studies to find scour depth around a cylindrical foundation due to propagation of unsteady flow:

$$d_{st} = \sqrt{\frac{6\tan\varphi}{\pi} q_{vt} + \frac{9D^2 \tan^2\varphi}{16}} - \frac{3D\tan\varphi}{4} \tag{2-22}$$

$$q_{vt} = \sum_{i=0}^{n} q_{st_i} \tag{2-23}$$

where q_{vt} is the volume of scour hole, q_{st} is volumetric sediment transport rate per unit movable width of scour hole (Lu et al., 2011).

Furthermore, the effect of flood as an unsteady flow on the final scour depth investigated experimentally which led to an empirical equation (Hager and Unger, 2010):

$$S = (0.068N\sigma_*^{-4/9} n^{-1/6}) \times (V_M^{3/2} t_M^{1/6} (g' d_{50})^{-2/3}) \times (h_M D^2)^{5/18} \tag{2-24}$$

where, N is element shape parameter, σ_* is sediment nor-uniformity parameter, n is hydrograph shape parameter, V_M is parameter size, t_M is time to peak maximum flood, ρ_s is sediment density, and h_M is maximum flow depth (Hager and Unger, 2010).

On the other hand, the effect of flow velocity and time on the formation and evolution of scour depth was investigated over some sequential equations. First, the effect of flow velocity and time of the dimensionless effective flow work which causes erosion examined (Link et al., 2017):

$$W^* = \int_0^{t_{end}} \frac{1}{t_R} \left(\frac{u_{ave} - 0.5U_c}{U_R} \right)^4 \delta dt \tag{2-25}$$

where, t_R is reference time, t_{end} is hydrograph duration, u_{ave} is average velocity, U_c critical velocity, U_R is reference velocity. Then, the associated scour connected to the dimensionless effective flow work as:

$$Z^* = c_1 (1 - e^{-c_2 W^{*C_3}}) \tag{2-26}$$

where, c_1, c_2, and c_3 are model parameters with values of 0.0075, 0.097, and 0.38, respectively (Link et al., 2017).

And finally, time-dependent scour evolution formulated as follows (Link et al., 2017):

$$\frac{dZ^*}{dt} = \frac{1}{t_R} \left(\frac{u_{ave} - 0.5U_c}{U_R} \right)^4 \delta c_1 c_2 c_3 \times \left[\int_0^{t_{end}} \frac{1}{t_R} \left(\frac{u_{ave} - 0.5U_c}{U_R} \right)^4 \delta dt \right]^{c_3 - 1} \times e^{\left[-c_2 \left(\int_0^{t_{end}} \frac{1}{t_R} \left(\frac{u_{ave} - 0.5U_c}{U_R} \right)^4 \delta dt \right)^{c_3} \right]} \tag{2-27}$$

2.3 Tsunami-bore induced scour

The geological specifications of affected areas can help address the intensity of soil-related damage. Long-period tsunami waves can result in shallower liquefaction depths, and moreover, tsunami-induced scour occurs in a shorter time span than river scour. Tsunami-induced scour is a combination of both live-bed and clear-water scour, as during runup, clear-water scour is predominant while as the wave moves back towards offshore, live-bed scour appears (FEMA, 2006). As noted by FEMA, there is a direct relation between scour depth and inundation velocity and depth (Figure 2-5). In September 2004, the preparation of a standard for designing structures capable of tolerating tsunami-induced forces was initiated by FEMA, and nowadays, this standard is widely used for designing coastal communities subject to tsunamis. In this guideline, the relationship between tsunami velocity and induced scour is described in the following figure.

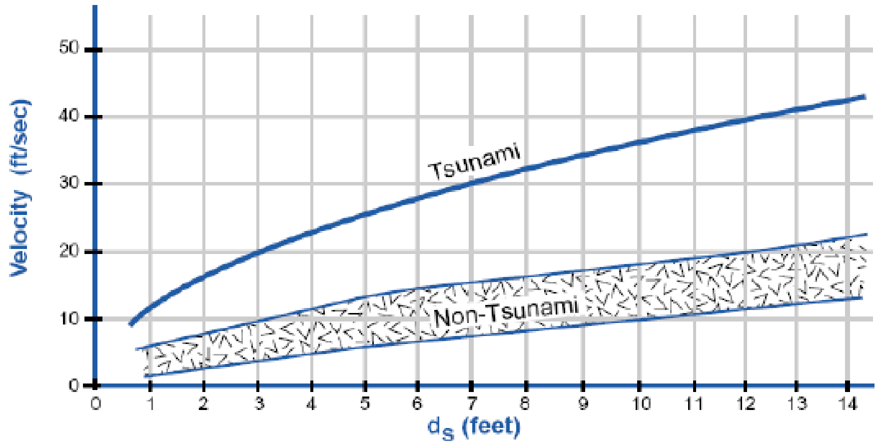

Figure 2-5. Tsunami velocity versus scour depth (FEMA, 2006)

Tsunami field investigations have documented useful information about the features of tsunami-induced scour, and based on the scour geometry and type of flow, it is categorized into six main groups, as follows.

Local scour is characterized by a deep scour hole next to the foundation of a structure. This scour can become deeper from the impact of pore pressure within the soil and losing the surrounding sediment (Tonkin et al., 2014).

Channelized scour occurs when a broad flow is conveyed into a focused area, and as a result, vertical scour forms along with a barrier (Tonkin et al., 2014).

General scour happens when a considerable portion of an area is lost because of either high flow velocity and the subsequent high shear stress acting on the soil, or liquefaction and a reduction of residual soil strength (Tonkin et al., 2014).

Sustained flow scour is formed by tsunami waves around coastal structures. This type of scour can be analyzed numerically and experimentally, along with studying the effect of liquefaction due to pore pressure variations (ASCE7-16, 2016).

Results of a series of scaled experimental studies are plotted in Figure 2-6 which suggests that regardless of the bed materials the upper envelope of normalized scour depth is constant for flows with Froude numbers higher than one (supercritical flow regimes) (Nistor et al., 2019).

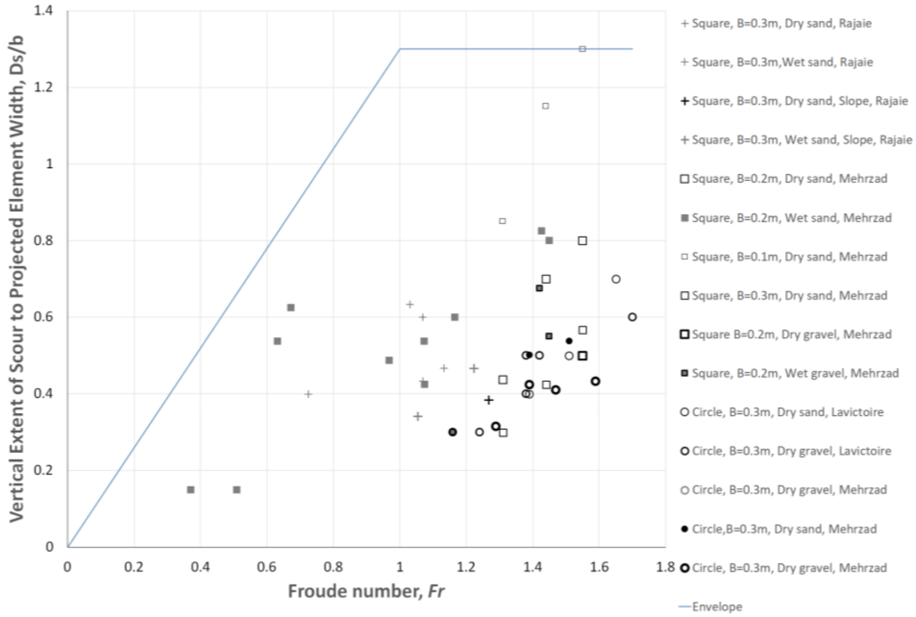

Figure 2-6. Correlation between normalized scour depth and Froude number (Nistor et al., 2019)

As suggested by Figure 8, a larger flow depth means more significant shear stress on a bed, which is the main reason for scour formation. The generated normal stress can be diminished by several mechanisms: 1) drainage of water through a seepage path from a high pore pressure region to a low pressure one, specifically during the drawdown process, which results in seepage erosion; 2) pore pressure accumulation within the soil because of the cyclic normal stress procedure, called “residual liquefaction”; and 3) a sudden reduction in the total normal stress, called “momentary liquefaction” (Yeh and Li, 2008). The analysis of previous studies on the relation between tsunamis and liquefaction shows that liquefaction development within a soil body is dependent on the tsunami’s wave height and period, and soil specifications, meaning that lower permeability can bring about deeper liquefaction (Francis and Yeh, 2006). Figure 2-7 depicts normal stress changes in the soil as a result of water elevation changes. The total normal stress (represented by σ_r) is calculated by the specific weight of soil and water. As the water flows back, the magnitude of this parameter will mitigate immediately due to the reduction in the height of the wave, and this brings about non-linear water table variations within the soil (Heibaum and Köhler, 2000).

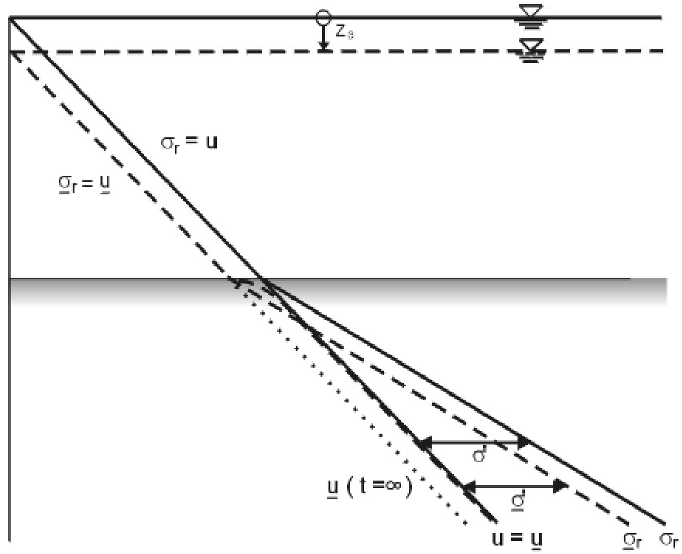

Figure 2-7. Normal stress within soil before and after drawdown stage (Heibaum and Köhler, 2000)

In the field observations conducted on the east coast of Japan after the Tohoku Tsunami, several collapsed buildings were inspected which had overturning failures due to liquefied soil underneath their foundations. Liquefaction can diminish friction between the foundation and the surrounding soil, and the bearing capacity of the soil decreases considerably. Rising and falling levels of a tsunami wave happen within a very short time and cause liquefaction; the combination of hydrodynamic forces and liquefaction has been considered as the influential factor in overturning buildings failures (Yeh et al., 2013). The likelihood of occurrence of liquefaction due to excess pore pressure can be assessed by considering the soil mechanics, which provides the grain size distribution curve of a soil sample and compares the S shape figure with a reference (Figure 2-8) (Sumer et al., 2007). During tsunami runup and drawdown, the water level on a beach can drop significantly, which causes excess pore pressure and a reduction of effective normal stress, making the beach prone to liquefaction failure (Young et al., 2009).

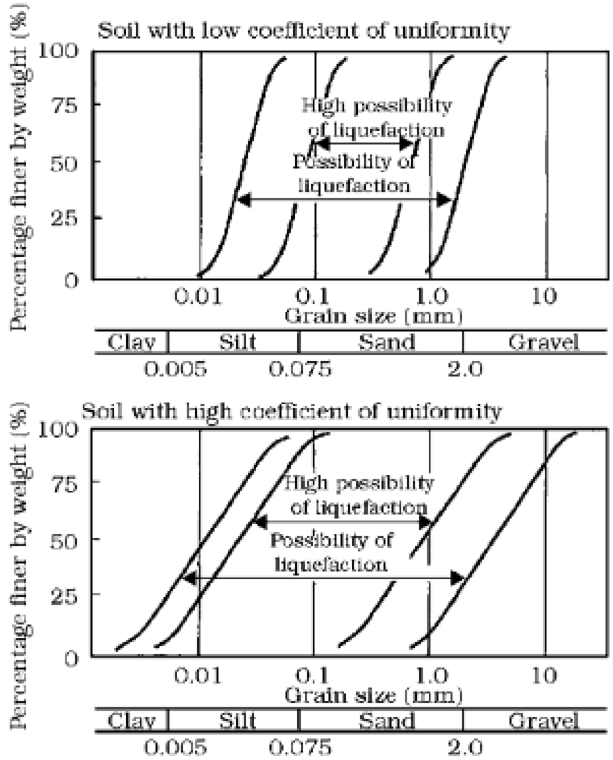

Figure 2-8. Grain size distribution curve with the presentation of the possibility of liquefaction occurrence (Sumer et al., 2007)

In a tsunami incident, sediment liquefaction can happen during the drawdown stage, leading to scour formation. At this stage, the water surface elevation and the flow velocity can decrease suddenly and create a vertical pressure gradient, causing a reduction in effective normal stress and the bearing capacity of the soil. The liquefaction phenomenon (or scour occurrence) is characterized by parameter Λ, which is the correlation between excess pore pressure and buoyant specific weight. $\Lambda = 1$ represents the equality of excess pore pressure and normal stress, which means that no resisting force remains among the soil particles and that the sediment can scour quickly. If $0 < \Lambda < 1$, the frictional forces are small and the sediments are unstable and prone to scour.

$$\Lambda = \frac{2}{\sqrt{\pi}} \times \frac{\Delta P}{\gamma_b \sqrt{c_v \Delta T}} \tag{2-28}$$

where c_v is the Terzaghi coefficient of consolidation, γ_b is the buoyant specific weight of the saturated soil, and ΔP is pore pressure variations in time duration of ΔT. Based on the results of laboratory experiments, the soil was slightly scoured out for $\Lambda \leq 0.5$ (Tonkin et al., 2003)

2.4 Soil mechanics concepts

A volume of soil skeleton encloses a combination of three main elements: water, soil particles, and air. After the application of different stress on soil, the soil particles and water act as incompressible, whereas air shows a compressible behavior. The ratio of compressibility depends upon the arrangement of soil particles which can be characterized by the void ratio, $e = Vv/Vs$ (in which V_v is the volume of voids and V_s is the volume of solid). As the water is considered an incompressible part, fully saturated soil can have compression and reduction in volume if the inner (pore) water is drained from the voids. However, in case of dry soils, the compression takes place due to the compression of the air trapped among the soil particles. Moreover, in fully saturated soil the normal stress can be withstood by an increase in pore pressure, whereas in the dry case the soil particles resist the applied normal stress (Knappett, 2012).

2.4.1 Principles of effective normal stress

In 1943 Terzaghi noticed the importance of applied forces on a soil skeleton and their transmission through the soil particles. The experimental results related the effect of three main stresses as follows:

$$\sigma = \sigma' + P \tag{2-29}$$

where

1. The total normal stress (σ) applied on a plane within the soil mass which is in fact the normal stress applied on the plane.
2. The pore water pressure (P) exists in a soil mass due to the presence of water in the void space between particles.
3. The effective normal stress (σ') applies on plane and only through soil particles as a result of interparticle forces

The pore water pressure imparts on the soil surfaces and in every direction. Presumably, if the water table is constant in the soil mass (which is called static pore pressure (P_s)) the soil particles move their positions and they rearrange tightly. In this case, if the particles move laterally no inner forces will be inserted on them unless the water is drained through the seepage paths. The pore water pressure consists of two main factors of static pore pressure (P_s) and excess pore pressure (P_e), and any increase in total pore pressure will be tolerated by the excess pore pressure. Terzaghi also figured out that if some degree of lateral displacement of the soil volume exists the particles can take up a new arrangement which causes a sudden increase in total normal stress. A hydraulic pressure gradient generated due to the increase in pore pressure and because of this hydraulic gradient the transient water flows to the draining boundary layers until the pore pressure decreases to the static pore pressure governed by the static water table. At anytime during the drainage process, the total pore pressure is affected by the sum of both static and excess pore pressures (Terzaghi, 1943):

$$P=P_s+P_e \tag{2-30}$$

At the initial stage of the drainage when the soil mass still includes the water it is called the undrained stage, but when the drainage starts and the excess pore pressure decreases gradually (dissipation state) the pore pressure would be equal to instantenous hydrostatic pressure ($P=P_s$) and in this stage the soil is in the drained condition. As drainage is taking place the soil particles will be rearranged, then the resulting inter-particles force will be effective, which increases the effective normal stress. The drainage can happen at different speeds depending upon soil permeability. This process is fast for soil with a high void ratio (high permeability), while in a low void ratio soil the drainage happens slower. The whole procedure is called consolidation (Knappett, 2012). The soil compression and behaviour are also governed by the combination of normal stress and pore pressure variation. This combination should be called effective normal stress as it is affected by both factors. Consolidation in saturated soil is mostly associated with changes in volume due to flow seepage through the soil voids. If the flow has enough time to seep into a drainage layer the soil volume can vary, otherwise pore pressure will be influenced (Atkinson, 2007).

Figures 2-9Ⅰ and 2-9Ⅱ show the effect of drainage and undrainage on the pore pressure and the effective normal stress. In Figure 2-9Ⅰa the total normal stress increases gradually due to a loading and at the same time the flow is able to seep out. As a result, the pore pressure is constant, but the effective normal stress increases. Finally, when the volume does not change both total and effective normal stress stay constant. But, in Figure 2-9Ⅱ the same total stress increment (loading) is applied on the soil mass quickly which does not let the interparticle water drain. Therefore, the pore pressure and the effective normal stress rise, consequently. After this initial phase, over time the volume and pore pressure slowly diminish while effective stress increases. As Figure 2-9II c presents, at the end of undrained loading the equilibrium pore pressure equals the initial hydrostatic pressure which means that the internal excess pore pressure causes some degree of drainage during the loading time leading to the volume change, decrease in excess pore pressure, and variations in the effective normal stress. It can be said that the consolidation (the volume change) is associated with the excess pore pressure changes over time. Importantly, at the end of the consolidation the values of pore pressure, the soil volume, the total and the effective normal stresses are same in both loading and unloading cases (Atkinson, 2007).

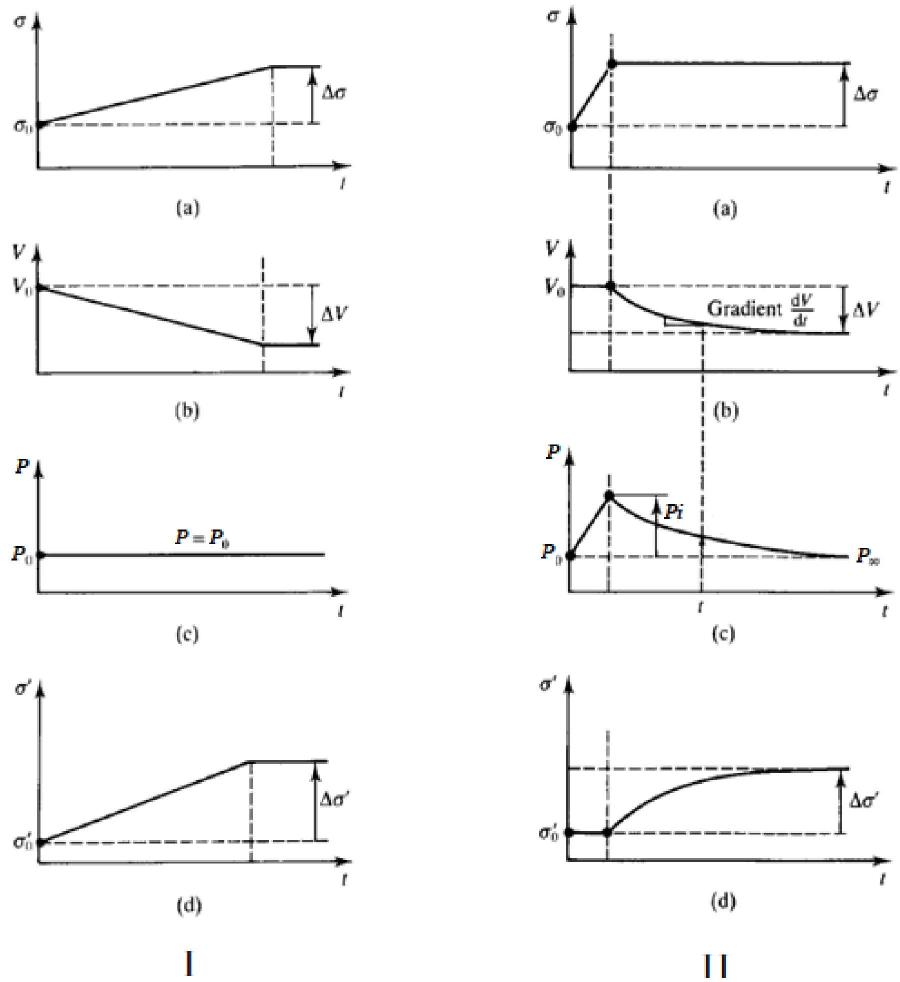

Figure 2-9. Pore pressure, soil volume and under I) drained loading; II) undrained loading (Atkinson, 2007)

The proposed formula by Terzaghi was developed in 1959 by Bishop. The developed equation considers the variation of effective normal stress in dry and partially saturated soils. In the partially saturated soils the part of the pore space is filled with water and the rest is occupied with air. The surface tension between water and soil particles makes the pore pressure always less than the air pressure (P_a) (Bishop, 1959).

The developed effective normal stress for partially saturated soils is:

$$\sigma = \sigma' + P_a - \chi (P_a - P_w) \qquad (2\text{-}31)$$

where P_a is pore air pressure, χ experimentally determined parameter in soil mass, and (P_a -P_w) shows the suction in among the soil particles. For fully saturated and dry soils χ equals 1 and 0, respectively.

Vanapalli and Fredlund (2000) performed a series of triaxial tests on five different soils to find correlation between χ and degree of saturation (S_r). They found that:

$$\chi = (S_r)^{k_f} \tag{2-32}$$

where k_f is a fitting parameter and a function of plasticity index (I_p) shown in Figure 2-10 and equals 1 for non-plastic soils. In addition, for dry and fully saturated soil χ is equal to 1 and 0, respectively (Vanapalli and Fredlund, 2000).

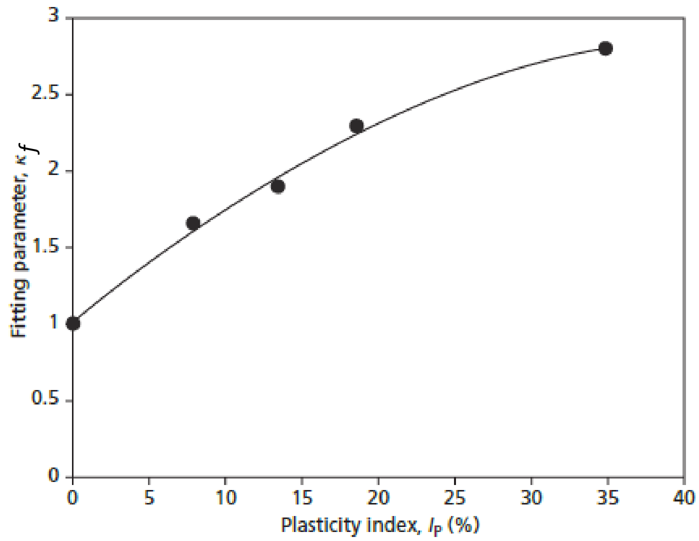

Figure 2-10. Correlation between fitting parameter k_f and soil plasticity (Vanapalli and Fredlund, 2000)

Jaeger and Cook (1979) developed Mohr-Coulomb diagram (Figure 2-11) by considering the contribution of pore water pressure on shear stress acting on soil particles surfaces as follows:

$$\tau = \psi(\sigma\text{-}P) \tag{2-33}$$

where, ψ is friction coefficient ranging from 0.6 to 0.85 (Byerlee, 1978). The Mohr-Coulomb diagram connects the normal and shear stresses applied on the particles' boundaries. In a 2D case, the bed shear stress plotted versus normal stress and the Mohr-Coulomb circle cuts the horizontal axis in two points which are the effective normal stresses. The element reaches the failure state when the circle touches the tangent line. This failure could happen at any point in the soil where the combination of the bed shear and normal stresses are critical. The shearing resistance originated due to interparticle forces and if the effective normal stress is zero it means that there is no further shearing resistance unless there is another bonding between the particles (Knappett, 2012).

The tangent line which is called the failure envelope is a linear correlation consisting of shear strength parameters developed as follows (Knappett, 2012):

$$\tau = c' + \sigma_f' \tan\varphi' \tag{2-34}$$

where, τ is bed shear stress, σ_f' is effective normal stress in a failure situation, c' is cohesion intercept, and φ' is the angle of shearing resistance. c' and φ' can be found using the Mohr-Coulomb diagram (see Figure 2-11), moreover, the failure envelope related formula can be written in two other ways(Knappett, 2012):

$$\tau_f = \frac{1}{2}(\sigma_1' - \sigma_3')\sin 2\theta \tag{2-35}$$

$$\sigma_f' = \frac{1}{2}(\sigma_1' + \sigma_3') + \frac{1}{2}(\sigma_1' - \sigma_3')\cos 2\theta \tag{2-36}$$

$$\theta = 45^\circ + \frac{\varphi'}{2} \tag{2-37}$$

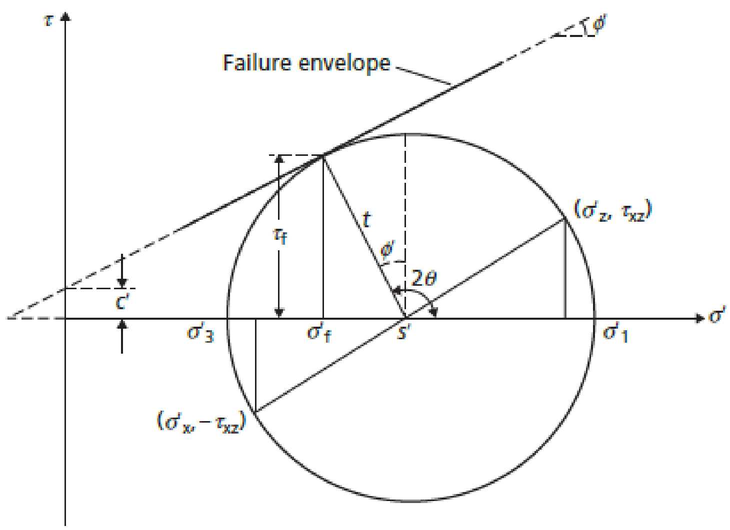

Figure 2-11. Mohr-Coulomb diagram (Knappett, 2012)

At the beginning of some incidents like an earthquake when water table rises up, the pore pressure dissipation is insufficient and the soil mass can be considered undrained. Then, the pore pressure propagation impacts the total normal stresses variations:

$$\Delta P = -\frac{1}{3}B'(\Delta\sigma_{xx} + \Delta\sigma_{yy} + \Delta\sigma_{zz}) \tag{2-38}$$

in which B' is Skempton's coefficient, $\Delta\sigma_{xx}$, $\Delta\sigma_{yy}$, $\Delta\sigma_{zz}$ are variations of normal stress in x, y, and z directions, respectively. An infinite and homogeneous soil mass produces normal stress changes, $\Delta\sigma_{yy}=0$. Moreover, for the plane strain the variations of normal stress in x and z directions are correlated as $\Delta\sigma_{yy}=\nu_u\,\Delta\sigma_{xx}$, where ν_u is the undrained Poisson's ratio. Thereby, the variations of pore pressure with respect to the normal stresses can be written as follows (Rudnicki and Rice, 2006):

$$\Delta P_x = -\frac{1}{3}B'(1+\nu_u)\Delta\sigma_{xx} \tag{2-39}$$

Skempton's coefficient is developed by considering both saturated and unsaturated soils (Yang, 2005):

$$B' = \frac{\dfrac{1}{K_s}-\dfrac{1}{K_g}}{\dfrac{1}{K_s}-\dfrac{(1+\phi)}{K_g}+\dfrac{\phi}{K_\omega}+\dfrac{\phi(1-S_r)}{p_o}} \tag{2-40}$$

$$K_s = \frac{2(1+\nu_p)G}{3(1-2\nu_p)} \tag{2-41}$$

where, K_ω is the water bulk modulus, and P_o is the absolute pressure the sum of total pore pressure and one atmosphere, K_s is the bulk modulus of the soil bed, ϕ is the porosity of soil, G is the soil's shear modulus, ν_p is drained Poisson's ratio, K_g is defined as $1/C_s$ the bulk modulus of the soil grains and C_s is the compressibility of the soil grains (Abdollahi, 2017).

The effect of unsteady flow propagation on pore pressure variations and soil instability has previously been studied experimentally. In 2003, Tonkin et al. used Terzaghi's (1925) soil consolidation theory to explain pore pressure variations due to transient flow. The pore pressure evolution was formulated as follows:

$$P_e(z,t) = P_{atm}(z,t) - \rho_w g[h-z] \tag{2-42}$$

where, z is vertically upward coordinate and P_{atm} is atmospheric pressure. Moreover, the concept of liquefaction hypothesized that the sediment grains liquefy if the vertical excess pore pressure surpasses the buoyant specific weight (γ_b) of saturated sediment. So, it can be said that:

$$\left.\frac{\partial P_e}{\partial Z}\right|_{z=z_0} = -(\rho_{sat} - \rho\ )g \equiv -\gamma_b \tag{2-43}$$

in which ρ_{sat} is the saturated soil bulk density. The large upward vertical pore pressure causes the generated lift and drag to exceed resistant gravitational forces. As a result, the sediments can scour rapidly (Tonkin et al., 2003).

The results of Tonkin's empirical research led to the definition of a parameter "Λ" that correlated the pore pressure gradient with scour development:

$$\Lambda(z) = \frac{P_e(z) - P_e(z_0)}{\gamma_b |z - z_0|} \tag{2-44}$$

where, P_e (z) is the excess pore pressure at the elevation z above the sediment bed. Based on the definition of Λ, pore pressure propagation among soil particles can diminish resistant forces and cause scour formation. This experimental study also determined a threshold for Λ in a range between 0 and 1 which means that in this range the frictional forces are small enough to be overcome by the upward buoyant force, thus the sediment could be scoured readily (Tonkin et al., 2003).

One-dimensional variations of time-dependent pore pressure can be expressed as follows after applying Terzaghi's theory in 1956:

$$\frac{\partial P}{\partial T} = c_v \frac{\partial^2 P}{\partial z^2} \tag{2-45}$$

where, c_v is Terzaghi's coefficient of consolidation which can be also written as:

$$c_v = \frac{k'}{\beta_c \mu} \tag{2-46}$$

in which, k' is permeability, β_c is water storage capacity, and μ is fluid viscosity (Faulkner et al., 2018).

The consolidation equation was modified in 1996 by Jeng and Hsu, as the soil skeleton is not purely one-dimensional and saturated:

$$\frac{\gamma_w}{k'_z}\frac{\partial c_v}{\partial t} = \frac{k'_x}{k'_z}\frac{\partial^2 P}{\partial x^2} + \frac{k'_y}{k'_z}\frac{\partial^2 P}{\partial y^2} + \frac{\partial^2 P}{\partial z^2} - \frac{\gamma_w n\beta'\partial P}{k'_z\partial t} \tag{2-47}$$

where, k'_x, k'_y, and k'_z are the soil permeability coefficient in x, y, and z directions, respectively, γ_w is the unit weight of water, n is soil porosity, and β' is the water compressibility (Jeng and Hsu, 1996).

Terzaghi's one-dimensional variations of pore pressure were further investigated by Carslaw & Jaeger (1959) to show the vertical changes in soil level due to the excess pore pressure (P_e) during drawdown time of ΔT:

$$P_e(z) = 4\Delta P i^2 erfc\left[\frac{-z}{2\sqrt{c_v\Delta T}}\right] \tag{2-48}$$

$$i^2 erfc(x) = \int_x^\infty dx'\int_x^\infty dx'' erfc(x'') \tag{2-49}$$

where z is the distance from bed surface.

The Shield's parameter was also modified to consider the vertical variations of pore pressure gradient in unsteady flows by performing numerical modeling (Yeh and Mason, 2014). In addition, the results of this numerical study determined that soil becomes entirely liquefied when the following condition occurs:

$$\frac{\Delta P_e}{\Delta z}\langle\frac{1-\rho_{sat}}{\rho} = 0.93 \tag{2-50}$$

Most importantly, Tonkin et al. (2003) and Yeh and Mason (2014) figured out that the liquefaction can take place even if the pore pressure gradient reaches at least half of the buoyant specific weight of saturated soil (i.e., $\Delta P_e > 0.5\ \Delta z$).

Finally, the original Shield's parameter was modified by adding the effective vertical pore pressure gradient in the denominator of the ratio:

$$\theta' = \frac{\tau_0(1-\varphi)}{d\left[(g(\rho_{sat}-\rho) + \frac{\Delta P_e}{\Delta z}_{z=0}\right]} \tag{2-51}$$

Importantly, during tsunami runup the values of pore pressure increase due to inland propagation of tsunami bores, then the value of $\Delta Pe/\Delta z_{z=0}$ are positive which make the ratio smaller than the original Shield's parameter. Then, the modified Shield's value can be smaller than the original (or critical) one which causes stability. In case of the drawdown stage, the variation of $\Delta Pe/\Delta z_{z=0}$ are negative and this can lead to sediment entrainment. Moreover, the maximum value of the modified Sheild's parameter is obtained during the drawdown when $g(\rho_{sat}-\rho)$ reaches $\Delta Pe/\Delta z_z$ which means the high likelihood of complete liquefaction (Yeh and Mason, 2014).

2.4.2 Definition of soil liquefaction

Soil liquefaction occurs when soil rigidity decreases as a result of shear strength reduction in a soil column over a short period of time after the application of sudden dynamic force such as that generated by earthquakes or explosions (Disfani and Moghaddam, 2020). In other words, when liquefaction occurs, the effective normal stress reaches zero at the same time as pore pressure in soil equals total normal stress (Naghizadehrokni, 2018). Since excess pore pressure induced by earthquakes builds up residually in soil, coastal regions located in earthquake-prone areas experience residual liquefaction (Abdollahi, 2017). In certain circumstances, vertically upward seepage causes liquefaction. In this situation, hydraulic gradient reaches a maximum value which is called critical hydraulic gradient (i_{cr}) and then a reduction in resistance force in soil (i.e., which would be equal zero) is expected. The critical hydraulic gradient is given by (Knappett, 2012):

$$i_{cr} = \frac{\Delta h}{L} = \frac{\gamma'}{\gamma_w} = \frac{G_s - 1}{1 + e} \tag{2-52}$$

And,

$$\gamma' = \gamma_{sat} - \gamma_w \tag{2-53}$$

where, Δh is the total head between two points, G_s is the specific gravity of soil particles, and e is the void ratio.

When the hydraulic gradient approaches the critical value (i.e., nearly 1), the upward seepage diminishes the effect of gravitational force among soil particles and the resistance between particles reduces significantly, especially for the case of sands. Moreover, if the hydraulic gradient exceeds its critical value the upward movement of the sand particles can be seen which is termed "boiling". However, for the finer particles (i.e., clays) liquefaction may not necessarily occur when the hydraulic gradient reaches its critical value (Knappett, 2012).

2.5 Physical modeling

A series of seminal experiments was conducted by Tonkin and colleagues (2003) to investigate the scour formation associated with a tsunami-like bore propagation around a cylindrical structure located in a sloping bed. The sand particles used in these tests were at full scale in order to reduce the scaling effects in sediment transport modeling, as fine sediments tend to act more cohesively. The study used a large-size tank which was 135m long, 2m wide, and 5 m deep. A sand section with a uniform upslope of 5% was filled with well-graded sands with a bulk density of $\rho_{sat}=1.93*10^3$ kg.m^{-3} and a 0.5m-diameter cylinder made of 1-cm-thick Plexiglas installed in the center of this bed. This model was surrounded with gravel with a main diameter of d_{50}=3.6 mm for thickness and depth of 0.25 m and then the sand particles surrounded the gravel section (Figure 2-12). A piston-type wavemaker (stroke of 2.4 m with a maximum speed of 1.11 m/s) was used to generate solitary waves (heights up to 30 cm in 3 m water depth), which propagated over the beach and created runup heights ranging from 0.4 m to 0.75m. Three cameras were located inside the structure facing outward in order to provide a wide view of scour evolution through the runup and drawdown processes. Video cameras were placed at the side of the transparent flume to record the experiments, wave heights were measured at three locations within the flume, and vertical and cross-shore velocity components were measured 3 m in front (offshore) of the structure. Finally, transducers were used to measure pore pressures at four locations within the sediment beach on each side of the structure, each at three different bed levels (10 cm, 20 cm, 30 cm below the sediment surface) (Tonkin et al., 2003).

During the experiments, it was observed that at the initial stage of wave impact, the downward flow which passed along the structure formed into a horseshoe vortex and rapidly started to cause local scour. Due to the large shear stress at the side of the structure, the sand was suspended into the water. After a short time, the runup flow became fully developed and the horseshoe vortex was no longer distinguishable. The dominant turbulence and scour formation were attributed to flow separation around the structure, which also generated additional vortices associated with pressure gradients around the cylinder. During the drawdown stage, which was a bit more complex than the runup stage, the flow running back down the sediment slope created counter-clockwise horseshoe vortices near the bed and clockwise vortices near to the water surface. At the highly turbulent separation point, a vortex sheet consisting of many small-size vortices was generated with a very short lifetime of 0.3 s. A great deal of scour occurred at the back (onshore) side of the structure during drawdown. As the wave receded in drawdown, the sediment slope at the back of the structure was exposed, with loss of overlying water pressure. However, the pore pressure did not diminish as rapidly deeper within the soil, resulting in loss of soil effective normal stress, which enabled rapid scour. At the end of the drawdown, slumping of the slides of the scour hole caused half of the scour hole at the back to be refilled with sediments, and this made the scour depth a function of time. In the second step of the physical modeling, the sand was replaced with gravel. In this case, a few seconds after the wave arrival, a considerable scour hole formed at the front face of the structure. The horseshoe vortex, in this case, was not strong enough to suspend the gravel, and the gravel moved along the flume as a bedload towards the back (Tonkin et al., 2003).

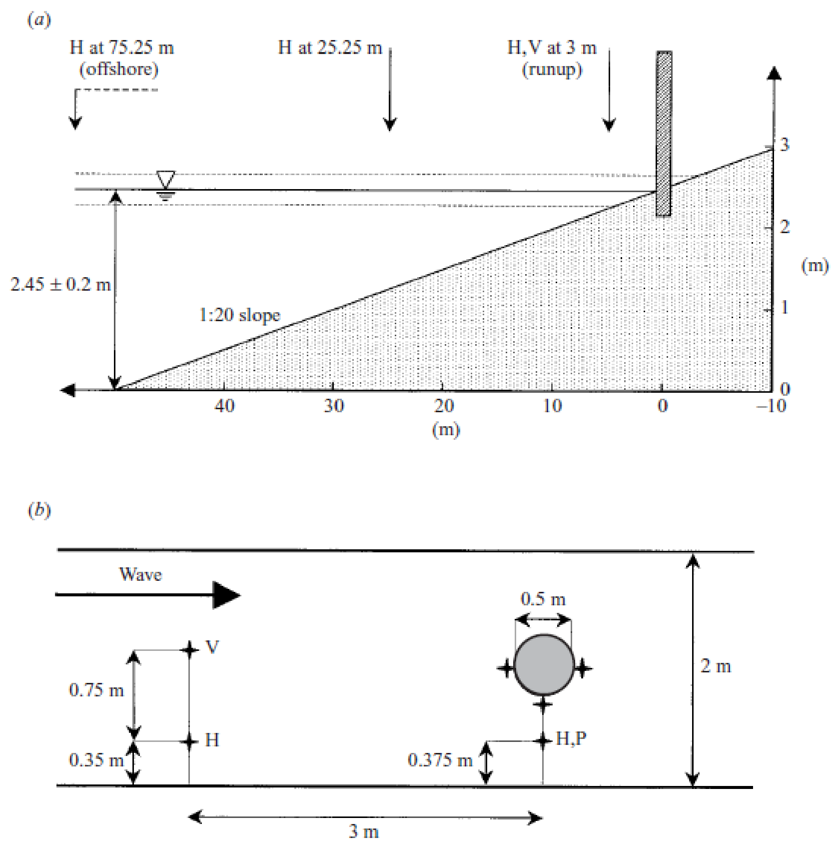

Figure 2-12. Experimental setup and determination of location of pore pressure transducers and wave gauges by “+” (Tonkin et al., 2003)

Tonkin et al. also provided detailed results of the pore pressure variations during these experiments. As shown in Figure 2-13, for the first series of the experiments with sand, at the front of the structure the pore pressure dropped more quickly during drawdown at the transducers located in the top layer (0.1 m) than lower layers (0.3 m). This was also observed at the back of the cylinder. The maximum scour depth coincided with the maximum pore pressure gradient. These pore pressure gradients indicate excess pore pressure, which led to low effective normal stress and associated reduction in resistance among the soil particles. Tonkin et al. (2003) provided a metric for scour potential based on effective normal stress, recognizing that liquefaction occurs as effective normal stress approaches zero when the vertical gradient in excess pore pressure exceeds the buoyant specific weight of the saturated soil skeleton. The authors also noted that the water pressure above the bed was not necessarily instantaneous hydrostatic pressure, as it also included hydrodynamic pressure. Based on estimates of vertical velocity, the authors concluded that the hydrodynamic pressure ($u^2/2g$) was comparable to the instantaneous hydrostatic pressure, which contributed to the generation of high pore pressures in the first few seconds into the run (Tonkin et al., 2003). It is worth noting that pore pressure gradients were largely not observed in the gravel-bed runs due to the high permeability of the gravel.

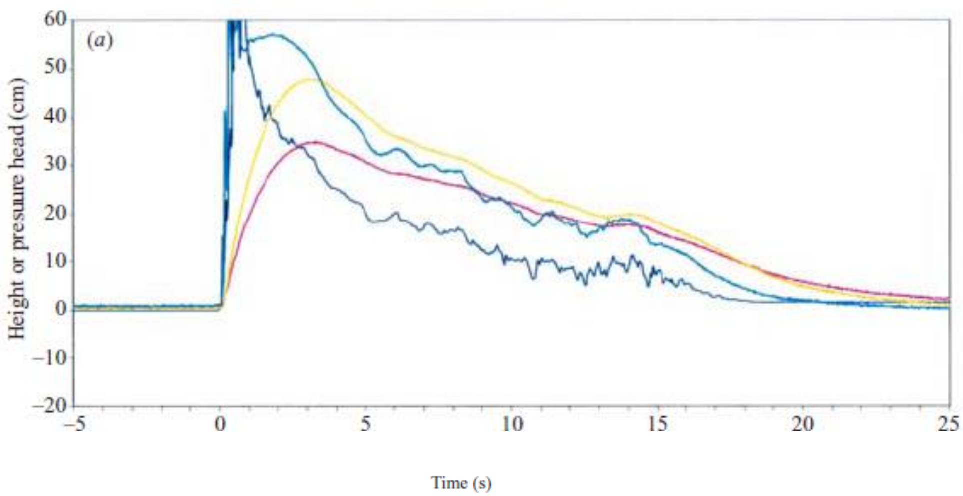

Figure 2-13. Pore pressure changes at the front face of the cylinder surrounded with sand. Blue line (water height), cyan line (transducers at 0.1 m), yellow line (transducers at 0.2 m), and pink line (transducers at 0.3 m) (Tonkin et al., 2003)

Comparison of the scouring mechanism for the sand- and gravel-filled beds illustrated that the horseshoe vortex generated due to the overturning motion of the wave formed a deeper scour hole at the front face of the cylinder for the gravel bed runs than for the sand bed runs. The authors speculated that high hydrodynamic pressure during wave runup without a corresponding immediate increase in pore pressure in the sand case may have increased soil resistance to erosion and inhibited scour. The scoured sand from the front and side faces was carried away from the structure mostly due to suspension, while the gravel was scoured as a bedload towards the back face and piled up and made an approximately uniform slope. Through the drawdown phase in the sand bed, the sand was scoured away from the back face of the cylinder, whereas the gravel returned. Furthermore, due to the return of the gravel, the scoured hole at the front face could be filled in, while in contrast, as noted above, a considerable amount of the sand was scoured and a scour hole could be observed at the back of the structure (Tonkin et al., 2003).

Another set of experimental investigations were conducted by Nakamura et al. (2008a) on the time history of scour hole development under a solitary wave at the seaward corner of a square structure placed on a sand bed. The objective of this modeling was to find the wave-seabed interactions and the final shape of the scour hole near the structure. The experiments were carried out in a flume 30.0 m long, 0.7 m wide, and 0.9 m high. An impermeable bed was implemented behind a revetment which had seaward slopes of 0.1 and 5 (Figure 2-14). In these experiments, different wave heights (H_o) and still water depths (h_o) were utilized to generate various wave conditions (H_o / h_o ≈ 0.04, 0.06, 0.08, 0.1, 0.12). Solitary waves with variable push times (wave periods) were generated by a piston and travelled towards a sandy bed with two median sizes (d_{50}= $2*10^{-4}$ and $4.5*10^{-4}$ m). To record and monitor the scour development over time, video cameras were installed inside and at one corner of the structure (Nakamura et al., 2008a)

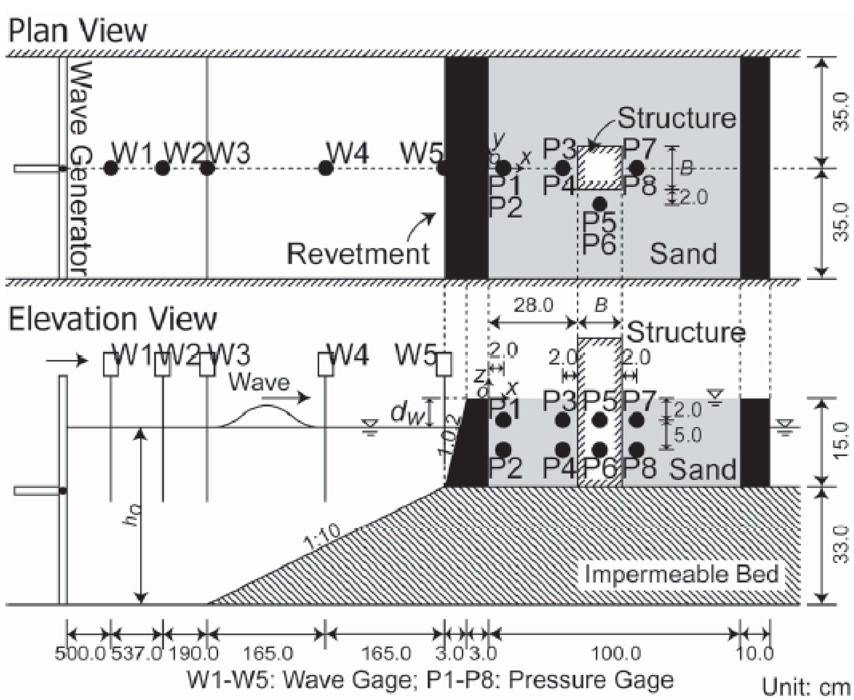

Figure 2-14. The experimental set-up and position of the instruments (Nakamura et al., 2008a)

The maximum scour depth was observed at the seaward corners of the structure, and the scoured sediments were deposited at the back of the structure (Figure 2-15a). The analysis revealed that the non-dimensional final scour depth (S_{sf}^{max}/b, where b is the structure width) increased with increases in overtopping heads ((2 H_o-d_w)/b); furthermore, the final scour depth was slightly less than the maximum scour depth, as a portion of the hole was filled in with the settled sand (Figure 2-15b) (Nakamura et al., 2008a).

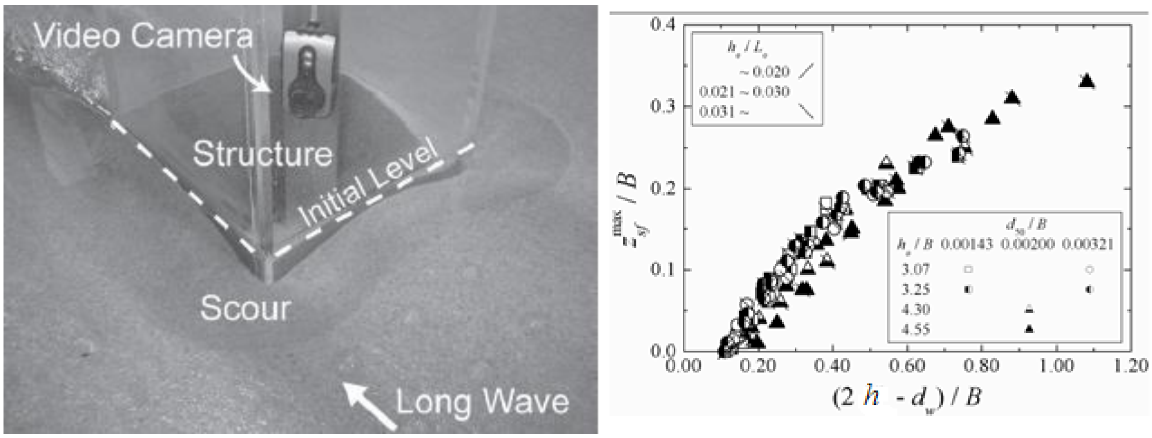

Figure 2-15. a) Local scour at the seaward side of the structure; b) Correlation between non-dimensional scour depth and overtopping head (Nakamura et al., 2008a)

The effect of still water level on the propagation of dam-break waves over both dry and wet beds was experimentally studied by Cagatary and Kocaman in 2008. The physical modeling studies were carried out in a rectangular channel 3m long, 0.3m wide, and 0.34 m high with a horizontal bed condition. An aluminum-coated plate used as a gate was raised suddenly over short times of 0.06 and 0.08 s to release impounded water with a depth of 0.25 m to generate dam-break waves (Figure 2-16a). The reservoir was 4.65 m long and the gate was installed at the downstream edge. Three different levels of still water (h_o=0.025 m, 0.05 m, 0.1 m) were set in the flume by using a steel gate downstream of the channel (Çağatay and Kocaman, 2008).

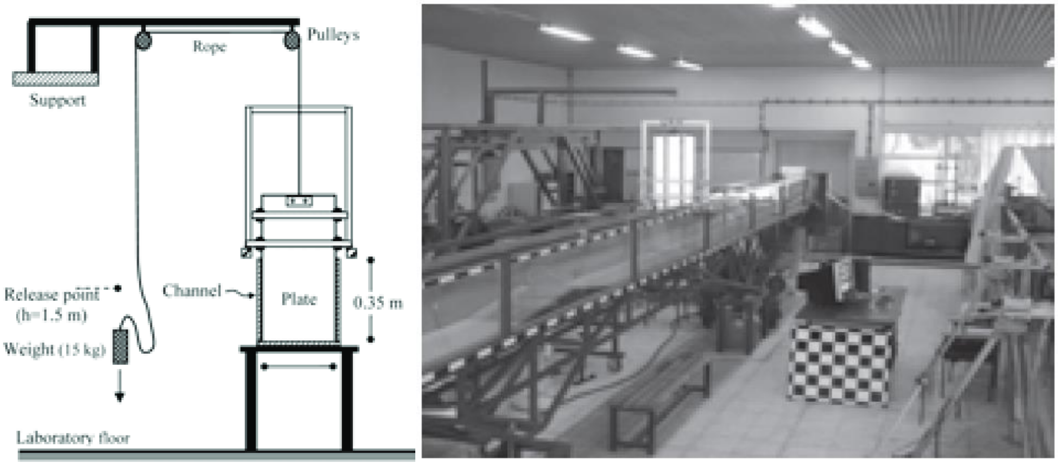

Figure 2-16. a) Schematic of the vertically releasing gate (left), b) Photo of the channel (right) (Çağatay and Kocaman, 2008)

As the walls of the channel were made of glass, the propagation of the generated dam-break waves was tracked by placing three video cameras at the side of the channel, and also the still and impounded water were colored by adding different colors of dye (Figure 2-17). These two colors were also helpful for specifically observing the interface of positive and negative waves moving downstream, or inversely, towards the reservoir. The analysis of the visual information from the video cameras showed that after removing the gate, the still water resisted being entrained by the bore, and this resistance increased as still water depth increased. This investigation illustrated that as the depth of the still water increased, the wave velocity decreased and the wave broke later and further downstream (Çağatay and Kocaman, 2008).

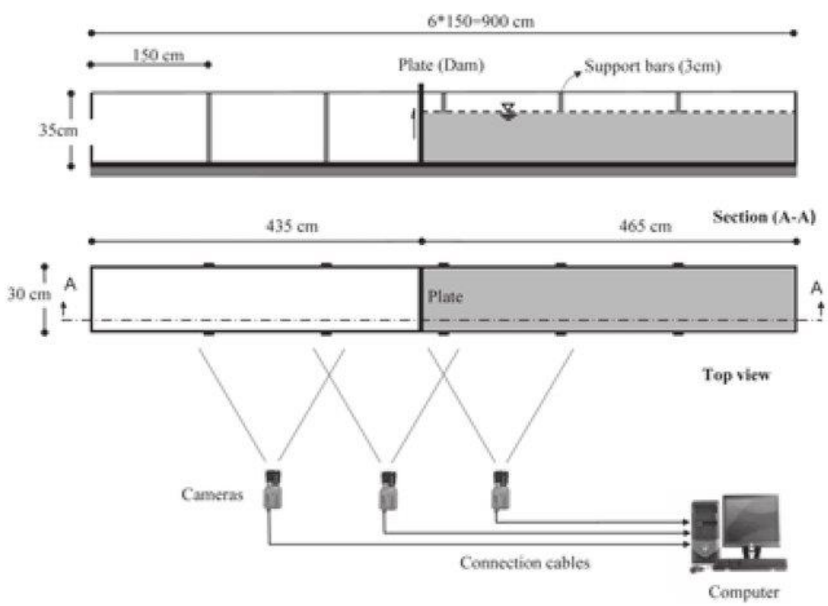

Figure 2-17. Location of the side cameras (Çağatay and Kocaman, 2008)

A series of experimental studies were conducted by Qi et al. (2012) in a large flume to observe the coupling mechanism of wave/current-structure-soil under combined waves and currents. They investigated the simultaneous interaction of scour depth, flow velocity, depth of the water, and pore pressure variations around piles with diameters of 0.2m and 0.08 m. The physical modeling was carried out in a flume 52 m long, 1 m wide, and 1.5 m high, and regular and irregular waves with 0.6 m/s velocity were generated by a piston located upstream of the horizontal flume (0.5 m impounded water pushed by the piston every 1.4 s). The combinations of waves and currents flowed over a saturated sand (d_{50}=0.38 mm) test section 0.6 m long, 1.8 deep, and 1.0 m wide (Figure 2-18) (Qi et al., 2012).

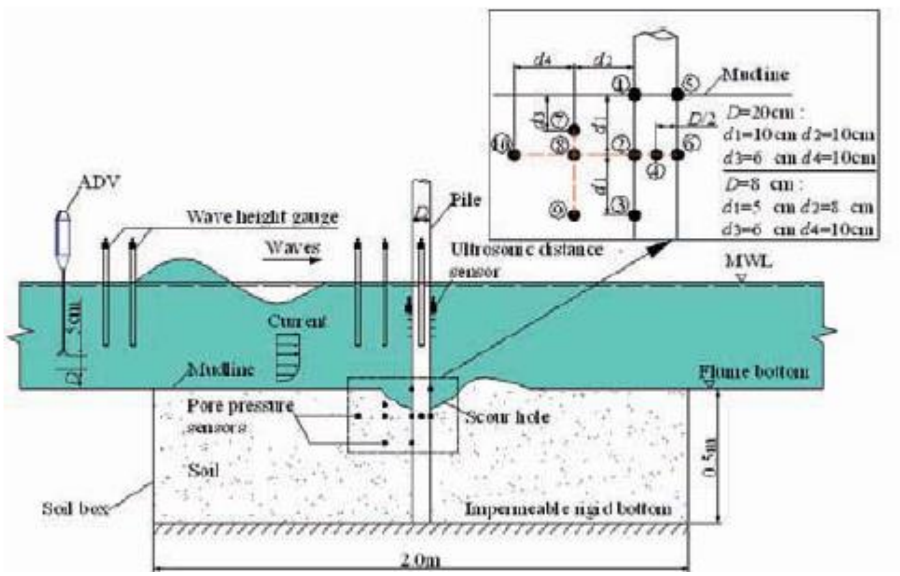

Figure 2-18. Experimental setup (Qi et al., 2012)

Analysis of the results showed that the scour rate around the pile with the smaller diameter was faster than for the bigger one, and that it took longer for the scour around the bigger pile to reach the equilibrium condition. Furthermore, in the case of the smaller pile, the scour hole extended faster towards the upstream and downstream sides of the pile. A direct relation was observed between wave height and generated pore pressure, such that as the wave height increased, the corresponding pore pressure within the soil increased as well (Figure 2-19).

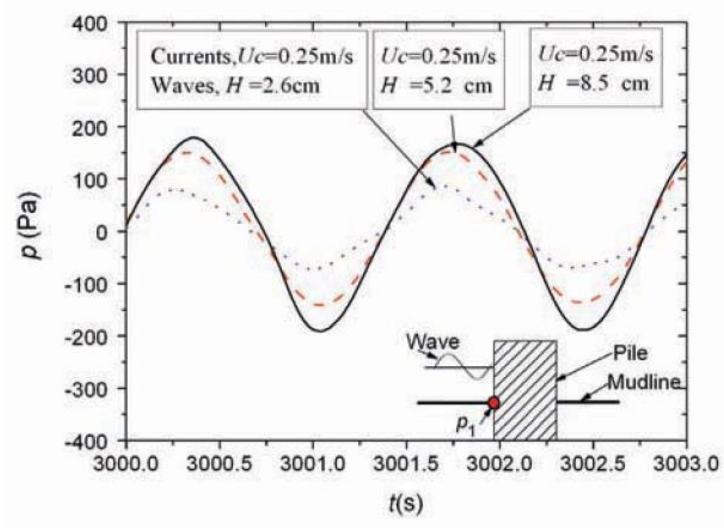

Figure 2-19. Comparison of the effect of the simultaneous impact of current and waves on pore pressure variations (Qi et al., 2012)

A direct relation was also observed between pore pressure and scour depth, and it even concluded that as the pore pressure increased, the pore pressure gradient and the area of the liquefied region around the structure also increased (Figure 2-20) (Qi et al., 2012).

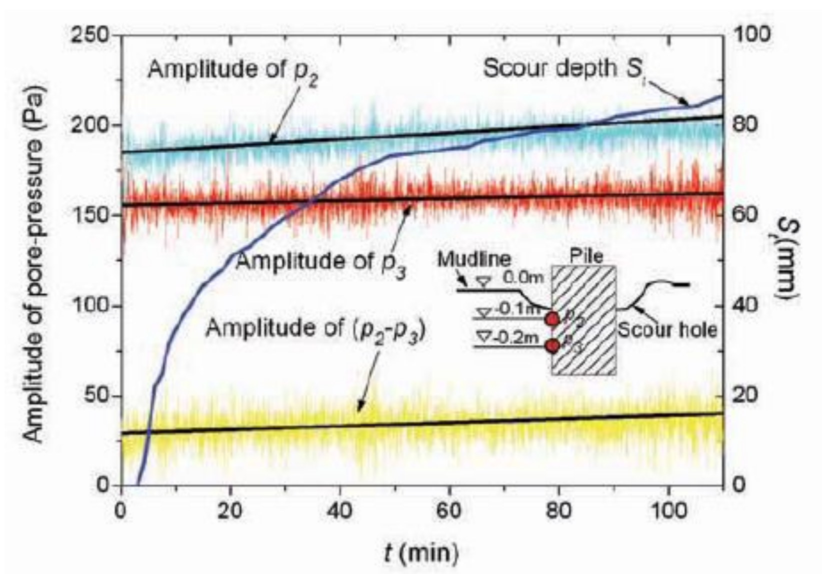

Figure 2-20. Correlation between scour depth and pore pressure (Qi et al., 2012)

The impact of different-sized square-shaped structures on scour formation as well as the effects of various still water and impoundment depths on bore propagation were investigated experimentally by Mehrzad and colleagues in 2016. In this study, the scour mechanism was investigated by setting different still water and impoundment depths. Multiple experiments were carried out in a flume 30 m long, 1.5 m wide, and 1 m deep, and dam-break waves were generated by suddenly opening a swing gate installed immediately before a false floor 4.15 m long and after a reservoir 21.55 m long and 1.5 m wide. The same flume will be used for the present study. The false floor was gridded by a 20 x 20 cm network and was used to calculate bore front and bore surface velocity based on particle tracking velocimetry (PTV). A 3.30 m long sediment test section filled with 1.0 mm sand was implemented after the upstream false floor (Figure 2-21). Finally, a 1.0 m long aluminum false floor was installed between the sediment section and the flume outlet in order to provide a framework for the sediment section (Figure 2-21). Square structures with diameters of 0.1, 0.2, and 0.3 m were placed at the center of the sediment section. The reservoir was filled with seven different water levels, and eight still water depths were used after the gate to create dry and wet bed conditions. In terms of bore propagation velocity, it was concluded that an increase in the still water depth and a decrease in impoundment depth could reduce the bore front velocity (Mehrzad et al., 2016).

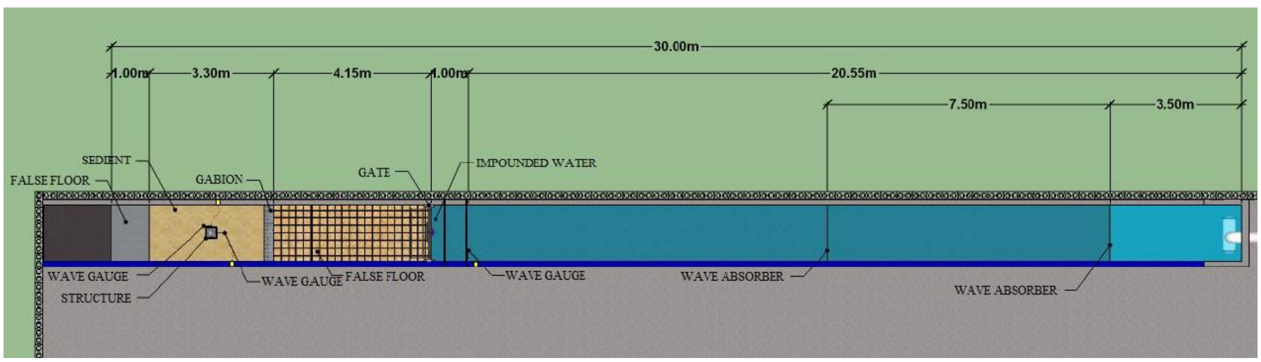

Figure 2-21. Experimental setup (Mehrzad et al., 2016)

The effect of structure width on scour propagation was examined through dry tests. Three dry tests were performed with different impoundment depths of 0.15 m, 0.2 m, and 0.25 m. The analysis of the results revealed that the influence of the water depth behind the gate was mostly seen on the smallest size of the structure, which experienced less erosion. On the other hand, the depth of the scour hole increased with an increase in structure width (Figure 2-22).

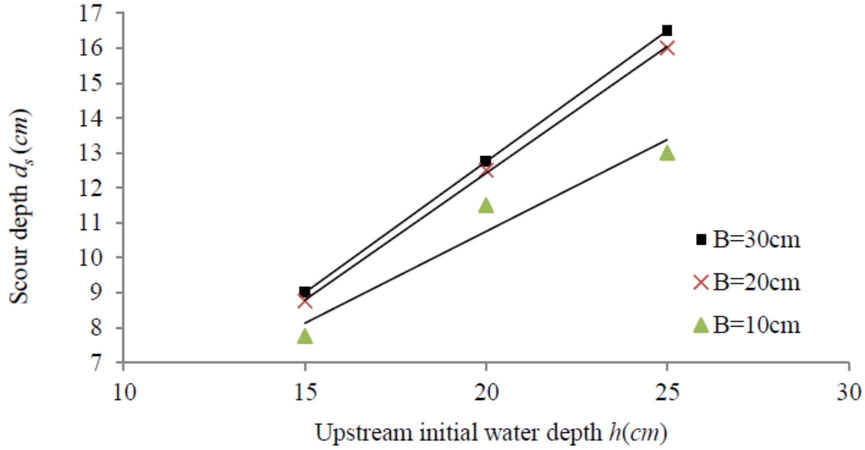

Figure 2-22. Scour depth variations based on different impounded water depths in the dry tests (Mehrzad et al., 2016)

2.6 Numerical simulation

Wave-seabed interactions were investigated numerically by Nakamura and colleagues in 2007, who used two sub-models: 1) a Volume of Fluid (VOF) method to simulate the air-water phase, and 2) a Finite Element Model (FEM) as a three-dimensional and wave-induced soil-water coupled model. Numerical validation was performed by comparing the results of experimental and numerical simulations. As Figure 2-23 illustrates, the numerical simulations for pore pressure variations are in satisfactory agreement with the experimental results, while the results for water surface elevations through the numerical simulation were slightly underestimated compared to the experimental results. The numerical simulation results also showed the maximum scour depths at the seaward corners of the structure. Importantly, scour at the corners began before soil liquefaction at the early stage of tsunami impact as a result of high flow velocity and adequately large Shields number (Nakamura et al., 2008b).

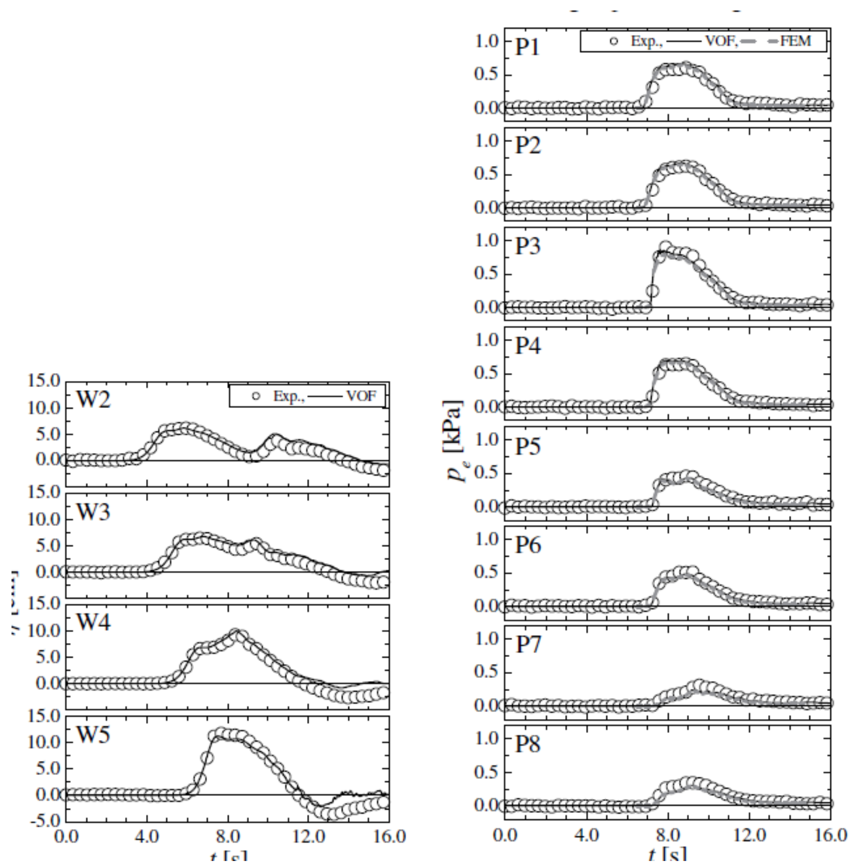

Figure 2-23. Comparison of numerical and experimental simulations results for water surface elevation (left), and pore pressure variations within the soil (right) (Nakamura et al., 2008b)

The effect of still water on the propagation of dam-break waves in terms of mixing and dissipation was studied by Crespo et al. in 2008. The numerical studies were performed using SPH; this software is able to accurately simulate the interaction and interface of two different liquids. Figure 2-24 presents the results of the interface of these two liquids. When the lock gate dividing the two fluids was first opened, the downstream still water pushed the tank water backwards, which can impact the breaking point of the wave as well. This interaction brought about vorticity generation and the vertical displacement of a considerable volume of water. The results of simulating different still water levels showed that as this depth increased, wave-breaking was delayed and the flow velocity in the advancing bore decreased. The fastest bore occurred with the lowest still water depth; however, this bore was more affected by the bed friction and experienced oscillations (Crespo et al., 2008).

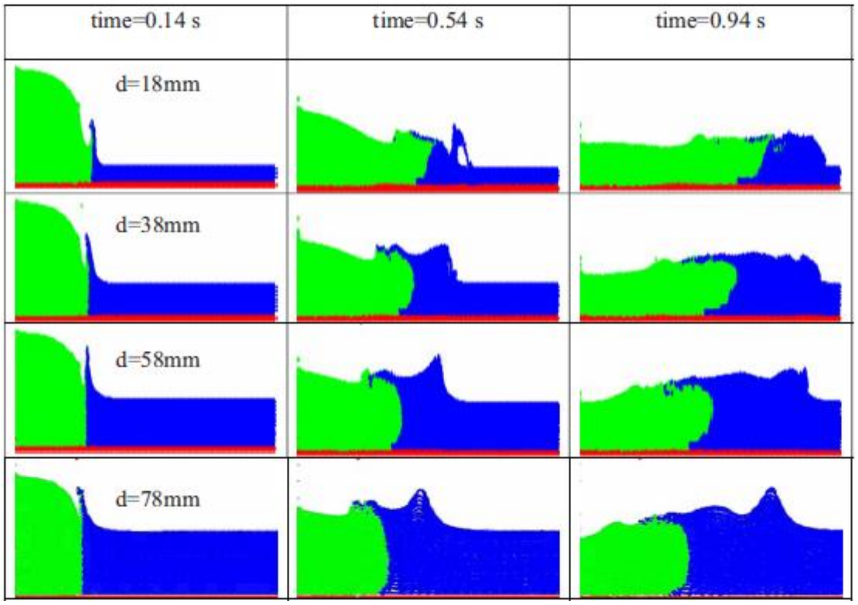

Figure 2-24. Different steps of dam-break bore propagation impacted by the still water depth (dark color) (Crespo et al., 2008)

The still water depth mostly affected the horizontal component of the velocity. As the still water depth increased, the flow velocity diminished, and the fastest bore occurred over a dry bed. However, the flow energy dissipated more over the dry bed, and this dissipation decreased with increased still water depth. The energy dissipation occurred due to two reasons: first, by the existence of some eddies after the wave-breaking, and second by the influence of bed friction. As the still water depth increased, wave-breaking and associated eddy generation occurred later, which reduced dissipation (Crespo et al., 2008).

The capability of tsunami-induced flows to scour out sediment and liquefy beds was explored numerically by Yeh and Li in 2008. 1D numerical simulations were conducted for a uniform 20 km-long beach covered by sand (d_{50}=0.35 mm) and with a 1/250 slope which had undergone tsunami-like flows with a maximum inundation distance of 1160 m and maximum runup of 4.6m. The initiation of sediment motion and bedload and suspension load were studied considering both the Shields and Rouse numbers. The proportion of shear stress to the buoyant weight of a sediment particle is represented by the Shields number, which is the fundamental parameter in determining the initiation of sediment movement (Yeh and Li, 2008).

An approximately constant value of critical non-dimensional shear stress ($\theta_c = 0.04 \sim 0.06$) determines the threshold for sediment motion. Post-processing analysis of the results of the numerical simulations illustrated that most parts of the beach had a Shields value greater than the threshold, and this result illustrated the capability of tsunami waves in moving sediment particles through the entire domain (Figure 2-25a). The second sediment motion classification was based on the Rouse number, which considers the ratio of sediment settling velocity (w_s) over shear velocity ($u_* = \sqrt{\frac{\tau_0}{\rho}}$).

$$R_o = \frac{w_s}{\beta k u_*} \tag{2-52}$$

where β is the ratio of sediment diffusion to fluid momentum diffusion (i.e, the inverse of sediment Schmidt number), and k is von Karman's constant equal to 0.4. The sediment settling velocity can be calculated as follows:

$$w_s = \frac{8\nu}{d_s}\left(\sqrt{1+\frac{(s-1)gd_s^{8}}{72\nu^2}}-1\right) \tag{2-53}$$

Sediments can be fully suspended at $R_o < 2.5$. Figure 2-25 shows the spatial and temporal distribution of bed entrainment (Shield parameter > 0.05, Figure 2-26a) and suspension ($R_o < 2.5$, Figure 2-25b) for a simulated tsunami. It is evident that entrainment and suspension begin offshore and increase as the tsunami propagates onshore. Comparison of the values of R_o during the runup and drawdown revealed that drawdown flows have greater potential for sediment suspension, which means more erosion and deeper scour (Yeh and Li, 2008).

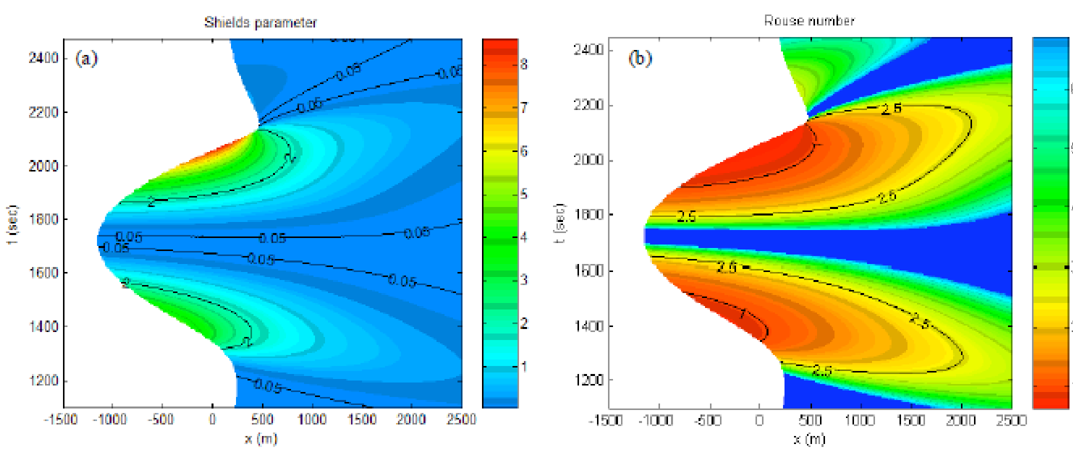

Figure 2-25. Spatial and temporal variations of a) Shields number and b) Rouse number for runup and drawdown on a beach with a 1/250 slope, where maximum runup distance for this simulation is -1150 m at t~1750 s (Yeh and Li, 2008).

Tsunami liquefaction failure of coastal beaches due to tsunami runup and drawdown over two different slopes was investigated through numerical simulations by Young and colleagues in 2009. As a result, the effect of slope on the time and location of liquefied zones was assessed. Tsunami-induced runup and drawdown over two sloping beds were modeled by solving depth-averaged nonlinear shallow water equations (SWE) and Boussinesq equations. As the influences of dispersion are significant before wave-breaking, the SWE and Boussinesq equations were solved before and after wave-breaking incidents. Wave-breaking events should be considered when a beach slope is greater than 0.36. Pore water pressure and bed formation were studied using a finite element (FE) model to evaluate simultaneous interactions of pore pressure and deformations. Prior to running the main simulations, the numerical modeling was validated by comparing the results of experimental studies with the obtained numerical results, and then the main numerical simulations were performed. Figure 2-26 illustrates the simulated case; note that pore pressure changes and water surface elevations were observed only at the initial section where the still water line met the sand beach. Here, a 0.6 m solitary wave with an initial height of 1 m was initiated offshore where still water depth was 1 m and propagated towards a beach with two different slopes, either 1:5 or 1:15, to represent a steep and a mild slope, respectively. The finite volume method (FVM) was utilized to simulate the full longitudinal extent of the flume throughout the domain under runup and drawdown, but the FE model simulated only the saturated part of the sand bed below the still water depth and until *x*=27 m (Young et al., 2009).

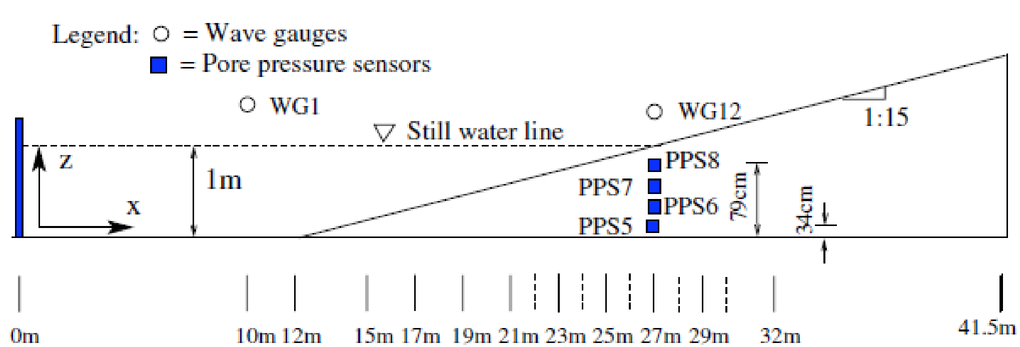

Figure 2-26. Experimental setup and locations of the instruments employed in the main experiment (Young et al., 2009)

The results of the numerical simulations showed high excess pore pressure near the shoreline and within the saturated part as the level of the water dropped below the still water surface during the drawdown, which made this region susceptible to liquefaction failure. On the beach with the steeper slope, the depth of soil subjected to the seepage force was greater, but the length of the seepage area decreased, meaning that the liquefied area was shorter for the steeper bed. Also, the rate of tsunami loading and unloading and the associated induced pore pressure gradients were greater on the larger slope. As a result, the steeper beach had a high possibility of facing liquefaction failure. Soil deformation was also highly affected by soil permeability and compaction (Young et al., 2009).

A two-dimensional finite element model was proposed to observe the interaction between soil characteristics, wave propagation, and a coastal structure and to explore pore pressure distribution at different depths and with different particle sizes (Jeng et al., 2001). The caisson was situated on a rubble mound consisting of gravel, with layers of coarse and then fine sand underneath. The region was broken down into six areas to explain the pore pressure distribution more precisely (Figure 2-27) (Jeng et al., 2001).

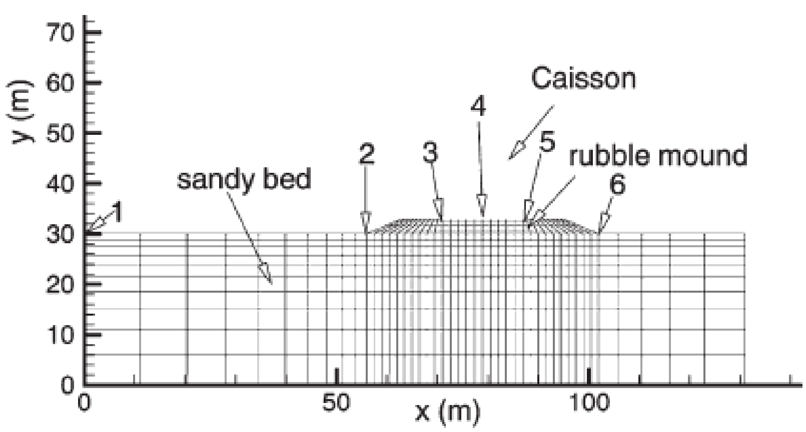

Figure 2-27. The allocated sections and finite element mesh used in the numerical simulation (Jeng et al., 2001)

The hydraulic specifications of the wave and soil particle characteristics are summarized in Table 2-1.

Table 2-1. The input data for the numerical simulation (Jeng et al., 2001)

Wave characteristics	
Wave period T	12.5 sec or various
Water depth d	15 m or various
Wave height H_o	2 m
Soil Characteristics	
Seabed thickness h	30 m or various
Degree of saturation S	0.98 or various
Porosity $\acute{n}$	0.35 (sandy bed) 0.4 (rubble mound)
Poisson ratio μ	0.35 or various (sandy bed) 0.3 (rubble mound)
Permeability K	10^{-1} m/s (rubble mound) 10^{-2} m/s (coarse sand) 10^{-4} m/s (fine sand)
Shear modulus G	$1.53 * 10^{8}$ N/m^2 (rubble mound) $1.15 * 10^{7}$ N/m^2 (sandy bed)

The vertical distribution of the pore pressure variations is presented in Figure 2-28. The solid lines are related to this distribution with the existence of a structure, and the dashed lines are for the distribution without a structure. As the figure shows, the pore pressure distribution was affected only for the area near the structure, and the considerable difference on the right side was due to the boundary conditions. For instance, in Region 1 (see Figure 2-28), as this region was quite far away from the caisson, it was not affected by the structure's presence and the lines for the pore pressure distributions almost overlap. The results depict that the center of the simulated domain was impacted by the existence of the structure. Maximum pore pressure was found at the interface of the caisson and the rubble mound and at the interface of the sandy bed and the rubble mound (Jeng et al., 2001).

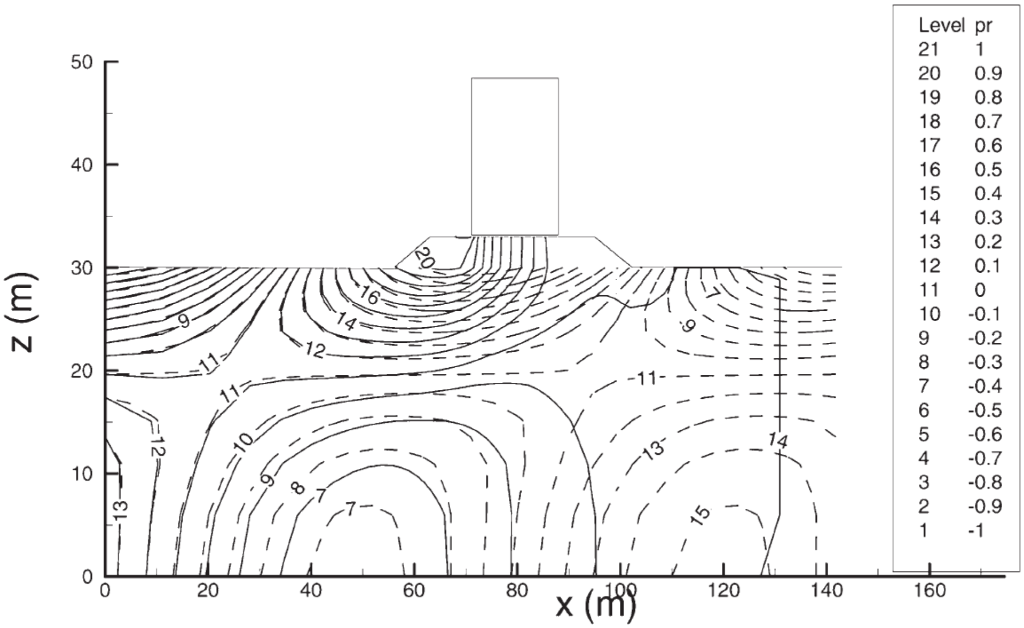

Figure 2-28. The contours of pore pressure variations (Jeng et al., 2001)

Changes in water surface elevation affected the pore pressure distribution. For sections filled with coarse sand, the pore pressure increased dramatically as the wave depth increased. On the other hand, the effect on the fine sand was less significant.

In order to observe the effects of the soil characteristics on pore pressure changes, different factors including soil thickness, Poisson's ratio, and saturation degree were investigated (Jeng et al., 2001). In general, the fine sand had variation in pore pressure near the soil surface, but constant pore pressure deeper in the soil. The coarse sand, on the other hand, had a gradient of pore pressure that extended deeper into the soil, due to greater permeability. Pore pressure variations increased with increased thickness of the coarse sand layer, while this effect was not considerable within the fine sand. For both sand sizes, as the degree of saturation increased, the pore pressure increased. Poisson's ratio, which is the ratio of transverse contraction strain to longitudinal extension strain, could govern the vertical variations of pore pressure; as the Poisson's ratio increased the pore pressure increased (became less negative), especially in the fine sand. However, overall, pore pressure in the coarse sand was more influenced by soil parameters than the fine sand (Jeng et al., 2001).

The impact of particle size, porosity, bed thickness and permeability on pore pressure variations under solitary and regular waves were numerically studied using a wave solver through two-dimensional Reynolds-averaged Navier-Stokes (RANS) simulations (Jiang et al. 2012). The different waves were modeled and solved simultaneously without considering the interface, and PLIC-VOF (piece-wise linear interface construction - volume of fluid) was applied to trace the water surface. Generally, greater pore pressures were observed as the soil thickness increased; however, the slope of these variations was different for the various waves (Figure 2-29) (Jiang et al., 2012). Also, a smaller sediment particle size reduced soil void volume and porosity, which increased pore pressure magnitudes (Jiang et al., 2012).

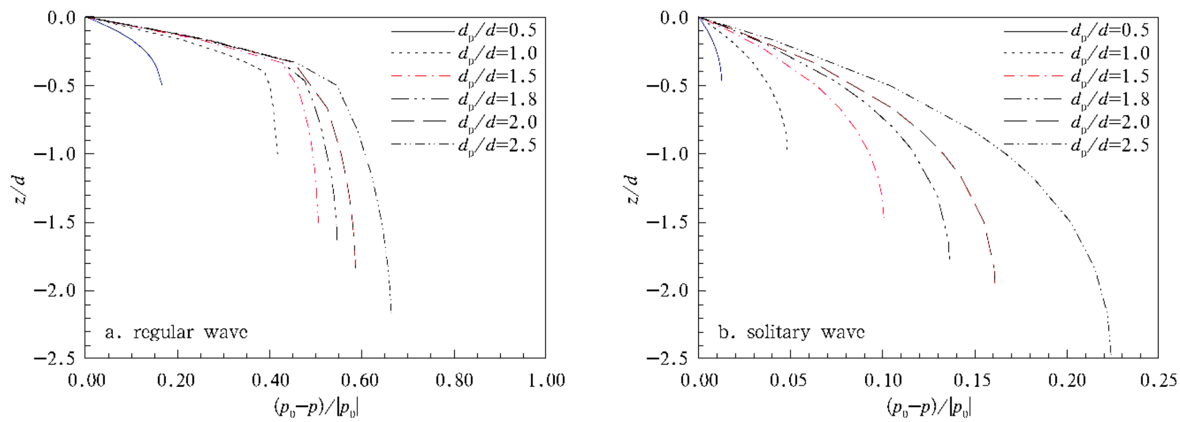

Figure 2-29. Variations in pore water pressures for different depths (Jiang et al., 2012)

Sediment around coastal structures is subjected to two kinds of loading: 1) vertical loading due to wave motion, and 2) lateral loading due to interaction between the soil and the structure. Cyclic mobility of the soil, effective normal stress, and excess pore pressure variations were evaluated by a three-dimensional finite element-finite difference code (Zhu et al., 2018). Specifically, the soil mechanics reactions of sediment particles with different densities and drainage situations under different wave loadings (cyclic or monotonic) were studied using the DBLEAVES program. A square structure and the surrounding soil were modeled, using symmetry to reduce the computational domain (Figure 2-30). The square structure had a linear dimension (D) of 1m and was embedded into 10 m of sand (coefficient of permeability of 10^{-5} m/s). Various points within the sediment bed were investigated (Figure 2-30). Points A, B, C, G, H, I, and J were located 1.25D below the bed surface, with point A at 0.25D in front of the structure, point C at 0.25D to the side of the structure, and B, G, H, I, and J respectively at 0.25*D*, 0.75*D*, 1.25*D*, and 2.25*D* behind the structure. Points D, B, E, and F were all at 0.25*D* behind the structure and at depths below the surface of 0.75*D*, 1.25*D*, 1.75*D*, and 2.25*D*, respectively (Zhu et al., 2018).

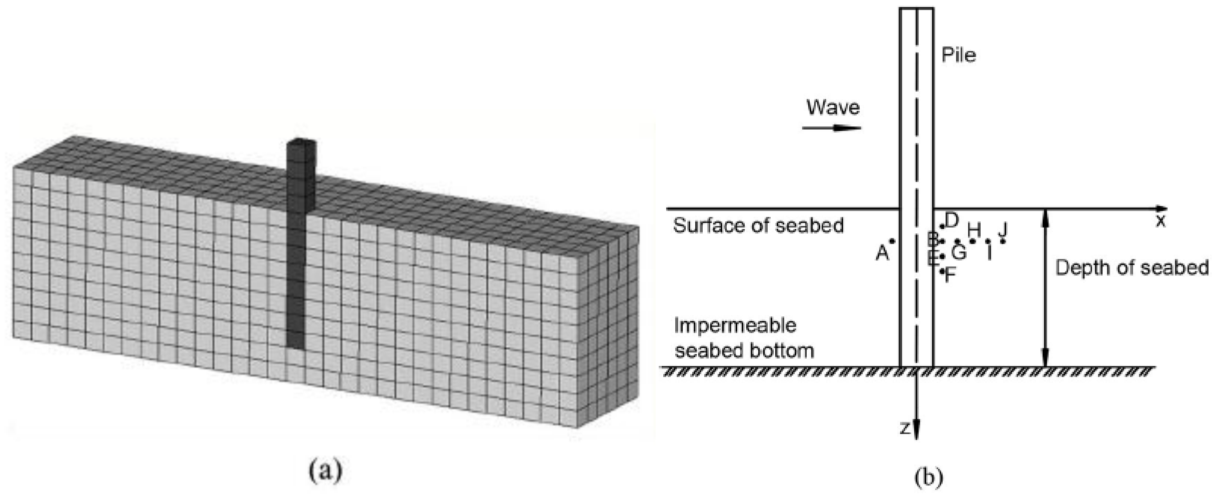

Figure 2-30. a) a three-dimensional model of the simulation, b) investigated points (Zhu et al., 2018).

The simulation results revealed that the pore pressure variations due to the wave motion were almost the same at points A (in front) and B (behind), while at point C (beside the structure) a lag was observed in the pore pressure response (Figure 2-31). Thus, the pore pressure variations near the structure were significantly affected by the soil-structure interaction. This interaction was considerable within the distance of two times the structure diameter from the structure, but diminished further from the structure (Zhu et al., 2018).

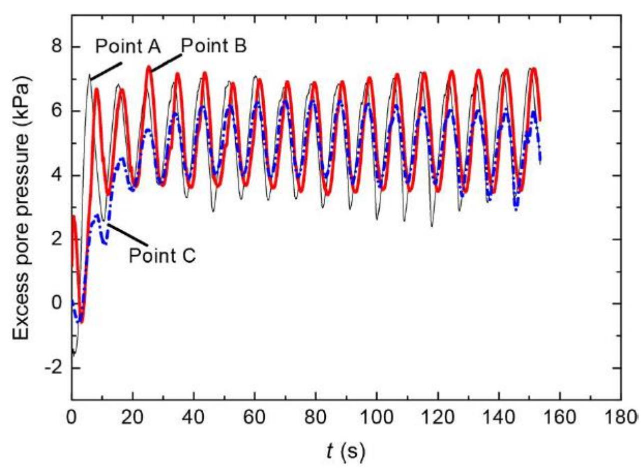

Figure 2-31. Pore pressure variations around the structure at the same elevation (Zhu et al., 2018).

Soil dilation and compaction behavior can be evaluated by examining the pore pressure changes at different depths (Figure 2-32). Less excess pore pressure was observed near the soil surface where soil dilation likely occurred (Figure 2-32.a), while in the bottom layer of the soil the excess pore pressure was higher and the soil particles likely underwent compaction (Figure 2-32.b) (Zhu et al., 2018).

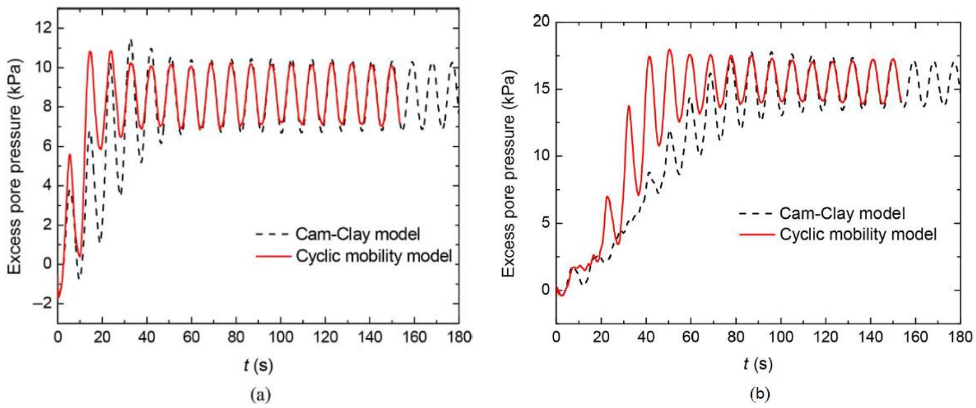

Figure 2-32. a) Excess pore pressure response at a depth of 1.25 D from the bed surface; b) Excess pore pressure response at a depth of 2.25 D from the bed surface (Zhu et al., 2018)

2.7 Dam-break wave studies

Studies on dam-break wave propagation and its characteristics began many years ago. Ritter (1892), who studied flowing fluid under an ideal condition, i.e., dam-break wave propagation over a frictionless, horizontal, and dry bed in a rectangular channel (Figure 2-33), could be named as a pioneer in this field. By solving the Saint-Venant equations, Ritter obtained an analytical solution for a parabolic free-surface profile of the ideal dam-break wave along with the flow velocity (Ritter, 1892).

$$\frac{d}{h} = \frac{1}{9} \times \left(2 - \frac{x}{t \times \sqrt{g \times h}}\right)^2 \quad \text{for} \qquad -1 \leq \frac{x}{t\sqrt{g \times h}} \leq 2 \qquad (2\text{-}54)$$

$$\frac{u}{\sqrt{g \times h}} = \frac{2}{3}\left(1 + \frac{x}{t\sqrt{g \times h}}\right) \quad \text{for} \qquad -1 \leq \frac{x}{t\sqrt{g \times h}} \leq 2 \qquad (2\text{-}55)$$

where x is the distance from the gate and t is the time corresponding to the wave location.

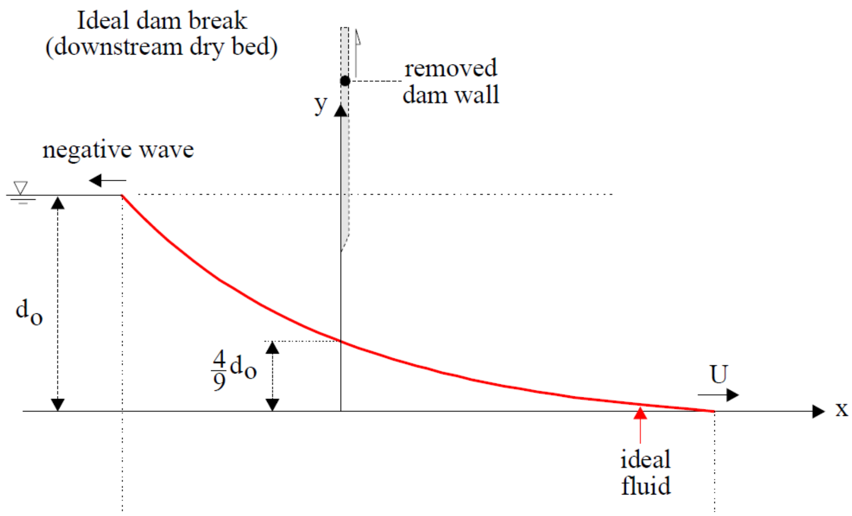

Figure 2-33. Sketch of dam-break wave propagation over a dry and frictionless bed (Chanson, 2005)

The propagation of a dam-break wave over a frictionless horizontal bed with an initial water depth was studied by Barré in 1871 (Barré, 1871). The idealized bore was generated by suddenly removing a vertical gate. Barré derived formulae to relate the Froude numbers and depths at three locations within a flume, including: 1) in the reservoir upstream of the gate, 2) the advancing bore downstream of the gate, 3) and further downstream in the still water body (Figure 2-34).

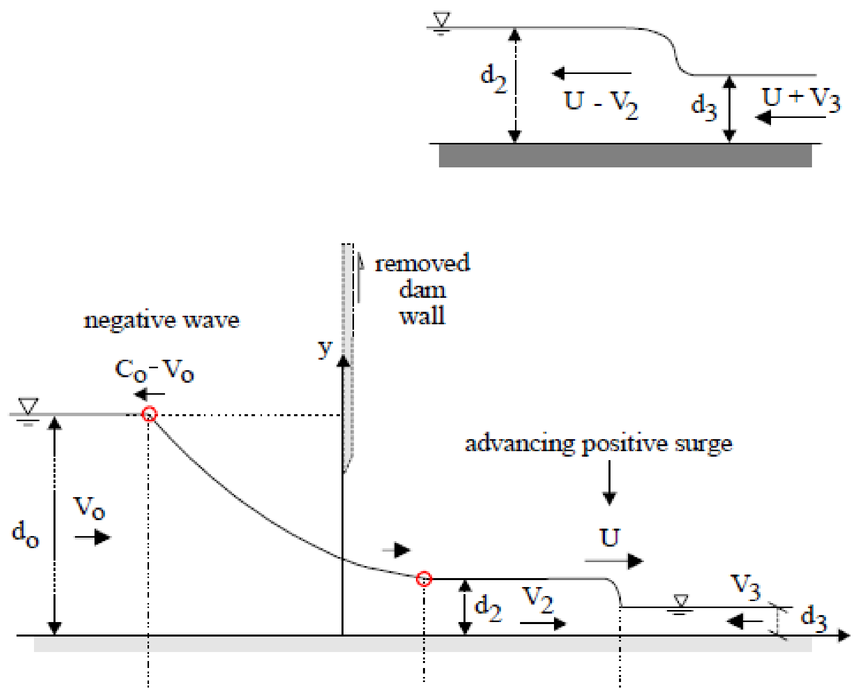

Figure 2-34. Schematic of dam-break wave propagation over a bed with still water depth (Chanson, 2005)

The continuity and momentum equations led to finding the correlation between the Froude numbers and depths in three regions (1, 2, and 3).

$$\frac{d_2}{d_3} = \frac{1}{2}\left(\sqrt{1+8Fr_3^2} - 1\right) \tag{2-56}$$

$$Fr_2 = Fr_3 * \left(\frac{2}{\sqrt{1+8Fr_3^2} - 1}\right)^{\frac{2}{3}} \tag{2-57}$$

$$Fr_1 = \frac{U + V_3}{\sqrt{g \times d_s}} \tag{2-58}$$

$$Fr_2 = \frac{U - V_2}{\sqrt{g \times d_2}} \tag{2-59}$$

which Fr_2, Fr_3 are the Froude numbers in upstream and downstream of the positive surge front and subscript 1 belongs to the wave tip region. In addition, d_2 is the bore depth at region 2, d_3 is the still water depth at region 3, d_o and V_o are flow initial depth and velocity in the reservoir prior to opening the gate, and C_o is initial velocity due to a small disturbance in the reservoir (C_o=(d_o*g)$^{\wedge 0.5}$).

By knowing the initial values of h and d_3 and using the graphs by Chanson (2005) (Figure 2-35), it is possible to find the flow velocity and bore velocity in region 2 (after the gate).

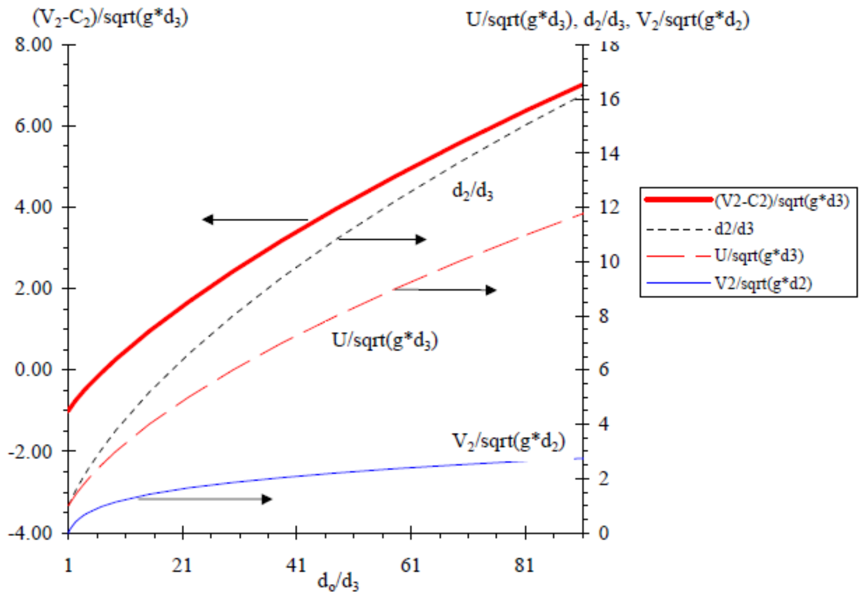

Figure 2-35. Flow specifications for dam-break wave over a horizontal bed with the still water depth (Chanson, 2005)

Even though Ritter's solution has satisfactory agreement with experimental results, particularly in the upstream section of a dam-break wave, Whitham (1955) modified Ritter's (1892) analytical solutions by considering the bed friction in a wide rectangular channel with a semi-infinite reservoir. In Whitham's solution, the Darcy friction factor is used and assumed as a constant within the wave tip region (Figure 2-36).

Bore front velocity at the wave tip region (U) can be found by the following formula:

$$\frac{8}{3}\times\frac{1}{f}\times\frac{\left(1-\frac{1}{2}\times\frac{U}{\sqrt{g\times d_o}}\right)^3}{\frac{U^2}{g\times d_o}}=\sqrt{\frac{g}{d_o}}\times t \tag{2-60}$$

in which d_o is the initial water depth in the reservoir.

The wave front location is (x_s) :

$$\frac{x_s}{d_o}=\left(\frac{3}{2}\times\frac{U}{\sqrt{gd_o}}-1\right)t\sqrt{\frac{g}{d_o}}+\frac{4}{f}\times\frac{1}{\frac{U^2}{gd_o}}\times\left(1-\frac{1}{2}\times\frac{U}{\sqrt{gd_o}}\right)^4 \tag{2-61}$$

and x_1 is:

$$\frac{x_1}{\sqrt{gd_o t}} = \left(\frac{3}{2} \times \frac{U}{\sqrt{gd_o}} - 1\right) \tag{2-62}$$

in which U is the bore front velocity.

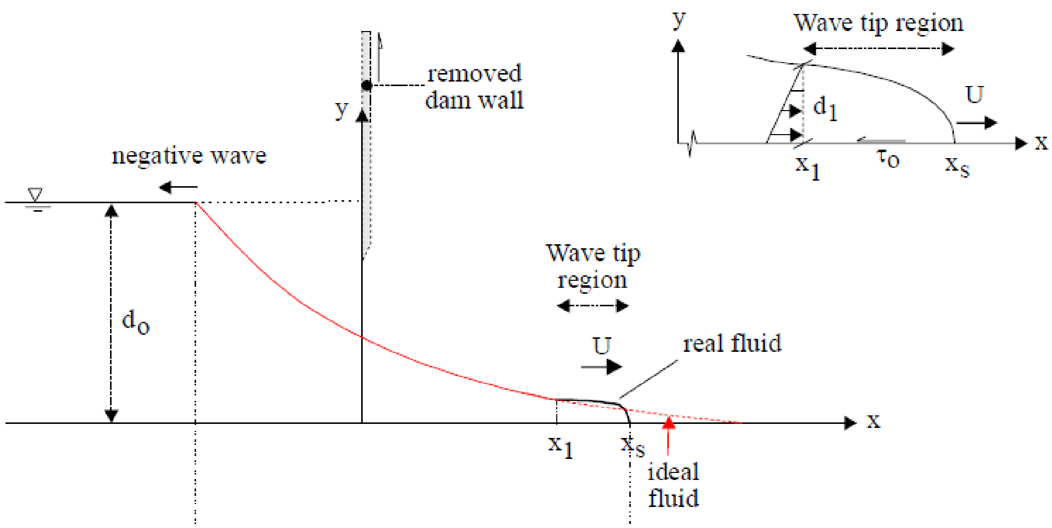

Figure 2-36. Sketch of dam-break wave propagation over a dry surface with friction on the bed (Chanson, 2005)

The previous investigations were extended by studying bore propagation over a dry and horizontal surface with an initial surge velocity of V_o (Figure 2-37). Negative velocity is generated by the instantaneous release of the vertical gate with the magnitude of $C_o = \sqrt{g * d_o}$. Considering also the initial velocity of the approaching wave (V_o), the slope of the negative wave that moves toward the upstream is $\frac{dt}{dx} = \frac{-1}{C_o - V_O}$.

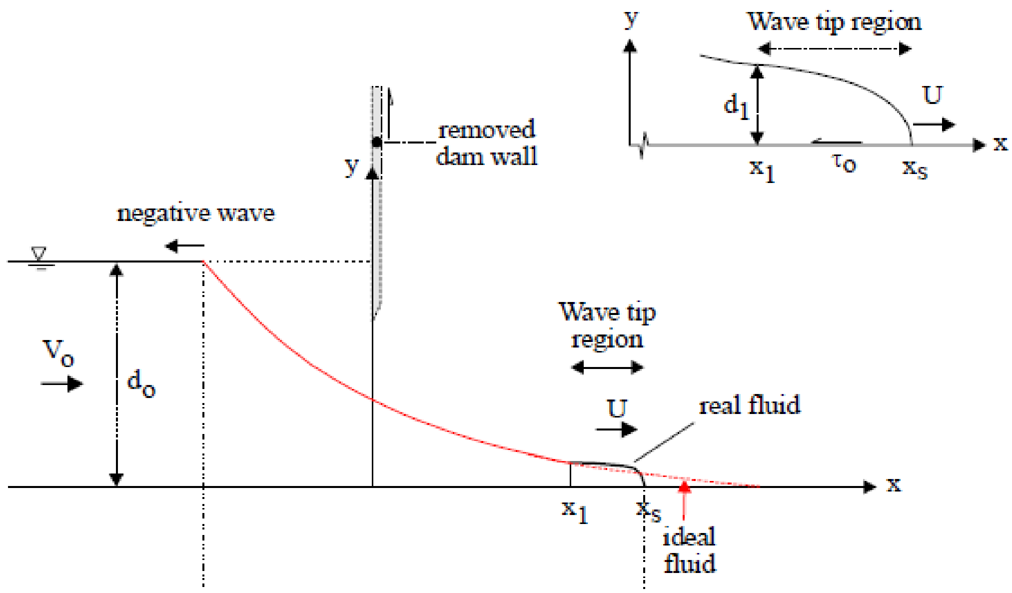

Figure 2-37. Sketch of dam-break wave propagation over a dry and horizontal bed with initial bore velocity and friction on the bed (Chanson, 2005)

The exact magnitude of the wavefront velocity (U) at the wave tip region can be found by this formula:

$$\frac{8}{3}\times\frac{1}{f}\times\frac{\left(1+\frac{1}{2}\times\frac{V_O}{\sqrt{gd_o}}-\frac{1}{2}\times\frac{U}{\sqrt{gd_o}}\right)^3}{\frac{U^2}{\sqrt{gd_o}}}=\sqrt{\frac{g}{d_o}}\times t \tag{2-63}$$

where Vo is the initial wave velocity in the reservoir.

The location of the beginning of the tip region (x_1) can be found by:

$$\frac{U}{\sqrt{gd_o}}=\frac{2}{3}\left(1+\frac{1}{2}\times\frac{V_o}{\sqrt{gd_o}}+\frac{x_1}{\sqrt{gd_o}\times t}\right) \tag{2-64}$$

Lastly, the wave tip region length is calculated by:

$$\frac{x_s-x_1}{d_o}=\frac{4}{f}\times\frac{gd_o}{U^2}\left(1+\frac{1}{2}\times\frac{V_o}{\sqrt{gd_o}}-\frac{1}{2}\frac{U^2}{\sqrt{gd_o}}\right)^4 \tag{2-65}$$

Chanson (2005) provides comprehensive and analytical solutions for a surge with initial velocity moving over a rectangular-shaped flume with a wide width towards an inclined bed with friction.

In this case, it can be assumed that the flow before the tip region is almost ideal and the wavefront velocity (U) is:

$$\frac{8}{3}\times\frac{1}{f}\times\frac{\left(1+\frac{1}{2}\times\frac{V_O}{\sqrt{gd_o}}+\frac{1}{2}\times\sqrt{\frac{g}{d_o}}\times S_o\times t-\frac{1}{2}\times\frac{U}{\sqrt{gd_o}}\right)^3}{\frac{U^2}{\sqrt{gd_o}}}=\sqrt{\frac{g}{d_o}}\times t \tag{2-66}$$

Where S_o is bed surface slope.

The wavefront occurs at this distance:

$$\frac{x_s}{d_o}=\left(\frac{3}{2}\times\frac{U}{\sqrt{gd_o}}-\frac{1}{2}\frac{V_o}{\sqrt{gd_o}}-\sqrt{\frac{g}{d_o}}\times S_o\times t-1\right)+\sqrt{\frac{g}{d_o}}\times t+\frac{4}{f}\times\frac{1}{\frac{U^2}{\sqrt{gd_o}}}\times\left(1+\frac{1}{2}\frac{V_o}{\sqrt{gd_o}}+\frac{1}{2}\sqrt{\frac{g}{d_o}}\times S_o\times t-\frac{1}{2}\times\frac{U}{\sqrt{gd_o}}\right)^4$$

(2-67)

Lastly, dimensionless length distance for the wave tip region can be calculated as follows (Chanson, 2005):

$$\frac{x_s-x_1}{d_o}=\frac{4}{f}\times\frac{gd_o}{U^2}\left(1+\frac{1}{2}\times\sqrt{\frac{g}{d_o}}\times S_o\times t-\frac{1}{2}\frac{U}{\sqrt{gd_o}}\right)^4 \tag{2-68}$$

2.8 Discussion and Research needs

The literature review has provided a summary of several experimental and numerical attempts regarding the effects of tsunami-like waves on scour mechanisms and pore pressure variations around obstacles or in sediment sections. However, there has been limited work studying this subject in an appropriate manner. There are some areas where this research needs further advancement:

1. Despite all the performed experimental and numerical research, little attention has been paid to the geotechnical side of the scouring process, including pore pressure under the impact of extreme transient flows such as tsunamis. Therefore, there is a need to continue the examination of the effects of tsunami-like bores on these two phenomena.

2. Limited studies have addressed the effects of more than two influential factors on the scour and pore pressure values at the same time. In this study, the complexity of scour under a turbulent flow is explored in a saturated bed condition and under the influence of several variables such as still water depth, impounded water depth, bed slope.

Chapter 3. Experimental investigations on hydrodynamic characteristics of tsunami-like hydraulic bores impacting a square structure

The article is in third review in Journal of Hydraulic Engineering (ASCE)

3.1 Introduction

Over the past few decades, many coastal communities around the world have suffered massive causalities due to violent tsunami wave incidents. Comprehensive forensic engineering field surveys conducted after recent tsunami events provide well-documented reports on the features and associated damages from tsunami-induced waves to coastal structures (Sassa and Tomohiro, 2019). For instance, post-tsunami field investigations in the populated Sendai Plain region after the 2011 Tohoku Tsunami documented that this tsunami had maximum inundation height and runup height of 19.50 m and 20 m, respectively (Mori et al., 2011). Figure 3-1 shows the inland propagation of the 2011 Tohoku Tsunami induced waves.

Figure 3-1. Tsunami inundation near Sendai during the 2011 Tohoku Tsunami Japan (Image courtesy of Kyodo News Images Inc.)

Similarly, field surveys conducted after the 2004 Indian Ocean Tsunami in Indonesia and Thailand revealed that the hydrodynamic loading induced by extreme tsunami waves significantly damaged coastal structures and communities (Saatcioglu et al., 2006). These documented investigations reported a range of the runup heights with the lowest of 4.50 m above the sea level in the southwestern coast of Sri Lanka and the highest one in Banda Aceh with magnitude of 41.50 m generated by the Indian tsunami event which affected nine different countries surrounding the Indian Ocean (Rossetto et al., 2007). The 2011 Tohoku Tsunami in Japan was triggered by a severe earthquake (with a moment magnitude Mw of 9.10); a maximum observed inundation heights of up to 19.50 m was reported for tsunami waves propagating over an area of over 400 km2 causing a maximum runup height of 40.40 m (Nistor and Palermo, 2015). In February 2010, 53 countries in and around the Pacific Ocean received an emergency warning because of a major tsunami incident that occurred after an earthquake of moment magnitude Mw of 9.20. The triggered tsunami wave reached the coastline of Chile after 18 to 35 minutes with a runup height of 29 m (Palermo et al., 2013). Such recent tsunami incidents underscore the importance of detailed laboratory and numerical investigations on the vulnerability of coastal structures against tsunami waves.

Two design documents are currently available to support coastal engineers in estimating the impact of tsunami bores on coastal structures. ASCE/SEI 7, Chapter 6, Tsunami Load and Effects, elaborated by the American Society of Civil Engineers (ASCE7-16, 2016) is the only tsunami standard written in mandatory language which provides design best practices and guidance, as well as information on tsunami characteristics, inundation depth, and tsunami amplitude maps elaborated based on probabilistic hazard analysis. A second guideline is the Federal Emergency Management Agency (FEMA) P-646 (2012) which provides general information about tsunami hazards, tsunami depth, the tsunami load that need to be addressed when designing inland coastal infrastructure as well as structural design considerations.

In general, during a tsunami event, the first inundation wave, in the form of a surge or a highly turbulent bore, advances over dry land (termed also “dry bed”) while the second wave propagates over a wet bed generated by the inundation of the previous wave. The still water depth varies based on the bed material characteristics, bed slope, and tsunami-wave characteristics such as wavelength and wave period. To replicate the effect of such waves in the laboratory, comparison of tsunami wave characteristics and the waves generated by different water release mechanisms has indicated that the bore generated by a dam-break model has the best similarity to those of broken tsunami waves propagating overland (Chanson, 2006; Leal et al., 2009; Nouri et at., 2010; St-Germain et al., 2014; Wüthrich et al., 2018a). Chanson (2006) compared experimentally-generated dam-break waves propagating over a dry bed to visual images of the 2004 Indian Ocean tsunami. The analysis of experimental data generated by a sudden release of impoundment depth revealed that a dam-break induced wave can accurately reproduce a tsunami-induced bore. Leal et al. (2009) conducted laboratory experiments to characterize the impact of different bed materials such as fixed and movable beds (sand bed with d50 = 0.80 mm), of the reservoir length, and of the initial still water depth on variations of peak wave height with time. It was found that sediment beds reached highly movable bed conditions, when the sediment reached a state in which sand particles in the top layer are moving under sheet flow condition, as the flow velocity increased with impoundment depth.

Further, the hydrodynamics of tsunami-induced waves generated by a dam-break mechanism over a wet bed were experimentally studied by Wüthrich et al. (2018a). A flume 15.50 m long and 1.40 m wide connected to an upper reservoir with a volume of 7.08 m3 was used in their study. Three reservoir depths of 0.40 m, 0.63 m, and 0.82 m, and four different still water depths of 0.01 m, 0.03 m, 0.05 m, and 0.10 m were employed. The analysis of experimental results showed that the average bore front velocity increased by 15% as the impoundment water depth increased by 57%. It was also found that the normalized bore front velocity was inversely correlated with ho/do. For instance, a 90% increase of the still-to-impoundment water depth ratio for do = 0.82 m showed a 50% decrease in the normalized bore front velocity. On the other hand, in terms of the variation of momentum, the results showed that with the constant still water depth (0.05 m), the maximum momentum corresponded to the highest impoundment depth (i.e., 0.82 m). Moreover, the maximum momentum was calculated when the ratio of the water depth to the maximum wave height reached 90% (Wüthrich et al., 2018a). Tomiczek et al., (2019) performed a series of experimental studies at a 1:10 reduced scale to examine the horizontal forces and pressure distribution on a vertical structure due to tsunami-like waves were generated with a piston-based machine travelling over a slope-varying bed with starting and ending slopes of 1:12 and 1:24, respectively. The measured pressures were compared with Goda equations modified for elevated structures. The modified Goda equation yielded promising agreement between the predicted and observed pressure due to non-breaking waves impacting the structure (Tomiczek et al., 2019). Through a numerical work the effects of solitary and cnoidal waves determined by Green-Naghdi (GN) equations on submerged decks were studied by Hayatdavoodi et al. (2019). Comparison of the results of empirical formulae with experimental measurements and CFD solutions showed acceptable agreement. In terms of the effect of the solitary waves, it was seen that the vertical and horizontal forces applied on the decks increased as the deck length ratio (submerged deck length/ water depth) increased. Moreover, the vertical forces showed better agreement with empirical equations than the horizontal forces. For the case of the cnoidal waves, increase in the wave height caused nonlinear increase in the vertical forces applied on the submerged decks (Hayatdavoodi et al., 2019). In 2019, Istrati and Buckle conducted large scale (1:5) experiments to study the destructive effects of tsunami-like waves on common shapes of bridge designs. For this purpose, a composite bridge consisting of a reinforced concrete deck and four steel I-grider was modeled in a horizontal bed that was connected to two sloping beds (with slope of 1:12) in an approximate distance of 30 m and 10 m from the center of the bridge deck. The deck was impacted by a range of unbroken solitary waves and realistic tsunami-like transient bores. The results of this experimental investigation showed that for all wave types the maximum horizontal forced applied on the deck occurred at wave impact. However, the trapped air associated with the type of the deck impacted the structural response. For instance, for solitary waves the pressures exerted on the bottom of the deck approached their maximum values prior to wave arrival as the pressure due to waves transferred to the bridge surface through the air pocket. However, this was not observed during the propagation of tsunami-like bores because of complex interactions between trapped air and the tsunami-like bores (Istrati and Buckle, 2019).

The motion of a dam-break wave with a constant impoundment depth of 0.30 m over a sand section (d_{50} = 0.21 mm) with four different sloping seabeds of S_o = 0, 10%, 20%, and 50% was examined to (1) observe the propagation of wavefront and (2) extract the wave velocity profiles (Lauber and Hager, 1998a). It was found that the maximum discharge was independent of the bed slope for $S_o \geq 10\%$ (Lauber and Hager, 1998a). A study on the effects of bed slope on solitary wave characteristics by Young et al. (2008), where waves had high still-to-impoundment depth ratio (h_o/d_o = 0.60) and sloping beds of 1:5 (i.e., S_o = 20%) and 1:15 (i.e., S_o = 6.66%), indicated that the runup reached its maximum height during a short time on a steeper slope, and it did not clearly break, in comparison with a wave advancing onto a milder slope.

In short, the effect of various still-to-impoundment water depths and bed slopes on the hydrodynamics of tsunami-induced inundation and their impacts on coastal infrastructure has been investigated for a variety of experiments using non-dam-break wave generation methods. As mentioned earlier, the results of these studies may further cause difficulties in comparing the studies' results e.g. numerically or experimentally with an actual tsunami case. Therefore, the current study aims to close this gap by studying the effects of bed slope and of the still-to-impoundment water depth ratio on propagation of dam-break induced, tsunami-like waves in both subcritical and supercritical flow regimes. Furthermore, this study is the first to investigate on the dam-break waves characteristics and their hydrodynamics aspects such as water surface elevation, turbulent flow velocity momentum flux, and specific impulse in both subcritical and supercritical flow conditions over both horizontal and up-sloped beds.

3.2 Methodology

3.2.1 Experimental setup

A series of laboratory experiments were carried out in the Hydraulic Laboratory of the University of Ottawa, Canada, to investigate the effects of the bed slope and of the still-to-impoundment water depth ratio on the hydrodynamics of dam-break waves. All waves were generated by the sudden release of impounded water behind a rapidly-opening swing gate and propagated through a horizontal concrete flume. The flume is 30 m long and has a rectangular cross-section 1.50 m wide and 0.80 m high. The effects of bed slope on propagation of dam-break waves were studied for horizontal and inclined beds with an upslope of +5%. Schematics of the experimental setup and the adopted coordinate system for both horizontal and inclined beds are shown in Figure 3-2. As coastal beaches are often not entirely horizontal areas it is important to study the inland propagation of dam-break bores over sloping bed. An inverse slope of 5% was selected because the experimental results of Lauber and Hager (1998a) showed flow depths and discharge are independent of bed slope if S_o> 5%. Note that, similar with horizontal bed tests, the still water stood 0.03 m on top of the first-row tensiometers in inclined bed tests (see Figure 3-2 b).

The flume is equipped with a rapidly-opening swing gate which is used to store and release a specific volume of water to further generate the dam-break waves. By opening the swing gate, the impounded water propagated towards the downstream end of the flume as a turbulent bore front. In order to maintain a quasi-steady flow, a relatively long upstream reservoir with a length of 21.55 m was used. The non-dimensional reservoir length L to depth d_o ratio in this study was varied between 53.90 and 86.20 which is much larger than the minimum recommended L/d_o of 11.05 reported by Lauber and Hager (1998b). In all experiments, the upstream reservoir volume ranged between 8.08 m^3 and 13.92 m^3. The impoundment water depths, d_o, varied between 0.25 m to 0.40 m and the still water depths downstream of the gate, h_o, were between 0.03 m and 0.10 m. The inclined bed was initially saturated in all wet experiments. However, in low still water depth (h_o = 0.03 m) a vadose zone (unsaturated area) was developed close to the building model due to water drainage. Experimental studies by Young et al., (2008) indicated that flow patterns within the vadose zone had a minor influence on the saturated area underneath.

The selection of still and impoundment depths provided a wide range of h_o/d_o ratios ranging between 0.10 and 0.28 for the horizontal bed tests. This wide range enabled us to investigate the hydrodynamic characteristics of hydraulic bores in both subcritical ($h_o/d_o > 0.20$) and supercritical ($h_o/d_o \leq 0.20$) conditions. Four tests were conducted with horizontal (i.e., H series) beds and two tests were performed for inclined bed slope (S series) with the still-to-impoundment depth ratios of 0.075 and 0.085. Test specifications, including still-to-impoundment water depth ratio and the range of Froude numbers ($\mathrm{Fr} = u/(gh)^{0.5}$) at a location 4.30 m downstream of the swing gate are listed in Table 1.

The variations of Froude number with time were calculated using the time-histories of flow velocity (u) and of the water surface elevations (h) measured in each test using an ADV and WG2, respectively, at the beginning of the sand section. The velocity presented in this study is the vector magnitude to overcome any possible error due to ADV orientation with respect to the streamwise direction. Note that this could have somewhat increased the measured u with respect to u_x as the magnitude is the vector sum of all the components. For instance, Figure 3-3 presents the time-history of the Froude number for Test H1 (h_o= 0.03 m, d_o= 0.30 m). As shown in this figure, during the first 5 seconds of this test (2 s < t < 7 s) the Froude number corresponds to a supercritical flow with a maximum value of Fr = 2. Subsequently, after passage of the bore front, the flow becomes subcritical (t > 8 s) and quasi-steady (t > 15 s) with Fr ~ 0.50. Table 1 provides the maximum and minimum Fr observed during each test.

Table 3-1: Experimental parameters of the performed tests.

Test number	Slope (%)	d_o (m)	h_o (m)	h_o/d_o	Time (s) / Fr. range
H1	0	0.30	0.03	0.10	$2.85<t<50$
					0.44< Fr <1.98
H2	0	0.25	0.03	0.12	3.26<t<50
					0.42< Fr <1.67
H3	0	0.40	0.10	0.25	3.03<t<50
					0.15< Fr <0.64
H4	0	0.35	0.10	0.28	3.50<t<50
					0.18< Fr <0.99
S1	5	0.40	0.03	0.075	2.63<t<50
					0.10< Fr <4.20
S2	5	0.35	0.03	0.085	2.33<t<50
					0.08< Fr <4.00
S2	5	0.35	0.03	0.085	2.33<t<50
					0.08< Fr <4.00

*h_o is still water depth

*d_o is impoundment depth

A sand section was constructed in the flume to study local scour around the building model. Two false floors were fabricated to provide sufficient space for the middle sand section (Figure 3-2).

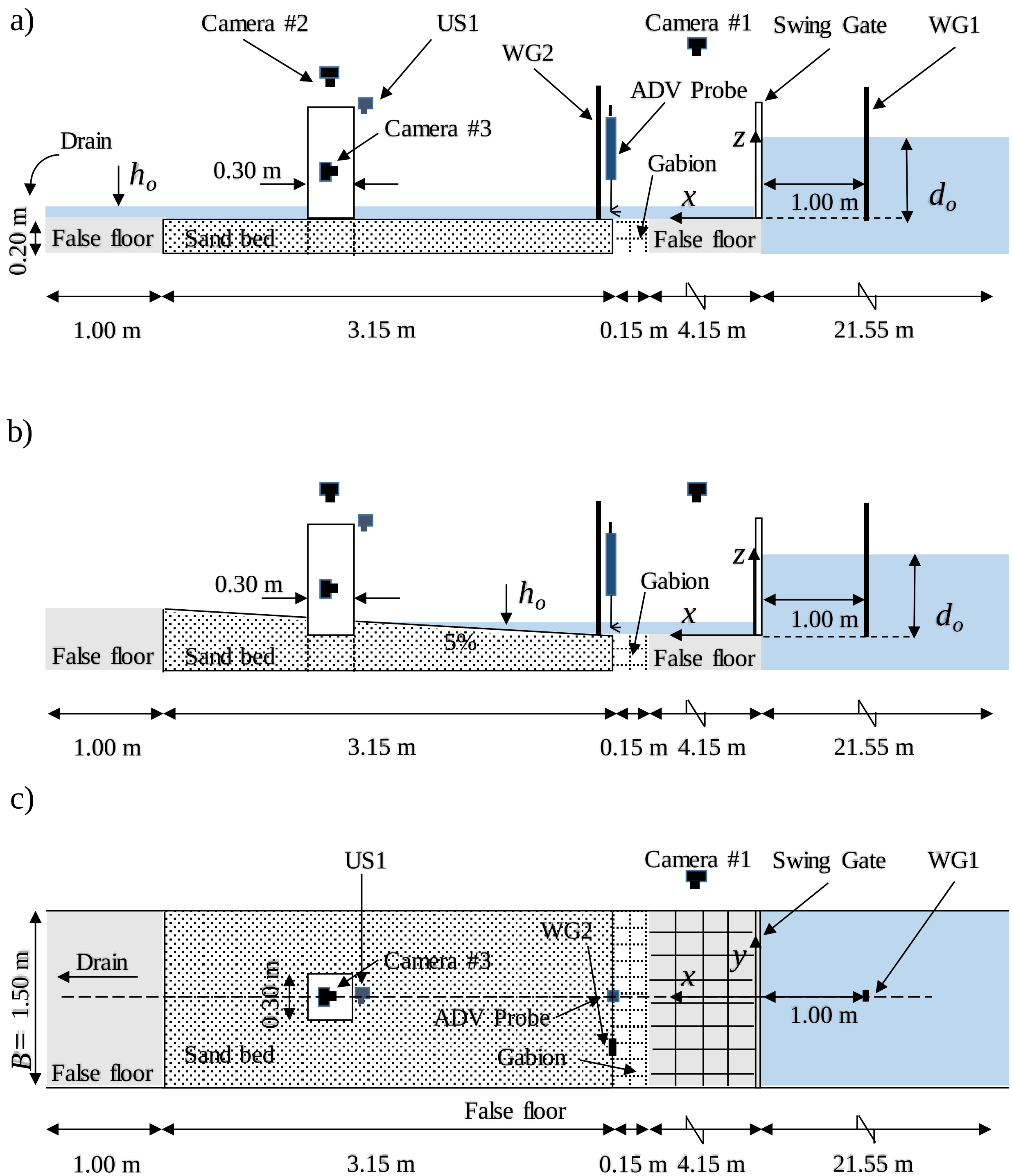

Figure 3-2. Experimental setup and adopted coordinate system; a) side view, horizontal bed; b) side view, inclined bed; c) top view.

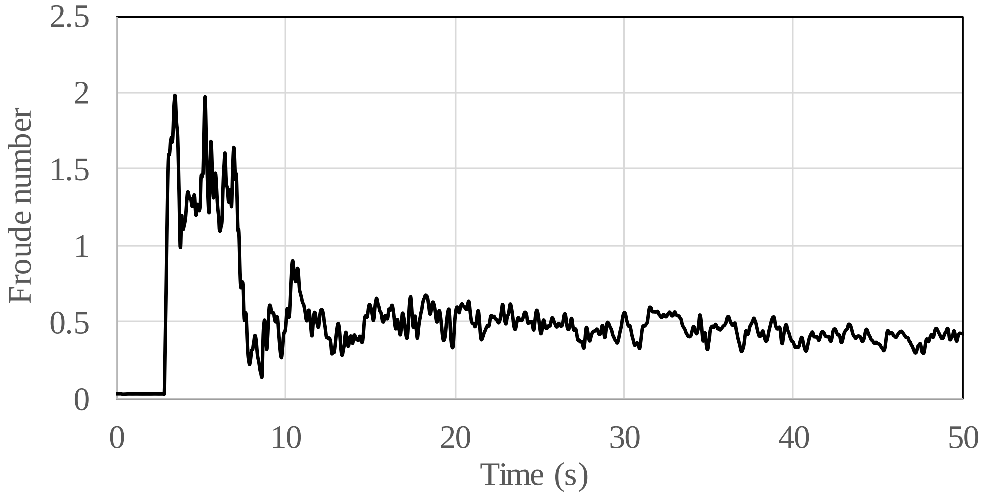

Figure 3-3. Time history of the Froude number for Test H1 (h_o = 0.03 m, d_o = 0.30 m)

The first false floor was 4.15 m in length and 0.20 m in height and it was installed right after the swing gate. A 0.20 m x 0.20 m grid was painted on the upstream false floor to facilitate measuring the bore front and flow surface velocity. To mitigate the transition of the bore waves from the solid false floor onto the sand bed, a 0.15 m wide gabion was installed across the width of the flume, at the upstream end of the sand test bed section. The gabion was filled with gravel with an average diameter of 30 mm. The sand bed section was 3.15 m long, 1.50 m wide, and 0.20 m deep and it was filled with well-graded sand particles with a mean diameter of d_{50} = 0.50 mm.

The bottom layer of the sand section was covered by a 10 mm gravel layer to ensure drainage flow in downstream direction. In addition, a geotextile sheet with a thickness of 1 mm was installed between this bottom gravel layer and the sand particles to prevent mixing of the two layers. A rigid 0.30 m square building model was built using 10 mm thick transparent Plexiglas sheets. The model was installed onto the concrete floor and it was located at the center of the sediment section at a distance of 5.87 m downstream of the swing gate. To control the still water depth and prevent sediment discharge through the drain, a vertically moving aluminum sharp-crested weir tail gate was located at the end of the second false floor. A sediment-trap box 0.76 m long, 1.43 m high, and 1.32 m wide, was installed in the drain to collect any remaining suspended sediments transported downstream of the test section.

3.2.2 Instrumentation

To measure the time-series of bore heights at different locations, two capacitance-type wave gauges (RBR WG-50, NRC, Ottawa, Canada) with measurement range of 0.50 m and an accuracy of ±0.40% were installed 1 m upstream (WG1) and 4.30 m downstream of the swing gate (WG2). An ultrasonic sensor (MASSA, M-5000/220, Massachusetts, USA) was mounted on the top of the front face of the building model to measure free surface elevation at 1.42 m downstream of the gate (US1). The ultrasonic sensor (US1) operated at a frequency of 220 kHz with a measuring resolution of 0.25 mm. A sampling frequency of 1200 Hz was selected for depth measurements which enabled the authors to detect the sudden wave peak at the arrival of a turbulent bore.

The bore front velocity was measured using an image analysis technique. Five Styrofoam balls with a 30 mm diameter and a density of 0.035 kg/m^3 were placed behind the swing gate before the start of each test. The velocity of each ball was calculated from consecutive image frames recorded with a wireless GoPro camera (GoPro-Hero5, San Mateo, CA, US) with a shutter speed of 60 frames per second. The instantaneous flow velocity of the bore after passage of the bore front was measured using a side-looking head Acoustic Doppler Velocimeter (ADV) probe (Nortek Vectrino, Vangkroken, Norway). The maximum velocity range was set to 2.50 m/s with an accuracy of ±1% of the maximum velocity range. The sampling frequency of the ADV probe was 200 Hz and a sampling volume of 45x10^{-7} m^3 was set for this study. The ADV probe was installed over the beginning of the sand section (i.e., 4.30 m downstream of the swing gate) and in the channel center. To improve signal detection and to ensure adequate signal-to-noise ratio (SNR), aluminum oxide seeding particles with an average diameter of 27 microns were mixed into the water for each experiment.

Three GoPro video cameras were used during the experiments. The first camera was placed above the upstream false floor to track the bore front and Styrofoam balls motion. The second camera was located inside the transparent structure (column) to record the time and spatial evolution of the scour hole around the structure while the third camera was positioned 2 m above the structure to monitor flow separation near the model. The waterproof GoPro cameras had internal power supply and memory storage and they were synchronized. Figure 3-4 shows the positioning of the structural model and instruments and includes also details of the swing gate, gabion weir, capacitance-type wave gauges (WG1 and WG2), ultrasonic wave sensor (US1), and the ADV probe in the channel.

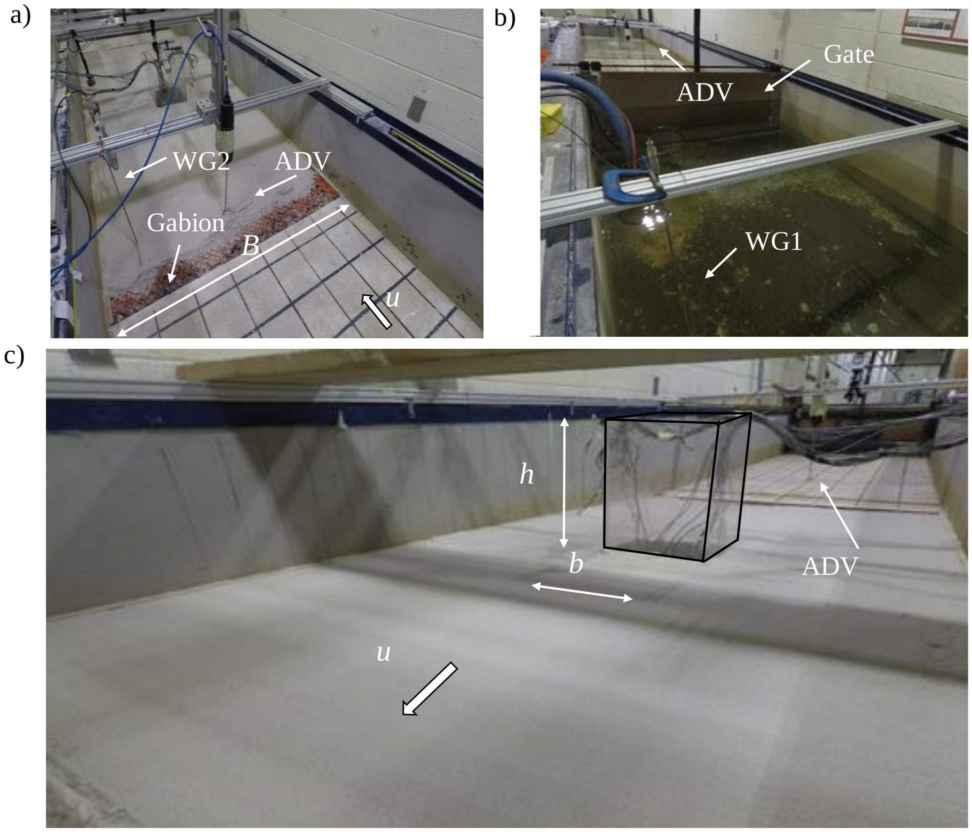

Figure 3-4. Positioning of instrumentation in the open channel and structural model; a) locations of the ADV probe and wave gage WG2 installed upstream of the structural model; b) position of wave gauge WG1 installed upstream of the swing gate; c) position of structural model in the middle of channel.

3.2.3 Data acquisition procedure

Two Data Acquisition Boards (DAQ) NI USB-6009 with 16 channels and NI USB-6210 with 8 channels (National Instruments Corporation, Austin, Texas, US) having an input voltage range of ±10 Volts were used to acquire analog signals from instruments and to produce digital signals from analog data. The digital signals were controlled and recorded using LabView software (National Instrument Austin, Texas, US), with a sampling rate of 40 Hz. Both DAQ boards were synchronized by integrating data from each instrument using virtual instrument subroutines (VIS) compiled on LabView software (Al-Riffai, 2014). Although the instruments had different sampling rates, utilization of the NI data acquisition boards ensured that all data streams were collected with the same sampling rate of 40 Hz. All video cameras were synchronized with each other using

GoPro Multi-Controller software (GoPro-Hero5, San Mateo, CA, US). The swing gate was connected to a friction switch that turned on an LED light installed next to the upstream false floor indicating the beginning of the experiments.

3.2.4 Gate opening time

Gate opening time is critical to allow the formation of well-developed dam-break waves and this subject has been investigated in several experimental studies carried out to identify a maximum opening time for dam-break problems (Lauber and Hager, 1998b; Chanson 2006; Oertel and Bung, 2012). A non-dimensional gate opening time was introduced by Lauber and Hager (1998b) to evaluate gate opening times as $T_o = t_o(g/d_o)^{0.5}$ where t_o is the gate opening time, g is the gravitational acceleration, and d_o is the impoundment water depth (Lauber and Hager, 1998b). Vischer (1998) defined T_o as an operating non-dimensional opening time to generate gate independent dam-break waves for $T_o \leq 1.25$ and Lauber and Hager (1998b) showed that sudden dam-break waves would be generated in a horizontal bed condition if the opening time reaches the condition of $T_o < 1.41$. The gate opening time in the present study was recorded using an LED light combined with a Gopro camera positioned above the first false floor. The preliminary tests indicated that this opening time was met in the current experimental studies ($T_o < 1.17$ or t_o=0.19 s). Also, for the gate used in the present study, Stolle et al. (2019) found that the gate opening time mainly affects the wave arrival time while the wave profile is not significantly influenced by the non-dimensional opening time. They also introduced a linear relation between the impoundment depth and the gate opening time as $T_o = 1.47-1.19d_o$. Considering the range of the impoundment water depth in this study, the dimensionless gate opening times were in the range of $0.99 < T_o < 1.17$, indicating that the gate opening did not affect the wave profile.

3.2.5 Signal preparation

A Butterworth low-pass digital filter (MatLab, MathWorks, U.S, 2018) was used to remove raw signal noises and signal spikes recorded by the two capacitance-type wave gauges, the ultrasonic sensor, and the ADV probe. The advantage of using the Butterworth low-pass filter was that the reported value of the arrival time of the turbulent bore front was not influenced by the filtering procedure (Saltzer, 2002; Mello et al., 2007). As the unified sampling frequency of the data acquisition boards was set to 40 Hz, the cut-off frequency was limited to the Nyquist frequency of signals (i.e., f_N = 20 Hz). A comparison between the filtered data and the cut-off frequencies of 20 Hz and 30 Hz indicated that the filtered data with a cut-off frequency of 30 Hz provided satisfactory filtered signals; this cut-off frequency was applied for all signals. As a result, a cut-off frequency of 30 Hz was selected for low-pass filtering. Figure 3-5a shows the ratio of the peak instantaneous magnitude of flow velocity and water surface elevation before and after de-noising for each test case.

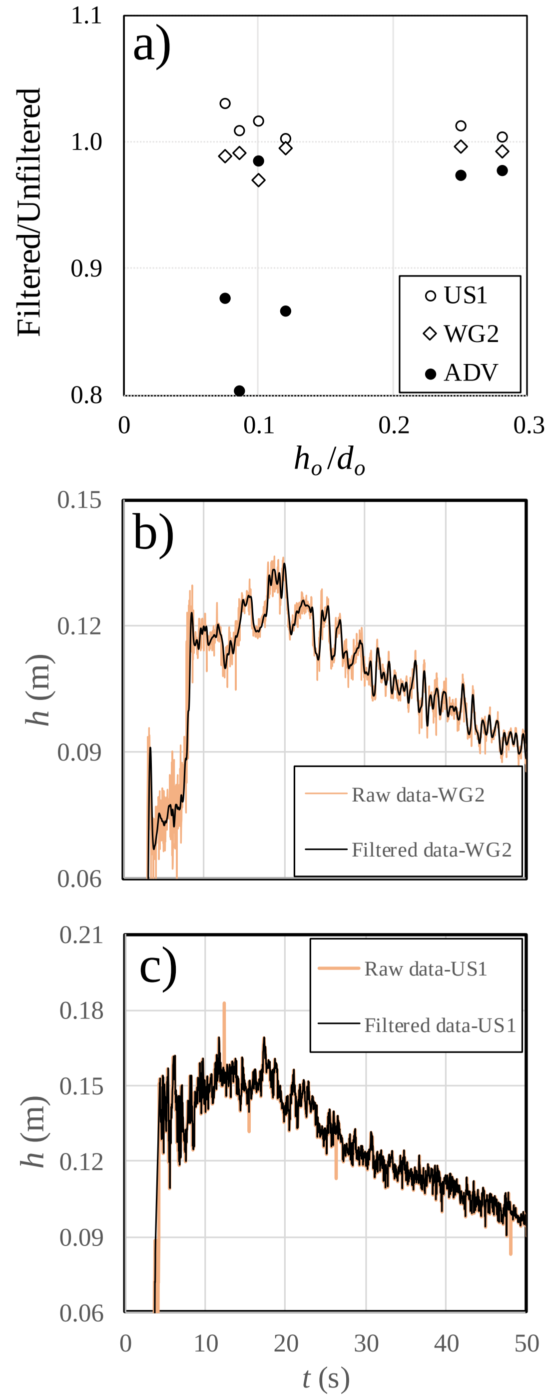

Figure 3-5. Effects of signal de-noising by Butterworth low-pass filter with a cut-off frequency of 30 Hz on water depths and turbulent bore velocity: a) effect of data filtering on the maximum depth and velocity; b) effect of data filtering on the time-history of WG2; c) effect of data filtering on the time-history of US1.

As the filtered/unfiltered ratio presented in Figure 3-5a approaches a value of one, collected data did not change significantly after de-noising (as shown in Figure 3-5b). Otherwise, the low pass filter attenuated the level of the signals by eliminating high level of noise (Figure 3-5c) (Magsi et al., 2018), leading to a lower value for the ratio of the filtered signals over non-filtered (original) values. As it can be seen in Figure 3-5a, the percentile of the difference between the filtered and unfiltered peak water surface level varied between 0.2% and 3%. On the other hand, due to spike removal the percentile difference between the filtered and unfiltered peak velocity ranged between 2% and 24%.

3.2.6 Repeatability

To verify the repeatability of depth and velocity signals, all tests were repeated three times in strictly identical conditions. Figure 3-6 shows the time-histories of the measured water surface profiles obtained from the capacitance-type wave gauge (WG2) for test H3 (h_o = 0.10 m, d_o = 0.40 m) and the ultrasonic wave sensor (US1) for test H2 (h_o = 0.03 m, d_o = 0.25 m).

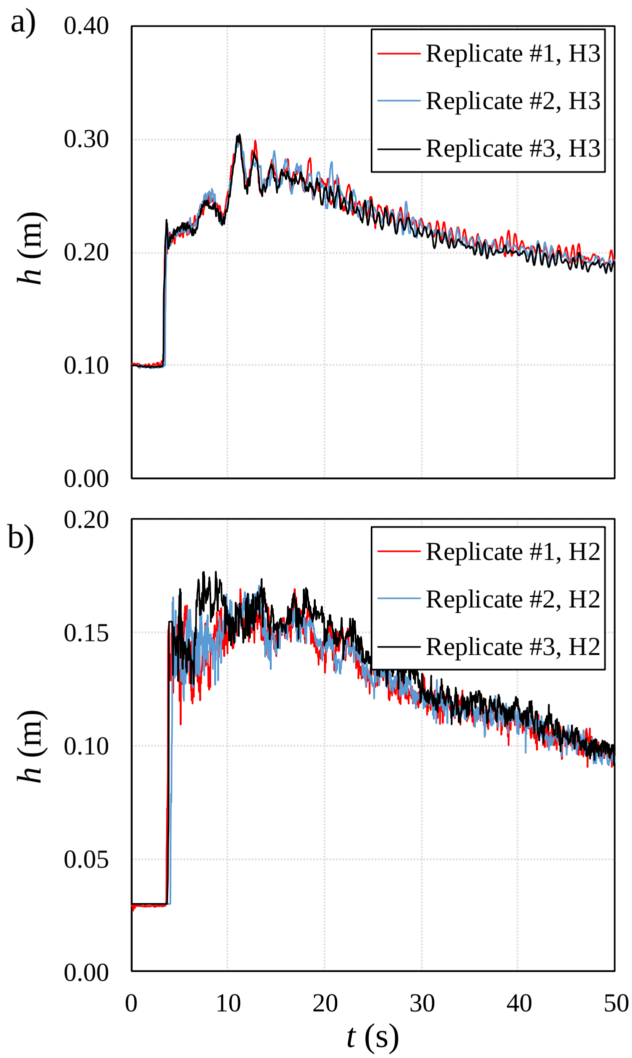

Figure 3-6. Repeatability of tests for water depths measured at the beginning of the sand section by WG2 and in front of the structural model by; a) WG2, h_o/d_o = 0.25, b) US1, h_o/d_o = 0.12.

As it can be seen, these time histories present similar profiles for each repeated test. The range of uncertainty in all the tests varies between 0.1%-1.30% which is less than the 5% uncertainty observed in other studies (Wüthrich et al., 2018a; Shafiei et al., 2016).

As shown in Figure 3-6a, both wave peaks were detected in the repeated tests for h_o/d_o = 0.25 and the variations of wave height measurements were within ±0.10%. The repeatability of wave signals obtained from (US1) is shown in Figure 3-6b. The first wave peak was detected in all three repetitions. The variations from the average signal values were found to be within ±0.04%. A comparison of the time series for the wave height indicated that the tests were repeatable.

3.3 Results and Discussion

3.3.1 Wave hydrodynamics in horizontal beds

The interaction of turbulent bore front and building model is of great interest for the analysis of flow separation and hydrodynamic forces on coastal structures. Figure 3-7 shows top view images of the propagation of a turbulent bore front (depicted by a white line) at the early stage of motion towards the building model for test H2 (h_o = 0.03 m, d_o = 0.25 m).

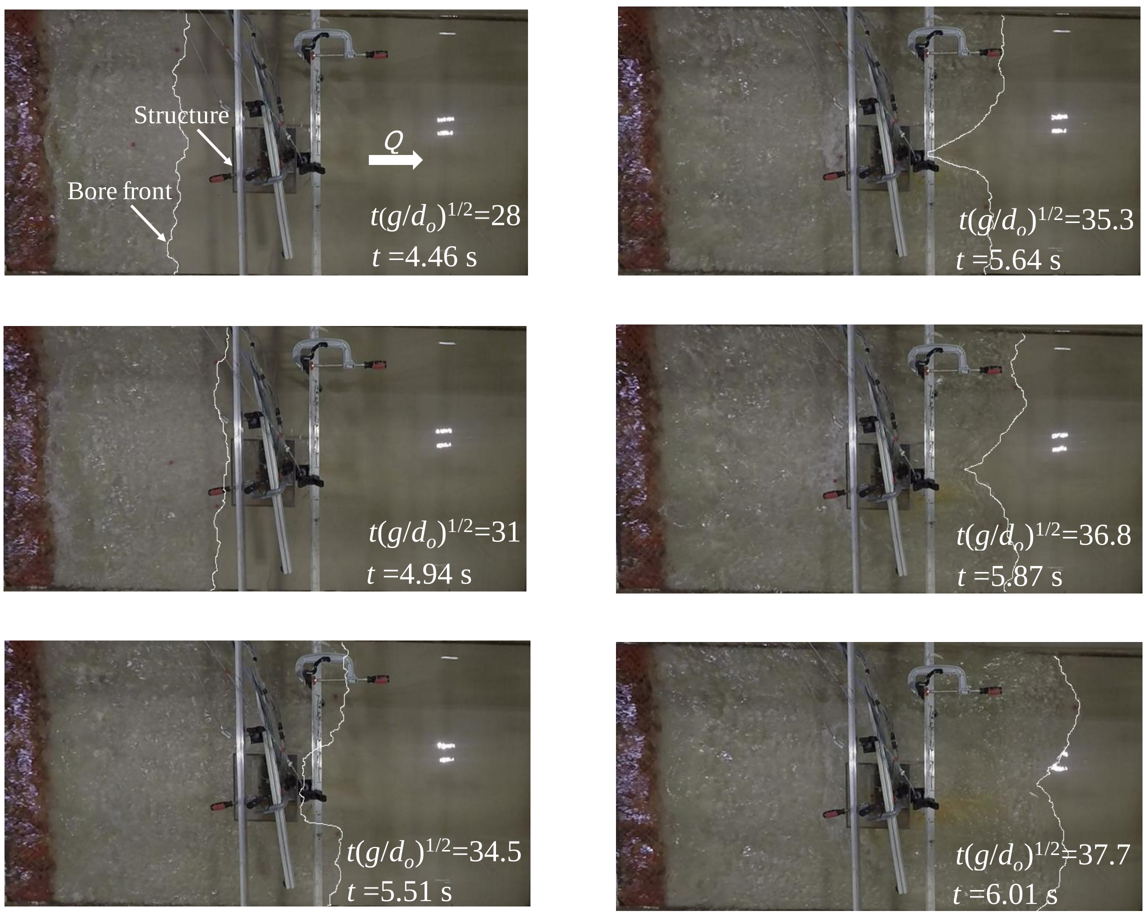

Figure 3-7. Top view images of bore front propagation with non-dimensional time $t(g/d_o)^{1/2}$ for Test H2, h_o/d_o = 0.12.

The propagation time was normalized with the characteristic time scale of impoundment depth ($t(g/d_o)^{1/2}$). As Figure 3-7c shows, the bore front hit the building model at a non-dimensional time of $t(g/d_o)^{1/2}$ = 31, and as a result, the water level suddenly rose at this normalized time (i.e., $t \approx$ 5 s) and kept rising until the bore front passed the entire sediment section and discharged to the drain located at the end of the flume at $t(g/d_o)^{1/2} \approx$ 42. Once the turbulent bore front passed the structure, the bore water level dropped and the runup gradually increased the water level for a duration of approximately 10 seconds (i.e., $t(g/d_o)^{1/2} \approx 97$).

In order to investigate the bore front hydrodynamics in both subcritical and supercritical conditions, the time histories of water wave depth and velocity for two supercritical cases of H1 and H2 (h_o/d_o = 0.10 and 0.12) and two subcritical cases of H3 and H4 (h_o/d_o = 0.25 and 0.28) were measured. Figure 3-8 shows the time history of water surface elevation measured in the beginning of the sand section (WG2, Figure 3-8a) and at the location of the building model (US1, Figure 3-8b) for different still-to-impoundment depth ratios, h_o/d_o.

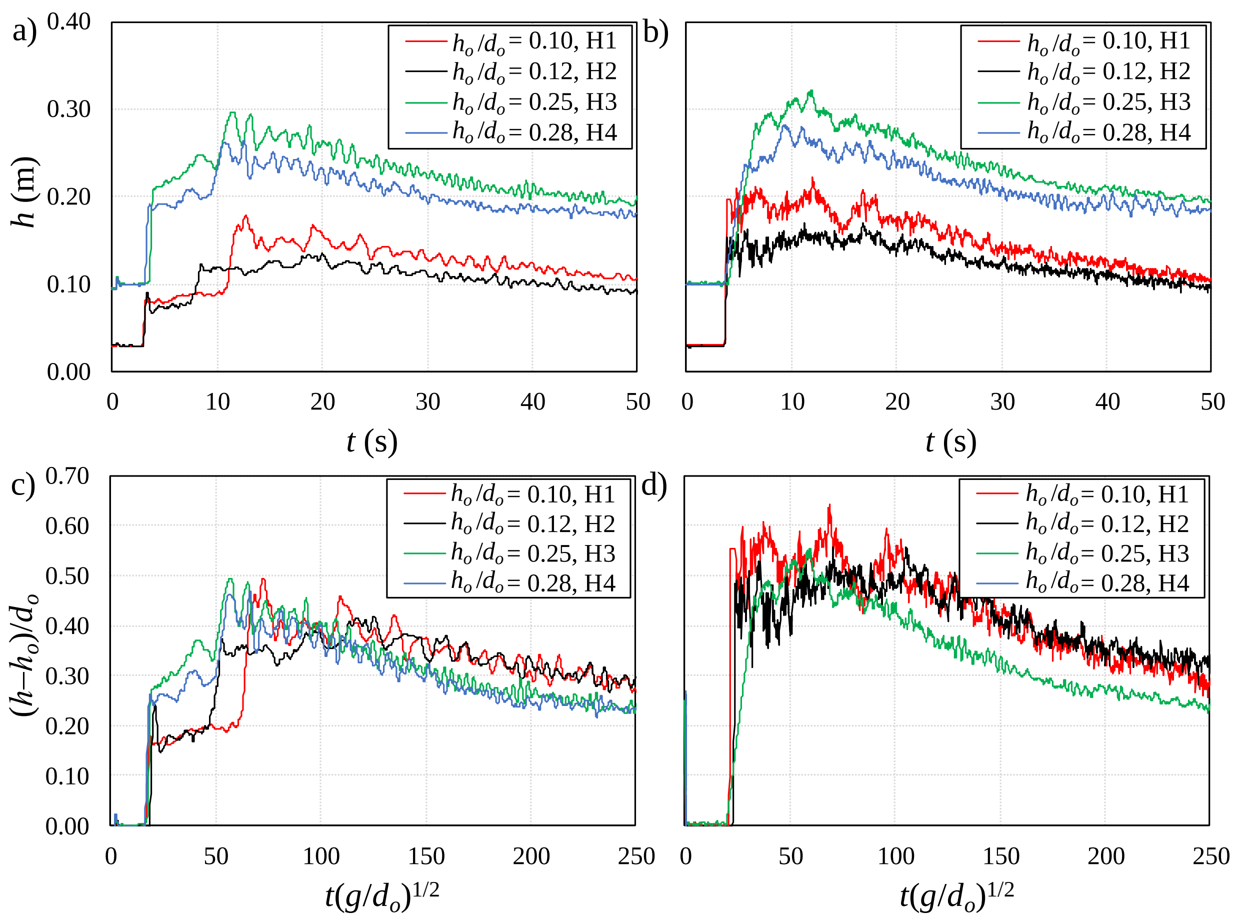

Figure 3-8. Time-history of the water depth at the beginning of sand bed section (WG2) and in the location of structural model (US1) for different still-to-impoundment depth ratios; a) measured water depth by WG2; b) measured water depth by US1; c) variations of normalized water depth $(h–h_o)/d_o$ with normalized time $t(g/d_o)^{1/2}$ for WG2; d) variations of normalized depth with normalized time for US1.

As it can be seen, the acquired water level signals accurately detected the constant still water levels in the first 3 seconds of data acquisition and then the magnitude of water levels indicates the effect of various impoundment depths. For instance, the highest impoundment depth was used in test H3 (h_o = 0.10 m, d_o = 0.40 m) which is clearly reflected in both measurements by WG2 and US1. A comparison between the wave depths at the two different locations indicates that the effect of the still-to-impoundment depth ratio was significant close to the gate and it faded out further downstream of the gate. A similar observation was reported by Nouri et al. (2010). The highest difference between the wave peaks was found between tests H3 (h_o = 0.10 m, d_o = 0.40 m) and H2 (h_o = 0.03 m, d_o = 0.25 m), with a value of Δh = 0.18 m at the location of WG2 and it reached Δh = 0.16 m at the location of US1.

In order to compare the hydrodynamic characteristics of the dam-break induced bores for tests with different still water depths, the absolute bore height, (h–h_o), was normalized with impoundment depth, do, and the propagation time was normalized with the bore characteristic time scale, (do/g)1/2. The variations of the normalized bore heights with normalized time are shown in Figure 3-8c (WG2) and Figure 3-8d (US1). The normalized absolute bore heights measured at the beginning of the sand section (i.e., location of WG2) show that the maximum normalized bore height was between 0.43 and 0.47 and that the initial peak occurred at the non-dimensional time between 50 and 130 regardless of the still and impoundment depths and flow regime. This indicates that the selected length and time scales were both appropriate.

A comparison between the time-series of the wave height in subcritical (tests H3 (h_o = 0.10 m, d_o = 0.40 m), H4 (h_o = 0.10 m, d_o = 0.35 m)) vs. supercritical (tests H1 (h_o = 0.03 m, d_o = 0.30 m), H2 (h_o = 0.03 m, d_o = 0.25 m)) flow regimes shows completely different flow patterns at the beginning of the sand bed section (Figure 3-8c), as well as in the location of the building model (Figure 3-8d). As Figure 3-8c shows, a sudden drop of the bore height was observed in the supercritical flow regime after the first peak and the runup was reached after a delay of approximately t(g.d_o)1/2 = 50. The time lag between the first and second wave fronts was found to be a function of ho/do and the time lag decreased as ho/do increased. The supercritical bores reached the peak bore height much faster in comparison with subcritical bores. This was likely due to the influence of the lower still water depths and the bore-breaking mechanism. For subcritical bores, the bore height continuously increased after the first wave front passed the sensors and reached the peak height slightly earlier than supercritical bores. The magnitude of the normalized peak bore height and the corresponding time to peak were found to be independent of ho/do for subcritical bores.

Figure 3-8d shows the bore height variations with normalized time in the model location (US1). As demonstrated, the still water resisted the dam-break bore motion and as a result, the normalized bore height and wave duration were much smaller in the subcritical flow regime. A comparison of the absolute wave height of the subcritical and supercritical bores (h_o/d_o = 0.10 and h_o/d_o = 0.28) with approximately similar impoundment depths (0.30 m and 0.35 m) indicates that the runup height in the subcritical bore (h_o/d_o = 0.28) was approximately 20% smaller than that of the corresponding supercritical bore (h_o/d_o = 0.10). In addition, the runup in supercritical bores occurred predominately in the front face of the structure and it lasted 1.40 times longer (time-wise) than the subcritical bore. The higher still water in subcritical bores also decreased the height of the runup wave and caused a delay on its arrival time, which was also observed in the studies of Çağatay and Kocaman (2008) and Ghodoosipour et al. (2019).

3.3.2 Wave hydrodynamics on inclined beds

Figure 3-9 demonstrates the time history of water surface elevation of supercritical bores over an inclined bed with an inverse slope of +5%.

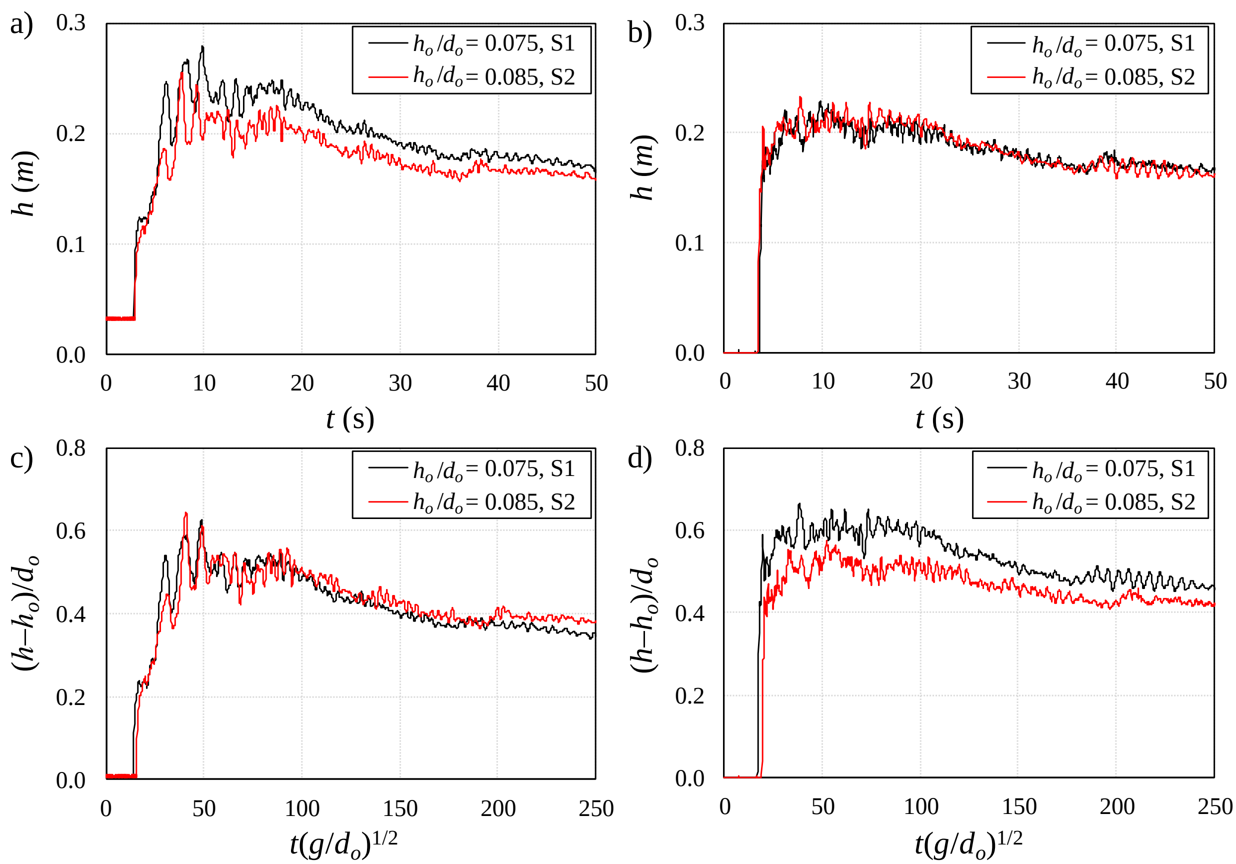

Figure 3-9. Effect of the impoundment depth on the water surface level for inclined bed tests; a) time-history of the water surface profile in the beginning of the sand section, WG2, b) time-history of the water surface profile in the location of the structural model, US1, c) variations of normalized the water surface level $(h\text{-}h_o)/(d_o)$ in the beginning of the sand section, WG2, with normalized time $t(g/d_o)^{1/2}$, d) variations of normalized the water surface level $(h\text{-}h_o)/(d_o)$ in the location of the structural model, US1, with normalized time $t(g/d_o)^{1/2}$.

The time history of water surface elevations in the beginning of the sand section (Figure 3-9a) shows the effect of ho/do on inclined bed tests, whereas the ho/do effect had diminished when the bore reached the building model (Figure 3-9b). Three bore height peaks were observed during the propagation of turbulent bores over the inclined bed and in the beginning of the sand bed section (Figure 3-9a). The first peak recorded in test S1 (h_o = 0.03 m, d_o = 0.40 m) was detected once the bore front arrived in the beginning of the sand bed section (i.e., $t \approx 3$ s) with a magnitude of h = 0.13 m and, then, the main wave reached the sand section approximately 2 seconds later, with a magnitude, h = 0.25 m. The second peak formed during the drawdown process (i.e., at $t \approx$ 7 s). At this time, the top water layer flew backward towards the upstream section of the flume while the bottom water layer rushed up again. Therefore, the second peak was associated with the runup and the drawdown process.

The loading time was relatively short for the inclined bed tests, i.e., the time difference between the bore front peak and the runup peak was very small ($\Delta t \approx 2$ s). Comparably, there was much longer loading time in horizontal bed tests (e.g., $\Delta t \approx 10$ s for H1 (h_o = 0.03 m, d_o = 0.30 m)). The observations showed that the impoundment depth increased the bore front height, but had less influence on the peak runup height and the time delay between the bore front and the runup peaks. A comparison of wave heights measured for horizontal and inclined beds for tests with similar impoundment depths (i.e., Tests H1 and S2) indicates that the wave-breaking event (demonstrated by the first wave peak) was detected more clearly for horizontal bed tests. Figure 3-9c shows the variations of normalized absolute wave height with normalized time detected by the WG2 sensor; it can be observed that the maximum absolute wave height occurred at the same normalized time of $t(g.d_o)^{1/2} = 50$ for both tests S1 (h_o = 0.03 m, d_o = 0.40 m) and S2 (h_o = 0.03 m, d_o = 0.35 m). However, the normalized peak value increased by 10% in Test S1 (h_o = 0.03 m, d_o = 0.40 m) compared to the case Test S2 (h_o = 0.03 m, d_o = 0.35 m). Figure 3-9d shows the time-series of the normalized runup height for dam-break waves for the inclined surface detected by the US1 sensor. It was found that the peak runup height increased by approximately 10% in test S1 (h_o = 0.03 m, d_o = 0.40 m) in the inclined bed once the bore propagated from the beginning of the sand section towards the building model. However, the arrival time was approximately the same for both tests ($t \approx 5$ s) (see Figure 3-9b).

Figure 3-10 shows a comparison of wave height variations with time for both horizontal and inclined-bed tests in supercritical flow condition for relatively similar still-to-impoundment depth ratios. It can be seen that the positive bed slope increased the wave height both upstream, at the start of the sediment bed (Figure 3-10a), as well as near the structure (Figure 3-10b).

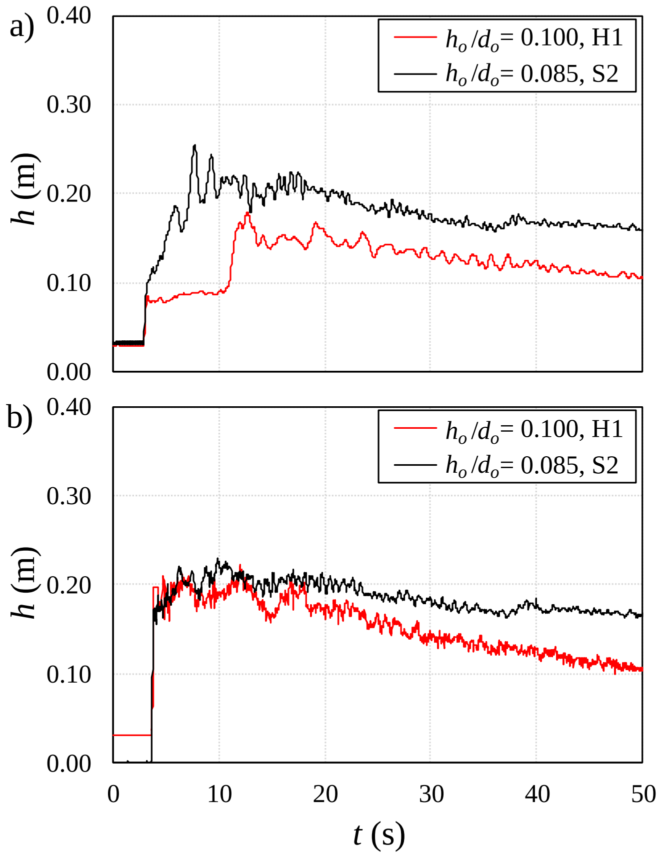

Figure 3-10. Effect of sand bed slope on variations of the measured water depth with time measured by; a) WG2; and b) US1.

As the hydraulic bore propagated over the inclined bed, the wave front decelerated and the wave height increased due to both the wave deceleration and the higher level of the inclined bed ($\Delta z = 0.08$ m at the structure location). Figure 3-10a shows that the inclined bed increased the peak wave height by approximately 40% and that the wave peak occurred approximately 5 seconds earlier than in the horizontal bed test. The earlier occurrence of the wave peak in the inclined test could be due to the loading and unloading times induced by the runup and drawdown processes (Young et al., 2008). The effect of soil saturation was found to be more pronounced for the inclined bed tests in comparison with the horizontal bed tests. The sand bed section was partially saturated due to relatively small still water depth of 0.03 m for the inclined bed tests. Therefore, the bore front partially penetrated through the wet and unsaturated sand bed section. The performance of the partially saturated bed in the inclined tests was more evident in variations of the wave height at the location of US1. The water wave height over the inclined bed test (i.e., test S1 (*ho* = 0.03 m, *do* = 0.40 m)) did not increase noticeably and the peak wave height was constant with a value of *h* = 0.20 m between 5 and 23 seconds after the gate opening (Figure 3-10b). Both horizontal and inclined bed tests had a still water depth of *ho* = 0.03 m; however, due to the positive upslope, the still water approached zero near the position of US1.

3.3.3 Flow velocity

Figure 3-11 illustrates the time history of bore flow velocity variations and the effects of ho/do at the beginning of the sand bed section (see Figure 3-4a), for both the horizontal and the inclined bed tests.

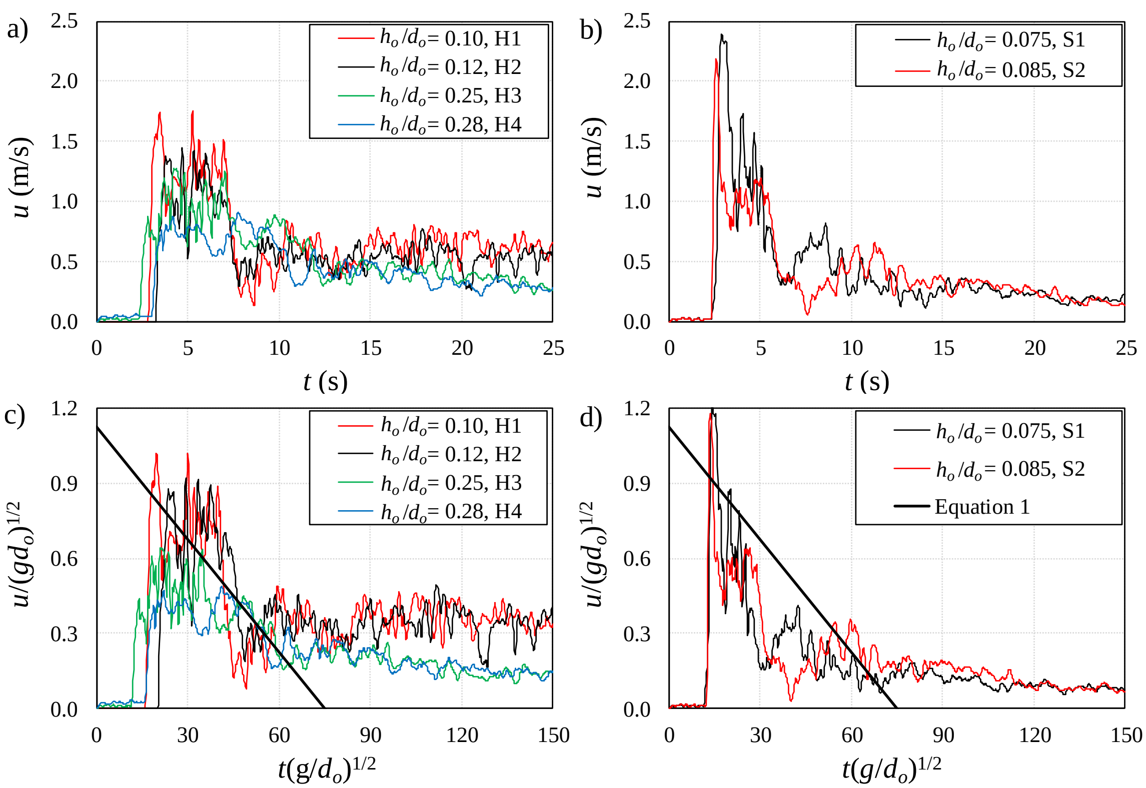

Figure 3-11. Time-history of the flow velocity at the beginning of sand bed section (WG2) for horizontal and inclined sand bed sections and for different still-to-impoundment depth ratios; a) measured water velocity in horizontal sand bed sections, H-series; b) measured water velocity in inclined sand bed sections, S-series; c) variations of normalized water velocity $u/(gd_o)^{1/2}$ with normalized time $t(g/d_o)^{1/2}$ for horizontal bed; d) variations of normalized velocity with normalized time for inclined bed.

Although the ADV probe was located at the beginning of the sand section, it could still capture the effect of bed slope on flow velocity reduction once the bore front propagated over the inclined bed. Figure 3-11a shows the effects of ho/do for both subcritical and supercritical flow regimes for horizontal bed tests. Relatively higher peak velocities were observed during supercritical flow regimes, with an average velocity range of 0.60 m/s to 0.90 m/s. In addition, higher velocity and turbulent fluctuations were observed for waves with higher impoundment depth. When the flow velocity becomes quasi-uniform, the velocity was approximately 0.40 m/s larger in supercritical than subcritical flow regimes (see Figure 3-11a). The effect of the still water depth on flow velocity is also shown in Figure 3-11a for tests H1 (h_o = 0.03 m, d_o = 0.30 m) and H4 (h_o = 0.10 m, d_o = 0.35 m) conducted with approximately the same impoundment water depths but with different still water depths. It was found that the maximum flow velocity decreased by 50% as the still water depth increased by 0.07 m. A similar still water depth effect was also reported in the study of Stoker (2011).

Figure 3-11b shows the time-series of flow velocity for inclined bed tests. In this case, a higher peak velocity (2.30 m/s) was observed, and the peak velocity lasted 2 seconds longer in test S1 (conducted with higher impoundment depth (i.e., h_o/d_o = 0.075)), compared to the case of test S2 (h_o = 0.03 m, d_o = 0.35 m). However, the flow velocity magnitudes in the equilibrium condition (i.e., t > 20 s) were equally about 0.30 m/s for both ho/do = 0.075 and ho/do = 0.085. Figure 3-11c and 11d show the variations of flow velocity normalized by the wave celerity (gd_o)1/2, with the normalized time for horizontal and inclined bed tests, respectively. A comparison between two similar experiments (H1 (h_o = 0.03 m, d_o = 0.30 m) and S2 (h_o = 0.03 m, d_o = 0.35 m)) for horizontal and inclined bed tests indicated that the positive 5% upslope increased the peak flow velocity by 25% and it occurred approximately one second earlier in the inclined bed test (S2 (h_o = 0.03 m, do = 0.35 m)). The effects of bed slope on the magnitude and arrival time of wave velocity were also reported by Leal et al. (2009).

3.3.4 Specific momentum and impulse

The momentum flux induced by tsunami waves can be also used to estimate the hydrodynamic forces exerted on coastal structures and has been used in design guidelines (Park et al., 2013). The FEMA building code (FEMA, 2018) uses the maximum momentum flux to design coastal structures and to analyze structure destruction (Park et al., 2017). Figure 3-12 shows the time history of the specific momentum flux per unit mass, hu^2, for both subcritical and supercritical flow regimes over horizontal and inclined beds.

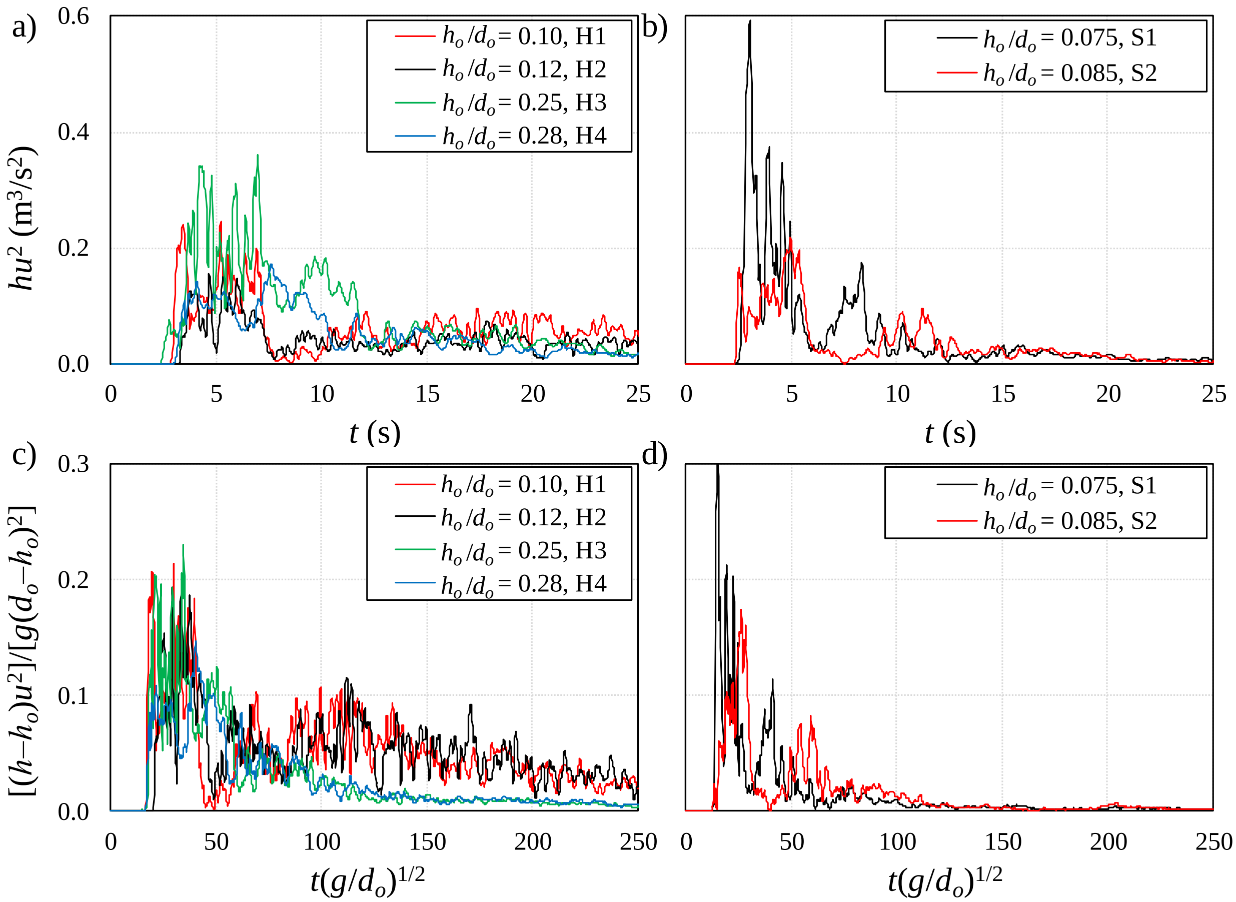

Figure 3-12. Effect of still-to-impoundment depth ratio on the specific momentum flux per unit mass of bores (hu^2) in the beginning of sand bed section (WG2) for: a) horizontal bed and b) inclined bed; c) variations of normalized specific momentum with normalized time for horizontal bed; d) variations of normalized specific momentum with normalized time for inclined bed.

Figure 3-12a shows higher specific momentum flux per unit mass peaks for tests H1 (h_o = 0.03 m, d_o = 0.25 m) and H3 (h_o = 0.10 m, d_o = 0.40 m), where those tests were in supercritical and subcritical flow regimes, respectively. The test H3 (h_o = 0.10 m, d_o = 0.40 m) had the highest wave height due to high still water depth, while H1 (h_o = 0.03 m, d_o = 0.30 m) had the highest bore flow velocity. Therefore, the source of high momentum flux per unit width value can be due to either wave height or flow velocity. A comparison of the specific momentum per mass width ($dM/dt = hu^2$) over horizontal beds and for different still-to-impoundment water depth ratios indicated that the subcritical bore (test H3 (h_o = 0.10 m, d_o = 0.40 m)) demonstrates approximately 60% higher momentum flux per unit width than the supercritical bore (test H1 (h_o = 0.03 m, d_o = 0.30 m)) with peak values of 0.38 m^3/s^2 and 0.23 m^3/s^2, respectively. Moreover, the maximum specific momentum flux per unit mass occurred 3 seconds earlier in test H3 (h_o = 0.10 m, d_o = 0.40 m) in comparison with test H1 (h_o = 0.03 m, d_o = 0.30 m).

Overall, a higher peak momentum flux per unit mass was found in subcritical bores, which could be due to the effect of the higher still water depth (i.e., h_o = 0.10 m). By excluding the still water depth effect and using the absolute bore height in calculation of normalized specific momentum flux (Figure 3-12c), the peak normalized specific momentum flux per unit mass became similar for both the subcritical and supercritical bores and could be expressed as (Eq. 3-1):

$$\frac{u^2(h-h_o)}{g(d_o-h_o)^2} = 0.21 \tag{3-1}$$

The effect of the bed slope on variations of specific momentum flux per unit mass with time is shown in Figure 3-12b. Test S2 (h_o = 0.03 m, d_o = 0.35 m), which used approximately the same impoundment depth and similar still water depth (i.e., h_o = 0.03 m) as test H1 (h_o = 0.03 m, d_o = 0.30 m), showed approximately the same specific momentum flux per unit mass with a value of hu^2 = 0.20 m^3/s^2. However, the maximum specific momentum per unit mass was delayed by approximately 3 seconds in the sloping bed test. This indicates that the 5% positive bed slope affected the arrival time and not the magnitude of the peak specific momentum flux per unit mass. The significance of the velocity component in the magnitude of specific momentum flux per unit mass can be ascertained by comparing tests S1 (h_o = 0.03 m, d_o = 0.40 m) and H3 (h_o = 0.10 m, d_o = 0.40 m), as shown in Figure 3-12a and 12b. The impoundment depth for both S1 (h_o = 0.03 m, d_o = 0.40 m) and H3 (h_o = 0.10 m, d_o = 0.40 m) tests is the same (i.e., d_o = 0.40 m), however, the flow velocity is 85% higher in test S1 (h_o = 0.03 m, d_o = 0.40 m) due to lower still water depth. A comparison of the two inclined bed tests, which had the same still water depth of h_o = 0.03 m, indicates that by increasing the impoundment depth from 0.35 m to 0.40 m the peak specific momentum flux per unit mass increases by 62% (see Figure 3-12b).

The non-dimensional time histories of the normalized specific momentum fluxes per unit mass, hu^2, in both subcritical and supercritical flow regimes for horizontal bed tests are shown in Figure 3-12c. A completely different pattern was observed in subcritical and supercritical dam-break flow regimes. The bore specific momentum flux per unit mass continuously decreased after the peak occurred at $t(g/d_o)^{1/2} = 40$ in subcritical bores and reached the quasi-steady state at a non-dimensional time of 150. A second peak was observed in supercritical bores at a non-dimensional time of $t(g/d_o)^{1/2} = 120$ and a gradual momentum attenuation occurred afterwards. Figure 3-12c also shows that the peak normalized momentum flux per unit mass was independent of the still-to-impoundment depth ratio and the time history of the specific momentum flux per unit mass only depended on the flow regime. Figure 3-12d shows the time history of the normalized specific momentum flux per unit mass of supercritical bores over inclined beds. A second peak was again observed in the time history of the normalized momentum flux per unit mass, hu^2, with a time lag of $t(g/d_o)^{1/2} \approx 50$ between the first and the second peak. Figure 3-12d also shows that a 14% reduction of impoundment depth reduced the first and second peaks of momentum flux per unit mass by 40% and 30%, respectively and that the peaks were delayed by $t(g/d_o)^{1/2} \approx 25$.

The maximum specific momentum flux per unit mass over horizontal beds took place after the flow reversal when the runup moved to the downstream after almost 4 s from the impact, whereas for the inclined bed tests, the maximum specific momentum per unit mass occurred during the drawdown process as the flow height increases at this stage at almost 3 s from impact (Figure 3-8a and 3-8b). The second wave velocity peak increased the specific momentum flux per unit mass to its maximum value at 7 s and 5 s in horizontal and inclined bed tests, respectively.

The magnitude of dynamic forces exerted by tsunami waves and their duration on coastal infrastructure can generate impulse which is the changes in momentum by the propagating waves (Wüthrich et al., 2018b). Therefore, the product of force and time (impulse) can be used to evaluate the potential damage of tsunami waves on coastal infrastructure. The time history of the normalized impulse for all tests was calculated by integrating the normalized specific momentum flux over time as (Eq. 3-2):

$$I = \int_{t=0}^{t=t_n} \rho \mathrm{Q} \mathrm{u}^2 \, dt \tag{3-2}$$

where t_n is the upper limit of the non-dimensional time integration and it is equal to $t(g/d_o)^{1/2} = 100$, Q is flow discharge, and u is the flow velocity (Wüthrich et al., 2018b). Figure 3-13 shows the variation of the non-dimensional specific impulse of hydraulic bores for both horizontal and inclined bed tests.

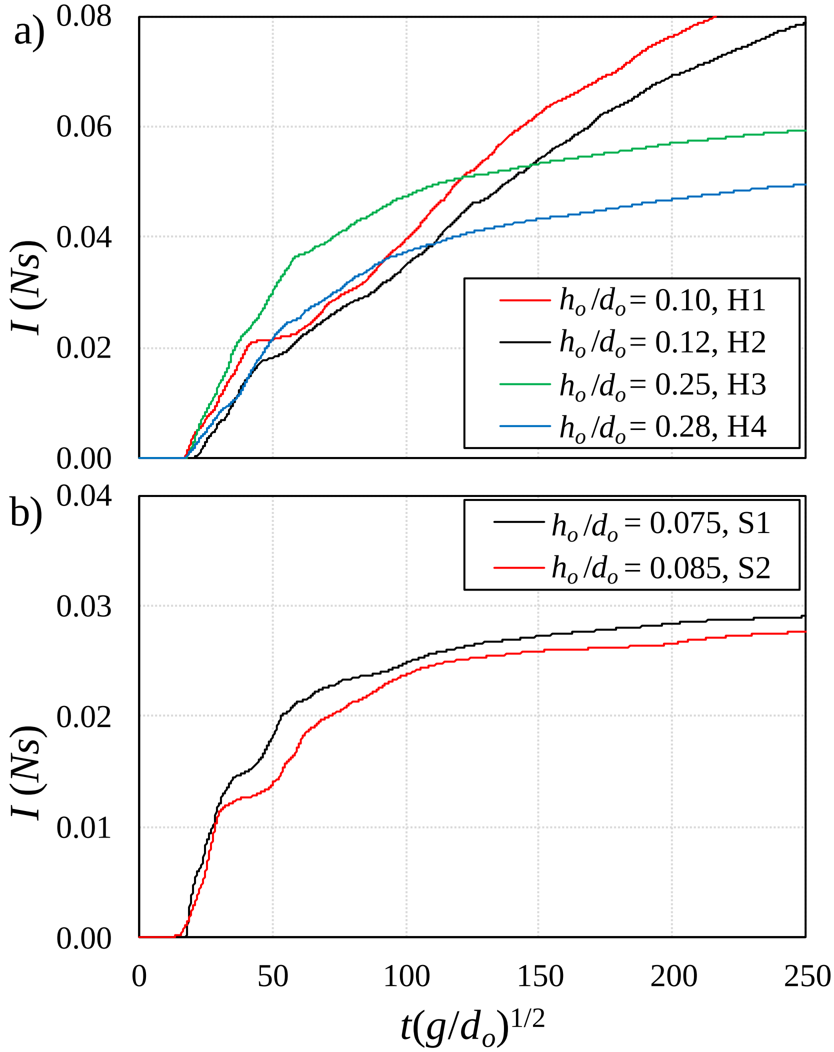

Figure 3-13: Effect of still-to-impoundment depth ratio on the specific impulse of bores (I) in the beginning of the sand bed section; a) horizontal bed; b) inclined bed.

The effects of flow regime and still-to-impoundment depth ratio on variations of non-dimensional specific impulse for horizontal bed tests are shown in Figure 3-13a. As it can be seen, specific impulses were larger in the case of the supercritical flow regime tests (i.e., H1 (h_o = 0.03 m, d_o = 0.30 m) and H2 (h_o = 0.03 m, d_o = 0.25 m)) than the subcritical flow regime ones (i.e., tests H3 (h_o = 0.10 m, d_o = 0.40 m) and H4 (h_o = 0.10 m, d_o = 0.35 m)). Moreover, the normalized impulse continuously increased with time for supercritical bores, while for subcritical bores, the specific impulse reached the peak impulse at $t(g/d_o)^{1/2} \approx 120$ and the growth rate became very small afterwards. This indicates that subcritical bores reached the quasi-steady state faster than the supercritical ones. For instance, at $t(g/d_o)^{1/2} = 250$, the specific impulse of supercritical bores for test H3 (h_o = 0.10 m, d_o = 0.40 m) was approximately 30% higher than those from test H4 (h_o = 0.10 m, d_o = 0.35 m). A comparison of subcritical and supercritical bores showed that the 2 time increase in still water depth resulted in 60% smaller specific impulse. This demonstrated the effect of still water on attenuating the destructive influence of the dam-break waves on structures.

A non-dimensional time of 100 was found as a criterion describing two distinct regimes in propagation of hydraulic bores over inclined bed. As it can be seen in Figure 3-13b, the normalized impulse rapidly increased with time and reached a value of 0.025 at $t(g/d_o)^{1/2} = 100$. The specific impulse then entered into the quasi-steady phase and the specific impulse increased with a very small slope. In addition, as h_o/d_o increased in both horizontal and inclined bed tests, the magnitude of the specific impulse decreased mainly due to lower flow velocity in subcritical bores.

Lastly, the magnitude of normalized specific impulse was smaller in hydraulic bores that propagated over a positive slope. A comparison of the normalized specific impulse between tests with similar still-to-impoundment depth ratios (i.e., tests H1 (h_o = 0.03 m, d_o = 0.30 m) and S2 (h_o = 0.03 m, d_o = 0.35 m)) indicated that the specific impulse in the horizontal bed test (H1 (h_o = 0.03 m, d_o = 0.30 m)) was approximately 2 times higher than the specific impulse in the inclined bed test (S1 (h_o = 0.03 m, d_o = 0.40 m)). A comparison of specific impulse generation over an inclined bed showed the role of impoundment depth on the magnitude of specific impulse. A 14% higher impoundment depth increased the specific impulse by 12%.

3.4 Conclusions

As shown in the literature review presented in the Introduction section, results of previous studies may further cause difficulties when comparing them with effects from an actual tsunami inundation due to use of the relatively short-period waves generated in such experiments. In addition, some other parameters related to the effects of the bed slope or the presence of water during the successive flood cycles during tsunami events have not been investigated. Therefore, the current study aims to close this gap by examining the effects of *bed slope* and of the s*till-to-impoundment water depth ratio* on propagation of dam-break induced, tsunami-like waves which propagate in both subcritical and supercritical flow regimes. As such, the present study investigates the hydrodynamic features of the propagation of hydraulic bores for six different still-to-impoundment depth ratios and two bed slopes, for both subcritical and supercritical flow regimes. The time-history of hydrodynamic characteristics such as the water surface profiles and bore velocities were measured prior to the erodible sand section in the experiment as well as in front of a structural model. The absolute bore heights in the beginning of the sand section showed that the maximum bore heights, $(h\text{-}h_o)/d_o$, were around 0.45-0.47 of the impoundment depth and they occurred at the non-dimensional time of 50-60, $t(g/d_o)$, regardless of the magnitudes of still-to-impoundment depth ratio and flow regime.

The analysis of the time history of water surface elevations over the horizontal bed revealed that the supercritical flows tests (i.e., H1 (h_o = 0.03 m, d_o = 0.30 m) and H2 (h_o = 0.03 m, d_o = 0.25 m)) exhibited higher runup heights in front of the model than subcritical bores. In addition, for the same still to impoundment depth ratio the peak bore heights were approximately 40% higher for the inclined bed tests than the horizontal bed one, which occurred 5 seconds earlier for inclined bores – the equivalent of $t(g/d_o)^{1/2} \approx 25$.

Over the horizontal bed, the flow velocity was found to be higher in the supercritical flow and increased also with an increase in the impoundment water depth. Variations of the time history of flow velocity with different still-to-impoundment depth ratios showed that the maximum flow velocity decreased by 50 % as the still water depth increased 2 times. The positive bed slope also increased the peak velocity of supercritical bores by 25% and it occurred approximately one second earlier than the corresponding supercritical flow in the horizontal bed.

In case of the horizontal bed tests, the maximum momentum flux for subcritical bores were approximately 60% higher than those of the supercritical bores generated by similar impoundment depths. However, for the similar impoundment depths the specific impulse is 60% smaller for the subcritical flows than the supercritical ones. The peak specific momentum of hydraulic bores over inclined surface increased by 62% as the impoundment depth raised by 14%. On the other hand, a comparison of the normalized specific impulse for two similar waves propagating over horizontal and inclined beds indicated that the wave impulse was 2 times higher for bores propagating over horizontal beds than over inclined beds. The specific impulse of hydraulic bores propagating over an inclined surface and in equilibrium condition increased by 12% as the impoundment depth rose by 14%.

Chapter 4. Experimental investigations on the impact of tsunami-like hydraulic bores on a square-shaped structure (Part 1): pore pressure variations

The article is in review in Journal of Waterway, Port, Coastal and Ocean Engineering (ASCE)

4.1 Introduction

Over the past few decades, tsunami-induced coastal inundation, in the form of overland propagation of highly turbulent tsunami bores or surges have led to loss of human lives and caused significant damage to infrastructure in many of the world's coastal regions (Ruangrassamee et al., 2006). More than 230,000 people lost their lives in the 2004 Indian Tsunami event (Ghobarah et al., 2006), while 15,894 people died and 2,561 were reported missing in the post-tsunami field investigations of the 2011 Japan Tohoku Tsunami (Jayaratne et al., 2016). The occurrence of these natural events and their destructive impacts on coastal communities necessitates further investigation on the stability of critical infrastructure, such as vertical evacuation shelters and hospitals (Wüthrich et al., 2020a). Scour around coastal structures is a leading cause of tsunami-induced structural failure (Jayaratne et al., 2016; Stolle et al., 2020). Figure 4-1 shows sediment erosion under the foundation of a coastal residential building in Palu Bay, Indonesia caused by the 2018 Indonesia Tsunami (Stolle et al., 2020). The magnitude and distribution of tsunami-induced loading and effects are influenced by: 1) tsunami inundation characteristics such as the inundation depth time history, 2) structural shape, dimensions and aspects ratio, and 3) the foundation material around the structure. Importantly, the simultaneous impacts of transient buoyancy force and the pore pressure responses in the soil and around the foundation of structures should be considered when studying erosion due to tsunami waves (Tonkin et al., 2003; Yeh et al., 2013; Yeh and Mason, 2014).

Figure 4-1. Scour under a coastal structure observed immediately following the 2018 Indonesia tsunami event in Palu Bay (courtesy of Jacob Stolle, 2018).

The low frequency of tsunami occurrence and the associated danger for field surveying make on-site data collection very challenging. Such difficulties with field data acquisition necessitate accurate experimental studies and numerical simulations to better understand soil response to different tsunami loadings (Exton et al., 2019). In order to generate precise and repeatable tsunami-like inland inundation conditions in the laboratory, a generation mechanism is required. A comparison of visual images of broken tsunami waves from the 2004 Indian Tsunami with a dam-break bore propagation over a dry bed showed that flow characteristics of the classical dam-break bore were in acceptable agreement with the field data (Chanson, 2006). As a result, several experimental researchers have since employed the dam-break mechanism to replicate tsunami-like waves in the laboratory (Imamura et al., 2008; Nistor et al., 2011; Liu et al., 2017).

Field and laboratory investigations of tsunami-like bores have shown the effects of controlling parameters such as the upstream impoundment depth, d_o, on the dam-break wave propagation and its frontal velocity, u. The Froude number has been used as a fundamental parameter to classify tsunami broken waves into supercritical and subcritical flow regimes (Montoya et al., 2017; Kramer et al., 2020). The Froude number is defined as the ratio of inertia to gravitational forces ($\mathrm{Fr} = u/(gd_o)^{0.5}$) where g is the gravitational acceleration. After breaking in the vicinity of the shoreline, tsunami bores are turbulent and supercritical with a Froude number larger than unity (Nandasena et al., 2012; Tanaka et al., 2014). As they propagate overland, depending on the onshore topography, the bore front velocity reduces and the flow regime changes from supercritical to subcritical with Froude numbers ranging between 0.7 and 1 (Fennema and Hanif, 1987; Zoppou and Roberts, 2003; Spiske et al., 2010). Recent laboratory experiments correlated bore regime classification with the still-to-impoundment depth ratio, h_o/d_o, and reported that hydraulic bores are supercritical for $h_o/d_o < 0.2$ and subcritical for $h_o/d_o > 0.2$ (Ghodoosipour et al., 2019).

Bore propagation over a bed and its penetration through soil cause dynamic pressure fluctuations and normal stress variations around structures in its path. The evaluation of the bore-induced pore pressure variation is particularly important to assess the stability and performance of structures during tsunami incidents (Yeh et al., 2013; Yeh and Mason, 2014). During tsunami runup, the weight of a wave compresses the top layer of soil and as a result, pore pressure and normal stress gradually increase within the soil. Due to the rapid onset of a tsunami inundation, during the initial passage of the bore front the soil pore pressure may be less than hydrostatic. The water table in the soil then subsides near the end of the tsunami drawdown process (Yeh et al., 2013) and the sudden reduction of water depth leads to the generation of excess pore pressure in the soil (Yeh and Mason, 2014). The excess pore pressure reduces the soil resistance and triggers upward forces underneath coastal structures located in the inundated areas. In non-cohesive soils, a buoyancy force is generated by the increasing upward pore pressure which reduces the soil resisting force and the possibility of overturning failure increases (Yeh et al., 2014). The lack of a drainage network around a structure accelerates pore pressure rise and causes instantaneous wave-induced normal stress in the vicinity of coastal structures (Jeng and Ou, 2010).

Pore pressure fluctuation during tsunami inundation propagation is correlated with soil specifications such as the mean aggregate size, soil density, soil permeability, and cohesiveness. Additionally, the rate of pore pressure propagation through a soil section depends on still water depth and tsunami wave characteristics such as wave height, length, and period (Rahman et al., 1978). Many attempts have been made to determine a relation between tsunami inundation-level fluctuations and pore pressure variations at different depths of soil around coastal structures. Several physical modeling studies have determined relation between various parameters such as wave height, flow velocity, and pore pressure variations around a pile with a diameter of either 0.2 m or 0.08 m (Qi et al., 2012). A piston-wave assembly made a combination of waves and currents with two different velocities of 0.25 m/s and 0.34 m/s. Ten pore pressure sensors were installed at different distances around the pile. The pile model was placed in a saturated bed consisting of sand particles with a mean grain diameter of 0.38 mm. The time histories of pore pressure, flow velocity, and wave height were recorded for initial solarity wave heights of H_o = 85 mm, 52 mm, and 26 mm. Their experimental results showed that by doubling the wave height, flow velocity and maximum pore pressure increased by 20% and 50%, respectively(Qi et al., 2012).

The effect of bed slope on pore pressure variation due to overland propagation of breaking and non-breaking waves was numerically studied by Jeng and Zhang (2005). The entire Gold Coast region was simulated with a maximum water depth of 120 m and the results depicted that the pore pressure of non-broken waves was 20% larger than the pore pressure of breaking waves under the same wave condition (Jeng and Zhang, 2005).

Numerical simulations were also performed on a series of detailed post-tsunami field investigations to examine the impact of soil permeability and drawdown velocity on pore pressure variation (Sawada et al., 2014). The maximum tsunami wave amplitudes were 10.8 m, 8.0 m, and 2.6 m with corresponding drawdown velocities of 0.025 m/s, 0.008 m/s, and 0.0022 m/s, respectively. The simulation results showed that the pore pressures were considerably smaller in zones with relatively smaller tsunami amplitude and drawdown velocity, but with the highest permeability (Sawada et al., 2014). The effects of tsunami-like inundations on pore pressure variations and the resulting upward forces were numerically studied around a breakwater in wet bed conditions (Matsuda et al., 2016). A 350-m-long reservoir was used in combination with a sand bed section with an upward slope of 1V:15H; the results on bearing capacity of the sediment section indicated that pore pressure increased with increasing impoundment depth. Numerical simulation also showed that the bearing capacity of the soil was reduced by 50% when the wave height increased by 30% (Matsuda et al., 2016).

The interactions between the soil and a structural model which occurs during the propagation of tsunami-like waves were also experimentally studied by Zhai et al. (2018). Solitary waves with different initial wave heights of H_o = 0.06 m, 0.08 m, 0.1 m, and 0.12 m were generated using a wave-piston assembly. The sediment section consisted of sand particles with a mean particle diameter of d_{50} = 0.15 mm and specific gravity of G_s= 2.67. An impermeable breakwater with two side slopes of 1V:2H was located at the center of the sand section. The breakwater was fitted with eight pore pressure transducers in the front and under the structure. The vertical variations of pore pressure in the front of the breakwater showed a 20% increase as wave height increased by 50%.

It was also reported that the frontal pore pressures were more sensitive to initial wave height than the pressure sensors located below the breakwater (Zhai et al., 2018).

The effects of maximum tsunami-induced bore depth, h_{max}, and tsunami period on excess pore pressure development were numerically investigated by Abdollahi and Mason (2019). Three tsunami waves of the same time period and different maximum heights of 10 m, 5 m, and 2 m were propagated over a sand bed with particles with a specific gravity of G_s = 2.65. The numerical results indicated that by increasing the tsunami height by a factor of 5, the maximum excess pore pressure increased by 6-fold. Moreover, when the loading time was increased approximately by 3.5-fold, the peak excess pore pressure increased 1.5-times compared to the initial wave.

During tsunami events, the first wave front usually propagates over dry land while the subsequent bores, which are relatively larger than the first wave, advance to the flooded shoreline (St-Germain et al., 2012). The wave propagation over horizontal dry beds was found to be a sole function of time whereas wave propagation over wet beds was correlated with other parameters such as impoundment and still water depths (Crespo et al., 2008). Previous research on the influence of bed conditions on tsunami loadings indicate that a thin layer of still water remarkably alters the bore characteristics (Douglas and Nistor, 2015). To the authors' knowledge, no experimental studies have been performed to investigate the effects of the presence of the water from the first tsunami inundation wave, expressed in the form of still-to-impoundment depth ratio, and of the bed slope on the simultaneous interaction of tsunami-induced bores and pore pressure distribution around structures located in tsunami inundation areas.

Hence, a comprehensive experimental program was initiated and various tests were performed to investigate the effects of impoundment and still water depths and two different bed slopes on the time history of pore pressure variation around a structural model at different depths from the bed surface. The effects of the still-to-impoundment depth ratio and bed slope on the time history of pore pressure and pore pressure distribution in the front and side walls of the structural model were explored. Furthermore, the role of different tsunami-like wave loadings on the spatial distribution of pore pressure with depth is discussed by providing pore pressure contour plots in the vicinity of both the front and side walls of the structural model and at different time intervals. The results of this study were also used to analyze the scouring mechanism around a square structure and are discussed in the companion paper (Part 2).

4.2 Experimental setup

A series of laboratory experiments were carried out in the Hydraulic Laboratory at the University of Ottawa, Canada to investigate the effects of bed slope and still-to-impoundment depth ratios on pore pressure variation around a square-shaped structural model. The structural model was placed at the center of a sand bed section in a flume with a rectangular cross section. Two different bed slopes (horizontal and inclined beds with an inverse slope of +5% upslope) were tested to study the effects of bed slope on pore pressure variation. Four still-to-impoundment depth ratios, h_o/d_o, were selected to represent both subcritical (i.e., $h_o/d_o > 0.2$) and supercritical (i.e., $h_o/d_o \leq 0.2$) flow conditions for the horizontal bed tests (i.e., H series). Two tests in the supercritical regime (i.e., $h_o/d_o < 0.2$) were conducted for the inclined bed condition (i.e., S series). Table 4-1 shows the experimental parameters and the flow regimes used in this study. Froude numbers in this table were calculated using time histories of water surface elevation (WG2) and ADV installed 4.3 m downstream of the gate and the maximum ranges of this parameter and its corresponding times are mentioned in the table.

Table 4-1. Experimental parameters of the performed tests.

Test number	Slope (%)	d_o (m)	h_o (m)	h_o/d_o	U (m/s)	Time (s) / Fr. range
H1	0	0.3	0.03	0.10	1.62	2.85<t<50
						0.44< Fr <1.98
H2	0	0.25	0.03	0.12	1.56	3.26<t<50
						0.42< Fr <1.67
H3	0	0.4	0.1	0.25	1.3	3.03<t<50
						0.15< Fr <0.64
H4	0	0.35	0.1	0.28	1.2	3.50<t<50
						0.18< Fr <0.99
S1	5	0.4	0.03	0.075	1.91	2.63<t<50
						0.10< Fr <4.20
S2	5	0.35	0.03	0.085	1.83	2.33<t<50
						0.08< Fr <4.00

The experimental apparatus consisted of a swing gate that can generate dam-break bores by the rapid opening of the gate and the subsequent release of water from the upstream impounding reservoir into the flume. The released water formed a hydraulic bore that propagated initially over fixed bed section and then a permeable sand bed section. In this type of bore-generation mechanism, the non-dimensional removal time of the gate should be shorter than 1.41 multiplied with the characteristic time scale $(d_o/g)^{1/2}$ in order to have a fully developed turbulent bore (Lauber and Hager, 1998a). In the present study, the non-dimensional removal times ($T_o = t_o(g/d_o)^{0.5}$) were in the range of $0.97 < T_o < 1.18$ indicating that the generated turbulent bores were fully developed. A solid false floor was installed downstream of the gate. A single layer of sand was glued to the false floor to induce roughness. A 200 mm x 200 mm grid was then painted on the false floor to measure the bore front position and to estimate bore front velocity. A 0.2-m-long, 1.5-m-wide, and 0.2-m-deep gabion section, used to prevent the formation of local scour at the interface of the sand section and the false floor, was installed immediately after the false floor and across the width of the flume. The gabion was fabricated using a wire mesh box and filled with gravel with a mean diameter of 30 mm. A 3.15-m-long, 1.5-m-wide, and 0.2-m-deep saturated sand bed section was installed to simulate the noncohesive and permeable soil around the structural model (Figure 4-2).

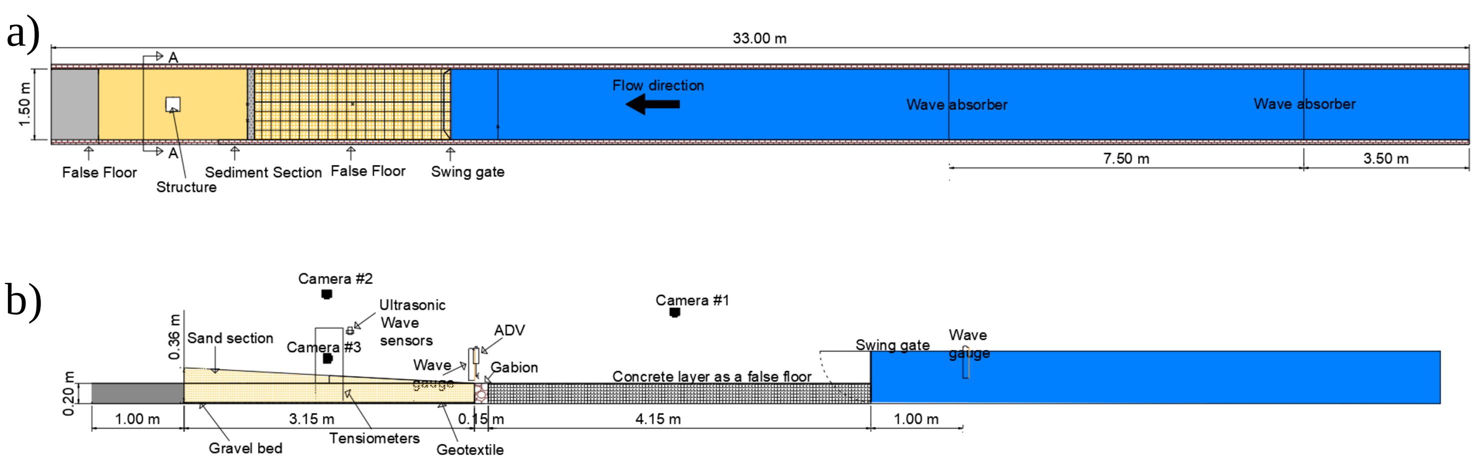

Figure 4-2. Experimental setup and adopted coordinate system; a) top view, horizontal and inclined beds; b) side view, horizontal and inclined beds.

A second false floor was installed after the sand bed section in form of a framework for the sand bed section and to protect sand from washing out. The sand bed section was filled with loosely packed, uniform sand particles with a mean diameter of $d_{50} = 0.5$ mm. A layer of fine gravel with a mean diameter of 10 mm was used under the sand bed section to drain the flow towards the downstream direction.

A structural model in the form of a transparent square-shaped cross section column with the side a of b = 0.3 m was made of 10-mm-thick Plexiglas sheets and installed at the center of the sand bed section and at 5.87 m downstream of the swing gate (see Figure 4-2). A vertically-moving aluminum sharp-crested weir was installed at the end of the flume to control the still water depth. A 1.32-m-long, 0.76-m-wide, and 1.43-m-high adjustable sediment-trap box was placed in the drain to collect the scoured and suspended sediments entrained downstream of the flume. Figure 4-2 shows the top and side views of the experimental setup and the adopted coordinate system.

4.2.1 Instrumentation

The time histories of the impounded water depth in the reservoir behind the gate and the bore height at the beginning of the sand bed section were recorded using two capacitance-type wave gauges (WG1) and (WG2), respectively (model RBR WG-50, NRC, Ottawa, Canada). The wave gauges had a level measuring range of 0.5 m and an accuracy of ± 0.4% of the full range. The first wave gauge was located 1.0 m upstream of the gate and the second wave gauge was installed 4.30 m downstream of the gate. The time history of runup heights onto the front face of the structural model was measured with an ultrasonic sensor (US1); (model MASSA, M-5000/220, Massachusetts, USA). The ultrasonic sensor had an electronic signal frequency of 220 KHz with a measuring resolution of 0.25 mm. The sampling frequency of water depth measurements was set to 1200 Hz to accurately detect the impact water levels and the maximum runup height. The instantaneous water velocity in the direction of flow was measured by a side-looking head Acoustic Doppler Velocimeter (ADV) probe (model Nortek Vectrino, Vangkroken, Norway). The probe was installed at the beginning of the sand bed section with a maximum velocity range of 2.5 m/s and a measurement accuracy of ±1% of the maximum velocity range. A sampling frequency of 200 Hz and a sampling volume of 45×10^{-7} m^3 were selected for velocity measurements.

Nine Micro Tensiometer Transducer Probe Assemblies (MTTPA) with ceramic probe tips of 2 mm and probe lengths of 20 mm (model SDEC 220, Reignac sur Indre, France) were installed in the front face of the structural model to measure the time histories of pore pressure in the sand bed section. The tensiometers were installed 70 mm apart in both vertical and transverse directions to form a three-by-three measuring matrix (see Figure 4-3a).

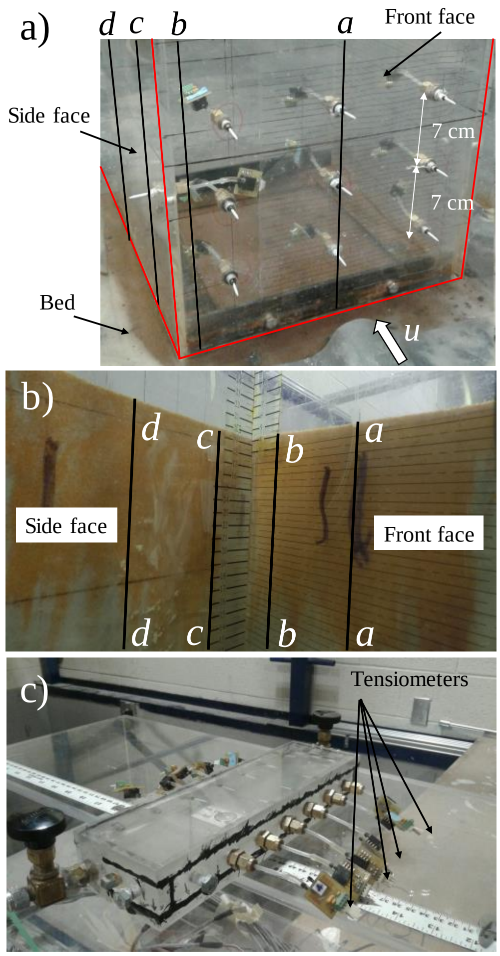

Figure 4-3. Images of instrumentation in the structural model; a) position of the tensiometers in the front face of the structural model; b) image of sediment bed from inside of the structural model; c) calibration setup for the tensiometers.

The first row of tensiometers was installed slightly below the sand bed in the horizontal bed tests and 80 mm below the sand bed in the inclined bed tests. To measure the time histories of pore pressure on the side face of the model, the latter was rotated clockwise by 90 degrees about its vertical (z) axis and the experiments were repeated with the same test conditions. Figure 4-3b shows the sand bed level and the two faces of the structural model before the dam-break bore propagation. Each tensiometer was connected to a pressure transducer capable of measuring both positive and negative pore pressure with a range of ±7 kPa, further the accuracy of the pressure measurements is 0.16% of the measured absolute pressure (Qi et al., 2011; Al-Riffai and Nistor, 2013). The tensiometers were calibrated for the wet soil condition by inserting de-aired water into the ceramic cups of the tensiometers and testing the pressure transducers using a calibration setup (see Figure 4-3c). The calibration setup uniformly distributes the dynamic pressure while applying different static pressures using a vertically moveable water tank.

4.2.2 Data acquisition procedure

Two Data Acquisition Boards (DAQ) NI USB-6009 with 16 channels and NI USB-6210 with 8 channels (model National Instruments Corporation, Austin, Texas, US), and having an input voltage range of ±10 volts, were used to acquire analog signals from instruments and to produce digital signals from analog data. All digital signals from the capacitance-type wave gauges, ultrasonic sensor, pore pressure tensiometers, and ADV probe were processed using LabView software (National Instrument, Austin, Texas, US). The sampling rate of the Data Acquisition Boards (DAQ) for velocity and depth measurements was set to 40 Hz. Both DAQ boards were synchronized by integrating data from each instrument using virtual instrument subroutines (VIS) compiled on LabView software (Al-Riffai, 2014).

All experiments in this study were repeated three times to ensure the repeatability of the time series of recorded data within the sand bed section. Figure 4-4 shows a sample of repeatability tests for pore pressure measurements in test H4 (see Table 4-1). The pore pressure signals varied slightly in each test due to variations of the drawdown flow and mixing the drawdown flow with the approaching waves. In all three repeated tests, the maximum pore pressure reached approximately 3.75 kPa with a variation within ± 0.1% of the maximum value. The maximum pore pressure occurred almost 12 s after the gate removal.

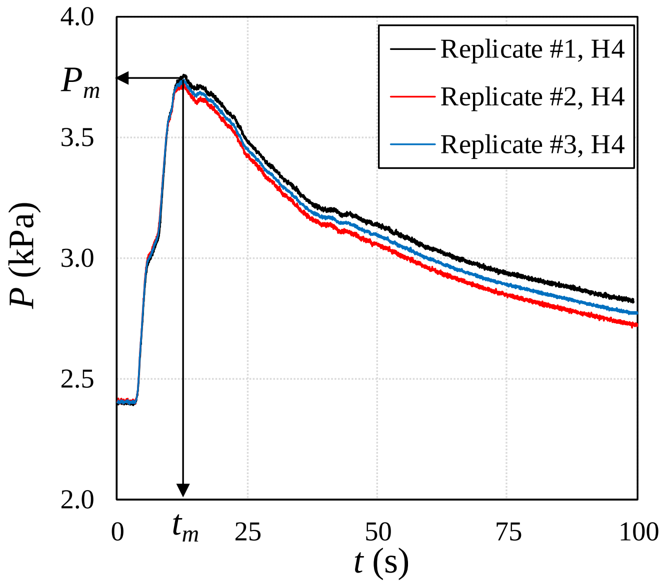

Figure 4-4. Repeatability tests for pore pressure measurements from tensiometer #2 for Test H4. P_m is the maximum pore pressure and t_m is the time from the beginning of the test to P_m.

4.3 Results and discussion

4.3.1 Effect of the tensiometer orientation (front or side wall)

Figure 4-5 shows the effects of flow regime and tensiometer orientation on the time history of pore pressure around the structural model and at different depths from the bed surface for the horizontal bed tests. The test H1 ($h_o/d_o = 0.1$) was selected to represent the supercritical bores and the test H4 ($h_o/d_o = 0.28$) was selected to represent the subcritical bores. Variations in hydrodynamic pore pressure with time are plotted in Figure 4-5.

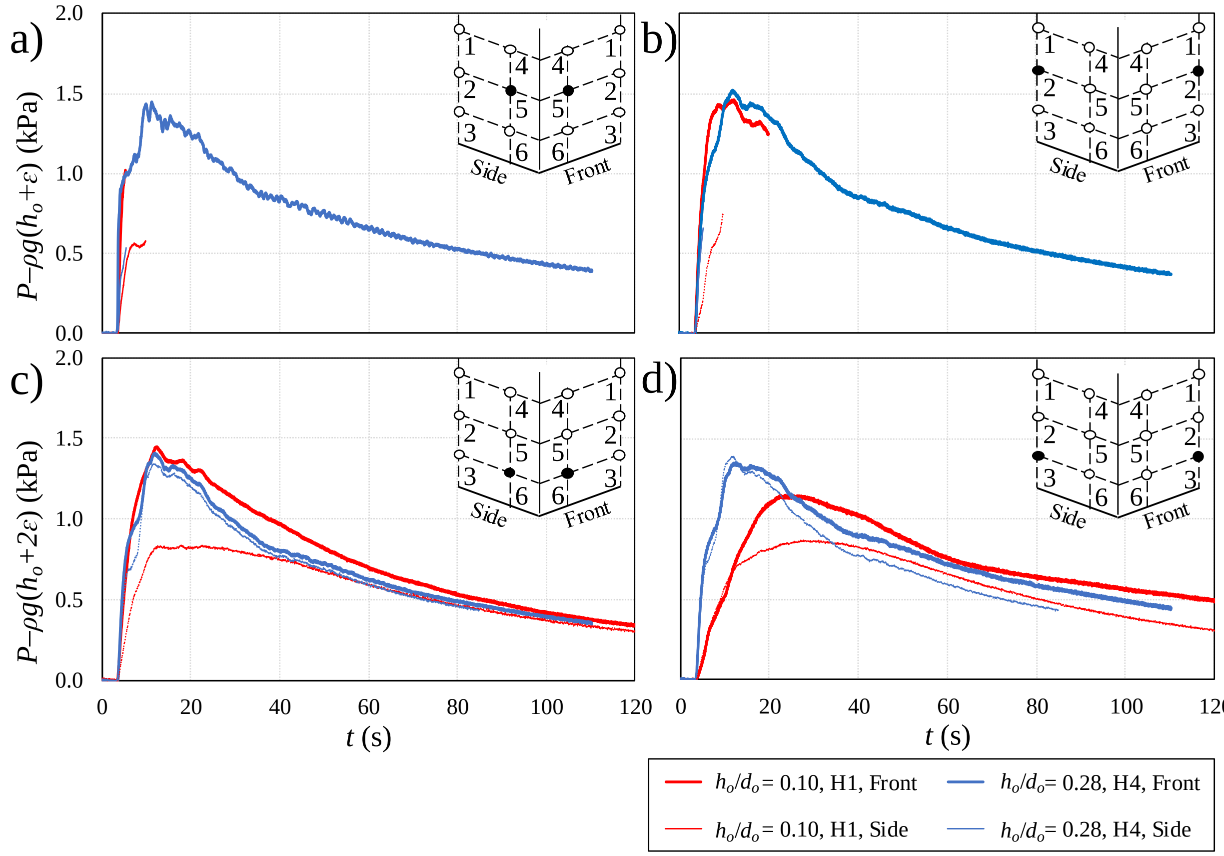

Figure 4-5. Variations of the effective pore pressure with time for the front and side of the structural model and for horizontal bed (H-Series) with h_o/d_o = 0.1 and 0.28; a) tensiometer #5 ; b) tensiometer #2; c) tensiometer #6; d) tensiometer #3.

The horizontal axis is the time and the vertical axis is the effective pore pressure. To isolate the effects of the still water depths, the effective pore pressures were calculated by subtracting the initial hydrostatic pressure ($\rho g h_o$) from the total pore pressure data. The pore pressures were measured in two different depths from the sand bed surface at z = – 0.07 m (second row of tensiometers) and – 0.14 m (bottom row of tensiometers) and for both front and side faces of the structural model.

As can be seen in Figure 4-5, the measured effective pore pressures increased steadily and reached the peak pressure value, P_m, regardless of tensiometer elevation and orientation to the flowing bores. The differences in the pore pressure variation were attributed to the initial impact of bores and the penetration of bore-induced pressure through the soil. Two local peak pressures were recorded by all tensiometers. The first peak indicated the presence of the first bore (i.e., runup) and the second wave displayed the fluctuations of the successive peaks. Figure 4-5a and 4-5b show the pore pressure variations at 70 mm below the bed surface and in the front and side of the structural model. Figure 4-5a presents the variations of pore pressure at the corner of the model and Figure 4-5b shows pore pressure variations in the middle of the structure. As shown in Figure 4-5a, the maximum pore pressure in the subcritical regime was 30% higher than the supercritical regime.

The scour depth generated by propagation of supercritical and subcritical bores exposed the tensiometers from the top row, therefore the time histories of pore pressure were truncated once these tensiometers were exposed to the water (see Figure 4-5a and 4-5b). Due to scour generated by flow separation around the sides of the model, the tensiometer exposure occurred faster along the side face of the structural model than on the front face. The bore front stagnated in front of the structure and caused a sudden water level rise and flow deceleration. As a result of the flow separation and formation of eddies in the corners and along the side faces of the structural model, the front tensiometers in the second row remained in the soil longer than those on the side of the model and, hence, they recorded higher pore pressures in comparison with the side tensiometers. Experimental results also showed that the tensiometers located in the front face were not exposed to the water in the subcritical flow conditions (see Figure 4-5a and 4-5b).

Figure 4-5c and 4-5d also show the time histories of pore pressure at 140 mm below the sand surface, a depth equally to approximately 50% of the width of the structural model. Experimental results indicate that all tensiometers remained in the soil during the hydraulic bore propagation and the subcritical bores caused a higher effective peak pore pressure compared to the supercritical bores. Figure 4-5c shows the time histories of the effective pore pressure in the front and side corners of the structural model. A noticeable difference was observed in the pore pressure variation of supercritical and subcritical flow regimes. For instance, in Test H1, the maximum pore pressure at the corner of the front wall was approximately 90% greater than the maximum pore pressure in the corner of the side wall. However, for the same tensiometer, their orientation (front or side wall) did not affect peak pore pressure in the subcritical regime (i.e., Test H4). The considerable difference in supercritical peak pore pressure is attributed to the initiation of the wake region in the side wall of the model (i.e., tensiometer #6). Flow velocity suddenly increased as flow passed around the structural model and this reduction caused a smaller peak pore pressure in the side face versus front face of the structural model. On the other hand, in a subcritical flow regime, peak pore pressures in the front and side faces were approximately similar and they were equal to 1.45 kPa. Both pore pressures reached their peak values at the same time (approximately 10 seconds).

Figure 4-5d depicts the time history of effective pore pressure variations in the middle of both the front and side faces of the model (i.e., tensiometer #3). As it shows, the maximum effective pore pressure took place at the same time 6 s after the gate opening with nearly same magnitudes (i.e., 1.3 kPa) in the subcritical test (Test H4). While, in the superitical test, this peak happened approximately 10 s later and the tensiometer installed in the front face recorded 40% greater value compared to the case of the side face one. Similar to the peak pore pressure differences observed in the corner of the side wall, the initiation of the wake region in the side wall did not let the pore pressure increase freely in the middle of this face.

4.3.2 Effect of the bed slope

The variations in the time history of effective pore pressure ($P-\rho g h_o$) around the structural model for the inclined bed tests are shown in Figure 4-6.

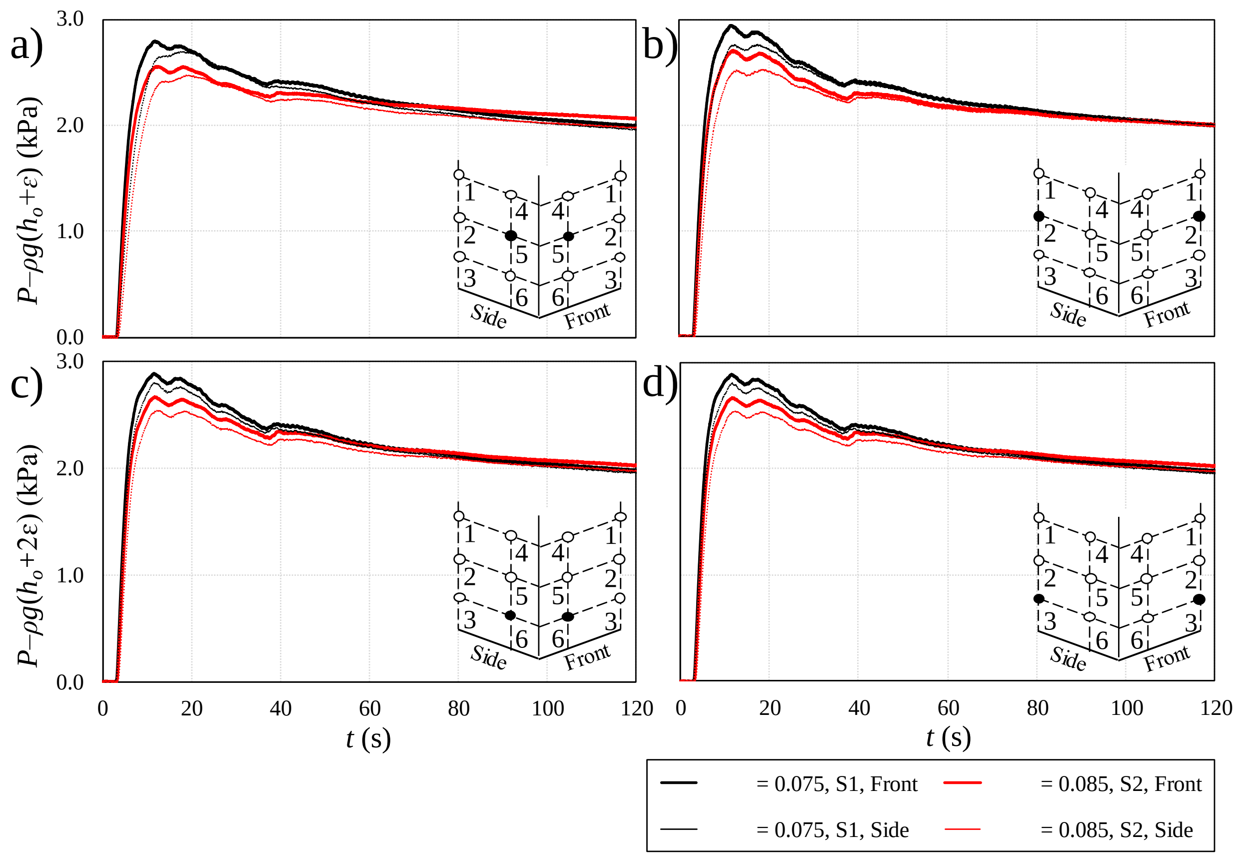

Figure 4-6. Variations of the effective pore pressure with time for the front and side of the structural model and for inclined bed (S-Series) with $h_o/d_o = 0.075$ and 0.085; a) tensiometer #5 ; b) tensiometer #2; c) tensiometer #6; d) tensiometer #3.

It should be noted that hydraulic bores propagating over the inclined bed tests were only performed in the supercritical flow regime. The time histories of the hydrodynamic pore pressure indicate an inverse relation between the magnitude of the peak pore pressure, P_m, and the still-to-impoundment depth ratio, h_o/d_o. Figures 4-6a and 4-6b show the time histories of the pore pressure at the corners and in the middle of the front and side walls of the model, respectively. In these two plots, tensiometers # 5 and #2 were installed at the same height of z = -150 mm with respect to the initial inclined bed sand surface (i.e., $z/b \approx -0.5$) and the effect of tensiometer orientation was analyzed by comparing the resulting pore pressure values. The results showed that the front face experienced on average a 15% higher peak pore pressure than the side wall of the structural model. The depth of the approaching wave was relatively smaller in the test with the larger still-to-impoundment depth ratio (i.e., Test S2). This resulted in a 3-second-lag between the peak hydrodynamic pore pressure of the middle and the corner of the structural model in Test S2. Experimental data in the inclined bed tests indicated that Test S1, with a 0.05 m greater impoundment depth than Test S2, had a 15% higher pore pressure in the front and side walls of the structural model. Figures 4-6c and 4-6d show the corresponding time histories of the pore pressure at z = -220 mm ($z/b = -0.73$). As it can be seen, the pore pressure values around the structural model were found to be fairly similar in both front and side walls. For instance, the maximum pore pressure in the front and side walls in Test S1 were 2.8 kPa and 2.7 kPa, respectively, while the time taken to peak was approximately 10 s for both tests. The similarity in time histories of the pore pressure at $z/b = -0.73$ indicated an isotropic pore pressure distribution in the x-y plane and around the structural model, whereas closer to the bed surface the pore pressure variations were non-isotropic.

The effects of bed slope on the propagation of the hydrodynamic pore pressure were studied by comparing Test H1 in Figure 4-5c (i.e., $h_o/d_o = 0.1$) and Test S2 in Figure 4-6c (i.e., $h_o/d_o = 0.085$) with approximately similar still-to-impoundment depth ratios. The time histories of the hydrodynamic pore pressure were recorded by tensiometer #6 and showed that 5% increase in bed slope resulted in a doubling of the hydrodynamic peak pore pressure in both front and side walls of the structure. All tensiometers in the inclined bed tests showed an instantaneous increase of pore pressure at approximately the same time and no significant time lag was observed. The pore pressure in the inclined bed tests increased within approximately three seconds of the bore arrival and reached maximum value at nearly six seconds (i.e., $3 \leq t \leq 10$) after the bore front passed the structure. Hydrodynamic pore pressure gradually decreased during the drawdown phase and eventually reached hydrostatic pressure. The advancing bore front in the inclined bed tests did not break prior to reaching the sand bed section; consequently, the advancing bore had a higher depth and caused higher pore pressure in the inclined bed tests in comparison with the horizontal bed tests.

4.3.3 Effect of the still-to-impoundment depth ratio

Figure 4-7 shows the variations in maximum pore pressure normalized with initial hydrostatic pressure with respect to still-to-impoundment depth ratio for both horizontal and inclined bed tests.

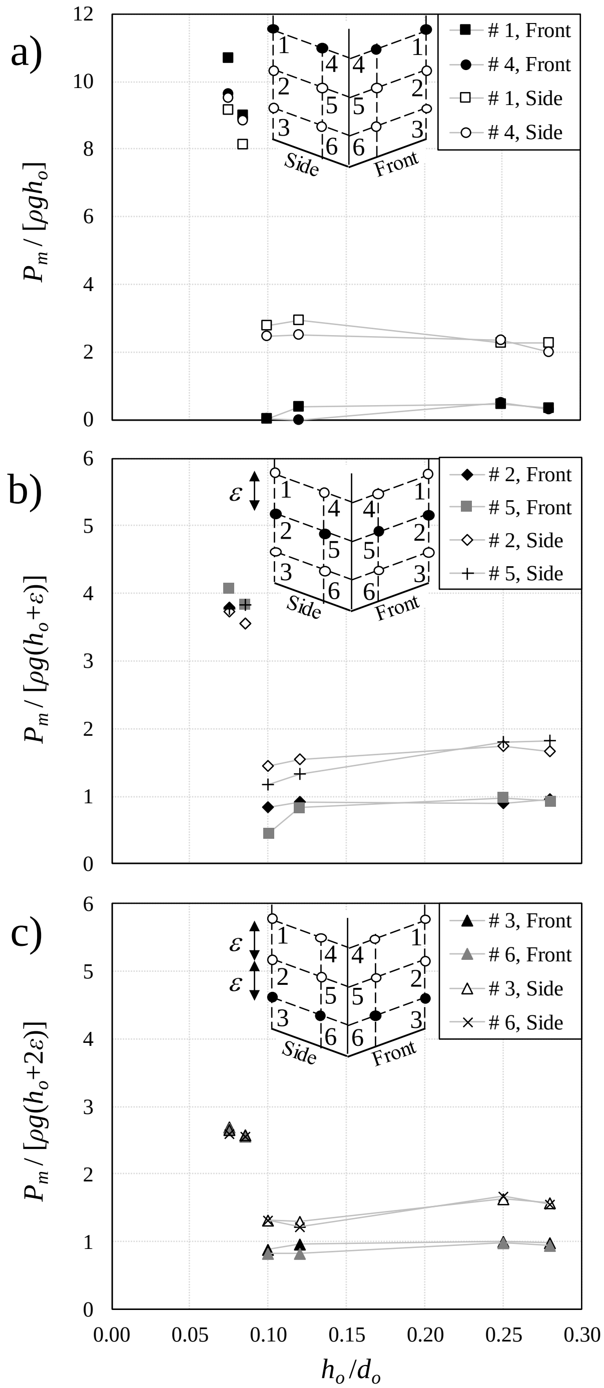

Figure 4- 7. Variations of the normalized maximum pore pressure with still to impoundment depth ratio h_o/d_o; a) tensiometers #4 and #1; b) tensiometers #5 and #2; c) tensiometers #6 and #3. The horizontal bed test data are connected by lines.

The effect of tensiometer elevation from the bed surface, ε, for both horizontal and inclined bed tests was considered in the calculation of the normalized peak pore pressure. It is worth noting that for the tensiometers located slightly below the sand bed, the peak pore pressures were collected before the tensiometers were exposed to water. Figure 4-7a shows the variations in normalized peak pore pressure at the row of tensiometers immediately below the bed surface for both horizontal and inclined bed tests with different h_o/d_o. As can be seen, the normalized pore pressures in the front wall of the horizontal bed tests were independent of h_o/d_o and for the side wall it decreased slightly with increasing h_o/d_o. Similar to the horizontal bed tests, the normalized maximum pore pressure decreased with increasing, h_o/d_o, in the inclined bed tests. The normalized peak pore pressures were within the range of $8 \leq P_m/[\rho g h_0+\varepsilon] \leq 11$.

Figure 4-7b and 4-7c show the normalized maximum pore pressures for the second and third rows of tensiometers, respectively. As shown in the inclined bed tests, the peak pore pressure decreased with increased distance from the bed surface with approximately 1.5 and 2.5 times the amount of equivalent initial hydrostatic pressure. For the horizontal bed tests, the peak pore pressures at z = – 70 mm and – 140 mm were almost independent of h_o/d_o and soil depth, z, and they varied within a narrow range of $1 \leq P_m/[\rho g h_0+\varepsilon] \leq 2$. For the second and third rows of tensiometers in the horizontal bed tests, the ratio of peak pore pressure to initial hydrostatic pressure was equal to unity in the front wall, indicating that maximum pore pressures between z = – 70 mm and – 140 mm were equal to the corresponding initial hydrostatic pressure. On the other hand, the peak non-dimensional pore pressure in the side wall of the structural model was somewhat greater than unity and slightly increased with increasing h_o/d_o. In contrast, for the inclined bed tests the peak pore pressure clearly depended on the soil depth. For instance, the normalized maximum pore pressure for the top row of tensiometers was on average 2.5 times more than the bottom tensiometers.

In the inclined bed tests, tensiometer orientation was less effective than the soil depth, except for the top tensiometers in which the front wall of the structural model exhibited a higher normalized maximum pore pressure than the side wall. Furthermore, the variation in normalized maximum pore pressure decreased with increasing still-to-impoundment depth ratio h_o/d_o. Comparisons of Figures 4-7a, 4-7b, and 7c revealed the effect of bed slope on variations in normalized maximum pore pressure. For both Tests S2 and H1 with approximately the same still-to-impoundment depth ratio, h_o/d_o, the measured maximum pore pressure in tensiometer #5 in the front wall of the structural model showed a 50% increase due to a 5% increase in the bed slope (Figure 4-7b).

Figure 4-8 shows the variations in time needed to reach the maximum pore pressure, t_m, with still-to-impoundment depth ratio. The time-to-peak pore pressure was normalized with the characteristic time scale of the bore $(g/d_o)^{1/2}$.

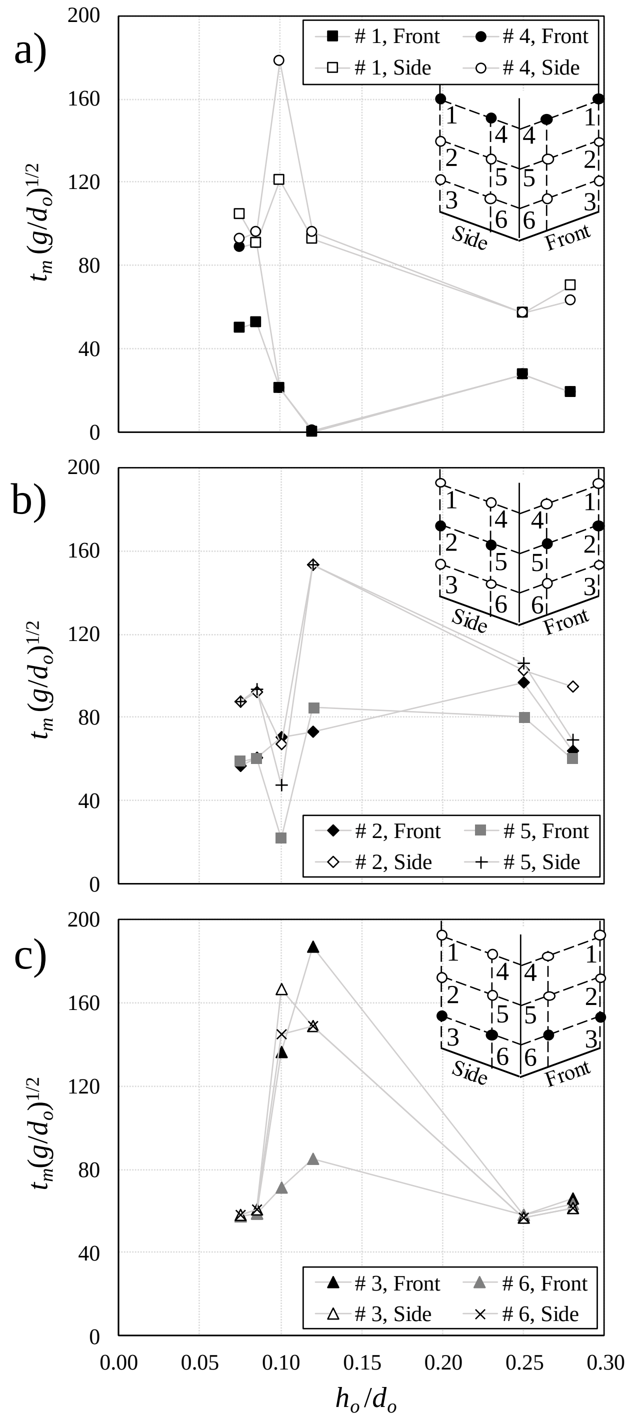

Figure 4-8. Variations of the normalized time to peak pore pressure with still to impoundment depth ratio h_o/d_o; a) tensiometers #4 and #1; b) tensiometers #5 and #2; c) tensiometers #6 and #3. The horizontal bed test data are connected by lines.

The effects of tensiometer depth from the bed and tensiometer orientation in both horizontal and inclined bed tests were also analyzed. Figure 4-8a shows the relation between the normalized time to reach P_m and h_o/d_o at the bed surface (z = 0). As observed, the front tensiometers sensed the peak pore pressure substantially faster than the side tensiometers for both horizontal and inclined bed tests. This relative time delay to reach P_m in the front and side walls can also be observed in Figure 4-5d (Test H1), and was due to the flow separation occurring in the front wall of the structural model. Figure 8a also shows that for the horizontal bed tests the time to reach peak pore pressure of supercritical bores decreased with increasing h_o/d_o. This trend was found to be similar for both the front and side walls of the model. In addition, generally the time-to-peak pore pressure increased by increasing h_o/d_o in the inclined bed tests. For instance, as h_o/d_o increased from 0.075 to 0.085, the maximum pore pressure in tensiometer #1 of the front wall occurred $t_m = (g/d_o)^{1/2} \approx 5$ earlier in Test S1 than Test S2.

Figure 4-8b shows the relation between the normalized time-to-peak pore pressure and h_o/d_o for the second row of tensiometers and for both horizontal and inclined bed tests. For the horizontal bed tests, the time to reach the peak pore pressure at the front and side faces of the model was between 80 ± 40 times that of the bore characteristic time scale, $(g/d_o)^{1/2}$. Some anomalies were observed for Tests H1 and H2 which may be due high pressure fluctuations in the vicinity of those tensiometers. Under the inclined bed, at the second row tensiometers ($z = -150$ mm) the normalized time-to-peak pore pressure increased with increasing h_o/d_o. The tensiometers in the side wall of the structural model recorded maximum pore pressure with an approximate delay of $t_m\,(g/d_o)^{1/2} = 30$ compared to the front face of the building with actual values of $t_m\,(g/d_o)^{1/2} \approx 90$ and $t_m\,(g/d_o)^{1/2} \approx 60$, respectively.

Figure 4-8c shows the variations of $t_m\,(g/d_o)^{1/2}$ with h_o/d_o for the third row of tensiometers. For the horizontal bed tests at a depth approximately equal to 50% of the model width, the pore pressure fluctuations in the supercritical bores ($h_o/d_o \leq 0.2$) propagated very slowly into the soil and resulted in a time delay ranging between $70(d_o/g)^{1/2}$ and $180(d_o/g)^{1/2}$. In the subcritical bores ($h_o/d_o > 0.2$), the time to reach the peak pore pressure became constant around the building structure at about $65(d_o/g)^{1/2}$.

No significant changes of t_m were observed in the front and side walls of the structural model for the inclined bed tests located at $z = -220$ mm. This indicated that at this elevation the pore pressures reached maximum pore pressure at the same time regardless of tensiometer orientation. Similar to t_m at the bed, a direct relation was found between the impoundment depth and t_m in the third row of tensiometer indicating that t_m decreased as the impoundment depth increased.

4.3.4 Spatial distribution of pore pressures

The spatial variation of pore pressure around the structural model and at different depths from the sand bed provided valuable information about the behaviour of the soil surrounding the model during hydraulic bore propagation. A series of contour plots was developed to visualize the temporal variation of the spatial distribution of pore pressure measured at the nine tensiometers, on each side of the structural model. Figure 4-9 shows the pore pressure variations with time for the front wall of the structural model in the horizontal bed tests.

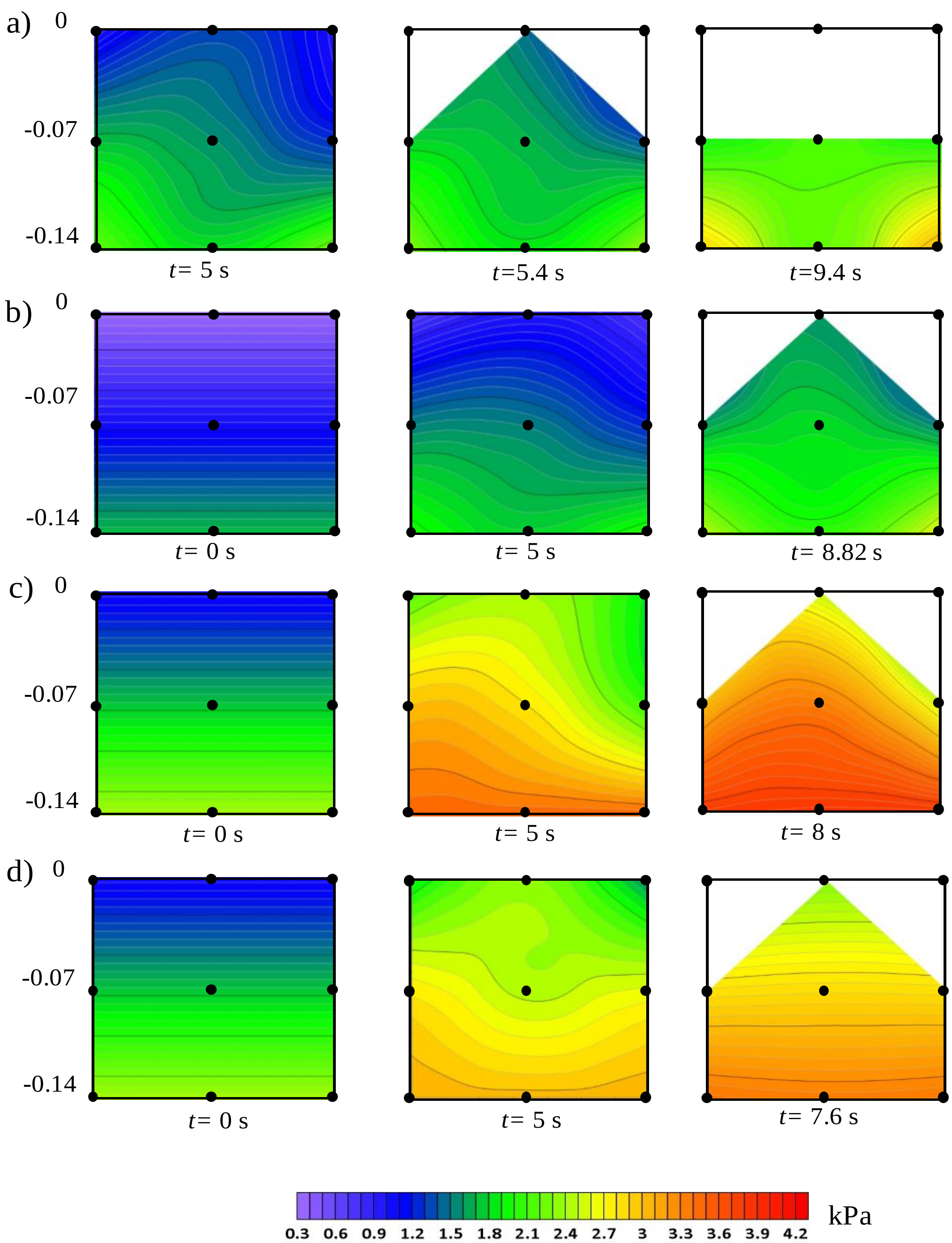

Figure 4-9. Contour plots of pore water pressure variations with time in front of the structural model for horizontal bed tests: a) h_o/d_o = 0.1; b) h_o/d_o = 0.12; c) h_o/d_o = 0.25; d) h_o/d_o = 0.28. The black circles in the first sub-plot show the locations of the tensiometers.

The locations of the tensiometers are shown as black dots in Figure 4-9 and each contour plot refers to a specific time during a given experiment. The upper halves of the contours are excluded in sub-plots at the instant the top tensiometers were exposed to water due to scour. Figures 4-9a and 4-9b display the pore pressure variations under supercritical bores, while Figures 4-9c and 4-9d present the subcritical bore cases. Note that both supercritical tests H1 and H2 had the same initial still water depth (h_o, Table 4-1), thus the same initial (hydrostatic) pore pressure distribution, and likewise both subcritical tests H3 and H4 had the same initial pore pressure distribution.

For the supercritical bores, the pore pressure values at t = 5 s near the bottom and in the middle of the wall of the model were greater for the test with smaller h_o/d_o (i.e., test H1 shown in Figure 4-9a versus test H2 shown in Figure 4-9b). This is expected, because smaller h_o/d_o is due to larger impoundment depth (d_o, Table 4-1) and thus deeper bores (see Rajaie et al., 2019 in review, Figure 3-8b) with greater instantaneous hydrostatic pressure. The impact of waves generated by a higher impoundment depth was also reflected in the exposure time of the tensiometers: the top row corner tensiometers were exposed to the water approximately three seconds earlier in Test H1 (i.e, t = 5.40 s) than in Test H2 (i.e, t = 8.82 s).

It is noteworthy that the pore pressure varied dramatically across the face of the structure in the supercritical bores. In particular, the pore pressure along the centreline of the front face of the structure was more uniform with depth, such that pore pressure near the soil surface increased more in the centre of the structure face than at the corners of the structure, while at depth the pore pressure increased more at the corners. It appears that the pore pressure along the entire centreline of the front face of the structure was influenced by the hydrodynamic stagnation pressure. On the other hand, it appears that pore pressures at the corners of the structure were more influenced by instantaneous hydrostatic pressure and possibly the hydrodynamic pressure associated with the horseshoe vortex and flow separation at the corner.

For the subcritical bores over horizontal beds (Figures 4-9c and 4-9d, for bores H3 and H4, respectively), the pore pressure distribution on the front face of the structure was again observed to be greater at depth for the deeper bore (Test H3). A comparison of the pore pressure distribution contours occurring during subcritical bores with pore pressures measured from the case of the supercritical bores illustrates that the tensiometer exposure occurred at relatively the same time for the top-row corner tensiometers, except supercritical Test H1 which had the highest bore velocity (see Rajaie et al., 2019 in review, Figure 3-11c). Although less vertical gradient was again observed in the middle of the structure face, for the subcritical cases the pore pressure was distributed somewhat more uniformly across the face of the structure than was observed for the supercritical bore cases. This suggests the subcritical bores caused more uniform hydrostatic pore pressure distribution during the loading time. Moreover, the subcritical bores induced larger pore pressure throughout the soil depth than was observed for the supercritical bores; this is likely due to larger instantaneous hydrostatic pressure and greater depth of the subcritical bores (see Rajaie et al., 2019 in review, Figure 3-8b). Moreover, a relatively higher pore pressure zone was observed at the right corner of the structure in Test H3 which is due to the existence of the strong horseshoe vortex in the region. In other words, the low-pressure zones ($0.3 < PWP < 1.2$) in the soil column during supercritical bores were considerably deeper compared to the subcritical ones.

Figure 4-10 shows the spatial distribution of the pore pressure on the side wall of the structural model for the horizontal bed tests.

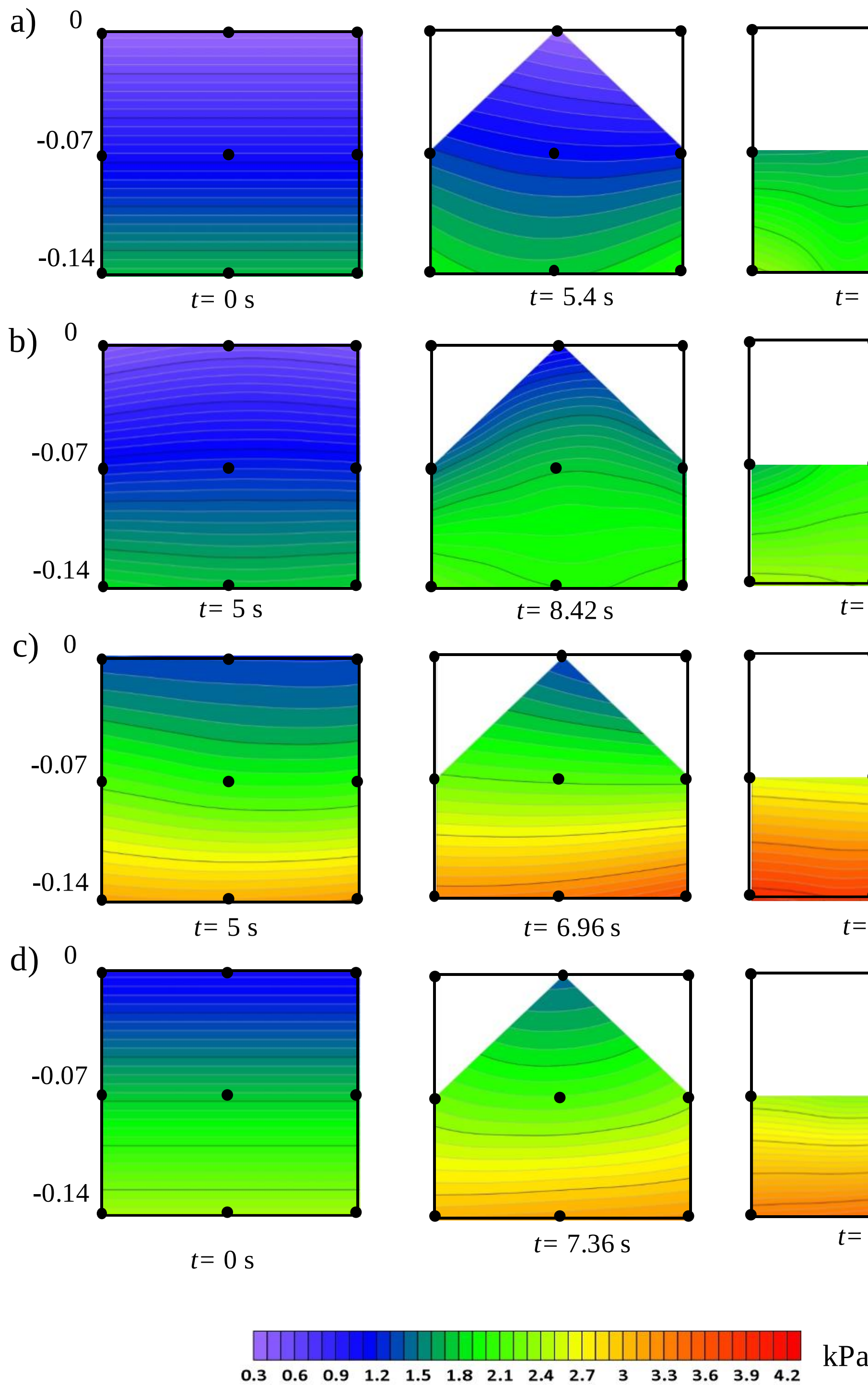

Figure 4-10. Contour plots of pore water pressure variations with time in side of the structural model for horizontal bed tests: a) h_o/d_o = 0.1; b) h_o/d_o = 0.12; c) h_o/d_o = 0.25; d) h_o/d_o = 0.28. The black circles in the first sub-plot show the locations of the tensiometers. Flow is from right to left.

Pore pressure distributions at the beginning of the experiments linearly changed with depth for all tests. At time t = 5.4 s in Test H1, the sediments scoured at the corners of the side face of the structure and pressure gradually increased across the entire face (see Figure 4-10a). In general, the exposure times on the side face of the structure increased with decreasing impoundment depth (i.e., greater h_o/d_o for tests with the same still water depths). This delay could have been due to weaker vortices induced by weaker bores. Lastly, similar to the front face, the pore pressure values were distributed more evenly laterally across the side face of the structure in the subcritical flows.

Figure 4-11 shows the contour plots of pore pressure distribution with time on the front wall of the model for the inclined bed tests.

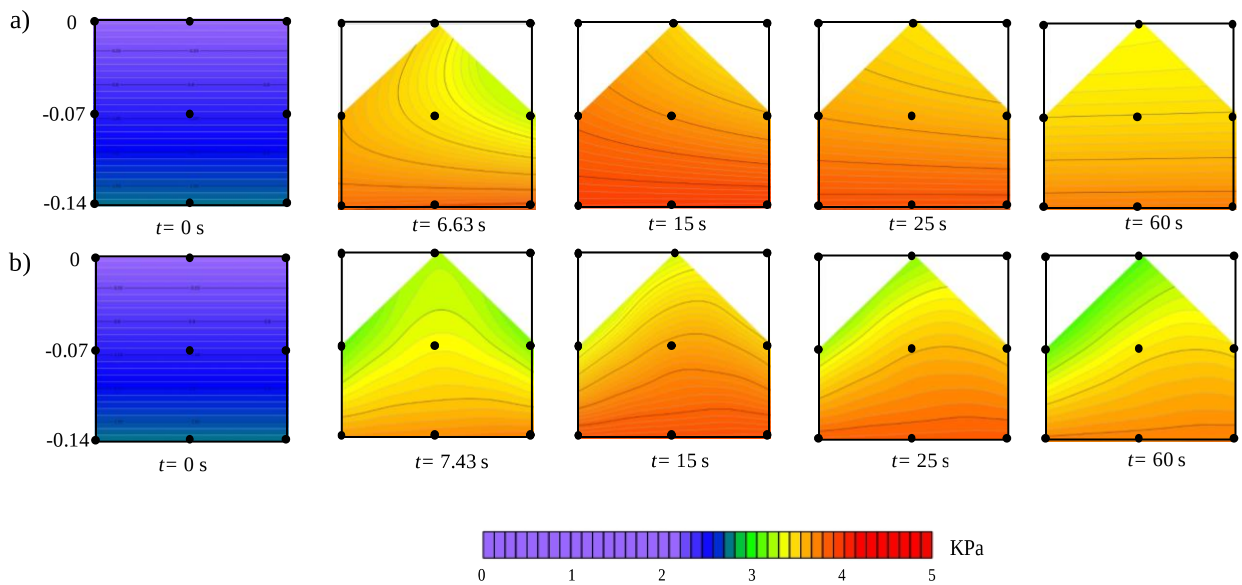

Figure 4-11. Contour plots of pore water pressure variations with time in front of the structural model for inclined bed tests: a) h_o/d_o = 0.075; b) h_o/d_o = 0.085. The black circles in the first sub-plot show the locations of the tensiometers.

The first contour plot at t = 0 appropriately shows a linear hydrostatic pore pressure distribution before the arrival of the bore. The arrival of the bore is indicated by the change in pore pressure distribution observed at nearly t= 6 s when scouring initiated at the corners of the front face at the same time. Similar to the horizontal bed case, the maximum pore pressure was observed along the centreline of the column, corresponding to the stagnation zone. It is difficult to explain the observed asymmetry in pore pressure between the two upper corners of the model in Test S1 at t=6.63 s, but this may have been related to small differences in bore propagation across the width of the channel. On the other hand, relatively lower pore pressures were observed at the upper corners of the structural model near the soil surface in Test S2 at t=7.43 s. Presumably, this was due to soil suction as the rapidly propagating bore accelerated around the corners of the structural model.

In general, greater soil pore pressure was observed throughout the soil column in Test S1 (h_o/d_o = 0.075) than Test S2 (h_o/d_o = 0.085), as expected due to higher impoundment depth (d_o = 0.4 m versus 0.35 m). Even 55 s after the bore arrival (equivalent to t= 60 s) Test S1 displayed increased pore pressure at the soil surface in the centre of the structural model, whereas by that time Test S2 had developed a more uniform lateral distribution of pore pressure with depth.

The effect of bed slope on pore pressure distribution in the front face of the structural model was also analyzed by comparing the contour plots of pore pressure distribution observed in horizontal and inclined bed tests. A comparison of Figure 4-9a and Figure 4-11b at first 10 s indicated that pore pressure values for inclined beds were larger than the pore pressure observed for horizontal beds.

The pore pressure distributions on the side wall of the model for the inclined bed tests are shown in Figure 4-12.

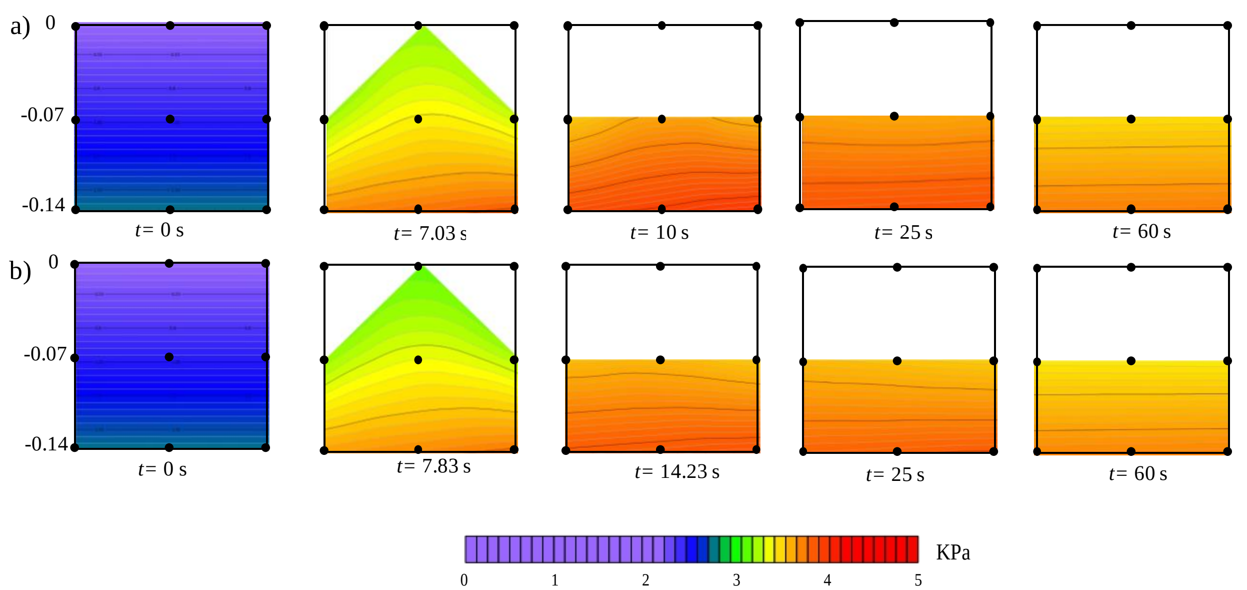

Figure 4-12. Contour plots of pore water pressure variations with time in side of the structural model for inclined bed tests: a) h_o/d_o = 0.075; b) h_o/d_o = 0.085. The black circles in the first sub-plot show the locations of the tensiometers. Flow is from right to left.

Relatively low pore pressure at the soil surface of the structural model at time of the bore arrival (i.e., t =7.03 s and t = 7.83 s in Tests S1 and S2, respectively) was likely due to flow separation at the building corner and corresponding low hydrodynamic pressure in the overlying fluid. Interestingly, the pore pressure distribution was symmetrical to the z-axis, despite the asymmetric wave hydrodynamics in the sidewall. Again, in general, slightly greater pore pressures were observed throughout the soil column for Test S1 (h_o/d_o = 0.075) than Test S2 (h_o/d_o = 0.085).

4.4 Conclusions

The effects of tsunami-like bores propagation around a nearshore building were investigated by employing a series of laboratory experiments. Time-history of the pore pressure variations around a square-shaped structural model and at the different depths from the soil surface were measured. Contour plots of spatial distributions of the pore pressure were extracted during the bore propagation and the wave interactions with the model were also investigated. The time variation of pore pressure with depth was examined for both horizontal and +5% inclined beds and the effects of the various still-to-impoundment depth ratios on the pore pressure variations were tested. The normalized maximum pore pressure and its occurrence time were also examined and it was found that the peak pore pressure and the time to peak were correlated with the still-to-impoundment depth ratios, the tensiometer orientation and location, as well as the bed slope.

The interaction of the horizontal supercritical bores with the soil around the structural model indicated that the maximum effective pore pressure in the front corner of the model and for third row tensiometers was approximately 50% larger than in the corresponding pressure in the side corner. However, the difference between the maximum effective pore pressures in the tensiometers installed at the same exact locations due to the propagation of the subcritical bores over the horizontal bed was less 10%. Furthermore, it was found that the front wall of the structural model experienced maximum 15% higher effective pore pressures than the side wall due to the propagation of hydraulic bores over the inclined bed. In the horizontal bed tests, the maximum normalized pore pressures in the middle of the front wall of the structural model were not strongly influenced by h_o/d_o. However, the maximum normalized pore pressures in the side wall increased slightly with an increasing h_o/d_o. Moreover, it took longer for the side tensiometers to record the maximum pore pressure.

A 5% increase in the bed slope approximately doubled the effective pore pressures around the structure. On the other hand, the normalized maximum pore pressures were not affected by soil depth and they varied between one to two times that of the initial hydrostatic pressure in horizontal bed tests. For the inclined bed tests, the peak pore pressures at the bed surface were approximately

5 times larger than the normalized maximum pore pressures at $z/b = 0.5$. However, the variations of normalized maximum pore pressure were nearly the identical in front and side walls of the structural model in these tests. The time-to-reach the maximum pore pressure was also impacted by the effect of bed slope. For the inclined bed tests, the tensiometers recorded the maximum pore pressure earlier than the horizontal bed tests.

When supercritical bores passed over the horizontal surface, the time to reach the maximum pore pressure in the first row of tensiometers decreased with increasing h_o/d_o. For the inclined bed tests, the peak pore pressure at the bed surface occurred earlier than in the tensiometers located at $z/b = 0.5$. Additionally, increasing h_o/d_o increased the time to reach the maximum pore pressure. Contours of spatial variations of pore pressure under different h_o/d_o showed that the supercritical bores had significant effects on the spatial variations of pore pressures versus subcritical bores. In supercritical bores, when the still water depth was smaller, low-pressure zone was deeper in the surface layer compared to that of the subcritical bores. Moreover, the flow separation formed high-pressure zones at the corners of the structural model for the bottom tensiometers. The bed slope increased the bore depths, therefore the pore pressures within the soil increased. As a result, significant consolidation occurred within the soil while low-pressure zones were extended further down and near to the middle row of the tensiometers.

Chapter 5. Experimental investigations of tsunami-like bores impacting on a vertical structure, Part II: local scour

The article is in review in Journal of Waterway, Port, Coastal and Ocean Engineering (ASCE)

5.1 Introduction

On March 11th 2011, an extremely strong earthquake with a magnitude of 9.0 Mw triggered an enormous tsunami which impacted the Tohoku region (Shibayama et al., 2013). According to detailed field investigations the affected area on the seafloor was permanently displaced 5 m horizontally and 1 vertically (Japanese Meteorological Agency, 2011). This massive earthquake caused exceptionally high tsunami inundation length, and runup height ranged between 20 m and 40 m along with the Tohoku shoreline (Tohoku Earthquake Tsunami Joint Survey Group, 2011). Field observations indicated that the hydrodynamic loadings generated by tsunami waves caused significant erosion around coastal structures which resulted in extensive structural failures (Chinnarasri et al., 2013; Chock et al., 2012). A number of post-tsunami field surveys have been carried out to understand the key factors in excessive erosion during tsunami incidents (Nistor, 2005; Saatcioglu et al., 2006; Kato et al., 2012; Nistor and Palermo, 2015). The analysis of field surveys along coastal dikes in Iwate region after the 2011 Tokohu Tsunami showed that approximately 50% of structural failures were due to excessive sediment erosion and local scouring around coastal structures (Kato et al., 2012). A report after the 2011 Tohoku Tsunami stated that scour depths had a direct relation with the tsunami flow depths (Goto et al., 2014), which shows the importance to futher study the development of scour due to different tsunami-like conditions. Figure 5-1 shows the erosion around a foundation of a residential building due to the 2018 Indonesia Tsunami in Palu Bay, Indonesia.

Figure 5-1. Image of extreme erosion around a foundation due to tsunami loading in Palu Bay, Indonesia (courtesy of Jacob Stolle, 2018).

New design guidelines ensure the ability of coastal structures to withstand the hydrodynamic pressure associated with tsunami loading (Jayaratne et al., 2014). Accurate estimation of scour depth around the foundation of coastal structures is also required to properly design and maintain these structures. Some design guidelines consider scour of coastal structures (FEMA P-646, 2012; ASCE7-16, 2016) and these standards have been updated based on recent research findings. For instance, the results of this experimental study presented in this paper, combined with a series of scaled experimental ones conducted in the past are then plotted as normalized scour depths versus Fr numbers. Based on this graph the normalized scour depth was constant for Fr numbers higher than one (Nistor et al., 2019). As an early guidance for design, Dames and Moore (1980) suggested the maximum scour depth in loosely packed shorelines can reach upto 80% of the flow depth. More recently, relation between the maximum scour depth and flow depth in the vicinity of coastal structures were described in the ASCE 7-16 Chapter 6 design standard (2016). Based on this ASCE standard, the maximum scour depth is 1.2 times of the flow depth for flow depths smaller than 3.048 m ($H_o \leq 3.048$ m), and for flow depths larger than 3.048 m, the maximum scour depth is constant with a value of 3.65 m (ASCE7-16, 2016). However, recent research studies have shown that parameters other than the flow depth influence the maximum scour depth and a simple relation of the scour depth with flow depth may overestimate the erosion in the vicinity of coastal structures (Tonkin et al., 2003; Qi et al., 2012; Daliri and Chegini, 2016; Mehrzad et al., 2016) or may not be appropriate for design purposes.

The rapid loading and unloading due to overland propagation of tsunami inudation generates a set of vortices around structures, such as horseshoe and wake vortices, which have significant effects in formation of local scour around coastal structures (Tonkin et al., 2003). Consequently, the evolution of local scour due to tsunami loading is associated with different mechanisms such as excess bed shear stress in comparison with particle inertia, turbulence augmentation, and vortex strength around coastal structures. Understanding the sediment-fluid coupling mechanism in transient flow is critical for the prediction of local scour around coastal structures. As the tsunami-like bore propagates and impacts the structure, bed shear stress and turbulence level amplify due to momentum transfer and as a result the sizes of vortices and scour depth increase with time (Qi and Gao, 2019). Furthermore, dynamic variations in pore pressure can influence scour (Tonkin et al. 2003). Understanding the effects of various controlling parameters on scour depth is important in mitigating the destructive effects of tsunami loads in coastal structures (McGovern et al., 2019). In the following, a review of laboratory and numerical studies related to aspects mentioned above is provided to elucidate relevant parameters.

In laboratory conditions, solitary waves are usually generated by a piston-type wave maker and have commonly been used to reproduce tsunami waves at experimental scale. However, recent experimental studies indicate that the tsunami waves in the field propagate with different time and space scales (Madsen et al., 2008; Madsen and Schaeffer, 2010; Wu et al., 2014). Solitary waves propagate over long distancse without significant energy loss and they are suitable to acquire high quality data (Wu et al., 2016) but, as mentioned in part I of this paper, dam-break waves have shown better hydrodynamic similarity with the field scale tsunami waves in comparison with solitary waves (Chanson, 2004). Consequently, the following review is differentiated between studies performed using solitary waves and those using dam-break turbulent hydraulic bores.

5.1.1 Solitary waves

The erosion due to the propagation of solitary waves around a cylindrical structure with 0.5 m diameter was experimentally investigated by Kato et al. (2001). The solitary waves propagated over an inclined bed with a slope of 1V:20H and the bed was filled with uniform saturated sand particles with a mean particle diameter d_{50} = 0.35 mm. Wave heights were between 2.25 m and 2.65 m and the still water depth was constant with a value of 2.45 m ± 0.2 m. Kato et al. (2001) proposed a linear relationship between the wave height and the eroded area around the cylinder and the scour area was independent of the location of the cylindrical structure. Moreover, the maximum scour depth was observed on the side face of the cylindrical model and it was approximately the same as the maximum scour depth formed in the front face of the structure. The maximum scour in the side of the structural model occurred 2 s earlier than that on the front face (Kato et al., 2001).

The effects of solitary wave propagation on local scour formation around a cylindrical structure were tested by surrounding it with gravel with a mean particle diameter d_{50} = 3.6 mm for a radius of 0.25 m and depth of 0.25 m underneath the model. The rest of the flume was filled with sand with the bulk density of ρ_{sat}= 1.93×10^3 kg.m^{-3} (Tonkin et al., 2003). The experimental results showed that the maximum scour depth occurred in the side face of the structure. The maximum scour depth in the gravel area was 4% less than in the fine sand section, and the maximum scour depth was observed after approximately 3 s from the wave impact in the gravel bed and it was delayed by 15 seconds in the sand section (i.e., t=18s). Furthermore, sediment re-deposition and secondary erosion occurred on the side face of the building in the fine sand bed area (Tonkin et al., 2003).

An extensive experimental and numerical study was performed to investigate the effects of solitary waves with different still water depths (i.e., h_o= 0.265 m, 0.290 m, and 0.315 m) on scour formation and pore pressure propagation around a square structure with two different widths of b = 0.1 m and 0.14 m by Nakamura et al. (2008a). The bed slope was 1V:10H and consisted of a mixture of sand particles with two mean particle diameters d_{50} = 0.2 mm and 0.45 mm. The maximum scour depth was scaled with the normalized wave height (i.e., $(2h_o–d_o)/b$). The results showed that the maximum scour depth increased linearly with an increase in the normalized wave height and it then became constant for $(2h_o–d_o)/b > 1.5$. A comparison of the erosion contour plots depicted that the maximum scour at the seaward corners of the structural model were independent of the structure's width. Moreover, the maximum value of the pore pressure was recorded on the front face of the structure and that it was 2.6 times greater than the maximum pore pressure measured at the back of the model (Nakamura et al., 2008a).

A series of experimental study performed to examine the effect of various heights of combined currents and waves on scour depth and pore pressure propagations around cylindrical columns with diameters of 0.2 m and 0.08m. Three different wave heights of 0.026 m, 0.052 m, and 0.085 m propagated over a saturated sediment section with particles with a median diameter of 0.38 mm. Analysis of their results determined that the magnitude of pore pressure increased by 1.25 with a

2.3 times increase in the wave height. On the other hand, a slight increase in pore pressure over time caused relatively considerable increase in the scour depth (Qi et al., 2012).

In 2019, McGovern et al. examined scour development around a square-shaped structure installed on a saturated and horizontal sediment bed filled with a fine sand mean particle diameter d_{50}=1.6×10^{-4} m. The sediment bed was installed after a sloping surface with a slope of 1:20. The sediment section was split into three section using wooden bay splitters. The structures located in the two sides of the flume was 0.4 m high and 0.2 m wide. The tsunami inundation was simulated by a wave generator (PLWG) installed about 45 m far away from the structure. These waves with three different wave pariods of 147s, 49s, and 25s were generated. The results of the scour development showed that the erosion development could be influenced by the flow velocity more than its duration. It was also shown that, regardless of the wave periods, scour initiated from the corners of the structure due to the formation of the lateral vortex and then gradually extended towards the centerlines of both the front and side faces of the structure (McGovern et al., 2019).

A series of numerical simulations were performed to investigate the effects of solitary waves of various heights and bed slopes on the erosion of fine particles with a mean particle diameter d_{50} = 0.18 m (Liu et al., 2019). The wave height, H_o, ranged from 0.02 m to 0.8 m and four bed slopes ranging from 1V:10H to 1V:25H were examined. It was found that the eroded volume of sand particles was directly correlated with the wave height. Also, it was observed that the volume of erosion increased by 1.5 and 2 times as the wave heights increased by 2 and 3 times, respectively. Furthermore, a linear relation was found between the bed slope and the eroded volume of fine sand particles (Liu et al., 2019).

5.1.2 Turbulent bores

Mehrzad et al. (2016) used a rapidly releasing swing gate to generate laboratory tsunami-like hydraulic bores. Multiple experiments were conducted to explore the effects of different still-to-impoundment water depth ratios, h_o/d_o, on scour around square-shaped structures with different sizes (0.1 m, 0.2 m, and 0.3 m). The turbulent bores propagated over a horizontal sand bed with a mean particle diameter of d_{50} = 1 mm (Mehrzad et al., 2016). The impoundment water depths ranged between 0.15 m and 0.375 m and the still water depths were between 0.025 m and 0.125 m which resulted in h_o/d_o between 0.1 and 0.41. The results showed that, regardless of the structure dimensions, the maximum scour depth occurred at the corners of the structures and that it had a linear and direct relation with the impoundment depth (Mehrzad et al., 2016).

A series of numerical simulations were performed to study the effect of dam-break induced wave propagation on the local erosion around a cylindrical structure (Triatmadja, 2017). The turbulent bores propagated over an inclined sandy surface with a slope of 1V:20H and a mean particle diameter d_{50} = 0.19 mm. Three impoundment depths of d_o = 0.45 m, 0.5 m, and 0.55 m and three still water depths of h_o = 0.18 m, 0.2 m, and 0.22 m were simulated which gave the still-to-impoundment depth ratio of $0.33 \leq h_o/d_o \leq 0.49$. The simulation results indicated a deeper scour depth in the side face of the structure than the front face. Moreover, a direct relation was found between the scour depth and impoundment depths such that by increasing the impoundment depth by 23% the maximum scour depth increased by 60% (Triatmadja, 2017).

Biswal et al. (2018) examined numerically the effects of impoundment depth, d_o, on sediment erosion. A vertical gate was used to generate tsunami-like turbulent bores and the bores propagated over a horizontal surface. The simulated horizontal bed had saturated sand particles with a mean particle diameter d_{50} = 0.45 mm. Three different impoundment depths (i.e., d_o = 0.25 m, 0.35 m, and 0.45 m) were simulated and the still water depths ranged from 0.023 m to 0.18 m (i.e., h_o/d_o = 0.013 to 0.18). The results showed that the scour depth correlated with impoundment depth and it inversely correlated with still water depth (Biswal et al., 2018).

As the literature review showed, several experimental and numerical studies were performed to investigate the effects of dam-break bore propagation on local erosion around coastal structures. Most previous physical model tests used solitary waves to investigate the impact of tsunami-like waves on local erosion around coastal structures. In more recent years, dam-break waves have shown to provide an improved approximation of the prototype tsunami waves. As research needs pointed out, in this study, dam-break hydraulic bores were used in laboratory conditions to study scour induced by tsunamis around structures.

5.1.3 Scaling considerations

Previous studies have normalized the maximum scour depth, d_s, with the structure's width, b, (Sumer et al., 1992; Moreno et al., 2016). Ettema et al. (1998) proposed a functional relationship based on the Π-theorem of dimensional analysis to correlate the normalized scour depth d_s/b with unidirectional steady flow and bed characteristics as:

$$\frac{d_s}{b} = f\left(\frac{u}{u_c}, \frac{u^2}{gd_o}, \frac{d_o}{b}, \frac{b}{d_{50}}, \frac{\rho u b}{\mu}\right) \tag{5-1}$$

where ρ is the fluid density, μ is the fluid viscosity and u_c is the critical flow velocity (Ettema et al., 1998).

Several empirical correlations have been proposed to predict the maximum scour depth due to tsunami-like wave propagation (Table 5-1).

Table 5-1. Proposed equations from the literature for the prediction of the maximum scour depth under tsunami-like loading around a structure.

Researchers	Forcing factor	Proposed scour estimation formula	Parameters
Triatmadja (2017)	Tsunami-like bore generated by a lifting gate	$0.35\ H_o < d_{sm} < 0.6\ H_o$	H_o
Triatmadja et al. (2011)	Tsunami-like bore generated by a lifting gate	$d_{sm}/d_o = 0.25$ to 0.3	d_o
Tonkin et al., (2003)	Solitary wave	$d_{sm} = \frac{\Delta P}{\gamma_b \Lambda}(1-4i^2 erf\left[\frac{d_{sm}}{2.cv.\Delta T}\right]$	Λ, P, c_v
Dames and Moore (1980)	Tsunami	$d_{sm}/H_o = 0.4$	H_o

The normalized maximum depth of scour (d_{sm}) has been correlated with the bore characteristics such as the flow depth, H_o) which, in dam-break generated bores, is determined by the impoundment (d_o) and still water (h_o) depths, as well as the bed slope, roughness, and propagation distance. The model of Tonkin et al. (2003) involves more complex correlations, because their study demonstrated that pore pressure variations can also influence scour depths. Based on Table 5-1, for assessment of maximum scour due to tsunami-like dam-break bores, the following terms can be considered in addition to those in Eq. 5-1:

$$\frac{d_s}{b} = f(H_o, d_o, \Lambda, P, c_v) \qquad (5\text{-}2)$$

where H_o is flow depth, d_o is impoundment depth, Λ scour enhancement parameter ($\Lambda=(2/\sqrt{\pi})\times(\Delta P/\gamma_b\sqrt{c_v \Delta T}$), P is pore pressure, and c_v is Terzaghi's coefficient of consolidation.

It should be noted that recent studies have reported an inherent scale effect in relatively small-scale physical models which resulted in a systematic overestimation of the scour depth (Lou et al., 2019). Three independent length scales are attributed to the scale effect: the impoundment depth, d_o, the width of the structural model, b, and sediment mean particle diameter, d_{50}. These length scales directly affect the size of vortex generated around the structure and sediment distortion (Qi and Gao, 2019).

For the present study, a series of laboratory experiments have been carried out by generating dam-break waves to study the effects of different still-to-impoundment depth ratios and bed slopes on the local erosion around a square-shaped structural model. The ratio of still-to-impoundment depth along with the bed slope determines the bore depth. As explained in the first companion paper Rajaie et al. (in review) (Rajaie et al., 2021), the runup and quasi-steady flow during passage of the tsunami-like bores resulted in spatio-temporal pore pressure variations in the sediment bed. The normal stress induced by propagation of the dam-break bores and the pore pressure variations caused scour development around the structure. This second companion paper aims to correlate pore pressure variations, bore hydrodynamics, and local bed erosion around a square-shaped structural model. The time-histories of scour profiles around the structural model were measured and the effects of still-to-impoundment depth ratios and bed slopes on the time-histories of bed erosion were analyzed. For a better understanding of the erosion mechanism, the time-histories of scour depth are correlated with Shields parameter. Finally, the normalized peak scour depths for different still-to-impoundment depth ratios are linked with peak pore pressure around the structural model and an empirical relation is proposed for prediction of maximum scour depth in different hydrodynamic conditions.

5.2 Experimental setup

A series of laboratory experiments were conducted in a straight, rectangular flume located in the Hydraulic Laboratory at the University of Ottawa, Canada. The flume is 30 m long, 1.5 m wide, and 0.8 m deep and equipped with a rapidly opening swing gate to generate dam-break waves (see Figure 5-2 of Part I). Dam-break waves were generated to investigate the impact of different bore heights on local erosion around a square-shaped structure (see Figure 5-2). The swing gate was placed at approximately one-third to the upstream end of the flume. Two wave absorbers were installed within the impoundment reservoir at a distance of 10.55 m and 18.05 m upstream of the swing gate to prevent the reflection of waves and their influence on water surface elevation.

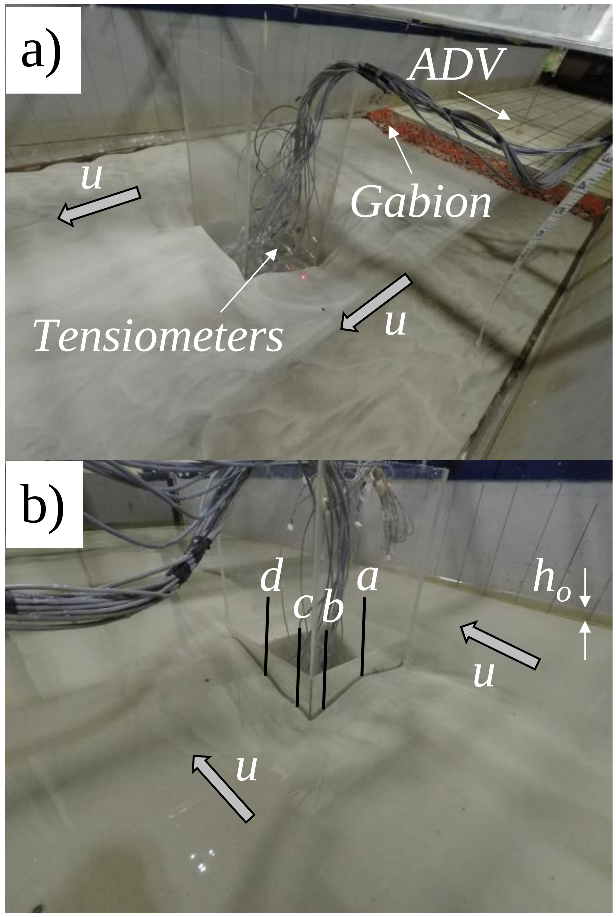

Figure 5-2. Images of local sediment erosion around the structural model: a) Test H2 (h_o/d_o = 0.12); b) test S2 (h_o/d_o = 0.085).

Four still-to-impoundment depth ratios, h_o/d_o, were selected to represent both subcritical (i.e., $h_o/d_o > 0.2$) and supercritical (i.e., $h_o/d_o \leq 0.2$) flow conditions for the horizontal bed tests and two still-to-impoundment depth ratios of 0.075 and 0.085 (i.e., supercritical flow) were selected for the inclined bed tests with +5% upslope (see Table 4-1 in Part I). The time histories of scour around the structural model were extracted from consecutive images taken by a wireless video-camera (GoPro-Hero5, San Mateo, CA, US) installed inside the structural model while the time histories of the bore depths and velocities were measured by ultrasonic gages and ADV. A summary of the instruments used in this study and their specifications is shown in Table 5-2. Time histories of flow depths, velocities, Froude numbers, and specific momentum for these cases were presented in (Rajaie et al., 2019).

Table 5-2. Instrumentation used in the current experiments.

Instrument	Manufacturer, Model	Sampling rate used in current tests
Wave gauge (WG)	RBR WG-50, NRC, capacitance-type, Ottawa, Canada	300 Hz
Ultrasonic wave sensor (US)	M-5000/220, Massachusetts, U.S.A	1200 Hz
Acoustic Doppler Velocimeter (ADV)	Nortek Vectrino, Vangkroken, Norway	200 Hz
Pore pressure tensiometer	SDEC 220, Reignac sur Indre, France	40 Hz
GoPro camera	GoPro-Hero5, San Mateo, U.S.A	60 fps

The video-camera had a resolution of 1920 x 1080 pixels and a recording speed of 60 frames per second. The recorded images were used to detect the sediment-water interface around the structure and to determine the time-history of erosion as well as to calculate the erosion rate in the front and along the side walls of the structural model. Details of experimental setup and instrumentation are reported in Part I (companion paper) discussing the results of this study.

5.3 Results and Discussion

5.3.1 Local scour around the structure

Figure 5-3 shows the effects of the still-to-impoundment depth ratios, h_o/d_o, on the variations of the normalized scour depth with normalized time for the horizontal bed tests in the front, side walls, and at the corner of the structural model.

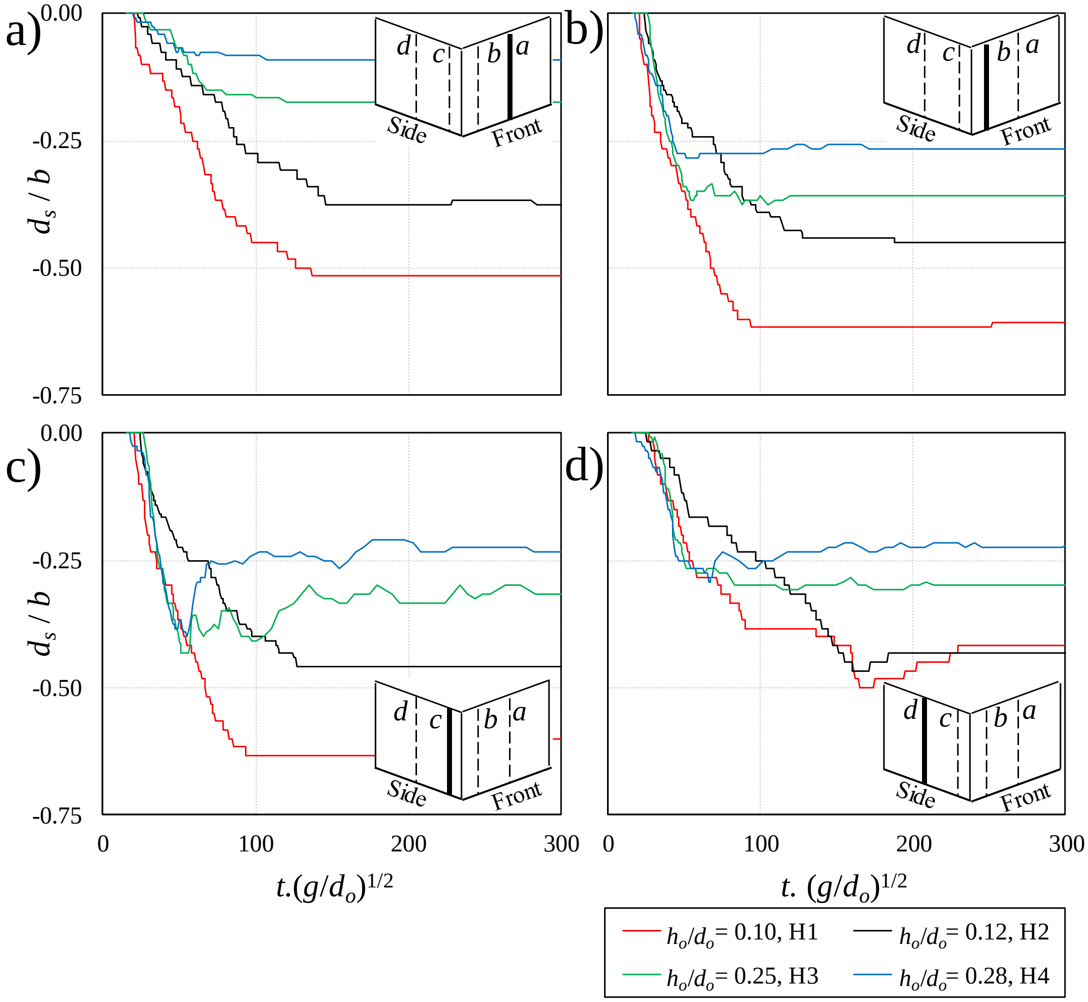

Figure 5-3. Effects of still-to-impoundment depth ratio h_o/d_o on variations of the normalized scour depth with normalized time for horizontal beds; a) *a-a*; b) *b-b*; c) *c-c*; d) *d-d*.

The scour depth was normalized with the width of the structural model and time was normalized with the characteristic time scale $(d_o/g)^{1/2}$. The vertical axis in Figure 5-3 shows the normalized scour depth ranging from elevations of 0 to −0.75 and the horizontal axis shows the normalized time variations ranging from 0 to 300. An inverse relation is evident between the maximum scour depth and the increase in the still-to-impoundment depth ratio, h_o/d_o, around the structural model. Furthermore, as can be seen in Figure 5-3, the scour profile reached equilibrium level faster in the subcritical regime (i.e., $h_o/d_o > 0.2$, tests H3 and H4) than in the supercritical regime (i.e., $h_o/d_o \leq 0.2$, tests H1 and H2). Figures 5-3a and 5-3b show the effect of flow regimes on the normalized scour depth in middle and corner of the front wall of the structural model, respectively. As shown in Figure 3a, the deepest scour recorded in the middle of front wall (section *a-a*) occurred in the supercritical regime (i.e., $h_o/d_o = 0.1$ and 0.12). On the other hand, the effects of initial impact and subsequent quasi-steady period of the bore are seen in Test H1 (h_o/d_o = 0.1). During the runup at $t(g/d_o)^{1/2} \leq 50$, the normalized scour was approximately -0.2 and in quasi-steady period (i.e., $50 \leq t(g/d_o)^{1/2} \leq 100$) the normalized scour depth increased by an additional -0.27. Additionally, a comparison of Tests H1 and H2 indicates that increasing the still-to-impoundment depth ratio by 20%, increased the normalized scour depth in the middle of front wall by approximately 40%.

The flow regime also affected the scour development over time. For instance, in the supercritical regime, the peak scour depth in middle front wall occurred at $130 < t(g/d_o)^{1/2} < 140$, whereas in the subcritical regime, the maximum scour depth occurred at $105 < t(g/d_o)^{1/2} < 110$ (see Figure 5-3a). Such a significant difference between the scour development over time in sub- and supercritical flow regimes indicates that the generated turbulence in the supercritical regime is dominant for a longer time than the subcritical bores (i.e., $\Delta[t(g/d_o)^{1/2}] \approx 50$). It is worth noting that in Test H1, the second-row tensiometers were exposed to the flowing bore at the same non-dimensional time that tensiometer #3 reached the peak pore pressure ($t(g/d_o)^{1/2} \approx 130$ (see Figure 4-5b in Part I). The effect of still water depth on the equilibrium erosion depth, $d_{s\infty}$, was studied by comparing the tests with the same impoundment and different still water depths. Tests H1 and H4 with h_o/d_o = 0.1 and 0.28, respectively, had relatively similar impoundment depths but different still water depths downstream of the gate. The equilibrium scour depth in the front wall of the structural model decreased by 80% as still water depth increased by 2.33 times.

Figure 5-3b shows the time-history of scour depth in the front corner of the structural model. Similar to the centre of the front wall, greater scour occurred in the supercritical flow regime (i.e., Tests H1 and H2), with 1.4 times larger maximum scour observed in H1 than H4. However, in both flow regimes, the equilibrium scour depths at the front corner of the structural model were deeper than that measured at the centre of the front wall. The higher scour depths at the corner were due to the formation of eddies at this region of the structural model. Experimental observations indicated that the separated flows at the corners of the structural model generated strong vorticity and turbulence. This mechanism resulted in formation of deeper scour holes. Similar experimental observations were reported by Tonkin et al. (2014). Again, at the corner of the structural model the equilibrium time occurred earlier in the subcritical regime than the supercritical cases, by at least $t(g/d_o)^{1/2} \approx 50$. The effect of the impoundment depth generating bores in the subcritical flow regime was studied by comparing the results from Tests H3 and H4 with h_o/d_o = 0.25 and 0.28, respectively. Both tests had the same still water depth, but Test H3 had

14.35% higher impoundment depth than Test H4. This 14.35% higher impoundment depth in Test H3 resulted in 35% greater scour depth at the corners of the front wall.

Figures 5-3c and 5-3d show the variations of normalized scour depth with time in the side corner and side wall of the structural model, respectively. The turbulent bores with shallower still water depth formed a deeper scour hole (i.e., Test H1 versus Test H4). A comparison of Figures 5-3b and 5-3c indicates that the local erosion due to propagation of the supercritical bores was the same at the side and front corners of the structural model, whereas, for the subcritical bores the bed erosion in side corner was relatively greater than the front corner. The considerable erosion at the upstream corner of the side wall (section *c-c*) was attributed to formation of a horseshoe-type vortex generated as a result of flow separation and eddies formation in the wake region near the side wall.

A single bore passage (initial impact followed by quasi-steady flow) in the subcritical regime was capable of refilling a portion of the eroded sand volume in the side corner of the model. For example, in the side corner of the structure in Test H3 the normalized scour depth at the equilibrium state was 35% smaller than the maximum normalized scour depth (see Figure 5-3c); for the same region (section *c-c*), the refilling process did not occur in the supercritical regime. On the other hand, at the side corner of the model, the maximum normalized scour depth in the supercritical regime was approximately 1.2 times larger than the maximum normalized scour depth in the subcritical regime. It is noteworthy to point out that in Test H4, the scour depth reached its maximum in the middle of side face at the same time (i.e., $t(g/d_o)^{1/2} \approx 55$) as the tensiometer #6 recorded the peak pore pressure (see Figure 4-5c in the companion paper - part I).

The time history of normalized scour depth in the middle of side wall is presented in Figure 5-3d. For both subcritical and supercritical regimes, the maximum normalized scour depths and the time to reach the peak scour were almost independent of the still-to-impoundment depth ratios. For instance, in the supercritical regime, the maximum normalized scour depths occurred at the same time of $t.(g/d_o)^{1/2} \approx 160$ which was almost $t.(g/d_o)^{1/2} \approx 100$ after the corresponding time for the subcritical bores. Contrary to the case of the erosion at the side corner, 25% of the maximum scour depth in section *d-d* was refilled in the supercritical Test H1. As it can be seen in Figure 5-3d, the equilibrium scour in Test H1 ($h_o/d_o = 0.1$) occurred later along the side wall (i.e., $t(g/d_o)^{1/2} \approx 230$) than at the front and corners of the structural model. Such (albeit, short) delay may be due to the formation of turbulent eddies and vortices which were active for a longer time along the side wall of the structure. The equilibrium scour profile occurred at the same time as the pore pressure in tensiometer #3 reached the maximum pore pressure (see Figure 4-5d in companion paper I).

The time histories of the normalized scour depth for the inclined bed tests with two different still-to-impoundment depth ratios are presented in Figure 5-4.

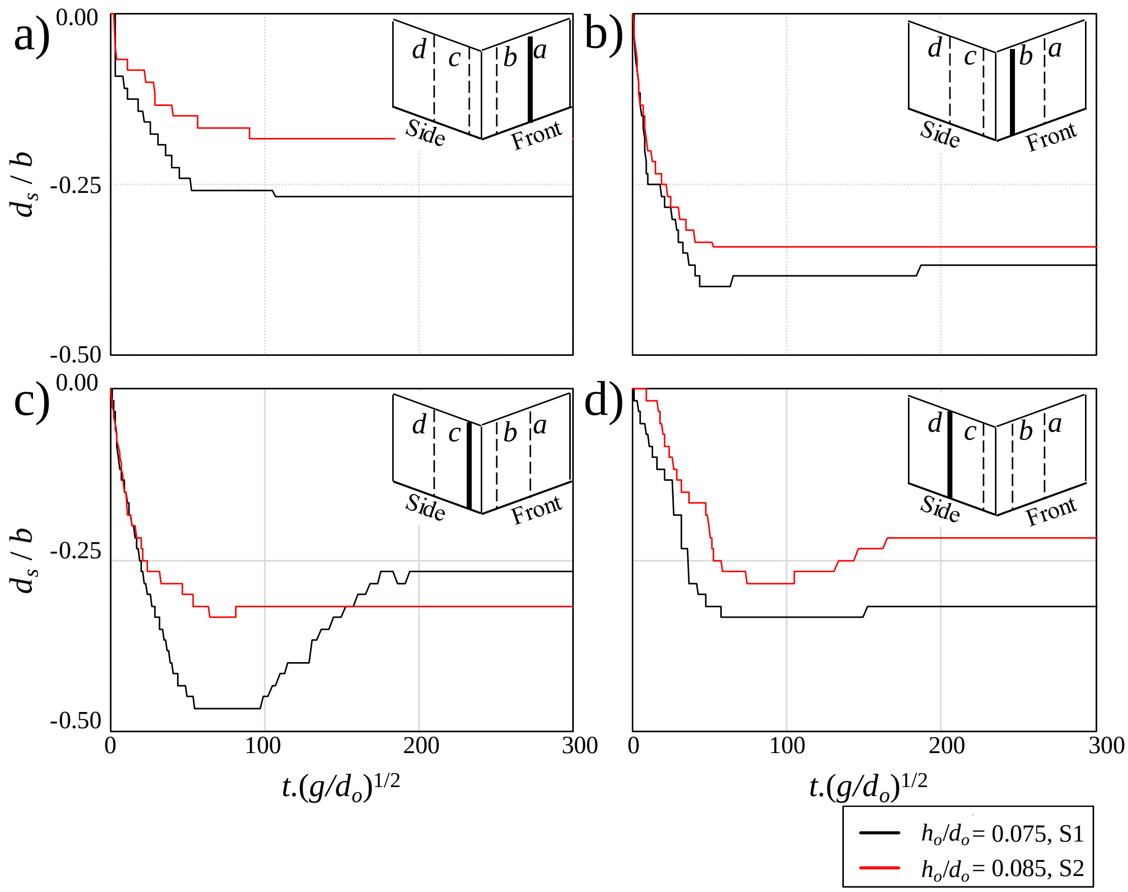

Figure 5-4. Effects of still to impoundment depth ratio h_o/d_o on variations of the normalized scour depth with normalized time for inclined beds; a) *a-a*; b) *b-b*; c) *c-c*; d) *d-d*.

Similar to the horizontal bed tests, the maximum scour depth formed at the two corners of the structural model (i.e., section *b-b* and section *c-c*). Figure 5-4a shows the variations of the normalized scour depth with time in the middle of the front wall of the structural model. Both tests shown in Figure 5-4 had the same initial still water depth (i.e., h_o = 0.03 m). Notably, the greater impoundment depth (Test S1) resulted in a deeper scour such that a 14.28% increase in impoundment depth increased the normalized maximum scour depth by 25%. As can be observed by comparing Figures 5-4a and 5-4b, the scour depth in the front corner of the structural model was substantially larger than at the middle front wall. The normalized maximum scour depth in

Test S1 was 60% deeper at the corner than the middle of the front wall. On the other hand, there was less difference in scour depths between Tests S1 and S2 at the front corner than that measured in the middle of the front wall. In addition, the time to reach the maximum scour depth in both Tests S1 and S2 was approximately the same in the front wall of the structural model ($t(g/d_o)^{1/2} \approx 100$), whereas it occurred earlier for Test S1 at the front corner of the structural model ($t(g/d_o)^{1/2} \approx 20$).

Figures 5-4c and 5-4d show the time histories of the normalized scour depths along the side wall of the structural model for the inclined bed tests. The time-histories of the scour depth development indicated substantially more bed erosion at the side wall than the front wall of the structural model. A noticeable difference was observed in the maximum normalized scour depth in the side corner of the model between Tests S1 and S2. This difference indicated the importance of the initial potential energy of turbulent bores in scour formation, as 14.3% increase in the impoundment depth (Test S1) increased the maximum normalized scour depth by approximately 30%. However, the equilibrium scour depth in Test S1 was approximately 15% less than that observed in Test S2 with a value of $d_s/b \approx -0.27$. The maximum normalized scour depth at the side corner (section *c*-*c*) was 30% higher than that measured at the front corner (section *b*-*b*) in Test S1. Such difference is attributed to the formation of eddies and horseshoe vortices in the side corner of the structural model. The remarkable bed level difference in section *c*-*c* indicated the effects of the considerable velocity fluctuation and pore pressure variations in this region as explained in part I of this companion paper.

Figure 5-4d shows the scour evolution along the side wall of the structural model. A noticeable scour depth difference was observed in the equilibrium state of inclined bed tests in which a 14.3% higher impoundment depth in Test S1 caused a 20% deeper maximum scour and 45% deeper equilibrium scour in section *d*-*d* compared to Test S2.

A comparison of the Tests H1 and S2, with relatively similar still-to-impoundment depth ratios of h_o/d_o = 0.1 and 0.085, respectively, indicated that the maximum normalized scour depths were larger in the front, corner, and the side walls in the horizontal bed tests by 2.5 times, 1.5 times, and 1.78 times, respectively. Since the loading time in the inclined bed tests was relatively shorter, the scour occurred earlier, the equilibrium time was shorter, and the turbulent bores formed scour with steeper slopes. Moreover, as a result of such a short loading time, the quasi-steady period of the flow commenced earlier and caused a faster sediment refill.

In order to acquire more information about the scour development and scour slope variations with time due to propagation of tsunami-like bores around the structural model, scour profiles were extracted from high-speed images and the results are plotted in Figures 5-5 and 5-6 for horizontal and inclined bed tests, respectively. The time evolution of the bed profiles in the front and side walls of the structural model for horizontal bed tests are shown in Figure 5-5.

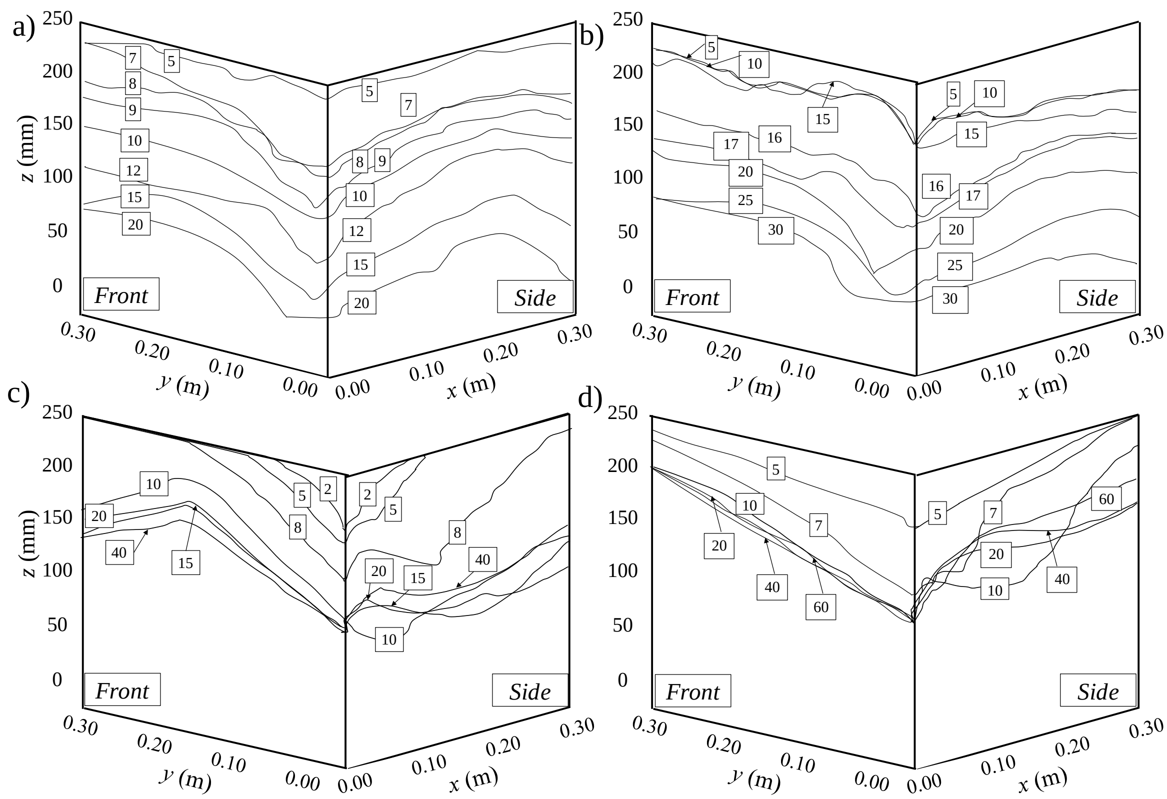

Figure 5-5. Variations of erosion profiles with time in front and side of the structural model for horizontal bed tests; a) ho/do = 0.1; b) ho/do = 0.12; c) ho/do = 0.25; d) ho/do = 0.28. The number in the box represents the time in second.

In this picture, the vertical axis is the bed level and the horizontal axis is the distance from the front corner of the structural model. The numbers on scour profiles indicate the time elapsed from the opening of the gate in seconds. Figures 5-5a and 5-5b show the scour profiles of supercritical bores (i.e., Tests H1 and H2). As Figure 5-5a shows, the scour initiated from the corner of the structural model and progressed towards the middle of the front and side walls. At each time interval, the front corner had a deeper scour than the side corner. Figure 5-5b shows the scour evolution for Test H2, which had 16.7% smaller impoundment depth than Test H1. As can be seen, the time to reach the maximum scour depth in Test H2 was 10 seconds later than in Test H1 (t_{max}

= 30 s). Moreover, the surrounding bed at the corner of the structural model was less eroded (~ 20%) in Test H2 in comparison with Test H1. Such a difference may be due to the lower initial potential energy of Test H2. As Figures 5-5a and 5-5b show, the maximum scour depth moved from the edge of the structural model towards the middle of the side wall.

Figures 5-5c and 5-5d show the evolution of scour depth in the subcritical flow regime for Tests H3 and H4, respectively. As shown in Figure 5-5c, the erosion initiated gradually from the front corner and moved to the middle of the side wall. The scour reached its maximum depth in 20 seconds and its equilibrium state in 40 seconds after the beginning of the test. Similar to Test H3, the local scour reached its maximum and equilibrium depths within 20 and 40 seconds from the beginning of the test in H4 in the side wall, respectively (Figure 5-5d). A comparison of Tests H1 and H4 indicated the effect of still water depth on time-histories of erosion profiles. It was found that the maximum scour depth was approximately 40% deeper at the front and side faces of the structural model in Test H1 than Test H4. The equilibrium time in Test H1 was considerably shorter than Test H4 with a time delay of 40 seconds.

Figure 5-6 shows the time history of erosion profiles in the front and side walls of the structural model for the supercritical bores propagating over the inclined bed.

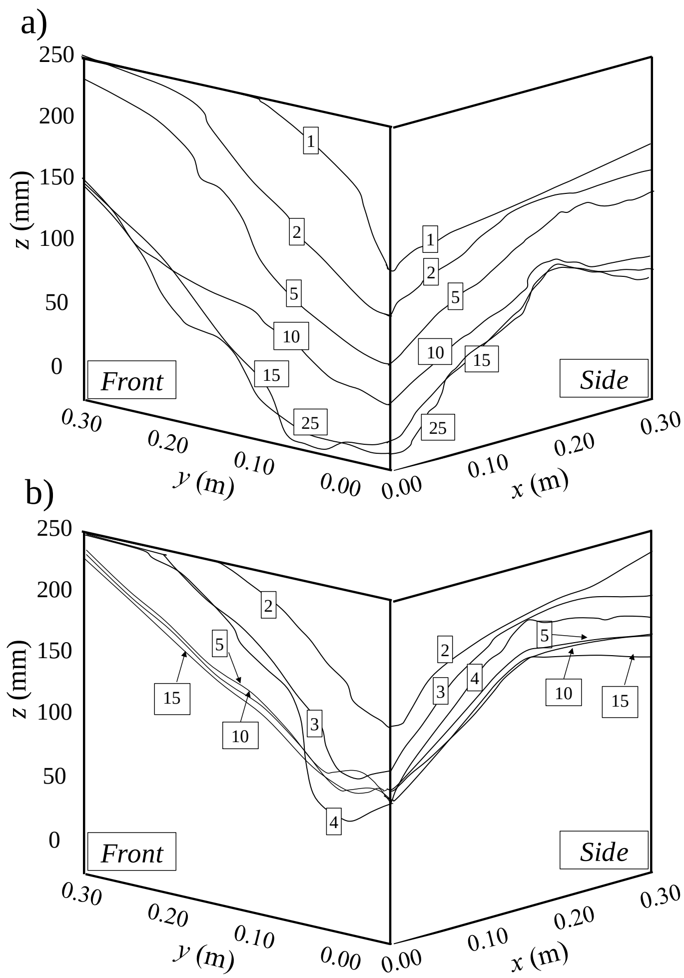

Figure 5-6. Variations of erosion profiles with time in front and side of the structural model for inclined bed tests; a) h_o/d_o = 0.075; b) h_o/d_o = 0.085; The number in the box represents the time in second.

Figure 5-6a presents the scour profiles of Test S1 with d_o = 0.4 m. The erosion occurred very quickly along both walls and continued until t = 25 s. The final maximum scour depth at the side wall of the structural model was approximately 50% deeper than the front wall, even though the maximum scour depth formed at the same time of t_{max} = 25 s. A comparison of the erosion profiles between Tests S2 and S1 indicated that Test S1 resulted into a deeper scour depth on both sides and the maximum scour depth occurred 10 s later (t_{max}=25 s) than the Test S2 (t_{max}=15 s).

A comparison of Figures 5-5a (Test H1) and 5-6b (Test S2) illustrates the effect of bed slope on the variations of scour profile with time. The scour at the both the front and side corners of the structure was deeper in Test H1 than Test S2. However, the equilibrium scour depth occurred earlier in the inclined bed test (t_e = 15 s) than the horizontal bed test (t_e = 20 s). Finally, the equilibrium scour hole was steeper at the front wall in the horizontal bed compared to that observed for tests on the inclined one, such that at the equilibrium state the maximum slope of the scour hole was 33° and 23° in the inclined bed and the horizontal bed, respectively.

The effects of still-to-impoundment depth ratio and bed slope on the variations of normalized maximum scour depth, d_{sm}, are shown in Figure 5-7.

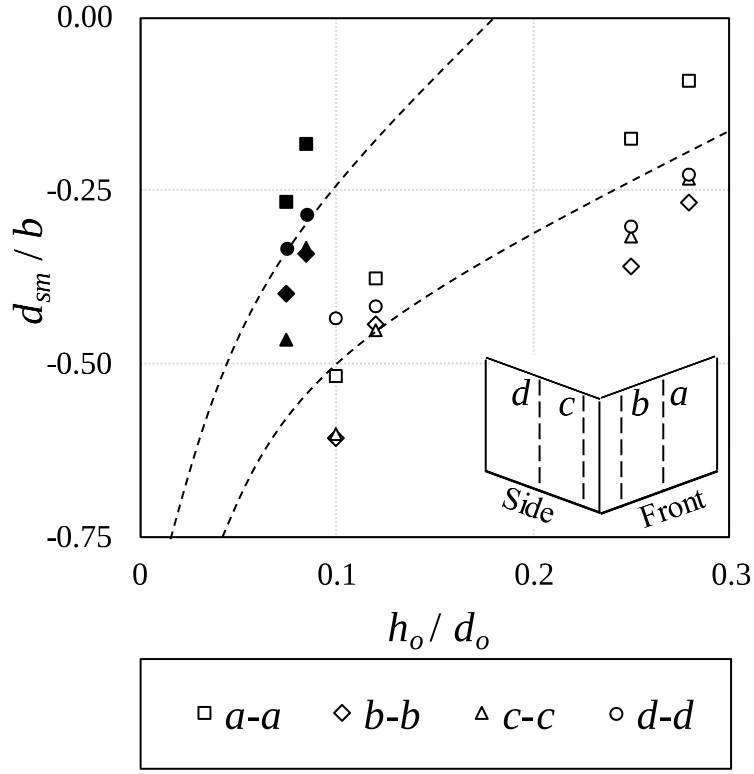

Figure 5-7. Effect of still to impoundment depth ratio h_o/d_o on normalized maximum scour depth around a structural model of width b. Open symbols representing scour depth in horizontal beds and solid symbols representing scour depth in inclined bed tests.

For instance, the ratio of $d_{sm}/b = –0.5$ indicates that the maximum scour depth is half of the model width. The variations of normalized maximum scour depth in the horizontal and inclined bed tests are represented by open and solid symbols, respectively. In general, as previously noted, greatest normalized scour depth occurred at the front and side corners (i.e., section *b-b* and *c-c*) while the least scour occurred at the middle front of the structural model (section *a-a*). Figure 5-7 demonstrates that the normalized erosion depth decreased with increasing the still-to-impoundment depth ratio. The following empirical formulations are proposed for the relation between the normalized maximum scour depth and h_o/d_o:

$$\frac{d_{sm}}{b} = 1.62\left(\frac{h_o}{d_o}\right) - 0.67 \tag{5-3}$$

$$\frac{d_{sm}}{b} = 11.25\left(\frac{h_o}{d_o}\right) - 1.21 \tag{5-4}$$

where Eq. (5-3) and (5-4) are developed for the horizontal and inclined bed tests, respectively. Application of Eq. (5-3) and (5-4) beyond the observed range of data should be exercised with caution.

Estimation of scour depth during a tsunami event is essential for a safe and economic design of foundations (Cheng et al., 2015). The ratio of equilibrium scour depth, $d_{s\infty}$, to the maximum scour depth, $d_{s(max)}$, can provide valuable information about the transient sediment transport induced by tsunami-like bores around a onshore building. This is particularly important given that post-event surveys record equilibrium scour, which is not necessarily maximum scour. The effects of still-to-impoundment depth ratios on $d_{s\infty}/d_{s(max)}$ are shown for both the horizontal and inclined bed tests in Figure 5-8 for the front, side, and corners of the structural model.

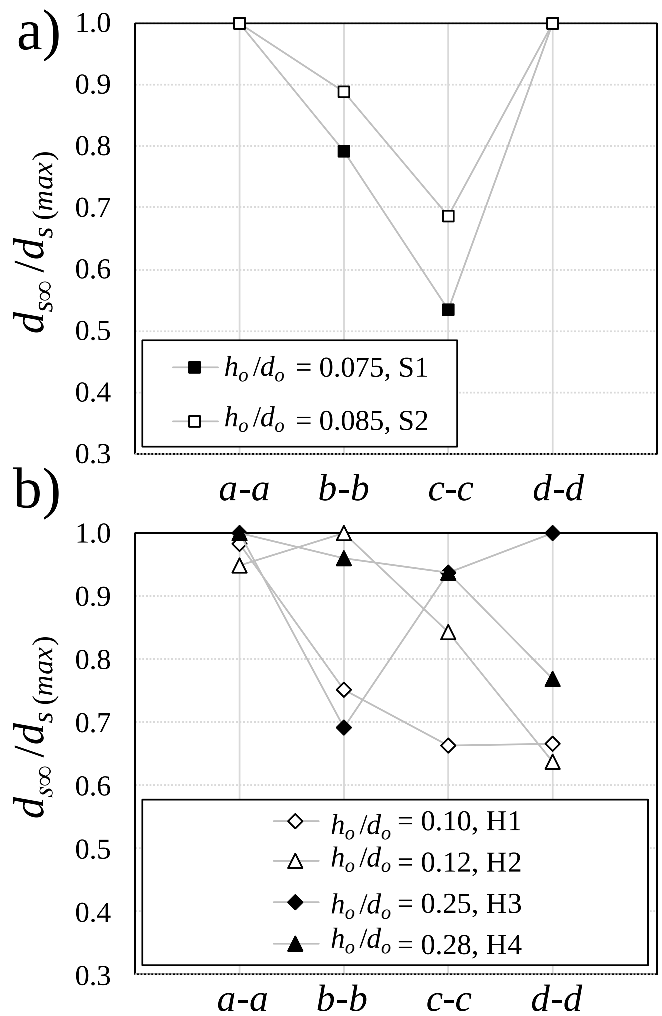

Figure 5-8. Variations of the ratio of the scour in equilibrium state $d_{s\infty}$ to the maximum scour $d_{s(max)}$ for sections *a-a*, *b-b*, *c-c*, and *d-d*: a) inclined bed; b) horizontal bed.

In the inclined bed tests (Figure 5-8a), the ratio of $d_{s\infty}/d_{s(max)}$ was equal to unity in sections *a-a* and *d-d* indicating that the sediment deposition process did not occur and the equilibrium scour depth was equal to the maximum scour depth. The maximum sediment deposition occurred in the side corner of structure (see section *c-c*) with an equilibrium scour value of 55% of the maximum scour depth for Test S1. A strong upward flow developed inside of the scour hole as it formed which resulted in considerable sediment suspension and acceleration in the scour process. Once the scour reached its maximum value, sediment suspension diminished as a result of the flow velocity decay, then all suspended sediments were deposited. During the period of upward flow acceleration and sediment suspension, the angle of the eroded bed temporally exceeded that of the sand's angle of repose (i.e., φ = 33°). Subsequently, as the upward flow decelerated, the unstable scour surface was stabilized (i.e., the bed angle reached the angle of repose) and re-deposition occurred.

Figure 5-8b shows $d_{s\infty}/d_{s(max)}$ as a function of h_o/d_o for the horizontal bed tests. The supercritical and subcritical bores are represented by open and solid symbols, respectively. In the supercritical bores, the minimum $d_{s\infty}/d_{s(max)}$ was found in the middle of the side wall of the structural model with a value of 0.65. This ratio increased from the middle of side wall to the middle of front wall. For example, the ratio of $d_{s\infty}/d_{s(max)}$ in Test H1 was around 0.65 in sections *c-c* and *d-d* and it increased to unity in section *a-a*. Such variations indicate the secondary deposition of the eroded bed in the side wall of the structural model. In the subcritical bores (i.e., Tests H3 and H4), $d_{s\infty}/d_{s(max)}$ equaled 1.0 at sections *a-a* and *d-d*, indicating no secondary deposition occurred at the middle faces of the structural model. Some secondary deposition occurred at the corners of the structural model, especially at section *b-b* for Test H3 (h_o/d_o = 0.25) with a value of $d_{s\infty}/d_{s(max)}$ = 0.7. The reason of this high secondary sediment deposition was the bed slope at that specific region (section *b-b*, Test H3). As the bed slope at the maximum scour depth stage was considerably higher than the angle of repose, bed slumping occurred, and the sediment filled the scour hole until the slope of the scour hole reached the sediment angle of repose.

To exclusively study the effects of bed slope, Tests S2 and H1 which had approximately the same h_o/d_o (i.e., 0.085 and 0.1, respectively) were compared. It was found that the maximum sediment deposition occurred at the side corner of the structure in both tests with a small difference of $d_{s\infty}/d_{s(max)}$ = 0.05. However, in the middle of side wall (i.e., section *d-d*) the inclined bed tests did not exhibit sediment deposition in comparison with horizontal bed tests.

In addition to the maximum and equilibrium scour depths, scour rate provides useful information on the erosion process around coastal structures during a tsunami event. The erosion rates were obtained by calculating the rate of change of scour depth with time (i.e., $u_s = d_s/dt$). The erosion rates were extracted using the high-speed images for various still-to-impoundment depth ratios, h_o/d_o, for both horizontal and inclined bed tests.

Figure 5-9a shows that, for the same hydrodynamic forcing conditions, the scour rate was noticeably smaller for the case of the inclined bed tests compared to the horizontal bed tests at the middle of both the front and side walls.

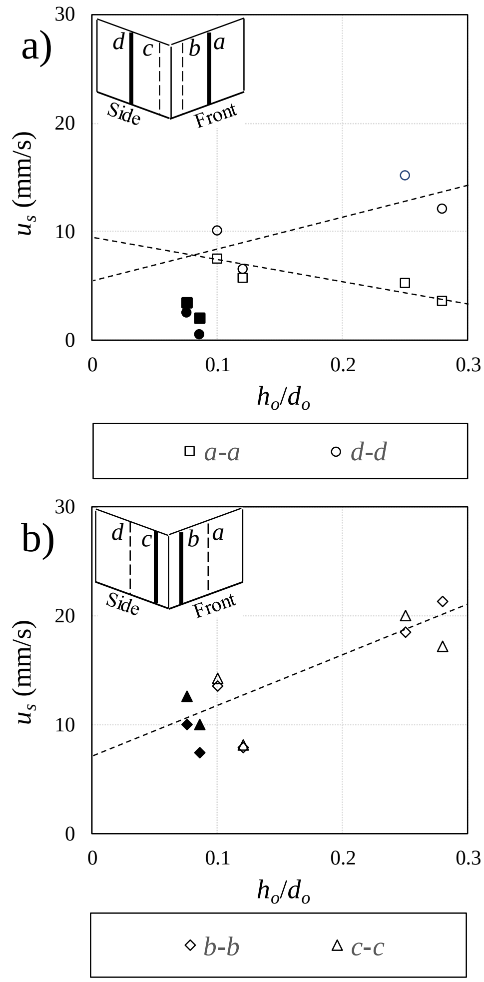

Figure 5-9. Effect of still to impoundment depth ratio on the erosion rate around a structural model of width *b*, a) front and side faces, b) front and side corners. Open symbols belong to the horizontal tests and solid symbols belong to the incline tests

For the inclined bed tests, increasing the impoundment depth by 14.3% (i.e., Test S1 vs. S2) increased the erosion rate in the front and side walls of the model by 1.5 times. It is noteworthy to mention that the side wall scour rate was less than the front wall in the inclined bed tests, whereas the opposite was observed in the horizontal bed tests. For the horizontal bed tests, the scour rate increased with increasing h_o/d_o in the middle of the side wall (section *d-d*), but the scour rate decreased with increasing h_o/d_o in the middle of the front wall (section *a-a*). In other words, the front wall eroded relatively slowly in the subcritical regime than the supercritical regime. Subcritical Test H4 resulted in 50% lower scour rate in the front wall and 30% higher scour rate in the side wall than supercritical Test H1 (Test H4 had still water depth 2.33 times greater than Test H1).

Figure 5-9b shows the variations of erosion rate at the corner of the structural model for both the horizontal and inclined bed tests. The erosion rate was found to be higher in the subcritical regime compared to the case of supercritical flows. As shown in Figure 5-9b, the side corner of the structural model experienced a slightly higher erosion rate than that observed at the front corner.

For the tests with a constant still water depth and different impoundment depths (Test H2 vs. Test H1), the erosion rate decreased by approximately 50% at the corners as the impoundment depth decreased by approximately 17%. A comparison of the erosion rate at the corner of the structural model between Tests H1 and H4 indicated that increasing the still water depth by 2.33 times increased the erosion rate on average by 40%. For inclined bed tests, increasing the impoundment depth by 14.3% (i.e., Test S1) increased the erosion rate at both corners (section *b-b* and section *c-c*) by approximately 30%. A comparison of Tests H1 and S2 showed that 5% increase in the bed slope decreased the erosion rate of the middle of front and side walls and the corner of the structural model by 70%, 90%, and 36%, respectively.

5.3.2 Application of the Shields parameter

The prediction of the onset of sediment motion during a tsunami inundation event can improve understanding of the erosion mechanism and scour formation. Sediment motion initiates once the shear force exerted by the hydraulic bore exceeds the bed particle resistance to entrainment. The force imbalance that stimulates sediment motion can be correlated with particle Reynolds number ($Re_p = u_* d_{50}/\upsilon$) where u_* is the shear velocity and ν is the kinematic viscosity. In this study, the values of Re_p were calculated based on the peak flow velocity in the beginning of the sand section. The incipient motion of uniformly distributed sand bed by uniform flow can be predicted by correlating the Shields parameter θ with particle Reynolds number Re_p (Shields, 1936). The Shields parameter, θ, modified to account for excess pore pressure gradient in the soil ($\Delta P_e/\Delta z$) and formulated as a function of the flow velocity, u, and sediment mean particle diameter, d_{50}, is (Yeh and Mason, 2014; Tonkin et al., 2003):

$$\theta = \frac{\tau(1-n)}{d_{50}[g(\rho_s - \rho_w) + \frac{\Delta P_e}{\Delta z}]} \tag{5-5}$$

where, τ is the bed shear stress, g is the gravitational acceleration, ρ_s is the density of sand, n is soil porosity, ρ_w is the density of water, d_{50} is mean particle diameter. In this study, the excess pore pressure gradient was calculated between second and third-row tensiometers installed in the middle of the front face of the structural model as long as they were under soil surface.

The bed shear stress is estimated as $\tau = (f/8)\rho u^2$, where f is Darcy friction with the value of 0.018 for sand with a median diameter of 0.5 mm and u is flow velocity (Van Rijn, 2013; Yeh and Mason, 2014).

The initiation of sediment motion occurs if $\theta \geq \theta_c$ where the critical Shields parameter, θ_c, was reported as a constant value of 0.045 (Lamb et al., 2008; Miller et al., 1977) and for fully rough turbulent flows, θ_c is in the range of $0.03 \leq \theta_c \leq 0.06$ (Chanson, 2004). The critical Shields numbers and Shields formula were modified for prediction of sediment motion for inclined beds by considering the angle of repose of sediments and bed slope (Julien, 1995; Damgaard, 1997; Chanson, 2004). An empirical formulation modiffied by considering the angle of repose was proposed for prediction of θ_c for horizontal surfaces as follows (Bohorquez et al., 2008; Julien, 1995; Chanson, 2004):

$$\theta_c = \begin{cases} 0.5\tan\varphi & for \quad d_* \langle 0.3 \\ 0.25 d_*^{-0.6}\tan\varphi & for \quad 0.3 \langle d_* \langle 19 \\ 0.013 d_*^{0.4}\tan\varphi & for \quad 19 \langle d_* \langle 50 \\ 0.06\tan\varphi & for \quad 50 \langle d_* \end{cases} \tag{5-6}$$

where $d_* = (d_{50}[(s-1)g]/v^2)^{1/3}$, $s = \rho_s/\rho_w$, and v is the kinematic viscosity with a value of 10^{-6} m^2/s. The critical shear stress was modified again by applying the effect of bed slope as follows (Bohorquez et al., 2008; Damgaard, 1997):

$$\theta_c{}' = \frac{\sin(\varphi - \alpha)}{\sin\varphi}\theta_c \tag{7}$$

where, α is the bed slope and, φ is the angle of repose. In the present study, the values of d_*, θ_c', φ, and θ_c were 13, 0.92, 33°, and 0.037, respectively.

The values describing the variations of critical Shields stress θ_c with particle Reynolds number Re_p for both horizontal and inclined bed tests were calculated from Eqs. (5-7) and the boundary describing the range of parameters are plotted in Figure 5-10.

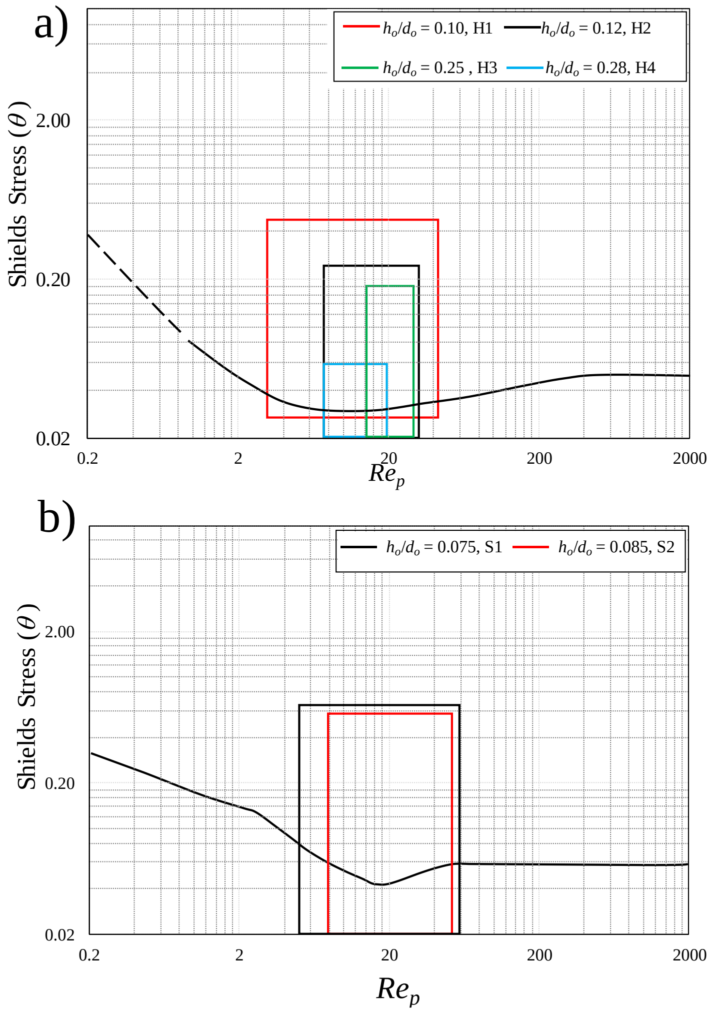

Figure 5-10. Boundary of Shields stress versus particle Reynolds number for turbulent bores: a) for horizontal bed tests; b) for inclined bed tests.

The erosion process initiates when the critical Shields stress exceeds the Shields threshold curve (Shields, 1936; Julien, 1995; Kiraga and Popek, 2019). The Shields stresses and particle Reynolds numbers in this study varied with time. Such time variations of θ_c and Re_p were calculated by employing the maximum and minimum flow velocities for each test.

Figure 5-10a shows the boundaries of Shields stress and particle Reynolds number for the horizontal bed tests. As it can be seen, the ranges of particle Reynolds numbers and Shields stresses were wider in the supercritical regime than the subcritical one. This indicated a higher possibility of early erosion in the supercritical regimes as confirmed in Figure 5-3. The boundaries of the Shields stress versus the particle Reynolds number for the inclined bed tests are shown in Figure 5-10b. It is noticeable that for the inclined bed tests, the Shields threshold curve is significantly lower than that of horizontal bed tests. The difference was attributed to the effect of bed slope which caused an early occurrence of erosion in the inclined bed tests (see Eq. (5-7)). This early initiation of scour can be verified by comparing Figures 5-3 and 5-4. At all four sections around the model, the scour occurred $t.(g/d_o)^{1/2} = 20$ earlier in inclined bed tests.

The variations of Shields parameter with time have been used in the past for better understanding and prediction of scour initiation and its magnitude (Tonkin et al., 2003). Time-histories of the particle Reynolds number and of the Shields parameter were calculated for the front wall of the structural model and for both horizontal and inclined bed tests. Figure 5-11 shows the effect of h_o/d_o on the time histories of Shields parameter and particle Reynolds number for horizontal bed tests.

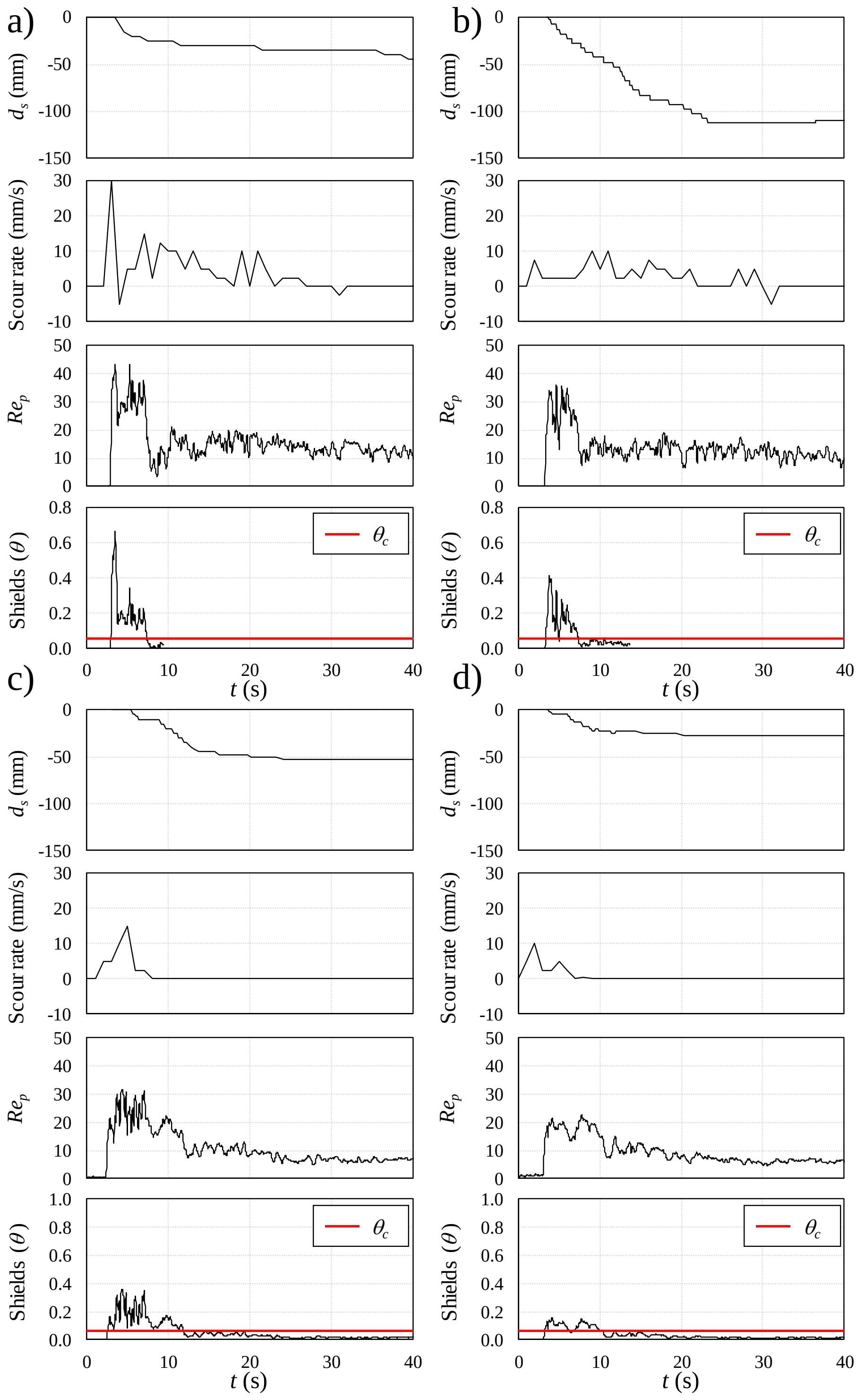

Figure 5-11. Time series of scour, scour rate, Shields parameter, and particle Reynolds number in front of a structural model and generated by propagation of hydraulic bores over a horizontal bed: a) $h_o/d_o = 0.1$, b) $h_o/d_o = 0.12$ c) $h_o/d_o = 0.25$, a) $h_o/d_o = 0.28$.

The time histories of scour depth and scour rate (d_s/dt) were added for better comparison. The relation between the Shields parameter and scour rate in the supercritical bores are shown in Figures 5-11a and 5-11b and the time-histories Shields were truncated in these two sub-plots when the second-row tensiometer became exposed to the flowing bore. As shown in Figure 5-11a, the Shields and particle Reynolds numbers reached their maximum value within the first 10 seconds from the beginning of the test due to a sudden increase in the flow velocity. Such a high velocity justified the highest scour rate observed within the same time period. The first peak in the Shields plot occurred approximately within the first 3 seconds, and almost one second after this peak the maximum scour rate was observed as the hydraulic bore hit the structural model. The second peak in the Shields number occurred after approximately 2 seconds from the first peak.

The time histories of Shields number in Figures 5-11a and 5-11b show that the Shields values were mostly above the critical Shields number for the first 10 s of the experiments. This observation concurs with the trends in the time histories of the scour rate and the scour depth evolution for the first 10 s of the measurements.

The effect of the 20% higher impoundment water depth in Test H1 than Test H2 on the sediment erosion process stems from comparing Figures 5-11a and 5-11b. The maximum Shields numbers occurred approximately at the same time for both Tests H1 and H2, but the maximum Shields value in Tests H1 was approximately 70% larger than the Test H2. The 70% higher Shields value in Test H1 resulted in scour depth and scour rate increase by approximately 50% and 2 times, respectively (see Figure 5-3a).

Figures 5-11c and 5-11d show the time history of particle Reynolds number and Shields parameter for the subcritical bores. The first peak in the time history of Shields parameter occurred at approximately 4 seconds after the gate opening in Figure 5-11c. A sudden rise in the scour rate was observed by the arrival of the runup. Such a sudden increase in the scour rate indicated the initiation of erosion process. The second peak in the time history of Shields number occurred after 8 seconds from the beginning of the test and the scour depth became constant after the third peak at $t \approx 13$ s. For higher still-to-impoundment depth ratios (Figure 5-11d), the Shields number reached its maximum at the same time as in Test H3; however the maximum value decreased by almost 50% since the impoundment depth was 12.5% less in Test H4. This reduction significantly impacted the scour rate and scour depth between Tests H3 and H4. The values of Shields numbers were considerably smaller in the subcritical bores which resulted in a smaller scour rate and scour depths. For instance, a comparison of tests H4 and H1 with approximately the same impoundment depth and having 2.33 times deeper still water in test H4 caused 70% and 67% reduction in the maximum Shields number and scour depth, respectively (see Figures 5-11a and 5-11d).

Figure 5-12 shows the variations of particle Reynolds number and Shields numbers with time for the inclined bed tests.

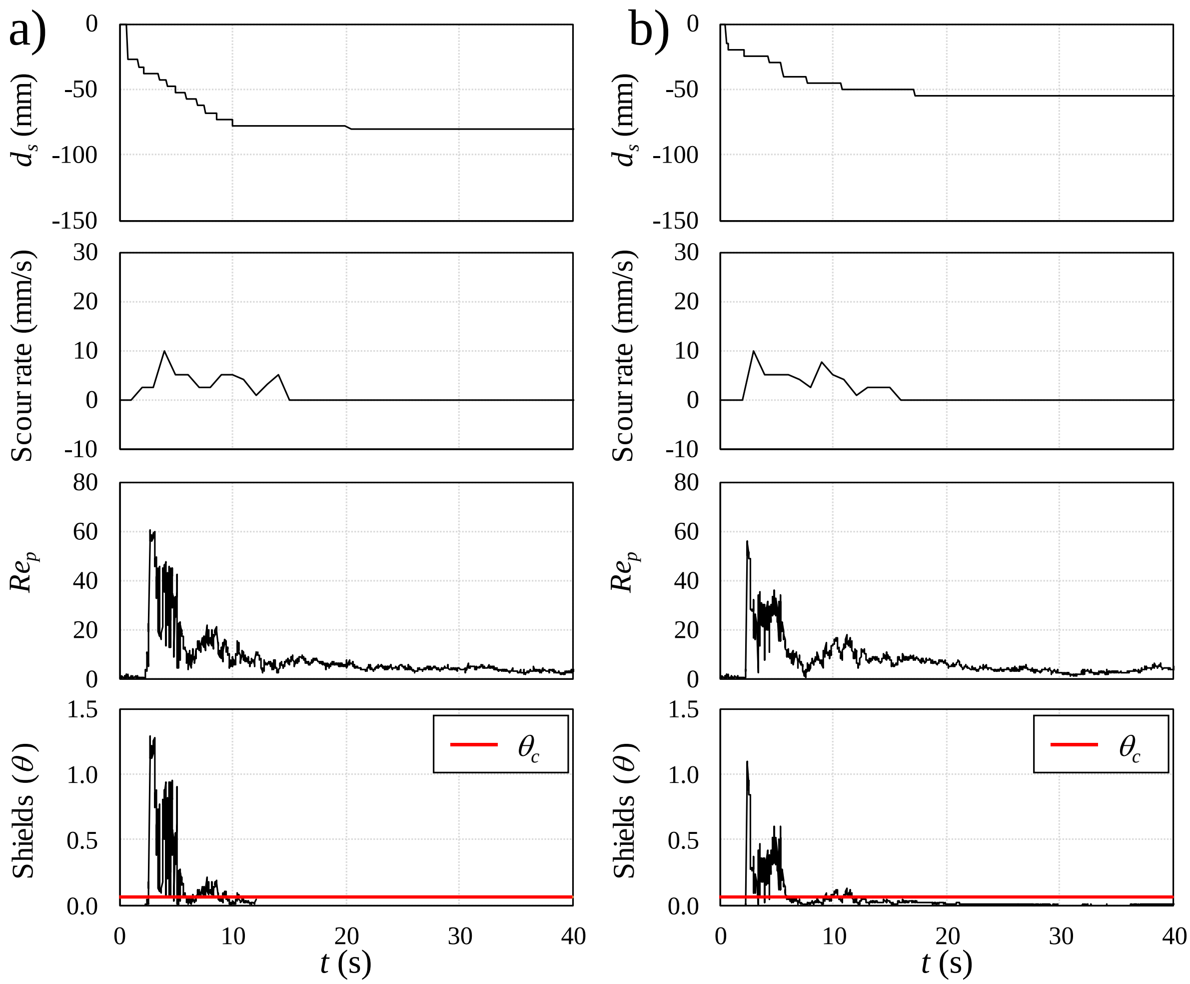

Figure 5-12. Time series of scour, scour rate, Shields parameter, and particle Reynolds number in front of a structural model and generated by the propagation of hydraulic bores over an inclined bed: a) $h_o/d_o = 0.075$, b) $h_o/d_o = 0.085$.

Since loading time was relatively shorter for the inclined bed tests, the initiation of sediment erosion occurred sooner after the beginning of the tests. Figure 5-12a shows the variations Shields parameter with time for Test S1 with an impoundment depth of 0.4 m. In this test, the Shields parameter, scour rate, and the particle Reynolds number reached their maximum value of 1.3, 10, and 60, respectively, after approximately 4 seconds from the beginning of the experiment. However, bed scour occurred slightly earlier at $t \approx 3$ s when the bore front hit the front wall of the structural model. The Shields parameter and, in sync, the scour rate increased when the first and the second runup hit the structural model. The second peak in Shields diagram was 30% smaller than the first one. The scour gradually decreased over the subsequent 10 seconds and it stopped at $t \approx 14$ s from the beginning of test when $\theta = \theta_c$ at the same time with the second-row tensiometer exposure to the flowing bore.

A comparison of Figures 5-12a and 5-12b shows the effect of impoundment depth on variations of particle Reynolds number and Shields parameter for the inclined bed tests. The impoundment depth in Test S2 was 12.5% smaller than that for Test S1; this resulted in an 18% smaller maximum Shields number. Further, at around 13 s, the Shields numbers became less than the critical Shields number which is also reflected in the time histories of scour rate and scour depth as they both stopped changing after about 13 seconds.

The influence of bed slope on the variations of Shields parameter was studied by comparing the time histories of Shields parameter in Figures 5-11a and 5-12b. Tests H1 and S2 had approximately similar still-to-impoundment depth ratios, but different bed slopes. A comparison of the time histories of Shields number indicated one major peak in Test S2 with 60% higher maximum value in comparison with Test H1. The peak in Shields number lasted about 2 seconds and it reduced the scour time by 10 s in Test S2 in comparison with Test H1. The value of critical Shields number in Test S2 was smaller than Test H1 due to the effect of bed slope and this caused earlier initiation of scour formation in Test S2 (i.e., nearly 4 seconds).

To observe the coupling interaction between scour depth evolution and pore pressure propagation in the soil versus various h_o/d_o, the scour depth is normalized with respect to the pore pressure induced head. Figure 5-13 shows scour depth normalized by the maximum value of pore pressure occurred at the bottom-center tensiometer for most cases, both taken at the time of maximum pore pressure and plotted as a function of still-to-impoundment water depth ratios.

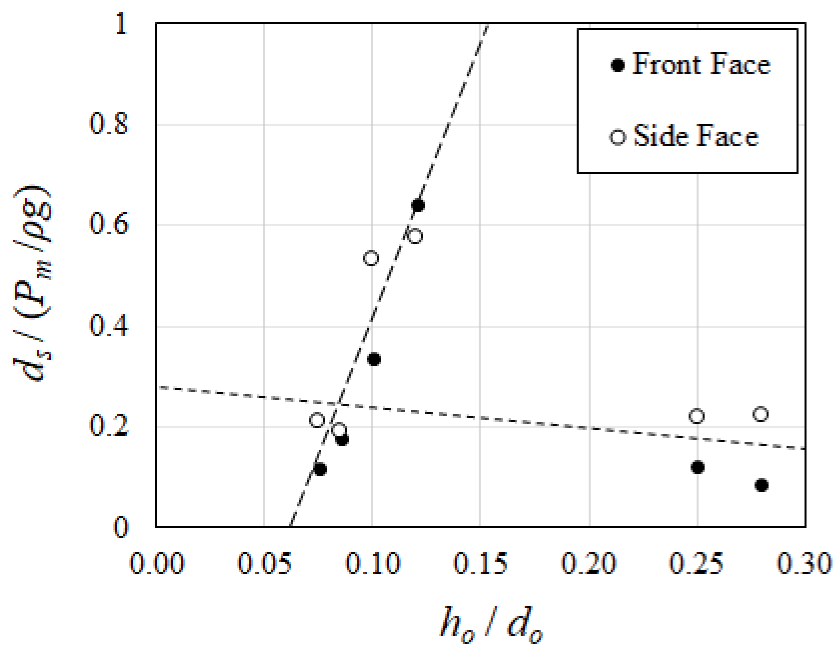

Figure 5-13. Scour depth normalized by pore pressure, as a function of still-to-impoundment water depth ratio, for both horizontal and inclined bed tests

Data collected at both the middle front (solid symbols) and middle side (open symbols) of the structural model are shown for both horizontal and inclined bed tests. A linear correlation is evident between scour depth normalized by peak pressure versus h_o/d_o, for the supercritical bores flowing over the inclined bed ($h_o/d_o \leq 0.2$) and the following fitted relation was derived accordingly:

$$\left(\frac{d_s}{\left(\frac{P_m}{\rho g}\right)}\right) = 10.53\left(\frac{h_o}{d_o}\right) - 0.63 \tag{5-8}$$

where P_m is maximum pore pressure, ρ is the fluid density, g is gravitational acceleration, d_s is corresponding scour depth, h_o is still water depth, and d_o is impoundment depth. Albeit much weaker due to paucity of data, another linear model is proposed for sub- and supercritical bores for the case of the horizontal bed tests (Eq. (5-9)) as:

$$\left(\frac{d_s}{\left(\frac{P_m}{\rho g}\right)}\right) = -0.43\left(\frac{h_o}{d_o}\right) + 0.28 \tag{5-9}$$

5.4 Summary and conclusion

A series of laboratory experiments were conducted to study the effects of different still-to-impoundment depth ratios h_o/d_o and bed slopes on time histories of the scour depth evolution and erosion rate induced by hydrodynamic loading around a square-shaped structural model. The spatio-temporal scour evolution was recorded along the front and side walls and the corner of the structural model. The employed hydraulic bores were classified into sub- and supercritical regimes with a threshold of $h_o/d_o = 0.2$. In general, it was found that, regardless of bed slope and different still-to-impoundment depth ratios, the deepest scour holes formed at the front corners of the structure. On average, the sub- and supercritical bores generated respectively 1.4 and 1.8 times larger scour depths at the side of the structural model than at the front wall. A considerable amount of sediment deposition was observed in the side corner and along side wall of the model during the equilibrium stage for both the horizontal and inclined tests. For instance, due to this sediment deposition the normalized maximum scour depth decreased by 35% and 20% in the side corner and side wall of the model in Test H4. On the other hand, the erosion rates in the inclined bed tests were almost the same at the front and side walls, whereas in the horizontal bed tests, the erosion rate at the side wall was much larger than at the front wall.

A comparison of the time histories of the scour depth normalized by the structure width showed an inverse relation between the maximum normalized scour depth and still-to-impoundment depth ratio. For instance, in the horizontal bed tests, as the still-to-impoundment depth ratio increased by 20% in the supercritical bores (i.e., H1 versus H2), the maximum normalized scour depth around the model decreased on average by 30%. Moreover, for the subcritical bores (i.e., H3 versus H4), the maximum normalized scour depth increased on average 15% around the model as impoundment depth increased by 14.28%. The time to reach the peak scour depth was found to be correlated with flow regime and the supercritical bores reached the peak scour depth later than the subcritical bores. For instance, the scour depth reached the peak value in the middle of the front wall at $130 < t(g/d_o)^{1/2} < 140$ in the supercritical bores and at $105 < t(g/d_o)^{1/2} < 110$ for the subcritical bores.

On the other hand, for the horizontal bed tests, a 2.33 times increase in the still water depth caused on average 67% decrease in the erosion rate around the model in Test H4 compared to Test H1. Moreover, the history of Shields number was also impacted by the increase in the impoundment depth height. For instance, for Test H1 and Test S1, with 20% and 14.3% greater impoundment depths than Tests H2 and S2, the maximum Shields number was 1.5 times and 16% larger, respectively.

The effect of bed slope on scour evolution around the structural model was studied by comparing similar tsunami loadings for both horizontal and inclined beds. It was found that, for the same hydrodynamic loading conditions, for the horizontal bed tests, the maximum scour depths around the structure normalized by the structure width were on average 2 times larger than those observed for the inclined bed tests. Moreover, regardless of bed slope, the maximum sedimentation observed in the corner of the model was larger rather than that observed at the other faces.

The erosion rate also affected by increasing the bed slope. It was observed that the erosion rate was on average 65% smaller around the structural model for the inclined bed tests than the horizontal ones. In addition, the maximum Shields number in the inclined bed test (i.e., Test S2) was 20% larger than the corresponding values in the horizontal bed (i.e., Test H1).

Chapter 6. Experimental investigations on relation among dam-break bores induced excess pore pressure, liquefaction, effective normal stress, and scour evolution around a rigid structure

The article is in review in …………………………………………..

6.1 Introduction

Many coastal areas around the world are prone to natural hazards including earthquake-induced tsunamis and strong surges in which the scour induced by such natural hazards have a potential to damage the inshore infrastructures. Some post-tsunami field investigations categorized the soil types in the affected areas into four distinct groups of saturated, poorly graded, fine graded, and alluvial sands (Abdollahi et al., 2017). During an earthquake incident, all soil types are highly vulnerable to earthquake-induced liquefaction due to water level rise and the force loading on the coastal areas (Abdollahi et al., 2017). On the other hand, the complex flow associated with tsunami bores results in excessive sediment transport and mixing in coastal regions (Chinnarasri et al., 2013). Therefore, the perception of interactions between highly unsteady and turbulent tsunami waves with the soil surrounding coastal infrastructures is vital to study soil instability and determine soil protection measures (Abdollahi et al., 2017). The 2011 Tohoku Tsunami was triggered due to a strong earthquake that caused tsunami waves with a runup height of approximately 10 m. Many large scour holes were observed around the onshore structures after the Tohoku Tsunami. In some cases, the scour holes were expanded far away from the structures (Hatogai et al., 2012; Iiboshi et al., 2014; Iiboshi et al., 2015).

Soil liquefaction occurrs in loose sand deposits with a relatively shallow groundwater level. The liquefaction can facilitate erosion by reducing soil particles' bearing capacity as unsteady bores passing around the structures (Mioduszewski and Maeno, 2003). The field surveys after the Tohoku Tsunami showed the effect of soil liquefaction on the affected coastal areas such as the Kanto region. However, due to the destructive impacts of the triggered tsunami bores in the Tohoku area, it was unlikely to track the liquefied regions (Abdollahi et al., 2017). Soil liquefaction was detected in a large area after the incidence of the 2018 Indonesia Tsunami. This tsunami was generated by an earthquake with a 7.5 magnitude and the tsunami waves caused extensive soil liquefaction in the affected coastal regions. The conducted field survey in Palu Bay showed liquefaction induced erosion and sedimentation in this region (Sassa and Takagawa, 2019). A part of the liquefaction induced scour took place around the foundation of a residential building in Palu Bay as shown in Figure 6-1.

Figure 6-1: Image of local bed erosion around a residential building due to the 2018 Indonesia tsunami in Palu Bay. (Courtesy of Jacob Stolle, 2018).

Two different loading mechanisms cause soil liquefaction induced by tsunami waves. When an earthquake takes place, the downward normal stress increases inside the soil element and soil compaction occurs. After soil restructuring, the excess pore pressure decreases gradually and liquefaction occurs. The magnitude and strength of the built-up liquefaction are a function of the soil's hydraulic conductivity and disconductivity due to the soil layering (Lowe, 1975). The total pore pressure consists of hydrostatic, P_h, and excess pore pressure, P_e. It is important to study the variations of excess pore pressure as it tolerates the water table variations in the soil (Terzaghi, 1943). In the beginning of each experiment and right before bores arrival, the soil particles around the structure model slightly swell which causes suction in this area. Moreover, pore pressure development in soil particles takes place slower than the propagation of instantaneous hydrostatic pressure, which also leads to negative excess pore pressure (Craig, 2004). As surface water penetrates through the voids, the excess pore pressure increases and reaches zero. In other words, in the final stage, the total pore pressure would be equal to the hydrostatic pore pressure (Craig, 2004).

Before the earthquake-induced excess pore pressure is entirely dissipated as tsunami bores reach the coastlines, the combination of excess pore pressure due to both tsunami passage and remained pore pressure in the quiescent phase plays an important role in soil liquefaction potential (Abdollahi and Mason, 2019). During the pressurizing stage (i.e., runup), the soil layers underneath the wave peaks are compressed over time and prevent the pore pressure to increase. Whereas in the depressurizing stage (i.e., after the passage of the runup) the pore pressure propagates therough the soil, the excess pore pressure propagates upward, and makes the soil particles unstable (Sumer, 2014).

The successive motions of runup and drawdown in sloping shorelines cause liquefaction failure. During the wave shoaling stage, when the bore breaks and runup forms, the excess pore pressure rises faster as a tsunami wave propagates over a sloping bed. This is due to the fast loading time in comparison with the drainage time of the excess pore pressure. Such variations in excess pore pressure can be associated with the soil liquefaction (Mioduszewski and Maeno, 2003) which emphasis the importance of investigating the occurrence of soil liquefaction. During the drawdown phase, the excess pore pressure diminishes the effective normal stress within sand particles and causes soil liquefaction which enhances erosion in coastal regions (Young et al., 2009).

The effect of tsunami-like waves on variations of excess pore pressure and soil liquefaction has been studied in the past (Yeh and Mason, 2014). Mioduszewski and Maeno (2003) performed experimental investigations to study soil liquefaction and scour hole development in an inclined bed with a slope of 1:500. A sediment section was located in the middle of the flume and it was filled with 1.28 mm sand particles. A spur was attached to the right wall of the flume and twenty pressure sensors were installed with increments of 0.03 m and 0.05 m from the middle and the edge of the structure. Two initially constant impoundment depths of d_o = 0.2 m and 0.3 m were used and surges were generated by opening a gate located at the end of the channel. It was found that a 50% increase in the impoundment depth increased the magnitude of excess pore pressure by 50% and reduced the liquefaction time by approximately 25%. The maximum scour depth and scour duration were also correlated with the impoundment depth. It was found that a 50% increase in the impoundment depth increased the maximum scour depth by 30% and decreased the start and end time of the scouring process by 30% and 20%, respectively (Mioduszewski and Maeno, 2003).

The effect of excess pore pressure on scour depths around a cylinder was experimentally investigated on an inclined bed with a 5% upslope (Tonkin et al., 2003). The sediment section was installed downstream of the reservoir with a constant still water depth of 2.45±0.2 m. The sand bed section was filled with 0.35 mm well-graded sand particles. The Plexiglas cylinder had 0.5 m diameter and was installed at the center of the sediment section. A series of solitary waves with two different depths of 2.45 m and 2.65 m were propagated towards the cylinder. A scour enhancement parameter (Λ) was defined based on the pore pressure and it was found that increasing the wave height by 45% increased scour enhancement parameter by 16.67% and scour depth by 4.17% (Tonkin et al., 2003). The Tonkin's experimental results were used to validate the numerical investigation by Pan and Huang (2012). A direct relation was found between sediment suspension, soil liquefaction, and pore pressure gradient (Pan and Huang, 2012).

The effects of bed slope on soil liquefaction were numerically studied on a sandy beach model with a mean sand diameter of d_{50} = 0.21 mm and two different slopes of 1:5 and 1:15 were considered. The flume had an initial water level, h_o, of 1 m and waves were generating using a piston installed 12 m far from the sediment section. The results showed that the depth of liquified area increased and its width decreased with increasing the bed slope (Young et al., 2009).

Takegawa et al. (2018) studied the effect of soil liquefaction and local erosion with the soil depth. Two different flow rates of 0.5 and 1.0 L/s were tested and a sediment section with the mean particle diameter of 0.3 mm was used. Scour evolution was observed in a saturated sediment section. The liquefaction was controlled by varying the water depth difference between the reservoir and the sediment section. It was found that the excess pore pressure increased by 0.15 kN/m^2 as the soil depth increased by 0.1 m and the relation was linear. The effect of liquefaction on the local scour was analyzed by correlating hydraulic gradient with scour depth. In case of the flow rate with magnitude of 1.0 L/s, the analyis of data indicated that as the hydraulic gradient increased by 4 times, the scour length increased by 17% and the maximum scour depth and scour area decreased both by 18% after 60 sec (Takegawa et al., 2018).

Most laboratory experiments in the past used solitary waves to study the effects of hydrodynamic loadings on the soil liquefaction and variations of the effective normal stress during wave runup and drawdown. However, the scaling up studies have shown that the solitary waves resembled the wind waves rather than the tsunami waves (Larsen et al., 2018). Hydraulic bores generated by a dam-break mechanism have shown better hydrodynamic consistency with the field observations of tsunami bores (Chanson, 2006). A visual comparison of the images of the 2004 Indian Tsunami bores with inland propagation of a dam-break bore over a dry bed indicated that the triggered dam-break bore had an acceptable agreement with the tsunami bores (Chanson, 2006). Many researchers have used dam-break model in their experimental studies to generate tsunami waves (Liu et al., 2017; Stolle et al., 2018; Häfen et al., 2018).

The present experimental study aims at investigating the effects of hydrodynamic loading such as impoundment and still water depths and bed slope on soil liquefaction mechanism and local scour around the foundation of coastal structures. To understand the key parameters on soil liquefaction under the influence of different tsunami loads, the time histories of excess pore pressure, effective normal stress, and scour depth around a square shape structural model were extracted from pore pressure data. Then, the results were linked with the time history of bed surface elevation around the structural model. The outcomes of the present study, based on a more realistic tsunami wave model improve the accuracy of the standards and useful for a proper design of coastal structures.

6-2 Material and Methods

6-2-1 Experimental setup

Dam-break bores with a scale 1:40 were produced in the Hydraulic Laboratory at the University of Ottawa, Canada. Laboratory experiments were conducted in a 30 m long, 1.5 m wide, and 0.8 m deep flume. Six different still-to-impoundment depth ratios, h_o/d_o, ranging from 0.075 to 0.28 were tested. The dam-break bores propagated over a sand bed section with horizontal and inclined bed slopes of +5%. Four tests were performed over a horizontal bed (i.e., H series) and two tests were run over an inclined bed with 5% upslope (i.e., S series). For the inclined bed tests the flow had only the supercritical condition with $h_o/d_o \leq 0.2$. The experimental parameters in this study are shown in Table 1.

Table 6-1: Experimental parameters of the performed tests.

Test number	Slope (%)	d_o (m)	h_o (m)	h_o/d_o	Time (s) / F_r Range
H1	0	0.3	0.03	0.1	$2.85<t<50$
					$0.44< Fr <1.98$
H2	0	0.25	0.03	0.12	$3.26<t<50$
					$0.42< Fr <1.67$
H3	0	0.4	0.1	0.25	$3.03<t<50$
					$0.15< Fr <0.64$
H4	0	0.35	0.1	0.28	$3.50<t<50$
					$0.18< Fr <0.99$
S1	5	0.4	0.03	0.075	$2.63<t<50$
					$0.10< Fr <4.20$
S2	5	0.35	0.03	0.085	$2.33<t<50$
					$0.08< Fr <4.00$

A pump filled up a 20.55 m long reservoir with water to set different impoundment depths, d_o, for each test. A swing gate was installed between the reservoir and the experimental section. The dam-break bores were generated by rapidly opening the gate, and then the impounded water was released to the experimental section. A non-dimensional parameter can determine the suitability of the gate removal speed by comparing the gate removal time with the threshold time, T_o, as introduced by Lauber and Hager (1988) (i.e., $T_o = t_o(g/d_o)^{0.5} = 2^{0.5} \approx 1.41$), where t_o is a measured gate opening time, g is the gravitational acceleration, and d_o is impoundment depth. Stolle et al. (2018) showed a linear c orrelation between the dimensionless gate opening time, T_o, and impoundment water depth as $T_o = 1.47–1.19d_o$. The non-dimensional gate removal times in this study ranged between 0.97 and 1.18 indicating that the gate was removed in a sufficiently rapid motion.

A concrete false floor was located downstream of the swing gate and it covered with a 0.2 m x 0.2 m mesh to track the front bore locations (see Figure 6-2a). A gabion section was installed between the concrete floor and sand bed section to prevent abrupt erosion. The gabion was 1.5 m long, 0.2 m wide, and 0.2 m deep and it consisted of a wireframe filled with coarse gravel with a mean particle diameter of 30 mm. A Plexiglas square structural model with 0.3 m x 0.3 m dimensions was installed at the center of the saturated sediment section (see Figure 6-2b). The sand-bed section was 3.15 m long, 1.5 m wide, and 0.2 m deep and filled with noncohesive and well-graded sand particles with a mean particle diameter d_{50} = 0.5 mm. A thin layer of gravel particles with a mean diameter of 10 mm was placed underneath of the sand and a thin layer of geotextile sheet was placed between the gravel layer and sand particles. The geotextile and gravel bed layers mitigated sediment suspension. A false floor was set after the sediment section to provide a framework for it. A vertical aluminum sharp-crested weir was installed at the end of the flume to set different still water depths, h_o. The sediments were trapped in an adjustable box of 1.32 m long, 0.76 m wide, and 1.43 m high. The trap was located after the weir and inside the sump and it was covered with a layer of geotextile sheet.

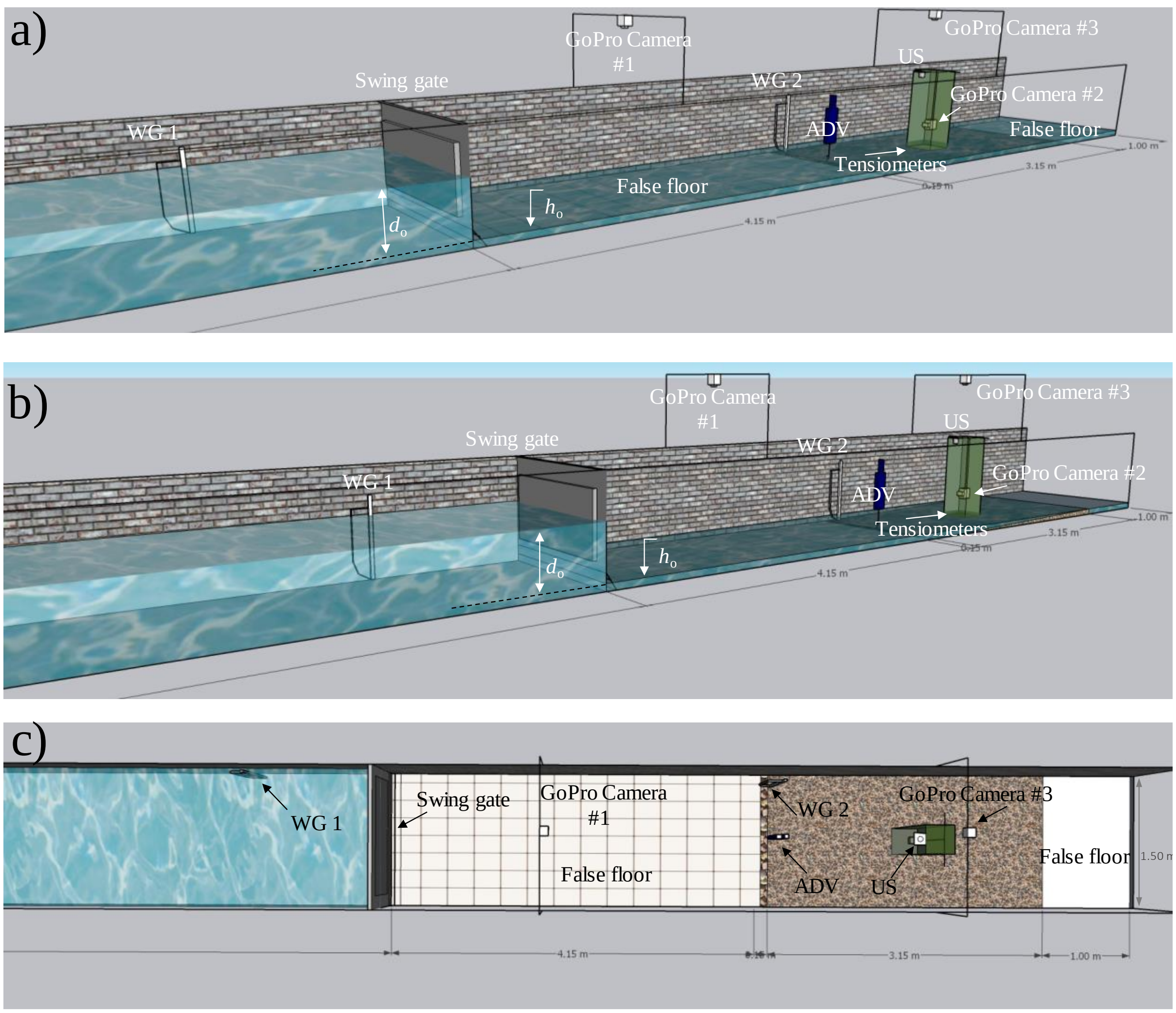

Figure 6-2. Experimental setup, instrumentation, and adopted coordinate system: a) side view, horizontal bed; b) side view, inclined bed; c) top view.

6-2-2 Instrumentation

The time histories of water surface elevations were recorded by two capacitance-type wave gauges (RBR WG-50, NRC, Ottawa, Canada) with an accuracy range of ± 0.4% and a measuring range of 0.5 m. The first wave gauge (WG1) was located 1 m upstream of the gate and the second wave gauge (WG2) was located 4.30 m downstream of the swing gate and at the beginning of the sand section (see Figure 6-2c). A side-looking head Acoustic Doppler Velocimeter (ADV) probe (Nortek Vectrino, Vangkroken, Norway) was installed 1 m aside from WG2 to record the time history of flow velocity (see Figure 6-2c). The ADV probe was installed to record the maximum velocity of 2.5 m/s with a measurement accuracy of ± 1%. The sampling volume and the frequency of the ADV probe were selected as 45×10^{-7} m^3 and 200 Hz, respectively. The flow velocity in this experimental study captured at a distance of 0.07 m from the bed surface and at the beginning of the sand bed section. Aluminum oxide seeding particles with an average diameter of 27 microns were mixed with the impounded water to improve signal detection and ensure reaching an adequate signal-to-noise ratio (SNR) of 15.

An ultrasonic sensor (US; MASSA, M-5000/220, Massachusetts, USA) was installed on the top of the structure's front face and 5.87 m from the swing gate to record the time history of runup heights. The ultrasonic sensor had a measuring resolution of 0.25 mm and an electronic signal frequency of 220 kHz. The sampling frequency of the sensor was set to 1200 Hz to accurately detect the maximum runup height. The time history of the spatial variations of bed level was recorded using a GoPro camera with an internal memory and a power supply (GoPro-Hero5, San Mateo, CA, US). The wireless camera has a shutter speed of 60 frames per second and was installed inside the Plexiglas structural model to record the erosion in the front and side walls of the structural model.

The time history of pore pressure was recorded by nine tensiometers (Micro Tensiometer Transducer Probe Assemblies, SDEC 220, Reignac sur Indre, France) that were installed with a distance of 70 mm apart. The tensiometers were located in the front wall of the model in both horizontal and vertical directions. The tensiometers had a 2-mm ceramic probe tip and 20 mm probe length. A 90-degree clockwise rotation of the model in the vertical axis enabled us to record the time histories of pore pressure in the side wall of the structural model under the same experimental conditions. The upper row of tensiometers was installed exactly below the bed surface in horizontal bed tests. Due to the 5% upslope in inclined bed tests, the top row of tensiometers was located 0.08 m below the soil surface.

6-2-3 Data acquisition procedure

The synchronization process was arranged by connecting the probes with two Data Acquisition Boards (DAQ) NI USB-6009 with 16 channels and NI USB-6210 with 8 channels (National Instruments Corporation, Austin, Texas, US) with an input voltage range of ±10 Volts. The collected digital signals from instruments were processed using Labview software (National Instrument, Austin, Texas, US). A virtual instrument subroutines (VIS) was complied on the Labview software to synchronize the instrument.

6-3 Results and Discussion

The total pore pressure, P_t, was recorded by tensiometers and the excess pore pressure, P_e, was calculated by subtracting the instantaneous hydrostatic pressure, P_h, from the total pore pressure (Atkinson, 2017) as:

$$P_e = P_t - P_h \tag{6-1}$$

The time history of excess pore pressure, P_e, in horizontal bed tests and for both sub- and supercritical flows are shown in Figure 6-3.

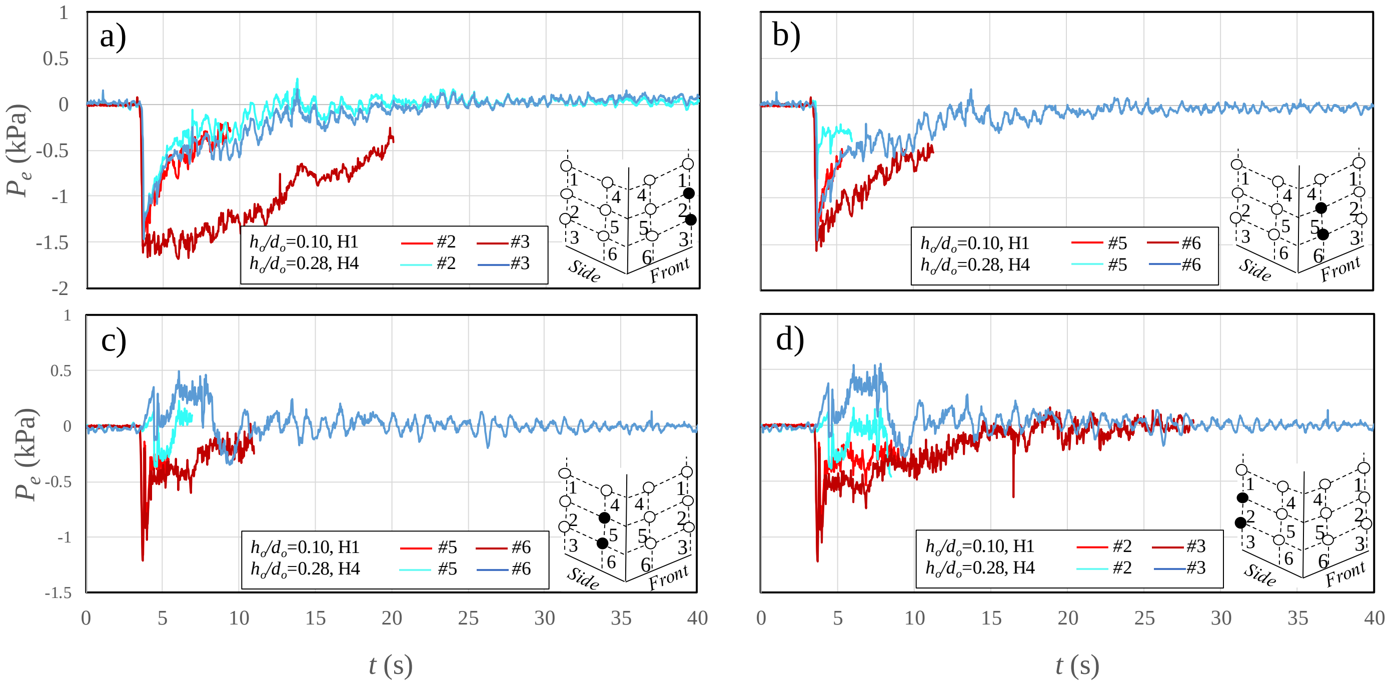

Figure 6-3: Variations of the excess pore pressure, P_e, with time, t, around the structural model for horizontal bed tests: a) middle of the front wall, b) corner of the front wall; c) corner of the side wall; d) middle of the side wall.

The total pore pressure in the soil section varied with time due to variations of the instantaneous hydrostatic pressure above the sand bed, hence, the excess pore pressure can be both positive and negative during bore propagation. Figures 6-3a and 6-3b show the time histories of excess pore pressure in the second and the third rows of tensiometers located in the middle and the corner of the front wall of the model, respectively. The first row of tensiometers was exposed to the flowing water a few seconds after the bore arrival. As can be seen in Figure 6-3a, the excess pore pressures in both depths are negative. The negative excess pore pressure indicates that the variations of total pore pressure developed within the sand and around the structural model are slower than the instantaneous hydrostatic pressure with time. In the middle of the front face (see Figure 6-3a), the negative excess pore pressures are significantly larger in tensiometer #3 than tensiometer #2 and it occurred for a longer time. The excess pore pressure was truncated when the tensiometer exposed to the bore at 20 seconds after the bore arrival. After exposure, the excess pore pressure reached the quasi-steady state condition for the rest of the tensiometers in the front wall of the structure model. The magnitude of the peak negative excess pore pressure was found to be independent of the flow regime and the tensiometers' depth.

Figure 6-3b shows the time history of excess pore pressures in the front corner of the structural model. Similar to the middle of the front wall, the negative excess pore pressures in supercritical flow were truncated due to exposure to the flow after 10 s. The tensiometer near the bed (i.e., tensiometer #6) showed greater excess pore pressure for a longer time in comparison with the rest of the tensiometers. As can be seen in Figure 6-3b, all tensiometers recorded the same maximum negative excess pore pressure. It is noteworthy to point out that the magnitude of the maximum negative excess pore pressure in the front face of the structure is independent of the flow regime, dam-break bore depths, and the depth of tensiometers and it is approximately equal –1.5 kPa.

Figures 6-3c and 6-3d show the variations of excess pore pressure in the corner and middle of the side wall of the structural model, respectively. As can be seen in the subcritical bore (i.e., Test H4), the maximum excess pore pressures were positive in all tensiometers. Such a positive excess pore pressure may be attributed to the soil-structure interaction. Soil particles are subjected to the water pressure and the lateral pressure due to soil-structure interactions. Laboratory experiments indicated that the soil-structure interactions extend up to two times of the structural model diameter (Zhu et al., 2018). As a result, in the side wall of the model, the hydrodynamic pressure is accumulated faster than the pore pressure which resulted in a positive excess pore pressure. For subcritical bores, the peak pore pressures were recorded by the bottom tensiometers and it was 50% greater than the peak pore pressure in the second-row tensiometers. A comparison of data presented in Figures 6-3c and 6-3d shows that the magnitudes of the maximum excess pore pressures and their corresponding time in supercritical bores were independent of tensiometers' location. However, in the side wall of the model and in the subcritical flow, the peak maximum pore pressure in the third-row of tensiometers was on average four times greater than the second-row tensiometers.

Figure 6-4 shows the time history of excess pore pressure for the inclined bed tests.

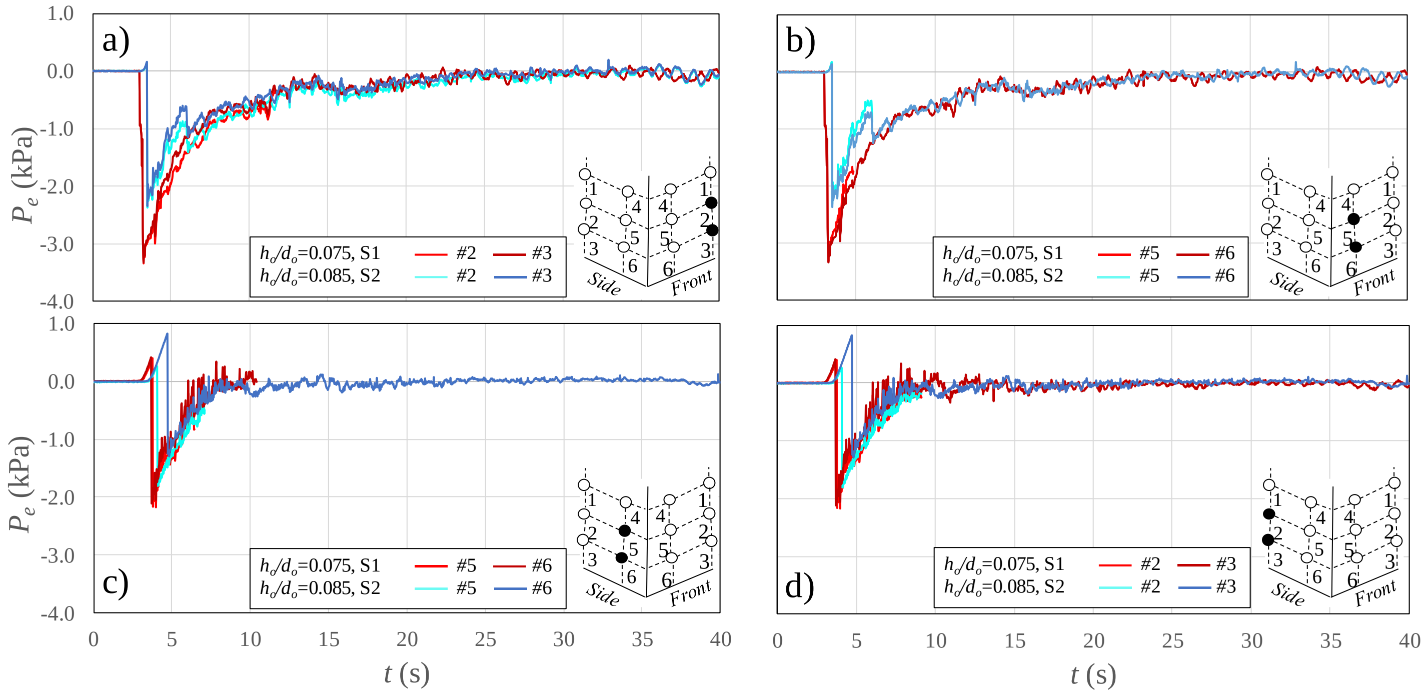

Figure 6-4: Variations of the excess pore pressure, P_e, with time, t, around the structural model for inclined bed tests: a) middle of the front wall, b) corner of the front wall; c) corner of the side wall; d) middle of the side wall.

Figures 6-4a and 6-4b show the time variations of the excess pore pressure in the middle and the corner of the front wall of the structure model, respectively. As can be seen, Test S1 with 14.28% greater reservoir depth than Test S2 had on average 43.5% larger peak excess pore pressure in both middle and corner of the front wall of the structure model. However, a comparison of the time histories of excess pore pressures in the front wall in each test shows that the maximum values of the excess pore pressure were independent of the depth of tensiometers.

Figures 6-4c and 6-4d show the time histories of excess pore pressure at the corner and in the middle of the model's side wall, respectively. As it is shown, both Tests S1 and S2 have positive excess pore pressure which are similar to the corresponding horizontal bed tests. The positive excess pore pressure may be due to the soil-structure interactions. Test S1 with 14.28% greater impoundment depth than Test S2 has 40% greater positive excess pore pressure and it occurred approximately two seconds earlier in Test S1. The maximum excess pore pressure in the front wall of Test S1 was on average 46% greater than the side wall of the structural model. Moreover, the negative excess pore pressure lasted approximately 15 seconds longer in the front wall than the model's side wall.

The effect of bed slope on variations of excess pore pressure can be evaluated by comparing the results of Tests H1 and S2 (Figures 6-3a and 6-3b with Figures 6-4a and 6-4b). Both tests have approximately the same still-to-impoundment depth ratio of 0.1 and 0.085. The maximum excess pore pressure around the structure model increased by two times as the bed slope increased by +5%. At each face of the structure model the values of pore pressure and the time to peak pressure were independent of the depth of tensiometers and flow orientation to the model. However, the greater negative excess pore pressure took place in the inclined bed test and it lasted 10 seconds less than the horizontal bed test. The negative excess pore pressures diminished right after the peak in inclined bed tests. Figure 6-4 shows that the maximum time duration of the excess pore pressure in inclined bed tests was approximately 20 s (i.e., in the front face) indicating the short loading time in inclined bed tests. Similar to Test H1, the maximum negative excess pore pressure in the side wall of the structural model in Test S2 was on average 40% smaller than the maximum pore pressure in the front wall of the structure model. This indicates the faster pore pressure accumulation in the front wall of the model in comparison with the side wall. A comparison of the peak bore depths in Tests H1 and S2 (Rajaie et al., 2019) emphasizes the effect of bore depth on the soil-structure interactions. The maximum bore depth in Test S2 is approximately 30% larger than the Test H1 which resulted in interaction between soil and structure and reflected in the positive excess pore pressure which not seen in Test H1. These results was also observed in the study of Zhu et al. (2018).

The simultaneous interactions between pore pressure and scour depth can be examined by studying the effective normal stress described as (Kato et al., 2000):

$$\sigma_x = \sigma_{vo} - (P_t - P_h) \tag{2}$$

$$\sigma_{vo} = \gamma_{sat} h_s \tag{3}$$

where σ_{vo} is the normal stress due to the soil depth, γ_{sat} is the specific weight of saturated soil, h_s is soil depth. For $\sigma_x = 0$, the initial normal stress, σ_{vo}, is equal to the excess pore pressure. The case in which $\sigma_x = 0$ does not necessarily indicates soil liquefaction, however, at this stage the surrounding soil particles are about to move (Kato et al., 2000). Figure 6-5 presents the normal and bed shear stresses that is applied on the soil element.

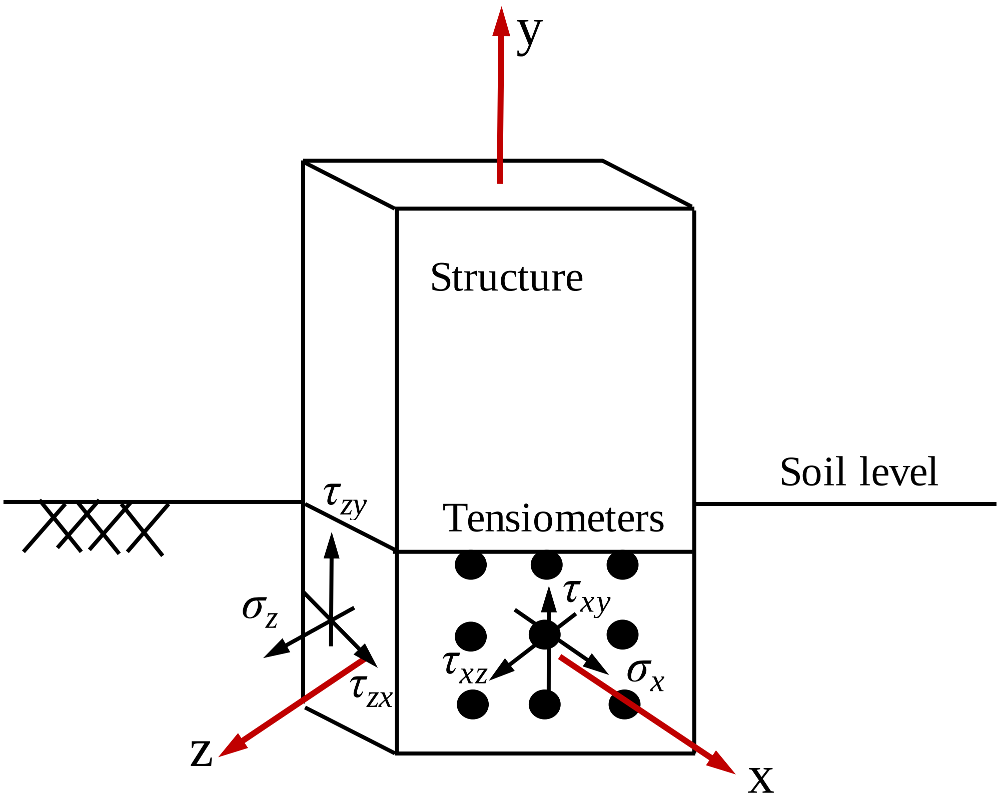

Figure 6-5: Schematic sketch showing the normal and shear stresses applied on a soil element.

The time histories of effective normal stress around the structure model and for horizontal bed tests are shown in Figure 6-6.

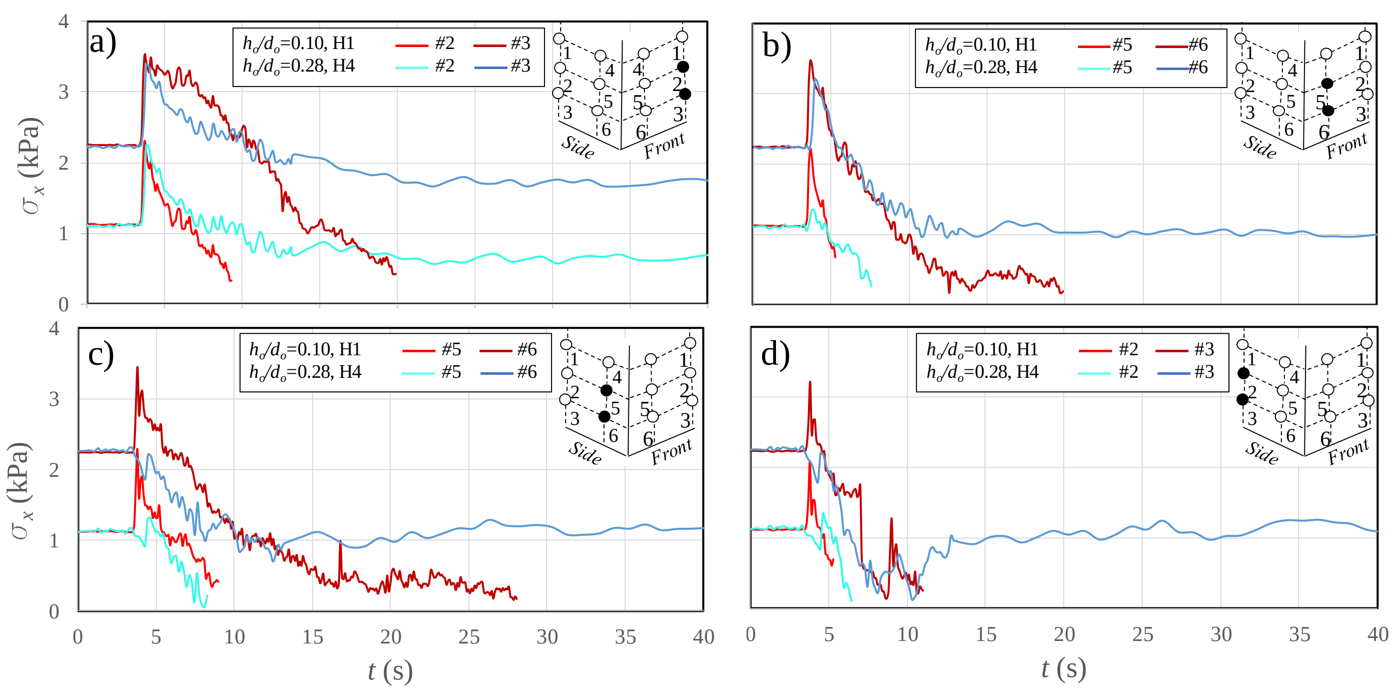

Figure 6-6: Variations of the effective normal stress, σ_x, with time around the structural model and for horizontal bed tests c) the middle of the front wall, d) corner of the front wall; e) corner of the side wall; f) middle of the side wall.

The time histories of scour depth (see Figures 6-S1a and 6-S1b) around the model are also included to study the relation between the effective normal stresses and scour depths. The two dash lines in Figure 6-S1 represent the locations of the second and third rows of the tensiometers. Figures 6-6a and 6-6b show the time histories of the effective normal stress in the inshore side (i.e., front wall) of the structure model. As it is shown, the effective normal stress increased abruptly when hydraulic bores reached the front wall. At the same time, the excess pore pressures also reached their maximum negative values (see Figures 6-3a and 6-3b). In addition, Figures 6-S1a and 6-S1b show that the erosion process started once the effective normal stress diminished suddenly.

The bottom tensiometers (i.e., tensiometers #3 or #6) presented 60% greater peak effective normal stress than the second-row tensiometers (i.e., #2 or #5) and the results were independent of the flow regime (see Figures 6-6a and 6-6b). The normal stress approached zero at the same time that the soil level reached the corresponding tensiometer. In the front face of Test H1 (see section *a-a* in Figure 6-S1a), the sand bed was eroded to the same level as tensiometers #2 and #3 at approximately 9 s and 20 s after the gate removal, respectively. At the same time, the effective normal stress approached zero. The effect of still water depth on effective normal stress was studied by comparing Tests H1 and H4. It should be noted that the still water depth in Test H4 is 2.33 times larger than Test H1. As can be seen Figure 6-6a, the scour propagated gently in Test H4 and did not reach the tensiometer #2. This is due to the fact that the higher still water depth diminished the impingement impact of the advancing bore. As a result, the effective normal stress in the middle of the front wall did not reach zero at the level of tensiometer #2.

Figures 6-6c and 6-6d show the time histories of effective normal stress in the corner and the middle of the side wall of the structural model, respectively. The impact of flow regime on the effective normal stress can be evaluated by comparing the maximum effective normal stress in tensiometer #5 for tests H1 and H4. As can be seen in Figure 6-7c, the peak effective normal stress in supercritical bores (i.e., Test H1) was 83% larger than the subcritical bores (i.e., Test H4). The effects of tensiometer’s orientation on the effective normal stress in subcritical bores (i.e., Test H4) are evaluated by comparing the time histories of the effective normal stress in tensiometer #3 (see Figure 6-6c and 6-6d). The peak effective normal stress in the front wall of the structure model was on average 40% higher than the side wall. Part of that that difference is due to the fact that the front wall experienced greater bore heights which resulted in greater pore pressure inside the soil section and less scour. Furthermore, sedimentation in subcritical bores affects the variations of effective normal stress in the middle and the corner of the side wall of the structure model. For instance, the effective normal stress in tensiometers #3 and #6 of Test #4 increased after around 12s (see Figure 6-6c and 6-6d) as the scour hole in the middle and the corner of the side wall was gradually refilled in sections *c-c* and *d-d* (see Figure 6-S1b).

The expression for the effective normal stress (i.e., Eq. (2)) can be modified to calculate the effective normal stress in inclined beds by considering the slope angle, α (Atkinson, 2017) as:

$$\sigma_x = (\sigma_{vo} + (p_t - p_h)) \times \cos^2 \alpha \tag{4}$$

The slope angle in this study is 2.86°. Figures 6-7a and 6-7b show the time histories of the effective normal stress in the middle and corner walls of the structure model, respectively.

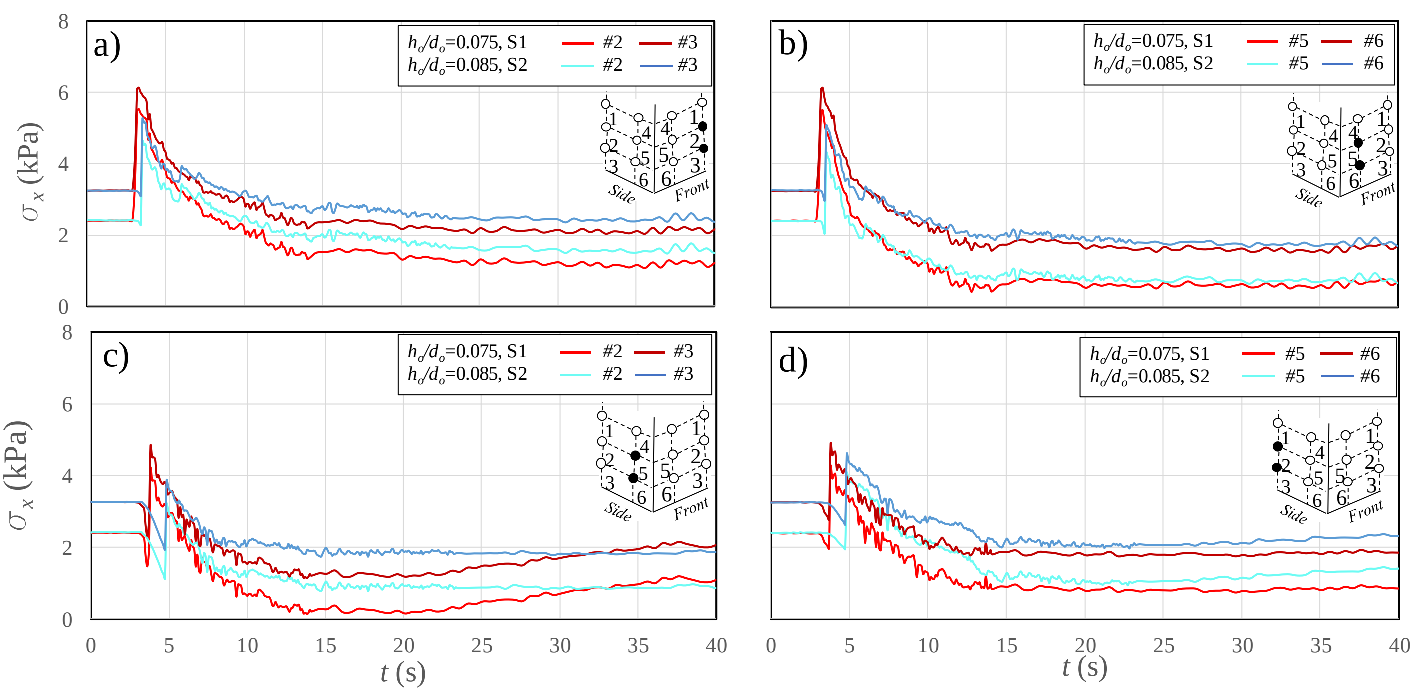

Figure 6-7: Variations of the effective normal stress, σ_x, with time around the structural model and for inclined bed tests: a) at the middle of the front wall, b) corner of the front wall; c) the corner of the side wall; d) middle of the side wall.

As can be seen in Figure 6-7a, the effective normal stress in the front wall of the model increased abruptly once the bore reached the structure model and a few seconds after the sudden stress raise the scour process initiated in the front wall (see section *a-a* in Figure 6-S2). The initiation of sediment erosion coincides with the reduction in the effective normal stress.

The impoundment depth in Test S1 was 14.28% higher than the Test S2 which resulted in 10% higher peak effective normal stress in tensiometer #3 in comparison with the peak effective normal stress in the same tensiometer depth in Test S2 (see Figure 6-7a). Moreover, the effective normal stress was affected by the depth of tensiometers and the third-row tensiometers had on average 10% larger normal stress than the second-row tensiometers. Although the effective normal stresses, σ_x, in the middle and corner of the front wall started with the same values; however, at the equilibrium stage, σ_x was on average 35% higher in the middle of the front wall than the corner. Such difference is reflected to the greater final scour as final scour depth in the corner of the front wall was approximately 40% greater than the middle of the front wall due to less effective normal stress and more soil stability.

Figures 6-7c and 6-7d show the time histories of effective normal stress in the corner and middle of the side wall of the structure model, respectively. Similar to the front wall, the effective normal stress was affected by the bore height. The peak effective normal stress in the side corner of the structure model in Test S1 was on average 25% higher than the Test S2 which is due to 14.28% higher impoundment depth in Test S1 (see Figure 6-8c). Such difference between Tests S1 and S2 delayed the formation of maximum effective normal stress by approximately three seconds. The effect of scour deposition on variations of the effective normal stress was observed in the middle of side wall of the structure model (see Figure 6-7d). Figure 6-S2b shows that the scour hole in the side wall (section *d-d*) was refilled with sand particles between 20 s and 35 s. The effect of such scour deposition is reflected by a gradual raise in the time history of effective normal stress as shown in Figure 6-7d.

The effect of bed slope on variations of effective normal stress with time is evaluated by comparing Tests H1 and S2 with approximately the same still-to-impoundment depth ratio of 0.1 and 0.085, respectively. Regardless of the location of tensiometers, the effective normal stress increased by two times in inclined bed tests which led to the formation of shallower scour depth in those tests (see Figure 6-S1a and Figure 6-S2a).

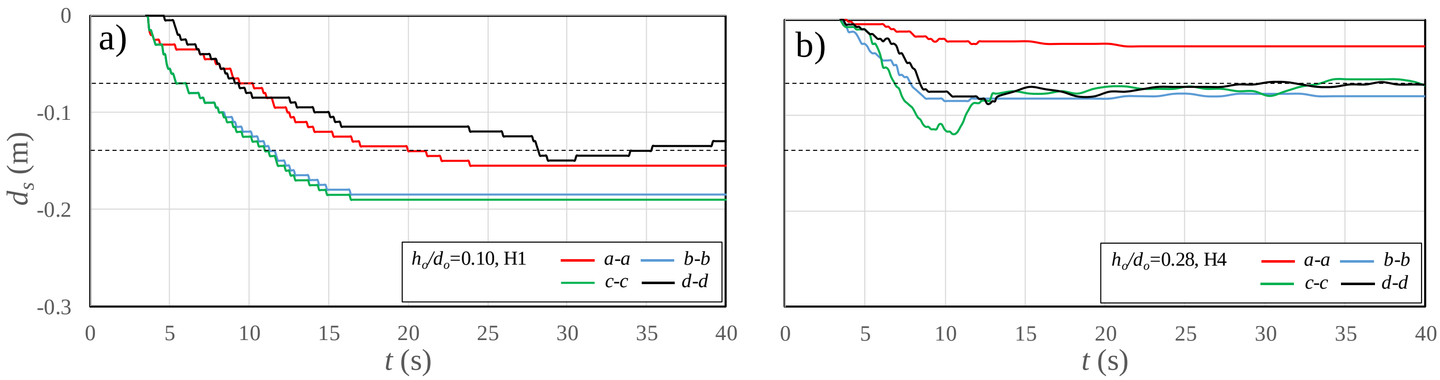

Figure 6-S1: Time history of scour depth, ds, for horizontal bed tests: a) h_o/d_o = 0.1; b) h_o/d_o = 0.28.

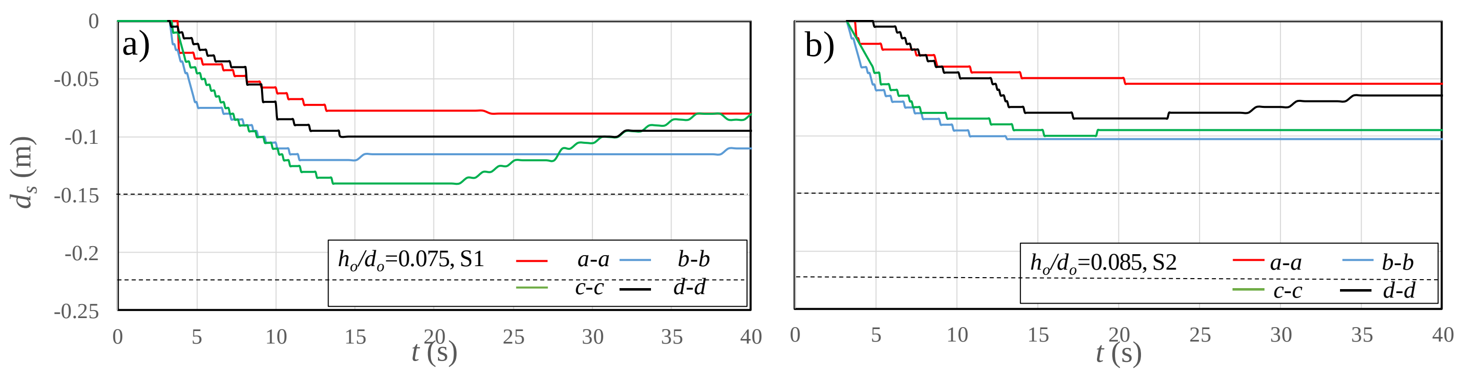

Figure 6-S2: Time history of scour depth, ds, for inclined bed tests: a) h_o/d_o = 0.075; b) h_o/d_o = 0.085.

Moreover, the effective normal stress in inclined bed tests reached the equilibrium condition after 20 s from the gate opening except with 10 s delay for tensiometers in the middle of side wall. Whereas the equilibrium state did not occur around the model in the horizontal bed test (see Test H1 in Figure 6-6a). Since the loading time is relatively shorter in inclined bed tests, the maximum effective normal stress dominated for a shorter period of time in inclined bed tests in comparison with the horizontal bed tests. For instance, the greater values of effective normal stress in the middle of the front wall (i.e., tensiometer #3) lasted for almost 15s in the horizontal bed (see Figure 6-6a), whereas the inclined bed the effective normal stress had the greater values and lasted for about 10s (Figure 6-7a).

Determination of the variations of effective normal stress with respect to scour depth is one of the imperative parts of studying the bearing capacity of coastal structures. Moreover, to improve the design standard of such structures, it is crucial to find a relation between scour dimensions and the effective normal stress (Lin and Jiang, 2019). The relation between scour depth and effective normal stress induced by hydraulic bores passing over a horizontal bed are presented in Figure 6-8.

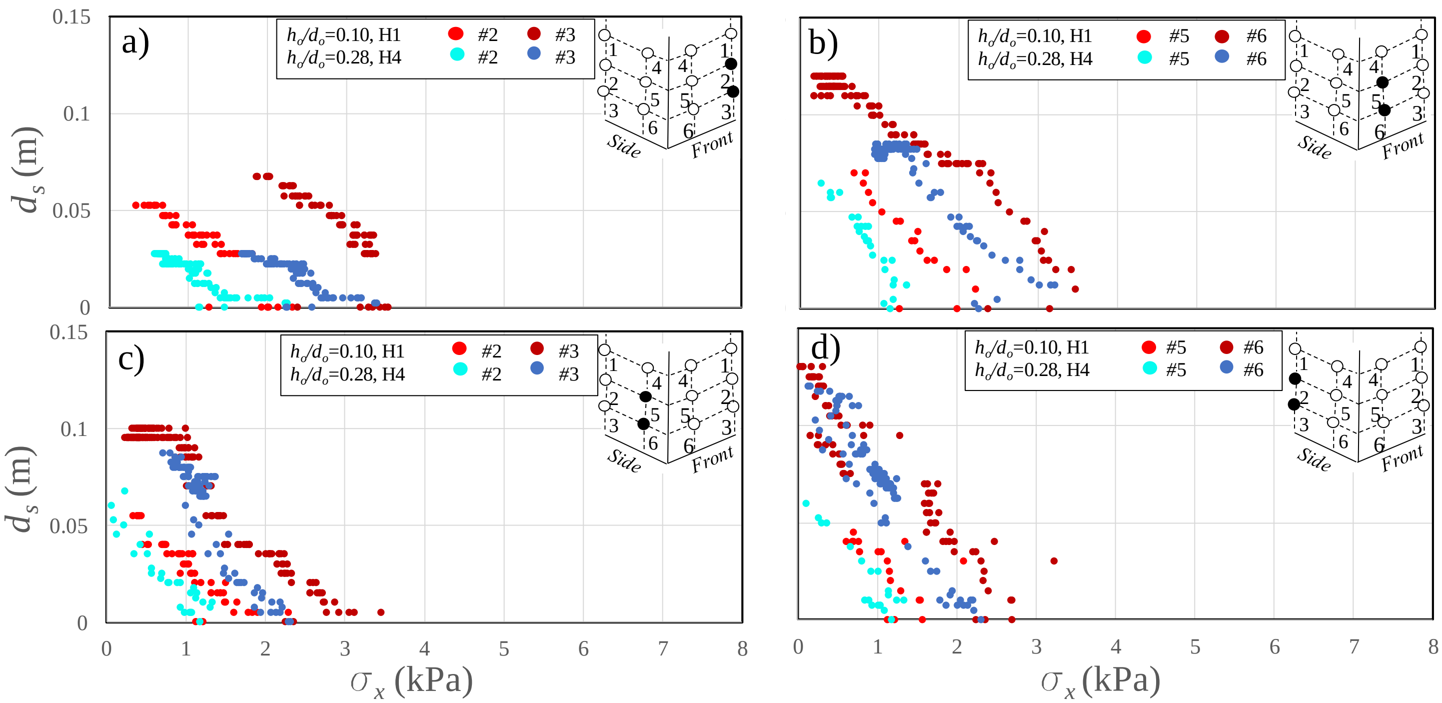

Figure 6-8: Relation between effective normal stress, σ_x, and scour depth, ds, around the structural model for horizontal bed tests: a) middle of the front wall, b) corner of the front wall; c) corner of the side wall; d) middle of the side wall.

Regardless of the flow regime, the scour depth increased at each point around the model as the effective normal stress decreased. In other words, the lowest scour depths were associated with the highest effective normal stress around the structure model. The effective normal stress was calculated by Eq. (2) with the consideration of the variations of hydrostatic pore pressures under different flow conditions. The effective normal stress was calculated from the values of the pore pressure recorded by each tensiometers as they remained under the soil.

Figures 6-8a and 6-8b show the variations of scour depth versus effective normal stress in the front wall of the structure model. The two equivalent effective normal stresses of the same tensiometer generated greater scour depth in supercritical bores (Test H1) than the subcritical bores (Test H4). In other words, the effective normal stresses applied on the soil particle due to the propagation of supercritical bores were greater than the subcritical bores as the instantaneous hydrostatic pressures in Test H4 were relatively higher than the supercritical bores (Test H1). In both middle and corner of the front wall, the scour formation, regardless of the flow regime, initiated with greater normal stress at the bottom (tensiometers #3 and #6) as the magnitude of total pore pressure was greater in the third-row tensiometers than the second-row tensiometers.

Figures 6-8c and 8d show the variations of effective normal stress with respect to scour depth in the corner and middle of side wall, respectively. Similar to the front corner of the structure model in supercritical bores (Test H1) the scour initiated with higher values of effective normal stress in comparison with the equivalent condition in subcritical bores. Since the flow velocity increased right after passing the front wall, the pore pressure values decreased in the soil which is the reason of having greater effective normal stress at this corner. Additionally, the generation of eddies in this region and their simultaneous interaction with pore pressure variations among soil particles accelerated the scour formation at corners of the front and side faces. The variations of effective normal stress versus scour depths in the middle of side wall is plotted in Figure 6-8d. Similar to other sections around the structure model, scour in the subcritical flow generated with smaller values in the horizontal axis due to 2.33 times greater still water depth. The higher still water depth decreased the effective normal stress and may cause less erosion.

Similar to horizontal bed tests, scour depths have inverse relation with the variation of effective normal stress in inclined bed tests. Figures 6-9a and 6-9b shows the scour depth versus the effective normal stress in the middle and corner of the front wall of the structure model.

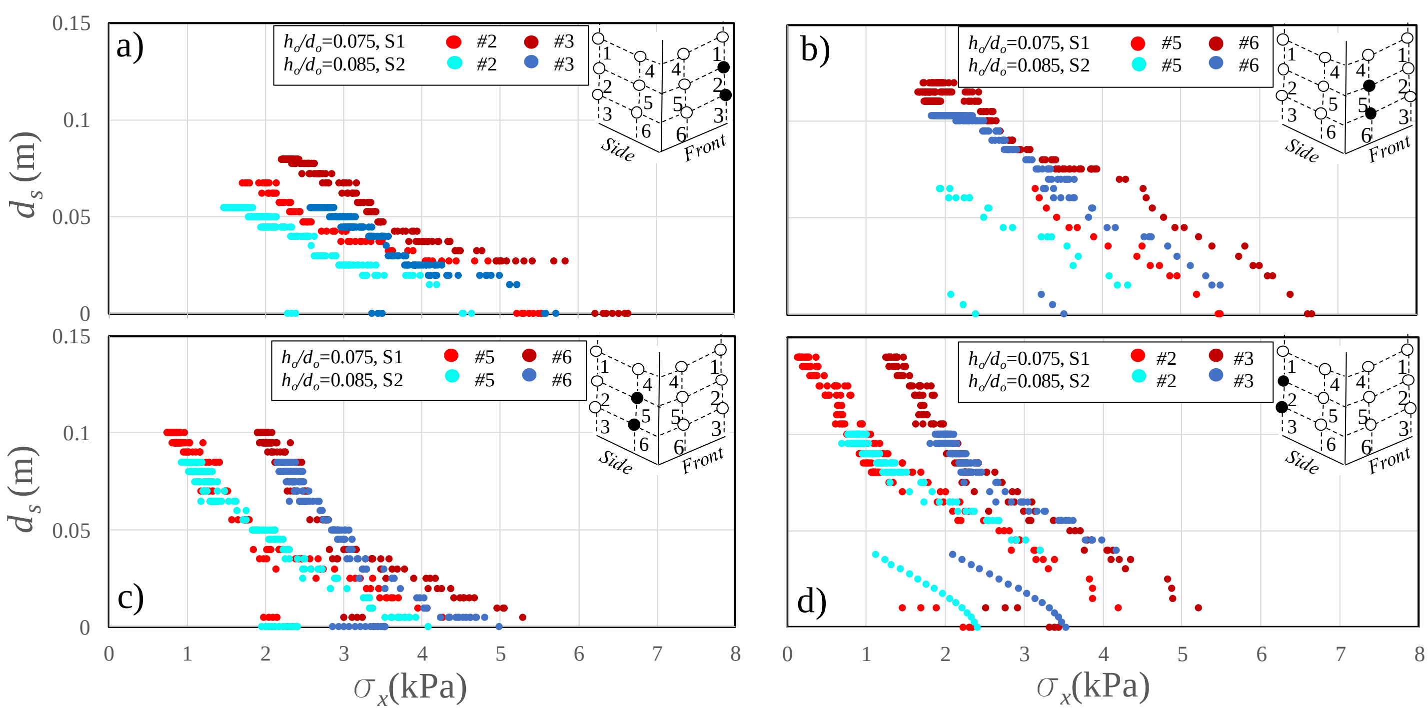

Figure 6-9: Relation between effective normal stress, σ_x, and scour depth, ds, around the structural model for inclined bed tests: a) middle of the front wall, b) corner of the front wall; c) corner of the side wall; d) middle of the side wall.

A comparison of the effective normal stress in these two sub-plots shows the effect of 14.28% greater impoundment water depth in Test S1 on variations of the effective normal stress versus scour depth. In the middle of the front wall and at the second-row of tensiometers, the scour initiated with 18% larger initial effective normal stress in Test S1 than the Test S2 (see Figure 6-9a). However, for each two points installed in the same depth in both sections of the front wall (i.e., tensiometers #2 and #5), the scour started at approximately the same effective normal stress; however, the final scour depth in the front corner of the model was 41.2% larger than the middle of the front face. The higher equilibrium scour is due to generation of vortices and flow separation. In addition, flow velocity increases at the front corner of the structure model which enhances the scour formation.

The variations of scour depth with the effective normal stress in the side wall of the structure model are shown in Figures 6-9c and 6-9d. The effective normal stress at the third-row tensiomentes (#6) at the equilibrium stage had 18% higher values in the side corner of the model which led to almost 23% shallower scour depth in this corner in comparison with the front corner (Figure 6-9b). Also in this region, the combination of generated eddies in the wake region and the fluctuations of the inner pore pressure resulted in greater scour depth. Figure 6-9d shows the relation between scour depth and effective normal stress in the middle of the side wall of the structure model. Similar to the side corner of the structure model, the relation between scour depth and effective normal stress affected by both flow depth and the depth of tensiometer. The scour depth in Test S1 continued for a longer time period than the Test S2. This is to 14.28% greater still water depth in Test S1 which increased final scour depth by 40% and decreased the effective normal stress by 30% in comparison with the Test S2.

The +5% increase in the bed slope affected the variation of scour depth with the effective normal stress. This can be explained by comparing the results of Test H1 and S2 with relatively similar still-to-impoundment depth ratio (h_o/d_o= 0.1 and 0.085, respectively). The scour initiated with on average 60% and 43% greater effective normal stress in the front and side walls of the structure model in Test S2 than Test H1. The initial soil height was 0.08 m and hydrodynamic pore pressure was two times greater in the inclined bed tests.

The dimensionless normal stress can be calculated as the scour depth is progressing and it is expressed as (Nago, 1982):

$$\sigma_z = 1 - \frac{\rho_w g h'}{(\rho_s - \rho_w).g.(Z - z).(1 - n)} \tag{5}$$

where h' is the height equivalent with excess pore water pressure, ρ_s is the soil density, z is the scour depth below the soil surface, Z is the initial soil level above the point of calculation, and n is the soil porosity with a value of 0.42 in this study.

Figure 6-10 shows the time history of dimensionless normal stress around the structure model in both horizontal and inclined bed tests.

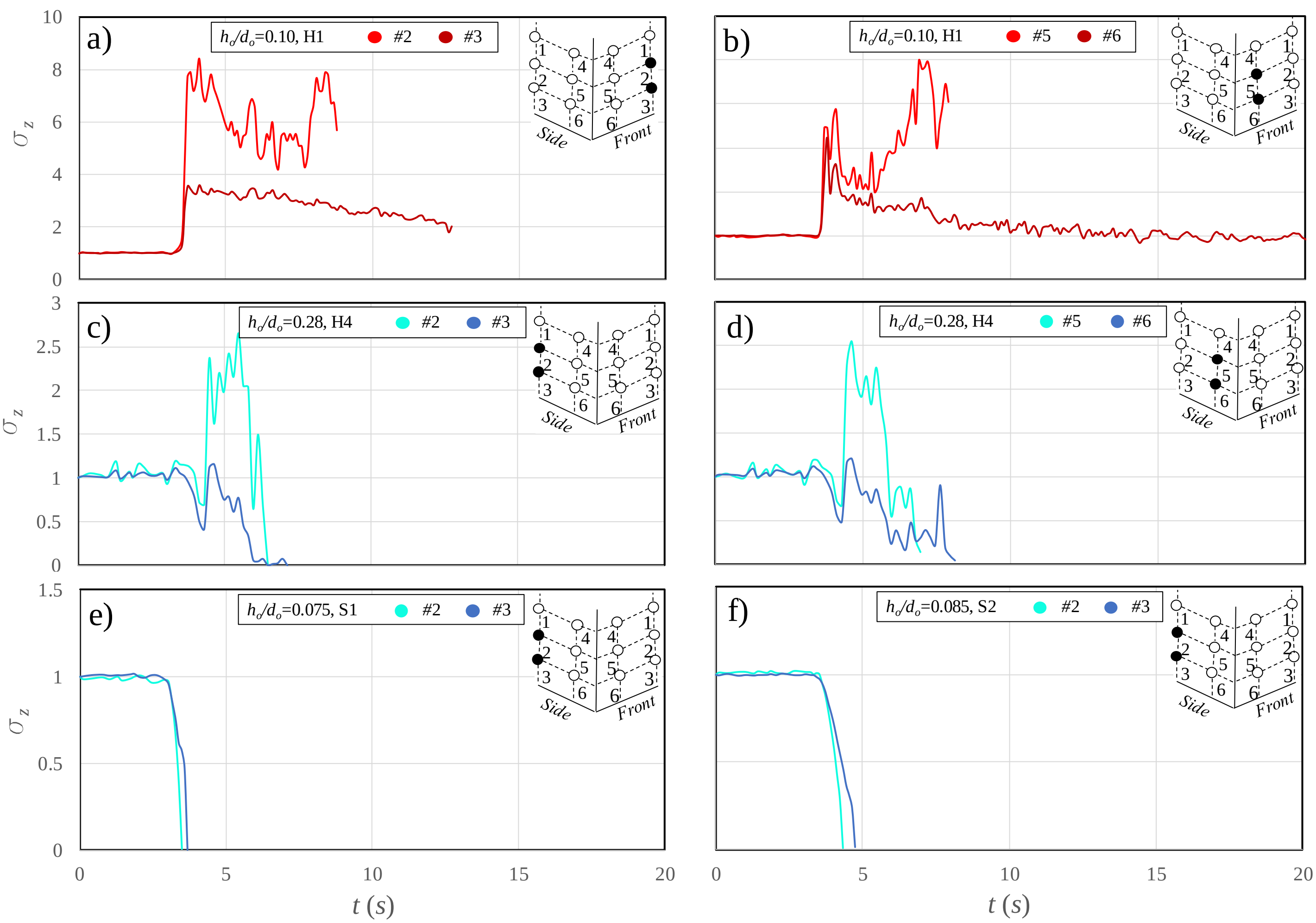

Figure 6-10: Variations of the dimensionless normal stress, σ_z, with time, t, around the structural model and for horizontal and inclined bed tests: a) middle of the front wall and horizontal bed, H1; b) corner of the front wall and horizontal bed, H1; c) middle of the side wall and horizontal bed, H4; d) corner of the side wall and horizontal bed, H4: e) middle of the side wall and inclined bed, S1; f) middle of the side wall and inclined bed, S2.

This stress was calculated for each tensiometers as long as they were in the saturated sand prior to exposure to the flow. The liquefaction took place when the dimensionless normal stress approached zero. Figures 6-10a and 6-10b show the time histories of the dimensionless normal stress in the front wall of the structure model for Test H1. The dimensionless normal stress had a constant value until $t \approx 4$s which is the time prior to the bore front arrival. The dimenssionless normal stress abruptly increased from their initial stage up to 7 and 3.5 times in the second- and third-row tensiometers, respectively. This significant increase indicates that the dimensionless normal stress was remarkably impacted by tensiometers elevation in the front wall of model. A comparison of Figures 6-10a and 6-10b demonstrates that the values of dimensionless normal stress are higher in the middle of the front wall for a longer period of time in comparison with the front corner. In the front wall and for the same tensiometer depth (i.e., #2 and #5), the first maximum dimensionless normal stress is 45.5% greater in the middle of the front wall in comparison with the front corner. On the other hand, for both sections the dimensionless normal stress truncated when the tensiometers exposed to the flowing bore. Such data truncation occurred earlier in the front corner than the middle of front wall (i.e, t = 13 s and 14 s, respectively). No soil liquefaction was observed as the dimenssionless normal stress did not reach zero in the front wall of the structure model in Test H1.

Figures 6-10c and 6-10d show the time history of dimensionless normal stress in the side wall of the structure model in Test H4. Similar to the front wall of the structure model in Test H1, the dimensionless normal stress had a constant value until $t \approx 4$ s with a magnitude of 1. Moreover, the peak normalized stresses were affected by the depth of tensiometers. For second-row and third-row tensiometers, the dimensionless normal stress increased 1.5 times and 30%, respectively, compared to the initial value (i.e., σ_z=1). As the time history of dimensionless normal stress shows there is a slight decrease before the first peak because of the sedimentation.

A comparison of the variations of non-dimensional normal stress in tensiometers with the same depth but with different locations (tensiometers #2 and #5) determines that the middle of side wall (i.e., #2) exhibites the liquefaction nearly two seconds earlier than the side corner. On the other hand, the time history of scour depth (Figure 6-S1b) in the side wall of the structure model for Test H4 shows that the liquefaction time in this wall occurres around the equilibrium time. Furthermore, a comparison of Figures 6-10a and 6-10b with Figures 6-10c and 6-10d shows that in the horizontal bed tests the liquefaction happened in the subcritical flows which can be due to the effect of 2.33 times greater still water depth, that reduces the resistant forces among soil particles more significantly.

The time series of dimensionless normal stress in the side wall of structure model for the inclined bed tests are presented in Figures 6-10e and 6-10f. Figure 6-10e shows the dimensionless normal stress variations in the middle of the side wall of the structure model in Test S1. As it can be seen, the liquefaction occurred a few seconds earlier in the second-row tensiometer than the third-row. A comparison of Figures 6-10e and 6-10f indicates that liquefaction happened nearly two seconds earlier in Test S1 with 14.28% greater impoundment depth than Test S2. The effect of 5% bed slope appears in the liquefaction occurrence as liquefaction was not observed in Test H1.

6-4 Conclusions

As mentioned earlier, this experimental study aimed to explore the interaction among the variations of excess pore pressure, scour development, and effective normal stress around the square structural model to better understand soil behaviour as dam-break bores with different hydrodynamic characteristics propagated downstream. Thereby, a series of laboratory experiments were performed to observe the effects of various still-to-impoundment depth ratios and two different bed slopes on the propagation of dam-break tsunami-like bores in both subcritical and supercritical flow regimes.

The front face of the structural model in the horizontal and inclined bed tests had 40% and 60% larger maximum excess pore pressure than the side face, respectively. On the other hand, for both bed slope cases, the side face of the model showed positive excess pore pressure earlier in the experiments, which was the case in the subcritical flows in the horizontal bed. In both horizontal and inclined bed tests, the effective normal stress had the equal maximum value for every two points placed in the same elevation of two different sides of the model. The relation between effective normal stress and the scour depth implied that in both horizontal and inclined bed tests the front face of the structure had relatively greater effective normal stress rather than the other sides of the model which caused shallower scour depths in this section.

14.28% greater impoundment depth in Test S1 caused having on average 55% greater maximum negative excess pore pressure around the model than Test S2. The comparison of the effective normal stress for Test H1 (h_o/d_o=0.1) with Test H4 (h_o/d_o=0.25) showed that 2.33 times greater still water depth in Test H4 decreased the impingement impact of the advancing bore that mostly affected the side face of the model. Then, in the side face of the model in Test H1 the maximum effective normal stress is 1.6 times greater than Test H4. Furthermore, effective normal stress had lower values in the subcritical flow (Test H4) compared to case of Test H1. Liquefaction was also occurred in the side face of the model as a result of subcritical bore propagation, which was not seen in the same face during supercritical test case.

+5% increase in the bed slope affected the time history of excess pore pressure variations around the model such that the peak of this pressure was 2 times larger around the structural model in the inclined bed (Test S2) compare to the case of horizontal bed test (Test H1). In addition, regardless of the structural model's face and the tensiometers' elevation the time history of effective normal stress displayed two times greater values around the model in the inclined bed than the horizontal bed. Due to the relatively short loading time in the inclined bed, the maximum effective normal stress applied on average 6s longer on the horizontal bed than the inclined one. The effective normal stress was influenced by increasing bed slope. The initial effective normal stress was on average 50% greater around the model located in the inclined surface than the horizontal one.

Chapter 7. Conclusions and Recommendations for Future Work

7.1 Conclusions

This thesis investigated the scouring process and pore pressure variations generated by the propagation of dam-break bores and the associated flow around a structural model installed in a sediment bed. Furthermore, the effects of the bed slopes in the saturated bed condition were investigated. This study aimed to improve the understanding of the interaction of the transient flows and soil behaviour by correlating scour development and pore pressure propagation within the soil. Based on the obtained results from this investigation, the following general conclusions can be drawn:

- It was found that for the case of bores propagating over the horizontal bed, the runup was higher for the case of the supercritical bores compared to the subcritical ones. For identical hydrodynamic conditions, the peak bore depth height was almost 40% higher and recorded 5 seconds earlier in the inclined bed test than for the horizontal bed test.
- The recorded time-history of the bore velocity exhibited higher values for the case of supercritical bores than for the subcritical ones. Almost three times increase in the still water depth downstream of the gate reduced the bore velocity by 50%. In addition, an increase in the bed slope by 5% increased the maximum velocity by 25%.
- For identical hydrodynamic conditions when propagating over the horizontal and inclined beds, it was observed that the wave impulse applied to the model was twice as high in the horizontal bed test compared to the inclined bed case.
- Based on the values recorded by the tensiometers, generally, the peak effective pore pressure recorded by the bottom tensiometers exhibited higher values compared to the other tensiometers located above it. Moreover, for the horizontal bed tests combined with the case of supercritical flows, the peak effective pore pressure values were close to 50% larger at the front corner of the model than the corresponding depth-location pore pressure at the side corner. However, the propagation of the subcritical bores did not significantly affect the maximum effective pore pressure recorded by the tensiometers installed in different depths in the soil.

- In terms of the effect of still-to-impoundment depth ratio for the case of the horizontal bed, it was observed that the maximum normalized pore pressures at the side wall were more sensitive to the variations of h_o/d_o compared to the same ratio for the front face of the model which exhibited close to no change to the variations of this ratio.
- For the inclined bed tests, the maximum pore pressures normalized by the initial hydrostatic pressure measured by tensiometers installed in the top row were almost five times greater than those recorded by the corresponding tensiometers installed in the third row. While, in the horizontal bed test normalized maximum pore pressures did not show significant sensitivity to their elevations.
- Under identical hydrodynamic conditions, the values of the maximum effective pore pressure, the maximum excess pore pressure, and the maximum effective normal stress values doubled in the case of the inclined bed compared to the horizontal bed.
- With the same flow regime condition, the time to peak pore pressure recorded by the first-raw tensiometers, when the column was installed in the horizontal bed, decreased with an increase in h_o/d_o compared to the inclined bed test where an increase was observed.
- Similar to previous experimental studies and post-tsunami field investigations (Nakamura et al., 2008b; Chock et al., 2012; Mehrzad et al., 2016), the maximum scour depth occurred at the seaward corners of the structural model, regardless of flow regime and bed slope.
- Due to the propagation of the same hydrodynamic bores, the final scour hole in the inclined bed was 45% shallower compared to the case of the horizontal bed and its longitudinal length extended two times shorter towards the upstream.
- For both the inclined and the horizontal bed tests, the maximum normalized scour depth decreased with an increase in h_o/d_o.
- In general, an increase in the still water depth reduced the erosion rate as well as the peaks of the time history of Shields number. Conversely, an increase in the impoundment depth caused an increase in these two parameters in both horizontal and inclined bed tests.
- For identical hydrodynamic conditions, a 5% increase in the bed slope additionally influenced the erosion rate and the peaks of Shields number. As such, the erosion rate around the structural model installed in the inclined bed reduced by 65% compared to that observed in the case of the horizontal bed. At the same time, the 5% upsloping bed increased the maximum Shields numbers by 20% compared to that calculated for the case of the horizontal bed test.

- For both horizontal and inclined bed tests, for identical hydrodynamic conditions, the initial maximum excess pore pressures exhibited negative values which were greater, in absolute value, at the front face of the model compared to the side face. By contrast, the excess pore pressure recorded in the first 10 seconds of the test had positive values for the subcritical bores propagating over the horizontal bed.
- Generally, tensiometers installed on different faces at the same depth exhibited the same effective normal stress for both horizontal and inclined bed tests. However, the time history of effective normal stress showed direct and adverse relation with the impoundment and still water depths, respectively.

The research presented in this study encompassed a comprehensive experimental program designed to investigate the anticipated relation between scour evolution and pore pressure variation around a structural model during the propagation of dam-break bores with different hydrodynamic characteristics and bed slopes in saturated bed condition. The results of this research will contribute to improving the better understanding of the complex connection between the scour depths and the pore pressure variations. A part of these experimental results have been included in the most recent version of the ASCE7 Chapter 6 - Tsunami Loads and Effects design and were voted favourably by the ASCE Main Balloting Committee. The newly revised ASCE7 Chapter 6 will be published in 2022.

7.2 Recommendations for Future Work

The research presented in this doctoral thesis examines the effects of some influential parameters such as the hydrodynamic characteristics of the dam-break bores and bed slope in saturated bed condition on the scour formation as well as the pore pressure propagation through soil volume. Conducting further research is essential to expand the understanding of these flow-soil-erosion mechanisms.

- The presented physical modeling tests were performed using uniform singular sediment size and the bores were propagating towards downstream. Therefore, using sediment mixed grains-size would be closer to the reality.
- The sediment used for this experimental study was noncohesive. Given that many of the coastal areas do exhibit cohesive soil, it would be interesting to study the effects of cohesive sediments on the scour evolution and the pore pressure variation. However, for such tests, a prototype scale would be the way to move forward.
- Due to time limitations, only a single-size square-shaped cross-section column was used in this experimental program. It is recommended to consider experimenting the impact of other various structural geometries and sizes.
- Due to limitations in experimental facilities, this experimental program was performed at a relatively small-scale flume (1:40). Using a larger scale is recommended in order to be able to run tests where the distortions caused by scale effects are reduced.

Reference

Abdollahi, A. and Mason, H.B. 2019. "Coupled seepage-deformation model for predicting pore-water pressure response during tsunami loading." *Journal of Geotechnical and Geoenvironmental Engineering, 145(3)* p.04019002.

Abdollahi, A., Adams, R.K. and Mason, H.B. 2017. "Earthquake-induced water level rise: Implications for tsunami-induced sediment instability in coastal areas." *In Geotechnical Frontiers 2017* pp. 428-438.

Abdollahi, Abbas. 2017. *Pore Water Pressure Response in Soil During Tsunami Loading:*. PhD Thesis, Oregon State University.

Al-Faesly, T.Q. 2016. *Extreme hydrodynamic loading on near-shore structures.* PhD thesis, Ottawa, Canada: University of Ottawa.

Al-Riffai, M. and Nistor, I. 2013. "nfluence of Boundary Seepage on the Erodibility of Overtopped Embankments: A Novel Measurement and Experimental." *In Proceedings of the 35th IAHR World Congress, Chengdu, China* pp. 8-13.

Al-Riffai, Mahmoud. 2014. *Experimental study of breach mechanics in overtopped noncohesive earthen embankments.* PhD thesis, Canada: University of Ottawa.

Ansari, S.A., Kothyari, U.C. and Raju, K.G.R. 2003. "Influence of cohesion on scour under submerged circular vertical jets." *Journal of hydraulic engineering,129(12)* 1014-1019.

Arneson, L.A., Zevenbergen, L.W., Lagasse, P.F. and Clopper, P.E. 2012. "Evaluating scour at bridges (No. FHWA-HIF-12-003)." *National Highway Institute (US).*

ASCE, 7-16. 2016. "Design for tsunami loads and effects."

Atkinson, J. 2017. "The mechanics of soils and foundations." *CRC press.*

BARRÉ de SAINT-VENANT, A.J.C. 1871. "Théorie du Mouvement Non Permanent des Eaux, avec Application aux Crues de Rivières et à l'Introduction des Marées dans leur Lit." *Comptes Rendus des séances de l'Académie des Sciences.* Paris, France. Vol. 73, No. 4, pp. 237-240.

Bishop, A.W. 1959. "The principle of effective stress." *Tekniche Ukeblad,39* p.p. 4–16.

Biswal, S.K., Moharana, M.K. and Agrawal, A.K. 2018. "Effects of initial stage of dam-break flows on sediment transport." *Sādhanā, 43(12)* p.203.

Bohorquez, P. and Fernandez-Feria, R. 2008. "Transport of suspended sediment under the dam-break flow on an inclined plane bed of arbitrary slope." *Hydrological Processes: An International Journal, 22(14)* 2615-2633.

Breusers, H.N.C., Nicollet, G. and Shen, H.W. 1977. "Local Scour Around Cylindrical Piers." *Journal of Hydraulic Research,15(3)* 211-252.

Byerlee, J. 1978. *Friction of rocks.* Birkhäuser, Basel: In Rock friction and earthquake prediction.

Çağatay, H. and Kocaman, S. 2008. "Experimental Study Of Tailwater Level Effects On Dam-Break Flood Wave." *Proceedings River Flow* (pp. 635-644).

Cao, Z., Pender, G. and Meng, J. 2006. "Explicit Formulation of the Shields Diagram for IncipientMotion of Sediment." *Journal of Hydraulic Engineering* 132(10), pp.1097-1099.

Carslaw, H.S. and Jaeger, J.C. 1959. "Conduction of heat in solids." Oxford University Press.

Chanson, H. 2005. *Applications of the Saint-Venant equations and method of characteristics to the dam break wave problem.* Brisbane, Australia: The University of Queensland.

Chanson, H. 2006. "Tsunami surges on dry coastal plains: Application of dam break equations." *Coastal Eng. J.* 48(4), 355–370.

Cheng, M.Y., Cao, M.T. and Wu, Y.W. 2015. "Predicting equilibrium scour depth at bridge piers using evolutionary radial basis function neural network." *Journal of Computing in Civil Engineering, 29(5)* 04014070.

Chinnarasri, C., Thanasisathit, N., Ruangrassamee, A., Weesakul, S. and Lukkunaprasit, P. 2013. "The impact of tsunami-induced bores on buildings." *In Proceedings of the institution of civil engineers-maritime engineering, Vol. 166, No. 1* pp. 14-24.

Chock, G., Robertson, I., Kriebel, D., Francis, M. and Nistor, I. 2012. *Tohoku Japan tsunami of March 11, 2011 – Performance of structures under tsunami loads.* Final report, ASCE.

Chock, G.Y., Robertson, I. and Riggs, H.R. 2011. "Tsunami structural design provisions for a new update of building codes and performance-based engineering." *Solutions to Coastal Disasters* 423-435.

Coleman, S.E. and Melville, B.W. 2001. "Case Study: New Zealand Bridge Scour Experiences." *Journal of Hydraulic Engineering* 127(7), pp.535-546.

Crespo, A.J., Gómez-Gesteira, M. and Dalrymple, R.A. 2008. "Modeling dam break behavior over a wet bed by a SPH technique." *Journal of waterway, port, coastal, and ocean engineering* 313-320.

Daliri, M. and Chegini, A.H.N. 2016. "Experimental assessment of changes of sandy beach profile and sediment transport caused by tsunami waves." *Turkish Journal of Engineering and Environmental Sciences, 38(3)* pp.392-403.

Dames and Moore. 1980. "Design and construction standards for residential construction in tsunami-prone areas in Hawaii." *prepared by Dames & Moore for the Federal Emergency Management Agency, Washington D.C.*

Damgaard JS, Whitehouse RJS, Soulsby RL. 1997. "Bed-load sediment transport on steep longitudinal slopes." *Journal of Hydraulic Engineering 123* pp 1130–1138.

Disfani, R.K. and Moghaddam, A.B. 2020. "Identification of soil liquefaction occurrence using wavelet analysis." *SN Applied Sciences, 2(10)* pp.1-6.

Douglas, S. and Nistor. 2015. "On the effect of bed condition on the development of tsunami-induced loading on structures using OpenFOAM." *Natural Hazards, 76(2)* 1335-1356.

Ettema, R., Melville, B.W. and Barkdoll, B. 1998. "Scale effect in pier-scour experiments." *Journal of Hydraulic Engineering, 124(6)* 639-642.

Ettema, R., Melville, B.W. and Constantinescu, G. 2011. "Evaluation of bridge scour research: Pier scour processes and predictions." *Washington, DC: Transportation Research Board of the National Academies.*

Exton, M., Harry, S., Kutter, B., Mason, H.B. and Yeh, H. 2019. "Simulating tsunami inundation and soil response in a large centrifuge." *Scientific reports, 9(1)* pp.1-12.

Faulkner, D.R., Sanchez-Roa, C., Boulton, C. and Den Hartog, S.A.M. 2018. "Pore fluid pressure development in compacting fault gouge in theory, experiments, and nature." *Journal of Geophysical Research: Solid Earth, 123(1)* pp.226-241.

Federal Emergency Management Agency. 2000. *Coastal Construction Manual,.* Department of Homeland Security, Washington, DC.: Principles and Practices of Planning, Siting, Designing, Constructing,.

FEMA,P-646. 2012. *Guidelines for Design of Structures for Vertical Evacuation from Tsunami.* Washington D.C., USA: Federal Emergency Management Agency.

Fennema, R.J. and Hanif Chaudhry, M. 1987. "Simulation of one-dimensional dam-break flows." *Journal of Hydraulic Research, 25(1)* pp.41-51.

Francis, M.J. and Yeh, H. 2006. "Tsunami Inundation Scour of Roadways, Bridges and Foundations. Observations and Technical Guidance from the Great Sumatra Andaman Tsunami." *EERI/FEMA NEHRP* (EERI/FEMA NEHRP) pp.2-53.

Froehlich, D.C. 1988. "Analysis of Onsite Measurements of Scour at Piers." *In Hydraulic engineering: proceedings of the 1988 national conference on hydraulic engineering* 534-539.

Ghobarah, A., Saatcioglu, M. and Nistor, I. 2006. "The impact of the 26 December 2004 earthquake and tsunami on structures and infrastructure." *Engineering structures, 28(2)* pp.312-326.

Ghodoosipour, B., Stolle, J., Nistor, I., Mohammadian, A. and Goseberg, N. 2019. "Experimental study on extreme hydrodynamic loading on pipelines. Part 1: Flow hydrodynamics." *Journal of Marine Science and Engineering, 7(8)* p.251.

Goto, K., Hashimoto, K., Sugawara, D., Yanagisawa, H. and Abe, T. 2014. "Spatial thickness variability of the 2011 Tohoku-oki tsunami deposits along the coastline of Sendai Bay." *Marine Geology, 358* pp.38-48.

Häfen, H.V., Stolle, J., Goseberg, N. and Nistor, I. 2018. "Lift and swing gate modelling for dam-break generation with a particle-based method." *7th International Symposium on Hydraulic Structure.* Aachen, Germany.

Hager, W.H. and Unger, J. 2010. "Bridge pier scour under flood waves." *Journal of Hydraulic Engineering, 136(10)* pp.842-847.

Hatogai, S., Suwa, Y. and Kato, F. 2012. "Hydraulic model experiments on scour landward of the coastal dike induced by tsunami overflow." *Proceedings of Coastal Engineering, JSCE, Vol. 68, No. 2* pp. 406-410.

Hayatdavoodi, M., Treichel, K. and Ertekin, R.C. 2019. "Parametric study of nonlinear wave loads on submerged decks in shallow water." *Journal of Fluids and Structures, 86* pp.266-289.

Heibaum, M.H. and Köhler, H.J. 2000. "Excess pore water pressure and slope stability." *ISRM International Symposium. International Society for Rock Mechanics and Rock Engineering,.*

Hsu, H.C., Torres-Freyermuth, A., Hsu, T.J., Hwung, H.H. and Kuo, P.C. 2014. "On dam-break wave propagation and its implication to sediment erosion." *Journal of Hydraulic Research, 52(2)* 205-218.

Iiboshi, T., Maeno, S., Yosida, K. and Takata, D. 2014. "Effect of shape of landward slope protection and toe protection works of coastal dikes on landward bed scouring due to tsunami overflow." *Journal of Japan Society of Civil Engineers, Vol 70* pp. 966-970.

Iiboshi, T., Maeno, S., Yosida, K., Takata, D. and Yamaura, A. 2015. "Effects of landward slope protection and toe protection work shape at coastal dikes on landward bed scouring caused by tsunami overflow." *E-proceedings of the 36th IAHR World Congress. .* Hagues, Netherlands.

Iida, T., Kure, S., Udo, K., Mano, A. and Tanaka, H. 2016. "Prediction of the 2011 Tohoku Tsunami Scouring near Structures." *Journal of Coastal Research, (75 (10075))* pp.872-876.

Imamura, F., Goto, K. and Ohkubo, S. 2008. " A numerical model for the transport of a boulder by tsunami." *Journal of Geophysical Research: Oceans* (Journal of Geophysical Research Oceans) 113 (C1): 236-254: 113(C1).

Istrati, D. and Buckle, I. 2019. "Role of trapped air on the tsunami-induced transient loads and response of coastal bridges." *Geosciences, 9(4)* p.191.

Jaeger, J. c., and Cook, N. G. W. 1979. *Fundamentals of rock mechanics (third edition).* London, United Kingdom: Chapman and Hall, 593 p.

Jain, S.C. and Fischer, E.E. 1980. "Scour around Bridge Piers at High Velocity." *Journal of Hydraulic Engineering, ASCE, 106(11)* 1827-1842.

Japanese Meteological Agancy. 2011. "Tsunami information (expected height and arrival time)."

Jayaratne, M.P.R., Premaratne, B., Adewale, A., Mikami, T., Matsuba, S., Shibayama, T., Esteban, M. and Nistor, I. 2016. "Failure Mechanisms and Local Scour at Coastal StructuresInduced by Tsunami." *Coastal Engineering Journal*, 58(04), p.1640017.

Jayaratne, R., Abimola, A., Mikami, T., Matsuba, S., Esteban, M. and Shibayama, T. 2014. "Predictive model for scour depth of coastal structure failures due to tsunamis." *Coastal Engineering Proceedings, (34)* pp.56-56.

Jeng, D.S. and Hsu, J.S.C. 1996. "Wave-induced soil response in a nearly saturated sea-bed of finite thickness." *Geotechnique*, *46(3)* pp.427-440.

Jeng, D.S. and Ou, J. 2010. "3D models for wave-induced pore pressures near breakwater heads." *Acta Mechanica, 215(1)* pp.85-104.

Jeng, D.S. and Zhang, H. 2005. "An integrated three-dimensional model of wave-induced pore pressure and effective stresses in a porous seabed: II. Breaking waves." *Ocean engineering*, *32(16)* pp.1950-1967.

Jeng, D.S., Cha, D.H., Lin, Y.S. and Hu, P.S. 2001. "Wave-induced pore pressure around a composite breakwater." *Ocean Engineering*, *28(10)* pp.1413-1435.

Jiang, C., Cheng, Y., Chang, L. and Xia, B. 2012. "The numerical study of wave-induced pore water pressure response in highly permeable seabed." *Acta Oceanologica Sinica* 46-55.

Julien, PY. 1995. *Erosion and Sedimentation.* Cambridge: Cambridge University Press.

Kato, F., Sato, S. and Yeh, H. 2001. "Large-scale experiment on dynamic response of sand bed around a cylinder due to tsunami." *Coastal Engineering 2000* pp. 1848-1859.

Kato, F., Suwa, Y., Watanabe, K. and Hatogai, S. 2012. "Mechanisms of coastal dike failure induced by the Great East Japan Earthquake Tsunami." *Coastal Engineering Proceedings*, *1(33)* pp.1-9.

Khan, M.K., Muzzammil, M. and Alam, J. 2016. "Bridge Pier Scour: A review of mechanism, causes and geotechnical aspects." *Proceedings of Advances in Geotechnical Engineering* 8-9.

Kiraga, M. and Popek, Z. 2019. "Bed Shear Stress Influence on Local Scour Geometry Properties in Various Flume Development Conditions." *Water, 11(11)* pp. 2346.

Kirkil, G., Constantinescu, G. and Ettema, R. 2005. "The Horseshoe Vortex System Around a Circular Bridge Pier on Equilibrium Scoured Bed." *Impacts of Global Climate Change* pp. 1-12.

Knappett, J. 2012. *Craig's soil mechanics (Vol. 8).* London: Spon Press.

Kothyari, U.C., Ranga Raju, K.G. and Garde, R.J. 1992. "Live-bed scour around cylindrical bridge piers." *Journal of Hydraulic Research, 30(5)* pp.701-715.

Kramer, O.J.I., Padding, J.T., van Vugt, W.H., de Moel, P.J., Baars, E.T., Boek, E.S. and van der Hoek, J.P. 2020. "Improvement of voidage prediction in liquid-solid fluidized beds by inclusion of the Froude number in effective drag relations." *International Journal of Multiphase Flow, 127* p.103261.

Lacey, G. 1930. "Stable channels in alluvium (induced appendices)." *In Minutes of the Proceedings of the Institution of Civil Engineers, Vol. 229, No. 1930,* 259-292.

Lagasse, P.F., Richardson, E.V., Schall, J.D., and Price, G.R. 1997. "Instrumentation for measuring scour at bridge piers and abutments." *NCHRP Report 396: TRB, National Research Council, Washington, D.C.*

Lamb, M.P., Dietrich, W.E. and Venditti, J.G. 2008. "Is the critical Shields stress for incipient sediment motion dependent on channel-bed slope?" *Journal of Geophysical Research: Earth Surface, 113(F2).*

Larsen, B.E., Arbøll, L.K., Kristoffersen, S.F., Carstensen, S. and Fuhrman, D.R. 2018. "Experimental study of tsunami-induced scour around a monopile foundation." *Coastal engineering, 138* pp.9-21.

Lauber, G. and Hager, W.H. 1998b. "Experiments to dambreak wave: Sloping channel." *Journal of Hydraulic Research* 761-773.

Lauber, G. and Hager, W.H., . 1998a. "Experiments to dambreak wave: Horizontal channel." *Journal of Hydraulic research, 36(3)* pp.291-307.

Lavictoire, A. 2015. *Bore-Induced Local Scour around a Circular Structure.* Doctoral dissertation, Canada: University of Ottawa.

Leal, J. G., Ferreira, R. M., & Cardoso, A. H;. 2009. "Maximum Level and Time to Peak of Dam-Break Waves on Mobile Horizontal Bed." *Journal of Hydraulic Engineering* 135(11): 995-999.

Lee, S.O. and Sturm, T.W. 2009. "Effect of sediment size scaling on physical modeling of bridge pier scour." *Journal of hydraulic engineering, 135(10)* 793-802.

Leng, J., Ye, G., Liao, C. and Jeng, D. 2018. "On the soil response of a coastal sandy slope subjected to tsunami-like solitary wave." *Bulletin of Engineering Geology and the Environment, 77(3)* pp.999-1014.

Lin, C. and Jiang, W. 2019. "Evaluation of vertical effective stress and pile tension capacity in sands considering scour-hole dimensions." *Computers and Geotechnics, 105* pp.94-98.

Link, O., Castillo, C., Pizarro, A., Rojas, A., Ettmer, B., Escauriaza, C. and Manfreda, S. 2017. "A model of bridge pier scour during flood waves." *Journal of Hydraulic Research, 55(3)* pp.310-323.

Liu, C., Liu, X., Jiang, C., He, Y., Deng, B., Duan, Z. and Wu, Z. 2019. "Numerical Investigation of Sediment Transport of Sandy Beaches by a Tsunami-Like Solitary Wave Based on Navier–Stokes Equations." *Journal of Offshore Mechanics and Arctic Engineering, 141(6).*

Liu, H., Liu, H., Guo, L. and Lu, S. 2017. "Experimental Study on the Dam-Break Hydrographs at the Gate Location." *Journal of Ocean University of China* 697-702.

Lou, X., Zhang, K. and Chen, Z. 2019. "Effect of Reynolds Number on Local Scour Around a Monopile in Steady Current." *In International Conference on Offshore Mechanics and Arctic Engineering (Vol. 58844).* American Society of Mechanical Engineers. V07AT06A010.

Lowe, D.R. 1975. "Water escape structures in coarse-grained sediments." *Sedimentology, 22(2)* pp.157-204.

Lu, J.Y., Shi, Z.Z., Hong, J.H., Lee, J.J. and Raikar, R.V. 2011. "Temporal variation of scour depth at nonuniform cylindrical piers." *Journal of Hydraulic Engineering, 137(1)* pp.45-56.

Madsen, P.A. and Schaeffer, H.A. 2010. "Analytical solutions for tsunami runup on a plane beach: single waves, N-waves and transient waves." *Journal of Fluid Mechanics, 645* p.27.

Madsen, P.A., Fuhrman, D.R. and Schäffer, H.A. 2008. "On the solitary wave paradigm for tsunamis." *Journal of Geophysical Research: Oceans, 113(C12).*

Magsi, H., Sodhro, A.H., Chachar, F.A. and Abro, S.A.K. 2018. " Analysis of signal noise reduction by using filters." *In 2018 International Conference on Computing, Mathematics and Engineering Technologies (iCoMET)* 1-6,IEEE.

Marieh Rajaie, Amir H. Azimi, Ioan Nistor, Colin D. Rennie. 2019. "Experimental investigations on hydrodynamic characteristics of tsunami-like hydraulic bores impacting a square structure ." *Journal of Hydraulic Engineering, in review.*

Marieh Rajaie, Amir H. Azimi, Ioan Nistor, Colin D. Rennie. 2021. "Experimental investigations on the impact of tsunami-like hydraulic bores on a square-shaped structure (Part 1): pore pressure variations ." *submitted to Journal of Waterway, Port, Coastal Engineering, ASCE, in review.*

Matsuda, T., Maeda, K., Miyake, M., Miyamoto, J., Sumida, H. and Tsurugasaki, K. 2016. "Instability of a caisson-type breakwater induced by an earthquake–tsunami event." *International Journal of Geomechanics, 16(5)* p.C4016003.

Mazumder, S. K. 2017. "Scour in bridge piers on non-cohesive fine andcoarse soil." *ISH Journal of Hydraulic Engineering, 23(2)* 111-117.

McGovern, D.J., Todd, D., Rossetto, T., Whitehouse, R.J.S., Monaghan, J. and Gomes, E. 2019. "Experimental observations of tsunami induced scour at onshore structures." *Coastal Engineering, 152* p.103505.

Mehrzad, S., Nistor, I. and Rennie, C.D. 2016. "Experimental modeling of supercritical flows-induced erosion around structures." *In Proceedings of the 6th International Conference on the Application of Physical Modelling in Coastal and Port Engineering and Science (Coastlab16).*

Mello, R.G., Oliveira, L.F. and Nadal, J. 2007. "Digital Butterworth filter for subtracting noise from low magnitude surface electromyogram." *computer methods and programs in biomedicine* 28–35.

MelvIille, B. W. 1975. "Local scour at bridge sites." Doctoral dissertation, ResearchSpace , Auckland, No. 117.

Melville, B.W. and Chiew, Y.M. 1999. "Time Scale for Local Scour at Bridge Piers." *J. Hydraulic Eng* 125(1): 59-65.

Miller, M.C., McCave, I.N. and Komar, P. 1977. "Threshold of sediment motion under unidirectional currents." *Sedimentology, 24(4)* pp.507-527.

Mioduszewski, T.M. and Maeno, S. 2003. "Experimental study of scouring process and flow behavior around a spur dike during the surge pass." *In The Thirteenth International Offshore and Polar Engineering Conference.*

Montoya, L., Lynett, P., Kie Thio, H. and Li, W. 2017. "Spatial statistics of tsunami overland flow properties." *Journal of Waterway, Port, Coastal, and Ocean Engineering, 143(2)* p.04016017.

Moreno, M., Maia, R. and Couto, L. 2016. "Effects of relative column width and pile-cap elevation on local scour depth around complex piers." *Journal of Hydraulic Engineering, 142(2)* p.04015051.

Mori, N., Takahashi, T., Yasuda, T. and Yanagisawa, H. 2011. "Survey of 2011 Tohoku earthquake tsunami inundation and run-up." *Geophysical research letters, 38(7).*

Mousavi, M.E., Bakhtiary, A.Y. and Enshaei, N. 2006. "Equilibrium profile of current-induced scour around submarine pipelines." *In International Conference on Offshore Mechanics and Arctic Engineering (Vol. 47497)* pp. 781-785.

Naghizadehrokni, M. 2018. "Liquefaction of sands and its effects on buried structures."

Nago, H. 1982. "Liquefaction of highly saturated sand layer under oscillating water pressure." *Memoirs of the School of Engineering, Okayama University, 16(1)* pp.91-104.

Nakamura, T., Kuramitsu, Y. and Mizutani, N. 2008a. "Tsunami scour around a square structure." *Coastal engineering journal, 50(02)* pp.209-246.

Nakamura, T., Kuramitsu, Y. and Mizutani, N. 2008b. "Tsunami-induced local scour around a square structure." *In Solutions to Coastal Disasters 2008: Tsunamis* 106-117.

Nandasena, N.A.K., Sasaki, Y. and Tanaka, N. 2012. "Modeling field observations of the 2011 Great East Japan tsunami: Efficacy of artificial and natural structures on tsunami mitigation." *Coastal Engineering, 67* pp.1-13.

Neill, C.R. 1964. *River bed Scour.* Calgary, Alberta, Canada: a review for bridge engineers. Contract No. 281, Res.Council of Alberta.

Nielsen, Peter. 1992. "Coastal bottom boundary layers and sediment transport ." *World scientific, (Vol. 4).*

Nistor I., Petroff C., Trisler D.,. 2019. *ASCE 7-16 Change Proposal Form.* ASCE, Structural Engineering Institute.

Nistor, I. and Palermo, D. 2015. *Post-Tsunami Engineering Forensics: Tsunami Impact on Infrastructure—Lessons from 2004 Indian Ocean, 2010 Chile, and 2011 Tohoku Japan Tsunami Field Surveys.* In Handbook of coastal disaster mitigation for engineers and planners (pp. 417-435), Butterworth-Heinemann.

Nistor, I., Palermo, D., Cornett, A. and Al-Faesly, T. 2011. "Experimental and numerical modeling of tsunami loading on structures." *Coastal Engineering Proceedings, (32)* pp.2-2.

Nistor, I.,. 2005. "The 26 December 2004 Earthquake and Tsunami-Hydrodynamic forces on physical infrastructure in Thailand and Indonesia." *In Proc. 2005 Canadian Coastal Eng. Conf.(Vol. 15).* Halifax, Canada.

Nouri, Y., Nistor, I., Palermo, D. and Cornett, A. 2010. "Experimental investigation of tsunami impact on free standing structures." *Coastal Engineering Journal* 52(01), pp.43-70.

Oertel, M., and Bung, D. B. 2012. "Initial stage of twodimensional dam-break waves: Laboratory versus VOF." *Journal of Hydraulic Research, 50(1)* 89–97.

Palermo, D., Nistor, I., Saatcioglu, M. and Ghobarah, A. 2013. "Impact and damage to structures during the 27 February 2010 Chile tsunami." *Canadian Journal of Civil Engineering, 40(8)* 750-758.

Pan, C. and Huang, W. 2012. "Numerical modeling of tsunami wave run-up and effects on sediment scour around a cylindrical pier." *Journal of engineering mechanics, 138(10)* pp.1224-1235.

Park, H., Cox, D.T. and Barbosa, A.R. 2017. "Comparison of inundation depth and momentum flux based fragilities for probabilistic tsunami damage assessment and uncertainty analysis." *Coastal Engineering* 122, pp.10-26.

Park, H., Cox, D.T., Lynett, P.J., Wiebe, D.M. and Shin, S. 2013. "Tsunami inundation modeling in constructed environments: A physical and numerical comparison of free-surface elevation, velocity, and momentum flux." *Coastal Engineering* 79, pp.9-21.

Paulik, R., Gusman, A., Williams, J.H., Pratama, G.M., Lin, S.L., Prawirabhakti, A., Sulendra, K., Zachari, M.Y., Fortuna, Z.E.D., Layuk, N.B.P. and Suwarni, N.W.I. 2019. "Tsunami Hazard and Built Environment Damage Observations from Palu Cityafter the September 28 2018 Sulawesi Earthquake and Tsunami." *Pure and Applied Geophysics, 176* 3305–3321.

Qi, G., Michel, J.C., Boivin, P. and Charpentier, S. 2011. "A laboratory device for continual measurement of water retention and shrink/swell properties during drying/wetting cycles." *HortScience, 46(9)* pp.1298-1302.

Qi, W., Gao, F., Han, X. and Gong, Q. 2012. "Local scour and pore-water pressure around a monopile foundation under combined waves and currents." *In The Twenty-second International Offshore and Polar Engineering Conference. International Society of Offshore and Polar Engineers.*

Qi, W.G. and Gao, F.P. 2019. "Local Scour around a Monopile Foundation for Offshore Wind Turbines and Scour Effects on Structural Responses." *Geotechnical Engineering-Advances in Soil Mechanics and Foundation Engineering.*

Rahman, H. Bolton Seed & M. S. 1978. "Wave-induced pore pressure in relation to ocean floor stability of cohesionless soils." (Marine Georesources & Geotechnology, 3:2,) (123-150).

Raikar, R.V. and Dey, S. 2006. "Pier scour and thin layered bed scour within a long contraction." *Canadian Journal of Civil Engineering, 33(2)* 140-150.

Raudkivi, A.J. and Ettema, R. 1983. "Clear-water scour at cylindrical piers." *Journal of Hydraulic Engineering,109(3)* 338-350.

Richmond, B., Szczuciński, W., Chagué-Goff, C., Goto, K., Sugawara, D., Witter, R., Tappin, D.R., Jaffe, B., Fujino, S., Nishimura, Y. and Goff, J. 2012. "Erosion, deposition and landscape change on the Sendai coastal plain, Japan, resultingfrom the March 11, 2011 Tohoku-oki tsunami." *Sedimentary Geology 282* 27–39.

Ritter, A. 1892. " Die fortpflanzung de wasserwellen. ." *Z. Ver. Dtsch. Ingenieure* 36 (33),947–954.

Rossetto, T., Peiris, N., Pomonis, A., Wilkinson, S. M., Del Re, D., Koo, R., & Gallocher, S. 2007. "The Indian Ocean tsunami of December 26,2004: observations in Sri Lanka and Thailand." *Natural Hazards* 105-124.

Ruangrassamee, A., Yanagisawa, H., Foytong, P., Lukkunaprasit, P., Koshimura, S. and Imamura, F. 2006. "Investigation of tsunami-induced damage and fragility of buildings in Thailand after the December 2004 Indian Ocean tsunami." *Earthquake Spectra, 22* pp.377-401.

Rudnicki, J.W. and Rice, J.R. 2006. "Effective normal stress alteration due to pore pressure changes induced by dynamic slip propagation on a plane between dissimilar materials." *Journal of Geophysical Research: Solid Earth, 111(B10).*

Saatcioglu, M., Ghobarah, A. and Nistor, I. 2006. "Performance of structures in Thailand during the December 2004 Great Sumatra earthquake and Indian Ocean tsunami." *Earthquake spectra, 22(3_suppl)* pp.355-375.

Saltzer, R.L. 2002. "Upper mantle structure of the Kaapvaal craton from surfacewave analysis—a second look." *Geophysical Research Letters* VOL.29,NO.6, 1093.

Sassa, S. and Takagawa, T. 2019. "Liquefied gravity flow-induced tsunami: first evidence and comparison from the 2018 Indonesia Sulawesi earthquake and tsunami disasters." *Landslides, 16(1)* pp.195-200.

Satake, K., Bourgeois, J., Abe, K., Abe, K., Tsuji, Y., Imamura, F., Lio, Y., Katao, H., Noguera, E. and Estrada, F. 1993. "Tsunami Field Survey of the 1992 Nicaragua Earthquake." *Eos, Transactions American Geophysical Union* 74(13), pp.145-157.

Sawada, Y., Miyake, M., Sumida, H. and Kawabata, T. 2014. "Pore water pressure and liquefaction in saturated sand bed induced by tsunami." *農業農村工学会論文集, 82(2)* pp.113-120.

Schooler, N.K., Dugan, J.E. and Hubbard, D.M. 2019. "No lines in the sand: Impacts of intense mechanized maintenance regimes on sandy beach ecosystems span the intertidal zone on urban coasts." *Ecological Indicators, 106* 105457.

Shafiei, S., Melville, B.W. and Shamseldin, A.Y. 2016. "Experimental investigation of tsunami bore impact force and pressure on a square prism." *Coastal Engineering, 110* pp.1-16.

Shen, H.W., Schneider, V.R. and Karaki, S.S. 1966. *Mechanism of local Scour.* EngineeringResearch Center, Colorado State Univ. Fort Collins, Colorado CER 66HWS22.

Shi, B.W., Yang, S.L., Wang, Y.P., Bouma, T.J. and Zhu, Q. 2012. "Relating accretion and erosion at an exposed tidal wetland to the bottom shear stress of combined current–wave action." *Geomorphology, 138(1)* pp.380-389.

Shibayama, T., Esteban, M., Nistor, I., Takagi, H., Thao, N. D., Matsumaru, R., Mikami, T.,Aranguiz, R., Jayaratne, R. & Ohira, K. . 2013. "Classification of tsunami and evacuation areas." *Natural Hazards, 67(2)* 365-386.

Shields, A. 1936. "Application of similarity principles and turbulence research to bed-load movement." *Mitteilunger der Preussischen Ver-suchsanstalt fu ̈r Wasserbau und Schiffbau, Berlin, 26*, p.p. 5–24.

Spiske, M., Weiss, R., Bahlburg, H., Roskosch, J. and Amijaya, H. 2010. "The TsuSedMod inversion model applied to the deposits of the 2004 Sumatra and 2006 Java tsunami and implications for estimating flow parameters of palaeo-tsunami." *Sedimentary Geology, 224(1-4)* pp.29-37.

St-Germain, P., Nistor, I. and Townsend, R. 2012. "Numerical modeling of the impact with structures of tsunami bores propagating on dry and wet beds using the SPH method." *International Journal of Protective Structures, 3(2)* pp.221-255.

St-Germain, P., Nistor, I., Townsend, R., & Shibayama, T. 2014,. "Smoothed-Particle Hydrodynamics Numerical Modeling of Structures Impacted by Tsunami Bores." *J. Waterway, Port, Coastal, Ocean Eng* 140(1): 66-81.

Stoker, J.J. 2011. "Water waves: The mathematical theory with applications." *John Wiley & Sons* Vol. 36.

Stolle, J., Ghodoosipour, B., Derschum, C., Nistor, I., Petriu, E. and Goseberg, N. 2019. "Swing gate generated dam-break waves." *Journal of Hydraulic Research* 57(5):675-87.

Stolle, J., Krautwald, C., Robertson, I., Achiari, H., Mikami, T., Nakamura, R., Takabatake, T., Nishida, Y., Shibayama, T., Esteban, M. and Nistor, I. 2020. "Engineering lessons from the 28 September 2018 Indonesian tsunami: debris loading." *Canadian Journal of Civil Engineering, 47(1)* pp.1-12.

Stolle, Jacob. 2019. *Debris Hazard Assessment in Extreme Flooding Events.* PhD Thesis, Ottawa: The University of Ottawa.

Sumer, B.M. 2014. "Liquefaction Around Marine Structures." *(With Cd-rom) (Vol. 39). World scientific.*

Sumer, B.M., Ansal, A., Cetin, K.O., Damgaard, J., Gunbak, A.R., Hansen, N.E.O., Sawicki, A., Synolakis, C.E., Yalciner, A.C., Yuksel, Y. and Zen, K. 2007. "Earthquake-Induced Liquefaction around Marine Structures." *Journal of waterway, port, coastal, and ocean engineering 133.1* 55-82.

Sumer, B.M., Fredsøe, J. and Christiansen, N. 1992. "Scour around vertical pile in waves." *Journal of waterway, port, coastal, and ocean engineering, 118(1)* pp.15-31.

Takegawa, N., Sawada, Y., Murai, K. and Kawabata, T. 2018. "Influence of liquefaction on scour behind coastal dikes due to tsunami overflow." *International Journal of Geotechnical Engineering, 12(1)* pp.40-45.

Tanaka, N., Yasuda, S., Iimura, K. and Yagisawa, J. 2014. "Combined effects of coastal forest and sea embankment on reducing the washout region of houses in the Great East Japan tsunami." *Journal of Hydro-Environment Research, 8(3)* pp.270-280.

Tavouktsoglou, N.S., Harris, J.M., Simons, R.R. and Whitehouse, R.J.S. 2017. "Equilibrium Scour-Depth Prediction around Cylindrical Structures." *Journal of Waterway, Port, Coastal, and Ocean Engineering, 143(5)* 04017017.

Terzaghi, K. 1943. *Theoretical Soil Mechanics.* New York, NY: John Wiley & Sons.

The 2011 Tohoku Earthquake Tsunami Joint Survey Group. 2011. Accessed October 19, 2015. Available at http://www.coastal.jp/ttjt/.

Tomiczek, T., Wyman, A., Park, H. and Cox, D.T. 2019. "Modified Goda Equations to Predict Pressure Distribution and Horizontal Forces for Design of Elevated Coastal Structures." *Journal of Waterway, Port, Coastal, and Ocean Engineering, 145(6)* p.04019023.

Tonkin, S., Yeh, H., Kato, F. and Sato, S. 2003. "Tsunami scour around a cylinder." *Journal of Fluid Mechanics, 496* pp.165-192.

Tonkin, S.P., Francis, M. and Bricker, J.D. 2014. "Limits on coastal scour depths due to tsunami." *International Efforts in Lifeline Earthquake Engineering* pp. 671-678.

Triatmadja Radianta, Nurul Hijah Siti, Nurhasanah Any . 2011. "Scouring around coastal structures." *6th Annual International Workshop & Expo on Sumatra Tsunami Disaster & Recovery.*

Triatmadja, R. 2017. "Simulation Of Scouring Around A Vertical Cylinder Due to Tsunami." *Science of Tsunami Hazards, 36(2).*

Van Rijn, L.C. and Walstra, D.J.R. 2003. "Modelling of sand transport in delft3d-online." *Deltares (WL).*

Van Rijn, L.C. 2013. "Simple general formulae for sand transport in rivers, estuaries and coastal waters." *Retrieved from www. leovanrijn-sediment. com* pp.1-16.

Vanapalli, S.K. and Fredlund, D.G. 2000. "Comparison of different procedures to predict unsaturated." *Proceedings of Geo-Denver 2000, ASCE Geotechnical Special Publication, 99* p.p. 195–209.

Vischer, D.L. and Hager, W.H. 1998. *Dam hydraulics.* Wiley,Chichester, UK: p.316.

Wang, X., Chen, S., Wang, R. and Zhang, J.M. 2020. "Large wave flume tests on wave-induced response of sandy seabed adjacent a water intake." *Ocean Engineering, 195* 106709.

Wei, Y., Chamberlin, C., Titov, V.V., Tang, L. and Bernard, E.N., 2013. "Modeling of the 2011 Japan tsunami: Lessons for near-field forecast." *Pure and Applied Geophysics*, 170(6), pp.1309-1331

Whitham, G. 1955. "The effects of hydraulic resistance in the dam-break." *Proceedings of the Royal Society of London. Series A. Mathematical and Physical Sciences* (Proceedings of the Royal Society of London. Series A. Mathematical and Physical Sciences) 399-407.

Wilson, R., Davenport, C. and Jaffe, B. 2012. "Sediment scour and deposition within harbors in California (USA), caused by theMarch 11, 2011 Tohoku-oki tsunami." *Sedimentary Geology, 282* 228–240.

Wu, N.J., Hsiao, S.C., Chen, H.H. and Yang, R.Y. 2016. "The study on solitary waves generated by a piston-type wave maker." *Ocean Engineering, 117* pp.114-129.

Wu, N.J., Tsay, T.K. and Chen, Y.Y. 2014. "Generation of stable solitary waves by a piston-type wave maker." *Wave Motion, 51(2)* pp.240-255.

Wüthrich, D., Pfister, M., Nistor, I. and Schleiss, A.J. 2020. "Effect of building overtopping on induced loads during extreme hydrodynamic events." *Journal of Hydraulic Research, 58(2)* pp.289-304.

Wüthrich, D., Pfister, M., Nistor, I. and Schleiss, A.J. 2018. "Experimental study of tsunami-like waves generated with a vertical release technique on dry and wet beds." *Journal of Waterway, Port, Coastal, and Ocean Engineering* 144(4), p.04018006.

Wüthrich, D., Pfister, M., Nistor, I. and Schleiss, A.J. 2018. "Experimental study on the hydrodynamic impact of tsunami-like waves against impervious free-standing buildings." *Coastal Engineering Journal, 60(2)* pp.180-199.

Yang, J. 2005. "Pore pressure coefficient for soil and rock and its relation to compressional wave velocity." *Geotechnique, 55(3)* pp.251-256.

Yanmaz, A.M. and Altinbilek, H.D.G.ˇ.A. 1991. "Study of time-dependent local scour around bridge piers." *Journal of Hydraulic Engineering, 117(10)* 1247-1268.

Yarnell, D.L., 1934. "Bridge piers as channel obstructions." United States Department of Agriculture, Technical Bulletin 442.

Yeh, H. and Mason, H.B. 2014. "Sediment response to tsunami loading: mechanisms and estimates." *Geotechnique, 64(2)* pp.131-143.

Yeh, H., Sato, S. and Tajima, Y. 2013. "The 11 March 2011 East Japan earthquake and tsunami: Tsunami effects on coastal infrastructure and buildings." *Pure and Applied Geophysics 170.6-8* 1019-1031.

Yeh, Harry, and Li Wenwen. 2008. "Tsunami scour and sedimentation." *In Proceedings 4th International Conference on Scour and Erosion (ICSE-4)* pp. 95-106.

Young, Y.L., White, J.A., Xiao, H. and Borja, R.I. 2009. "Liquefaction potential of coastal slopes induced by solitary waves." *Acta Geotechnica, 4(1)* 17-34.

Young, Y.L., Xiao, H., White, J.A. and Borja, R.I. 2008. "Can Tsunami Drawdown Lead to Liquefaction Failure of Coastal Sandy Slopes?" *The 14th World Conference on Earthquake Engineering.* Beijing, China.

Zen, K., Yamazaki, H. 1991. "Field observation and analysis of wave-induced liquefaction in seabed." *Soil Found.*, 31(4),161−179.

Zhai, Y., Zhang, J., Jiang, L., Xie, Q. and Chen, H. 2018. "Experimental study of wave motion and pore pressure around a submerged impermeable breakwater in a sandy seabed." *International Journal of Offshore and Polar Engineering, 28(01)* pp.87-95.

Zhu, B., Ren, J. and Ye, G.L. 2018. " Wave-induced liquefaction of the seabed around a single pile considering pile–soil interaction." *Marine Georesources & Geotechnology* 150-162.

Zoppou, C. and Roberts, S. 2003. "Explicit schemes for dam-break simulations." *Journal of Hydraulic Engineering, 129(1)* pp.11-34.

Appendix A

ASCE 7-16 Change Proposal Form

Proposals to revise the ASCE 7-16 Standards must be submitted using this form. Proposals from outside the Committee/Subcommittees are to be submitted via email to Jon Esslinger, Director, Codes and Standards, at Jesslinger@asce.org

Submitted by: Ioan Nistor, Catherine Petroff, Dan Trisler
University of Ottawa, 115 Seraphin-Marion, Room HGN215, Ottawa, ON, K1N 6N5, Canada
(613) 562-5800 x6147
nistor@uottawa.ca , cpetroff@uw.edu, dan.trisler@hartcrowser.com

Submission date: 9/6/2019

Considered by ASCE 7 Subcommittee on: Ch. 6: Tsunami Loads and Effects

---

FILENAME: TS-CH06-20r00 by Nistor-Petroff-Trisler 6.12.2.4.1 Pile Foundation Scour determined by Froude number
BRIEF DESCRIPTION: Adding an Alternate Sustained Flow Scour Calculation for Pile Foundation Elements

SCOPE: 6.12.2.4.1 Sustained Flow Scour
PROPOSAL FOR CHANGE: (Use ~~strike-out~~ and underline format to indicate text to be removed or added, respectively; related modification/proposed addition to Commentary shall be included below.)

6.2 **PILE:** Deep foundation element, which includes piers, caissons and piles.

6.12.2.4.1 **Sustained Flow Scour**. Scour, including the effects of sustained flow around structures, shall be evaluated at the foundations of building corners and at the extreme ends of structural piers or walls within 22.5 degrees of perpendicular to the flow and having a projected width to maximum inundation depth ratio of 3 or more. Calculated sustained flow scour depth shall be taken to be at the flow-facing surface of the foundation element. The assumed spatial extent shall be considered to encompass the indicated building perimeter elements and to extend from those foundation elements at a 1 vertical to 1 horizontal slope for consolidated or cohesive soils and at a 1 vertical to 3 horizontal slope for unconsolidated or granular soils. Scour depth need not be taken lower than the top surface of intact rock strata or other nonerodible strata that are capable of preventing scour from tsunami flow of 30 ft/s (9.14 m/s), nor be determined for Open Structures. Sustained flow scour design depth and ~~area~~ extent shall be determined by one of the following methods:

a. Dynamic numerical or physical modeling or empirical methods in the recognized literature.

b. ~~It shall be permitted to determine~~ Sustained flow scour ~~and~~ with associated pore pressure softening effects determined in accordance with Table 6.12-1 and Figure 6.12-1. Local scour depth caused by sustained flow given by Table 6.12-1 and Figure 6.12-1 shall be permitted to be reduced by an adjustment factor in areas where the maximum flow Froude number determined in accordance with Eq. (6.6-3) is less than 0.5. The adjustment factor shall be taken as varying linearly from 0 at the horizontal inundation limit to 1.0 at the point where the Froude number is 0.5. ~~The assumed area limits shall be considered to encompass the indicated building perimeter elements and to extend from those foundation elements at a 1 vertical to 1 horizontal slope for consolidated or cohesive soils and at a 1 vertical to 3 horizontal slope for unconsolidated or noncohesive soils.~~

Table 6.12-1 Design Scour Depth Caused by Sustained Flow and Pore Pressure Softening

Inundation Depth *h*	Scour Depth D_s
<10 ft (3.05 m)	1.2 *h*
≥10 ft (3.05 m)	12 ft (3.66) m

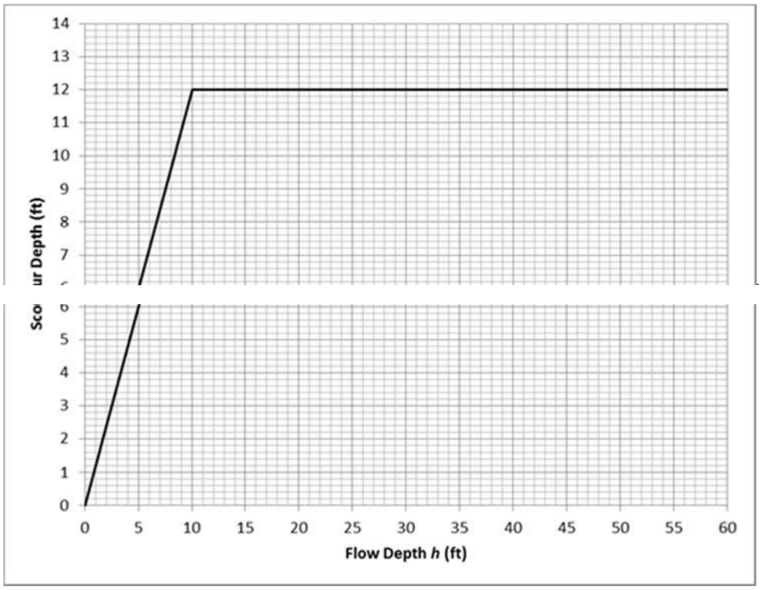

FIGURE 6.12-1 Design Scour Depth Caused by Sustained Flow and Pore Pressure Softening [1 ft = 0.305 m]

c. Where vertical foundation elements, with cross sections not exceeding an aspect ratio of 2:1, become exposed to flow due to Local Scour determined in accordance with method a or b, or due to General Erosion as determined in accordance with Section 6.12.2.3, and where the Froude number is less than 1.7, it shall be permitted to calculate the vertical extent of Pile Scour along the length of the vertical foundation element using Table 6.12-2 and Figure 6.12-2. The width, *b*, is the projected foundation element width in the direction perpendicular to the flow. The total scour for the foundation need not exceed the depth determined by Figure 6.12-1.

Table 6.12-2 Vertical Extent of Pile Scour to Projected Element Width Ratio

Froude Number, *Fr*	**Pile Scour Extent to Projected Element Width Ratio, D_s/b**
≤1.0	1.3 *Fr*
≥1.0	1.3

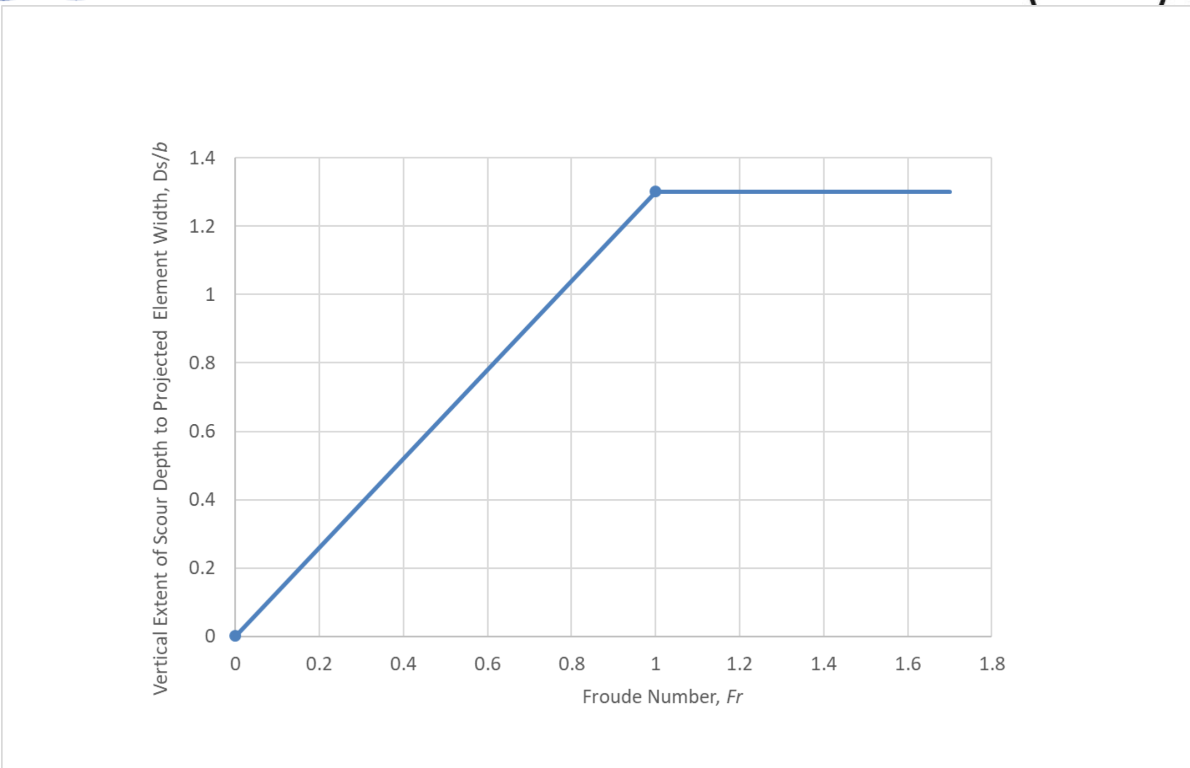

FIGURE 6.12-2 Vertical Extent of Pile Scour to Projected Element Width Ratio

COMMENTARY CHANGE: (Use ~~strike-out~~ and underline format to indicate text to be replaced and new text, respectively.)

C6.12.2.4.1 Sustained Flow Scour. Sustained flow scour is caused by tsunami flow around a structure. Numerical, physical modeling or empirical methods may be used to evaluate sustained flow scour; the analysis method should consider the effects of pore pressure softening.

The methodology used to develop Table 6.12-1 and Figure 6.12-1 is described in Tonkin et al. (2013) and is based on a comparison of post-tsunami field observations of scour around structures in Chock et al. (2013b) and Francis (2008) with the model of Tonkin et al. (2003).

The methodology used to develop Table 6.12-2 and Figure 6.12-2 for Pile Scour is based on experiments carried out by Razieh et al. (2017, 2019), Mehrzad et al. (submitted for publication) and Lavictoire et al. (2014). Figure C6.12-3 presents experimental data from these studies regarding the vertical extent of scour to element width ratio and Froude number.

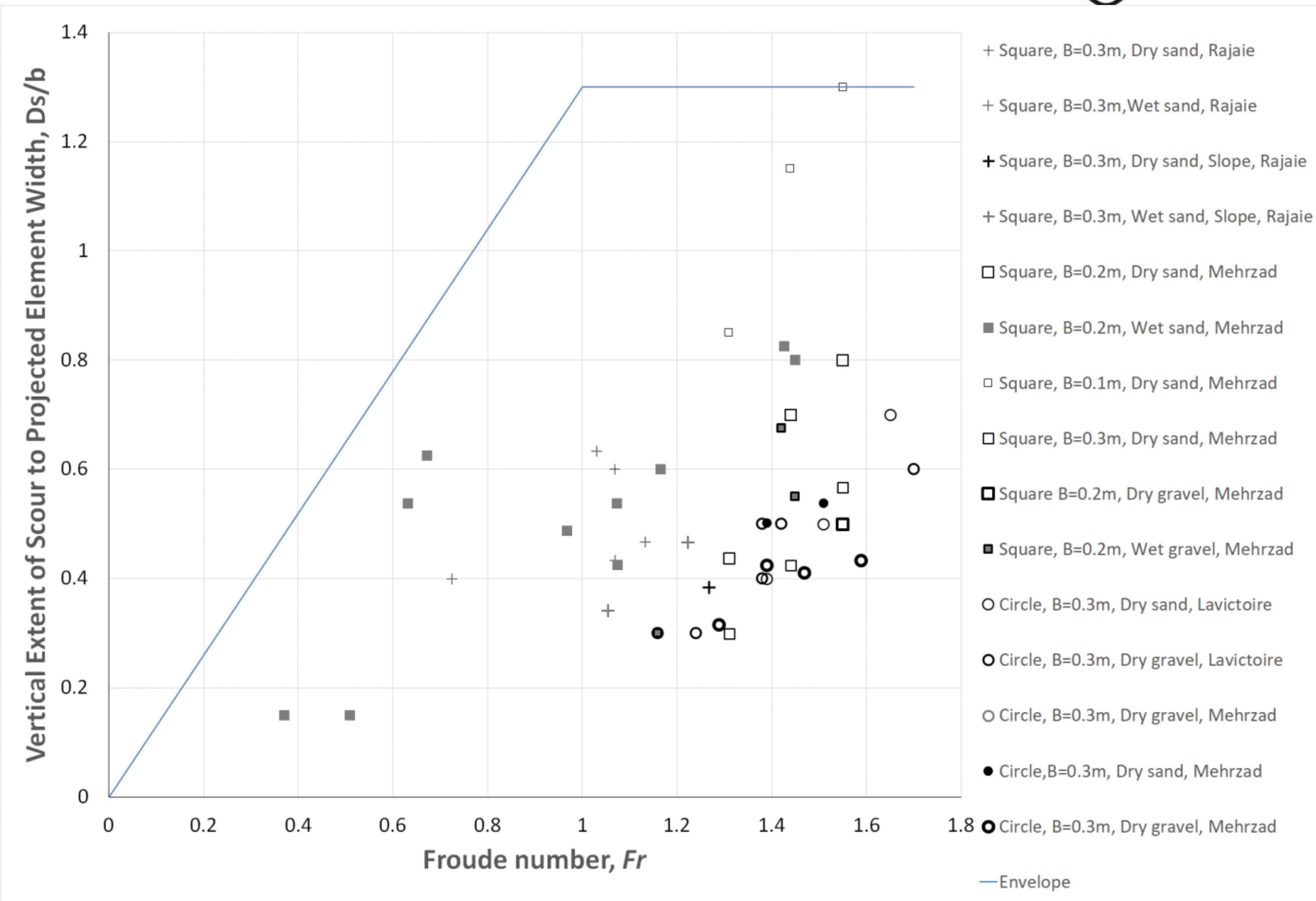

Figure C6.12-3 Vertical Extent of Scour to Element Width Ratios for Foundation Elements with Different Soil Conditions and Froude Numbers in Scaled Laboratory Experiments

The use of the Froude number relates the inertial energy of the flow and the accompanying flow turbulence to the associated maximum scour depth around a structural element with a given geometry. A maximum Froude number of 1.7 is specified for use of Figure 6.12-2 since this was the upper limit for the Froude number of the experimental data. As shown in the experiment data presented in Figure C6.12-3, scour around foundation elements depends on the physically-based parameters of flow conditions (Froude number), sediment characteristics (sand, gravel, and soil saturation), foundation element geometries (square and circular columns were tested), and slope of the soil bed.

For deep foundation systems with pile caps, grade beams, or similar load-carrying or horizontal tie elements, the scour depth calculated using Figure 6.12-1, which includes the effects of general erosion, is used to determine whether scour extends down to the top of the pile. Subsequently, Figure 6.12-2 is used to determine the vertical extent of scour along the length of the pile itself.

The-spatial extent of scour around a structure is primarily based on field observations in Francis (2008) and Chock et al. (2013b); a schematic representation of the extent and geometry of sustained flow scour is illustrated in Figure C6.12-~~3~~4.

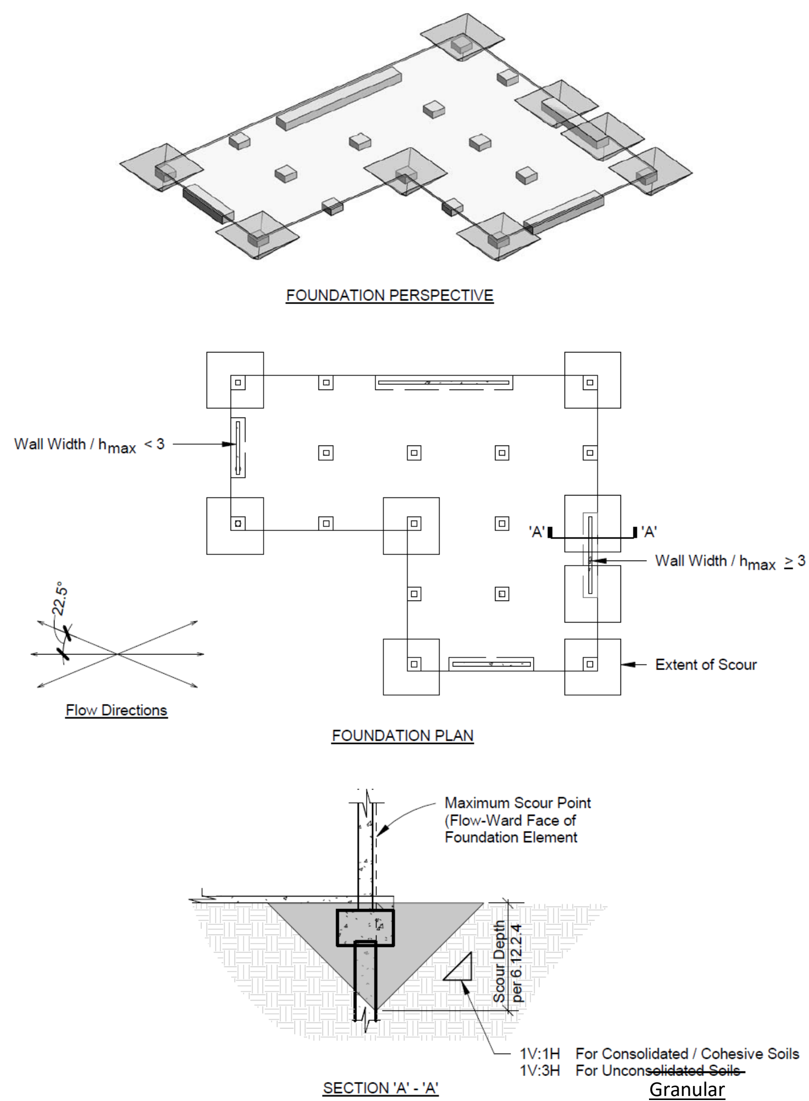

C6.12-4
FIGURE C6.12~~-3 Sch~~ematic of Sustained Flow Scour Extents

Additional References:

1. Lavictoire A., Nistor I., Rennie C., (2014). Local scour around structures due to hydraulic bores, Annual Conference of the Canadian Society for Civil Engineering, CSCE, Halifax, Canada, 10 p.
2. Razieh, S., Nistor, I., Rennie, C. (2017). Modeling supercritical flow-induced scour around structures, 23rd Canadian Hydrotechnical Conference, CSCE, Vancouver, Canada, 10 p.
3. Razieh, S., Nistor, I., Rennie, C. (2019). Scour mechanics of a tsunami-like bore around a square structure, JWPCOE/JHE ASCE, 31p (in submission)
4. Mehrzad, Effect of extreme hydrodynamic flows on scour around structures, JWPCOE - ASCE (in preparation, expected 2020).

[Note: ASCE 7-16 Figure C6.12-4 Schematic of Tsunami-Induced Loading of Exterior Slabs on Grade referenced in C6.12.4.2 to be renumbered to Figure C6.12-5

REASON FOR PROPOSAL: (a reason statement providing the rationale for the proposed change must be provided – attach additional pages if necessary).

The proposed change is submitted to allow for a reduction in the design scour depth by considering the geometry of deep foundation elements and the speed of the incoming flow. Experimental data (Razieh et al. (2017, 2019), Mehrzad et al (2020), and Lavictoire et al (2014)) allow for an empirically-based assessment of the scour extent that takes into consideration the Froude number for vertical foundation elements. Additional editorial changes are proposed for clarity and conformity of language with engineering practice.

CONSTRUCTION COST COMMENTS: [Click to Select] [OPTIONAL: Click to enter comments on construction cost impacts.]

Committee Action on Proposal: Approve Tsunami Loads and Effects Subcommittee has 11

Voting Members, 17 Associate Members

Voting Members 8 affirmative, 2 affirmative with comments (editorial); 0 negatives.

Committee Notes including Negative or Opposing Comments to send forward:

[Click or tap here to provide summary of Negatives resolved to send forward; OPTIONAL: Also include opposing comments if submitted.]

Appendix B

Scale Effects

The current study has its limitations when it comes to physical modeling at small scales.

Chanson (2006) assessed images and characteristics of the 2004 Indian Tsunami, and determined tsunami bores are similar to a dam-break bore propagating over a dry bed. In the present study conducted in the Hydraulic Laboratory at the University of Ottawa, tsunami waves were simulated using dam-break bores generated by the rapid opening of a swing gate which impounded a set volume of water with a controlled level. In previously performed experiments, Mehrzad et al. (2016) utilized this dam-break method to examine the impacts of the three different sizes of a square-shaped structure and various hydrodynamic dam-break bore characteristics on scouring around the models. Similarly, Lavictoire (2015) generated the dam-break bores in the same lab facility to study the effects of different sediment sizes and impoundment depths on scour depths around a cylinder. However, the analytical solution of the free-surface profile of the dam-break bores showed steeper wave tip in these bores compare to real tsunamis, which depends upon the flow resistance (Chanson 2005; Stolle 2019).

The downscaling considered in this experimental work was determined based on flow depth (H_o) and the structural model diameter (D). The scour formation around a structure can be influenced by the flow depth and flume width. The effect of the flow depth on the scour depth is examined by the ratio of H_o/D introduced by Arneson et al. (2012) and Ettema et al. (2011). The results of their investigations indicated that when this ratio is larger than 1.4, the pier is classified narrow, but for $0.2<H_o/D<1.4$ the pier is classified as transitional. Particularly for transitional cases, adjustments in flow depth or pier width can alter the vortex structures around the pier and influence scour depth (Ettema et al. 2011). The maximum flow depth in this study is 0.33 m which yields $H_o/D = 1.1$, given D= 0.3 m. The studied case is thus in the transitional regime. As for flume width, it is generally accepted that flow blockage ratio influences scour depth (e.g., Yarnell 1934), and this can be accounted for in design when estimating contraction scour (Arneson et al. 2012). In the present case, flume width was 1.5 m and pier width was 0.3 m, thus the blockage ratio was 0.2. There is a possibility that this blockage ratio may have increased observed pier scour depth. The candidate acknowledges this limitation; however, based on the observed scour contour plots scour did not extend near the wall, thus this flume scale effect should not have been excessive. Froude scaling was employed for some experiments, with experimental Froude numbers both above and below the critical threshold value of 1. Observed Froude numbers in prototype tsunamis bores are on the order of 1-2 (Chock et al. 2012; Lavictoire 2015), thus the supercritical cases presented in this thesis have Froude numbers similar to actual tsunamis.

The chosen length scale for this experimental study is 1:40 in order to simulate the maximum bore depth recorded during the 2011 Japan Tsunami. Due to the limitation in the flume depth (1 m), the 1:40 length scale enabled replication of the maximum flow depths of at least 15 m and average flow velocity of 6.2 m/s; the corresponding model scale values being almost 0.4 m impoundment depth and flow velocity of at least 1 m/s (Nandasena et al., 2012). In addition, the experiments were run for 2 minutes which is equivalent to 12 minutes prototype inundation time for the first tsunami wave inundating the shoreline during the 2011 Japan Tsunami (Wei et al., 2013).

The sand used in this experimental investigation exhibited a mean particle diameter of 0.5 mm. This sediment size was selected because of its lack of cohesiveness and accessibility. However, Ettema et al. (1998) indicated that utilizing cohesionless grains to investigate local scour can cause scour holes deeper than what would be usually observed at the prototype scale after upscaling the scour depth. This consequence was described as a scaling effect by Lee and Strum (2009); they explained that the sediment size in experimental scale distorts the ratio of pier width to sediment grain size compared to the equivalent prototype case, which can lead to a deeper scour hole. The sediment size cannot be scaled in the same way that piers can be (Yanmaz and Altinbilek, 1991). However, the sediment particles can be scaled down based on the Shields diagram. The sediments smaller than 0.1 mm tend to act cohesively and those smaller than 0.6 mm ripple on the bed surface. Therefore, the sediments using in experimental studies are often coarser than obtained based on the scaling. This scaling inaccuracy causes an imperfect scaling ratio of physical models (Lee and Sturm 2009). Thus, most of the physical modeling investigations are coping with distorted models (Raikar and Dey, 2006). Nonetheless, to minimize the effect of sediment size (d_{50}) on scour depth, the criterion proposed by Melville and Chiew (1999) was considered, i.e., one should ensure that D/d_{50}>50. In the case of the present study, this ratio is 600, such that the obtained scour depths in these experiments were considered independent of the sediment size.